Doctoral thesis

Search for Minimal Universal Extra Dimensions in the final state involving muons, jets and missing transverse energy in $\sqrt{s} = 8$ TeV pp collisions with the ATLAS detector

Ljiljana Morvaj

High Energy Physics Laboratory
Department of Physics, Nagoya University

November 2014

名古屋大学
NAGOYA UNIVERSITY

Abstract

This thesis presents the search for Minimal Universal Extra Dimensions (mUED) in $\sqrt{s} = 8$ TeV proton-proton collisions in the final state involving low momentum (soft) muons, jets and missing transverse energy. The dataset used corresponds to the integrated luminosity of 20.1 fb^{-1} delivered by the Large Hadron Collider (LHC) in 2012 and recorded with the ATLAS detector.

The mUED model is an extension of the Standard Model (SM) of particle physics which postulates the existence of one flat extra spatial dimension accessible to all the SM fields. Particles propagating in the compactified extra dimension form a tower of Kaluza-Klein (KK) states. Due to the symmetry called the KK-parity, the lightest KK-particle (LKP) is stable and is a plausible dark-matter candidate. The preferred mass of the dark-matter LKP lies at the TeV scale, making it accesible at the LHC. Due to typically small mass splittings between the mUED states in the phase-space region of interest, the decay products of KK-particles have relatively low momentum. Thus the characteristic signature of mUED at the LHC consists or relatively soft leptons and jets, in addition to the missing transverse energy (E_T^{miss}) caused by the LKP escaping detection.

The search for mUED is conducted in the final state containing two muons with transverse momenta between 6 GeV and 25 GeV. In order to ensure efficient prompt-lepton identification at low momenta a dedicated lepton performance study, in terms of lepton isolation optimisation, is performed as a first step. The optimised isolation results in a considerable improvement in the separation of signal leptons from the non-prompt (fake) lepton background. Next, the event selection is optimised to increase the signal-to-background ratio. Large part of the SM backgrounds is suppressed by requiring relatively large E_T^{miss}, in addition to placing an upper bound on muon momenta. Top-quark pair production ($t\bar{t}$) is further suppressed by vetoing the presence of $b-$quark-initiated jets in the final state. The fake muon background is estimated in a fully data-driven way, where the probability of non-prompt muons being identified as prompt is measured in the data and used as an input to the method. The contribution of the $t\bar{t}$ background is estimated in a semi data-driven way, where the $t\bar{t}$ normalisation factor is extracted with a profile-log-likelihood fit to the data in the $t\bar{t}$ control region, and the Monte Carlo simulation is used for the extrapolation of the fit result to the signal region. Purely Monte Carlo based estimate is used for other minor backgrounds.

No excess above the SM expectation is observed in the signal region. The upper limit at 95% confidence level (CL) on the number of non-SM events of 7.7 is set using the CL_S method. This limit corresponds to an upper limit on the visible cross section of 0.39 fb. Limits are also set on the parameters of the mUED model. Values of the inverse compactification radius R^{-1}, corresponding approximately to the LKP mass, below 940 GeV are excluded at 95% CL for $\Lambda R \sim 5$, where Λ is the ultra-violet cut-off of the theory.

The analysis presented in this thesis places the most stringent limits on the LKP mass for $\Lambda R \sim 5$ region up to date. It is the first dedicated search for mUED in the final state involving soft muons, the signature which is challenging in the high-luminosity and high-energy environment of the LHC. As various other new-physics models could exhibit similar final states, in particular compressed Supersymmetry, the significance of the work in this thesis extends beyond testing the mUED model. Subsequent reinterpretations of the model-independent limits on the visible cross section could constrain other new-physics scenarios resulting in similar signatures.

Contents

Chapter 1

Theory and motivation

The Standard Model (SM) represents our current best understanding of the elementary particles and forces that make up our Universe. It is a theory that has succeeded in explaining almost all experimental results, as well as successfully predicted a wide range of phenomena. Ever since its beginning in the 1970s, it has been tested in various experiments up to a remarkable precision.

However, there are still mysteries in particle physics and cosmology for which the SM does not have an answer. This has motivated various models of beyond-the-Standard-Model (BSM) physics which attempt to provide solutions to these problems. One such model, Universal Extra Dimensions (UED), is the primary scope of this thesis. In its minimal form, only one extra spatial dimension in which all the SM fields propagate, the UED model provides a viable candidate for dark matter – the lightest Kaluza-Klein photon. When extended to the case of more spatial dimensions it addresses also some of the other question of the SM, such as the hierarchy problem or why there are exactly three generations of fermions.

Sec. 1.1 describes the basic properties of the Standard Model. The shortcomings of the SM are introduced in Sec. 1.2, while Sec. 1.3 discusses the dark-matter problem in more detail. Physics in extra spatial dimensions is explained in Sec. 1.4, while the properties and the theoretical framework of the minimal UED model are discussed in more detail in Sec. 1.5. Sec. 1.6 describes the lightest Kaluza-Klein photon as a dark-matter candidate. Finally, Sec. 1.7 lists all the present bounds on mUED parameters coming from various experimental and theoretical constraints.

1.1 The Standard Model of particle physics

According to the Standard Model [1], the basic building blocks of matter are fermions, divided into two categories: quarks and leptons (see Fig. 1.1). While leptons can exist as free particles, quarks are always found in a bound state inside composite hadrons: mesons and barions. The four fundamental forces in the Universe are the strong, the weak, the electromagnetic and the gravitational force. For the first three, the bosonic force-carrier particles (also known as

gauge bosons) are well known and established in the Standard Model: gluons carry the strong, W- and Z-bosons the weak, and photons are the messengers of the electromagnetic force. The corresponding force-carrier of the gravity, the graviton, has not yet been experimentally observed. What is more, the quantum theory used in describing the small-scale phenomena of strong, weak and electromagnetic interactions, has not yet been successfully combined with the general theory of relativity used in describing the large-scale gravity phenomena. As a result, although well understood at the large distances characteristic of the Universe, the gravity is not a part of the Standard Model framework. The last piece of the Standard Model, responsible for the generation of the elementary-particle masses, is the Higgs boson. It has been pointed out in 1964 as a particle emerging out of theories proposed to explain the masses of gauge vector bosons [2], [3]. On July 4 2012, the LHC experiments ATLAS and CMS announced the discovery of a new boson [4], [5]. Subsequent measurements confirmed that the particle has properties of the SM Higgs boson. In October 2013 the Nobel prize in physics was awarded jointly to Franois Englert and Peter W. Higgs "for the theoretical discovery of a mechanism that contributes to our understanding of the origin of mass of subatomic particles, and which recently was confirmed through the discovery of the predicted fundamental particle, by the ATLAS and CMS experiments at CERN's Large Hadron Collider" [6]. With the experimental confirmation of the Higgs boson, the Standard Model is complete.

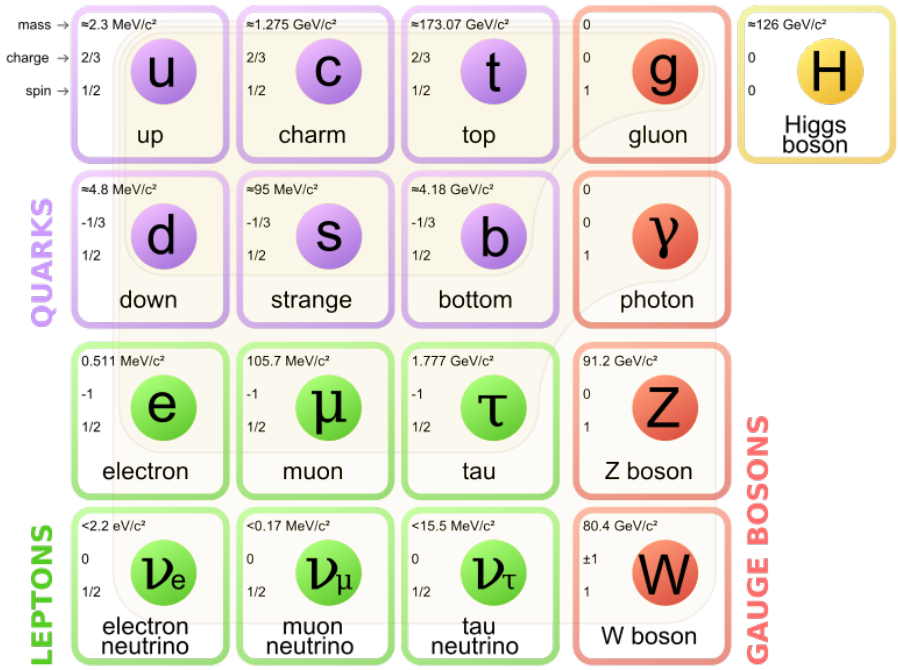

Figure 1.1: The elementary particles in the Standard Model of particle physics (image from [7]).

1.1.1 Quantum chromodynamics

Quantum chromodynamics (QCD) is the theory of strong interactions. The symmetry group of QCD is $\mathrm{SU}(3)_C$, where "C" stands for color, the conserved charge of the interaction. The local gauge invariance implies the existence of massless spin 1 bosons which mediate the interaction – the $\mathrm{SU}(3)_C$ symmetry gives rise to 8 massless gluons. Due to the non-abelian nature of $\mathrm{SU}(3)_C$, gluons themselves carry the color quantum number and can interact among themselves (resulting in the "anti-screening" effect at low energies, see below).

The value of the QCD coupling, $\alpha_S = g_S^2/4\pi$, depends on the scale μ_R at which it is evaluated (see Fig. 1.2). At the leading-logarithm approximation it can be expressed as

$$\alpha_S(\mu_R^2) = \frac{\alpha_S(\mu_0^2)}{1 + b_0\alpha_S(\mu_0^2)\ln\frac{\mu_R^2}{\mu_0^2}} = \frac{1}{b_0\ln\frac{\mu_R^2}{\Lambda_{QCD}}}, \tag{1.1}$$

where $b_0 = \frac{11C_A - 2n_f}{12\pi}$, with C_A being the number of colours, and n_f the numbers of quark flavors with their mass below the scale μ_R. That is to say, the value of α_S can be expressed in terms of the value of the coupling at a reference scale μ_0, or in terms of a non-perturbative constant Λ_{QCD}, the scale at which the coupling diverges. At scales $\mu_R \gg \Lambda_{QCD}$, the coupling becomes weak and the quarks and gluons behave almost as if free – this phenomenon is called the asymptotic freedom. At large momentum transfers μ_R it is thus possible to calculate the QCD related quantities using the perturbation series in the small α_S coupling. At low scales, $\mu_R \sim \Lambda_{QCD}$, the coupling becomes strong, which results in quarks and gluons being tightly bound into hadrons, and the perturbative description breaks down. Being a non-perturbative quantity, Λ_{QCD} is not very well defined, but corresponds roughly to 200 MeV – the scale of hadron masses. The scale μ_R at which the coupling is to be evaluated, is called the renormalisation scale. There is no unique choice for this scale, but it should roughly correspond to the momentum transfer involved in the interaction of interest.

1.1.2 Electroweak theory

$\mathrm{SU}(2)_L \times \mathrm{U}(1)_Y$ is the group proposed by Glashow, Salam and Weinberg in 1960 in order to achieve the unification of the electromagnetic and weak interactions. The $\mathrm{SU}(2)_L$ is the gauge symmetry group of the weak isospin. It has the "$V - A$" (vector − axial) form, i.e. its three massless gauge bosons (denoted as $W_\mu^1, W_\mu^2, W_\mu^3$) couple only to left-handed fermions. The "$V - A$" form of the $\mathrm{SU}(2)_L$ interaction ensures that parity is violated, and violated maximally, in the charged weak interactions.

The hypercharge operator Y generates the symmetry group $\mathrm{U}(1)_Y$, its gauge boson is neutral and denoted as B_μ. The weak boson masses are generated through couplings to the scalar Higgs field. The form of the Higgs potential is such, that although the potential itself is symmetric, its ground state is not, i.e. the symmetry is spontaneously broken (see Fig.1.3). The Higgs field acquires a vacuum expectation value, denoted as v, which is then responsible for generating

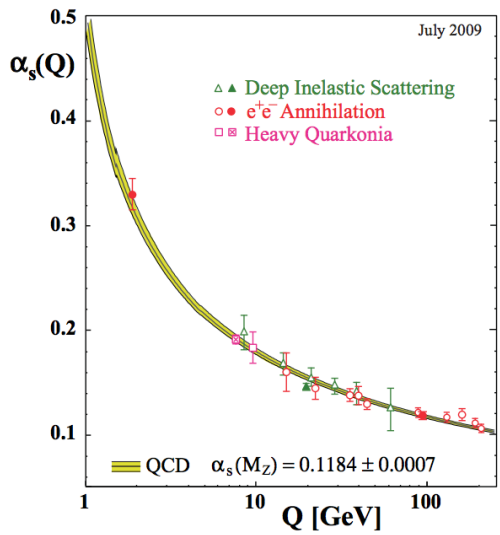

Figure 1.2: Summary of measurements of α_S as a function of the respective energy scale Q (the 2009 world average). The curves are QCD predictions for the combined world average value of $\alpha_S(M_Z)$. Full symbols are results based on N3LO QCD, open circles are based on NNLO, open triangles and squares on NLO QCD. The cross-filled square is based on lattice QCD [49].

the weak boson (as well as fermion) masses. The $\mathbf{W}_\mu$ and B_μ bosons mix to form the physical states, namely massive charged $W_\mu^\pm$

$$W_\mu^\pm = \frac{1}{\sqrt{2}}(W_\mu^1 \mp iW_\mu^2), \tag{1.2}$$

and neutral bosons – massless photon A_μ and massive Z_μ

$$A_\mu = B_\mu \cos\theta_W + W_\mu^3 \sin\theta_W, \quad Z_\mu = B_\mu \sin\theta_W + W_\mu^3 \cos\theta_W. \tag{1.3}$$

The gauge symmetry of $\mathrm{SU}(2)_L \times \mathrm{U}(1)_Y$ is spontaneously broken down to $\mathrm{U}(1)_Q$ of electromagnetism. The mixing angle θ_W appears in many electroweak processes and is measured to be $\sin\theta_W \simeq 0.23$. The corresponding $\mathrm{SU}(2)_L$ and $\mathrm{U}(1)_Y$ coupling constants g and g' are related to the electric charge e with the relation

$$e = g \sin\theta_W = g' \cos\theta_W. \tag{1.4}$$

The connection between the electric charge Q, the third component of weak isospin I^3 and the hypercharge Y is given by

$$Q = I^3 + \frac{Y}{2}. \tag{1.5}$$

The fermions are arranged in weak isospin multiplets as summarised in the Table 1.1. Left-handed quarks Q_L and leptons L_L form $\mathrm{SU}(2)_L$ doublets with I^3 eigenvalues corresponding to

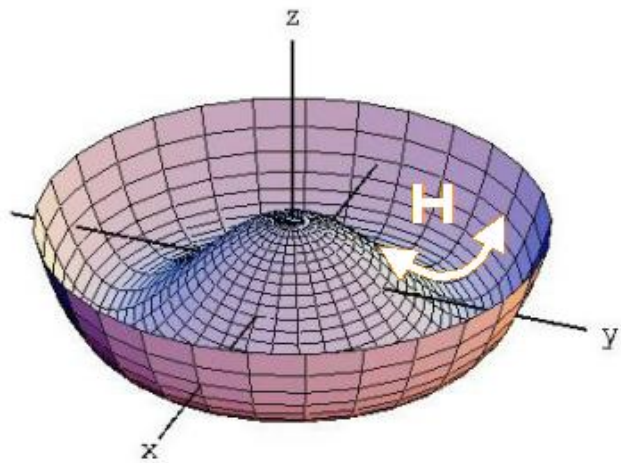

Figure 1.3: The potential of the Higgs field. The field value at the minimum of the potential is different form zero, i.e. the field has a vacuum expectation value.

$1/2(-1/2)$ for the upper (lower) component. The right-handed quarks and charged leptons are $\mathrm{SU}(2)_L$ singlets. Due to the product of symmetry groups, the generator Y has to commute with he generators I^i. As a result, all the members of an isospin multiplet have the same value of the hypercharge.

1.2 Short-comings of the Standard Model

Although the Standard Model is able to explain many phenomena in particle physics and tested to remarkable precision at electroweak scales, it seems not to provide the complete picture of our physical reality [9], [10]. There are theoretical, as well as experimental, observations that indicate existence of physics beyond the SM (BSM). From a theoretical point of view, the existence of about 20 undetermined parameters in the SM, the Higgs mass hierarchy problem, the unification of couplings, and the existence of three quark and lepton families are some of the arguments. General attitude is that a complete theory should be able to predict values of all of its parameters, while the SM does not. The hierarchy problem addresses a question about the huge difference in energy scales of the fundamental interactions, i.e. why the weak force is 10^{32} times stronger than gravity ($G_F/G_N = (M_{Pl}/M_{EW})^2 \sim 10^{32}$, where G_F (G_N) is the Fermi (Newton's) coupling constant). The scale hierarchy has implications on the Higgs mass as well. Since quantum corrections to scalar masses are proportional to the square of some cut-off scale (the scale where new physics appears), there is no apparent reason why Higgs mass would not be high up in e.g. Planck range ($M_{Pl} = 1/\sqrt{G_N} \sim 10^{19}$ GeV). Unless protected by some symmetry, huge fine-tuning in cancellations of higher order contributions is needed to keep the Higgs mass down at the level of 125 GeV. Such cancellations seems highly unnatural, it is argued. By evaluating the energy dependence of the electromagnetic, weak and

		SU(2)$_L$ multiplets			I	I^3	Y	Q
Q_L	=	$\begin{pmatrix} u_L \\ d_L \end{pmatrix}$	$\begin{pmatrix} c_L \\ s_L \end{pmatrix}$	$\begin{pmatrix} t_L \\ b_L \end{pmatrix}$	$\begin{pmatrix} 1/2 \\ 1/2 \end{pmatrix}$	$\begin{pmatrix} 1/2 \\ -1/2 \end{pmatrix}$	$\begin{pmatrix} 1/3 \\ 1/3 \end{pmatrix}$	$\begin{pmatrix} 2/3 \\ -1/3 \end{pmatrix}$
q_R^u	=	u_R	c_R	t_R	0	0	$\frac{4}{3}$	$\frac{2}{3}$
q_R^d	=	d_R	s_R	b_R	0	0	$-\frac{2}{3}$	$-\frac{1}{3}$
L_L	=	$\begin{pmatrix} \nu_{eL} \\ e_L \end{pmatrix}$	$\begin{pmatrix} \nu_{\mu L} \\ \mu_L \end{pmatrix}$	$\begin{pmatrix} \nu_{\tau L} \\ \tau_L \end{pmatrix}$	$\begin{pmatrix} 1/2 \\ 1/2 \end{pmatrix}$	$\begin{pmatrix} 1/2 \\ -1/2 \end{pmatrix}$	$\begin{pmatrix} -1 \\ -1 \end{pmatrix}$	$\begin{pmatrix} 0 \\ -1 \end{pmatrix}$
ℓ_R	=	e_R	μ_R	τ_R	0	0	-2	-1

Table 1.1: The SU(2)$_L$ multiplets and the corresponding quantum numbers: the weak isospin I, its third component I^3, hypercharge Y and electric charge Q.

strong coupling constants, it is observed that they meet almost at the same value at a very high energy. This suggests that, provided there is some additional mechanism (e.g. new particles) that would slightly alter their running, the three coupling may be indeed be unified at high scales.

The experimental evidence for BSM physics is provided by neutrino-oscillation experiments. Neutrinos were initially thought to be massless, however, we now know that in order to oscillate, neutrinos must have a mass. The SM does not offer a mechanism for neutrino masses. A number of phenomenological evidence comes from cosmology and astrophysics, e.g. the mechanism of the baryon number asymmetry generation (i.e. why is there more matter than anti-matter in the Universe), and the nature of dark matter and dark energy, are presently unknown (dark matter is discussed in the next section). As a result, the Standard Model is believed to be only the low-energy limit of a more fundamental theory. Many BSM theories are developed providing different solutions for SM problems. So far, the best candidate for the "theory of everything" is the string theory.

The Universal Extra Dimensions (UED) provide an elegant solution to the dark-matter problem. The lightest particle of the model, usually the Kaluza-Klein photon, has just the right properties required to explain the dark-matter related phenomena. UED models with more than one extra spatial dimensions also offer a reason for the existence of exactly three generations of quarks and leptons. This thesis focuses on the search for the dark-matter candidate provided by the UED model in its minimal form – the case with only one extra spatial dimension. The evidence for the existence of dark matter and a general solution provided in the form of Weakly-Interacting Massive Particles (WIMPs) are introduced in the next section (Sec. 1.3). The UED model and specific properties related to the UED dark-matter candidate are discussed in Sec.

1.6.

1.3 The problem of dark matter

The existence of dark matter (DM) is supported by a number of astrophysical and cosmological observations. Its nature is, however, still unknown. While there exist theories of modified Newtonian gravity able to reproduce a number of observational data without assuming the presence of some hidden matter, they can not explain e.g. the offset in visible vs. invisible mass distribution in cases like the "bullet" cluster (see below). Therefore the most common solution to the DM problem comes in the form of some new BSM particle[1]. In order to make a plausible DM candidate, such particle should be stable, neutral, colourless and able to produce the right relic abundance. Particle-candidates for dark matter include WIMPs (Weakly-Interacting Massive Particles), sterile neutrinos, axions and particles from hidden sectors [11]. The lightest UED particle (usually the Kaluza-Klein partner of a photon) [12], [13] and the supersymmetric neutralino [14] are WIMP candidates.

1.3.1 Evidence for dark matter

The evidence for dark matter come from various astronomical and cosmological observations and measurements [15], some of which are explained in more detail below. One of the first evidence for the existence of dark matter came from discrepancies between the mass measurements of galaxies and galaxy clusters using two approaches: mass determined by studying the gravitational effects, and mass calculated from the luminous matter – stars, gas and dust. The presence of dark matter is needed at the time of the Big Bang to set the right conditions, both for the primordial nucleosynthesis yielding the measured abundances of elements, and for the early structure formation which is in accordance with the observed CMB (cosmic microwave background).

Rotational curves of galaxies and clusters: Objects rotating at distance r from the centre of gravitational potential produced by total mass $M(r)$ inside that radius experience the centripetal force equal to the gravitational force

$$G_N \frac{M(r)m}{r^2} = \frac{mv^2}{r}, \tag{1.6}$$

where G_N is Newton's constant, m is the mass of the object and v its orbital velocity. Solving for v we find

$$v = \sqrt{\frac{G_N M(r)}{r}}, \tag{1.7}$$

i.e. the further the object from the centre, the lower its orbital velocity. That is, unless there is additional mass $M(r)$ distributed at increasing radii. Fig. 1.4 (left hand side) shows an

[1]The most plausible non-particle candidates for dark matter are the primordial back holes.

example where the measurement of orbital velocities of stars in a galaxy are found to be in conflict with the result expected from the amount of luminous matter observed. Inside the luminous central region of the galaxy, the rotation speed rises slowly with increasing distance from the center, as more mass enters the region inside the orbit. At distances far from the luminous region we would expect the orbital velocities, based on the Eq. (1.7), to go down. However, the velocities are observed to be approximately constant (or rising slowly). Unless the theory of gravity is modified, it must mean that there is some mass-source extending very far away from the luminous center, and not giving any visible light - the dark matter.

Gravitational lensing: The "bullet" cluster (Fig. 1.4, right hand side) is a famous example of evidence for dark matter inferred from the observation of the gravitational lensing. In a collision of two galaxy clusters, the hot X-ray gas (shown in pink), which contains most of clusters' baryonic matter, slowed down due to, mainly, electromagnetic interactions. However, the mass distribution measured by the gravitational lensing (blue) shows that the most of the mass contained in the clusters continued its motion as though the collision never occurred. This separation between the luminous baryonic matter and the center of the total mass distribution is only possible if the dominant fraction of the clusters' mass is contained in the non-baryonic collision-less component.

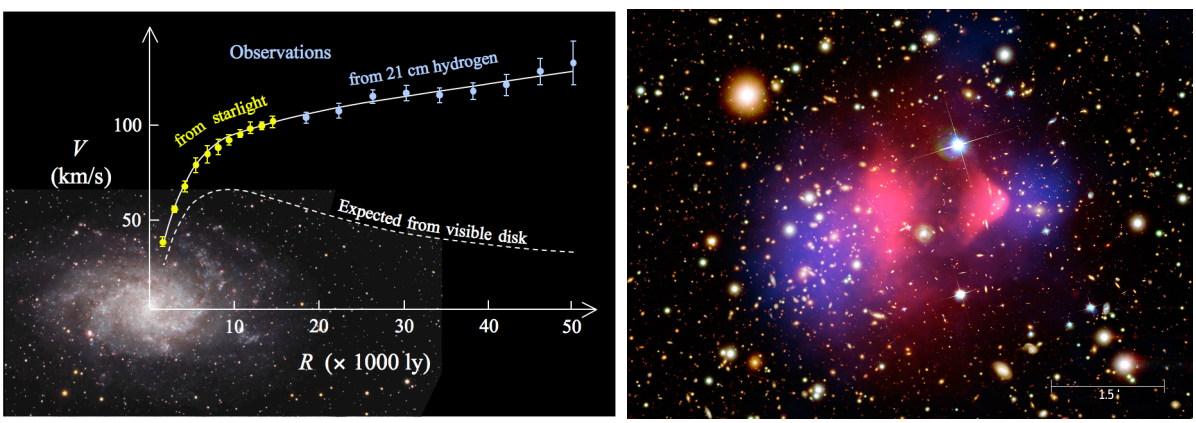

Figure 1.4: Left: The rotation curve of a galaxy [16]. Closer to the galaxy center star velocities are measured using starlight, at large radii the 21-cm hydrogen line is used to measure the velocities of interstellar hydrogen. Right: The optical image from Magellan and HST shows galaxies in orange and white. Hot gas in the cluster, which contains the bulk of the normal matter in the cluster, is shown by the Chandra X-ray Observatory image in pink. Most of the mass in the cluster is shown in blue, as measured by gravitational lensing, the distortion of background images by mass in the cluster. This mass is dominated by dark matter (source Chandra X-Ray Observatory: 1E 0657-56).

Primordial nucleosynthesis: The Universe in its early times was in extremely hot and dense state, consisting mainly of protons, neutrons, electrons and photons (for the "normal" matter component). The intense radiation ionised all the gas and neither atoms nor atomic nuclei could form. The primordial nucleosynthesis could start only at latter times when the

Universe cooled-off and the density of the high-energy photons decreased. However, primordial production of elements (mainly ^{4}He, D, ^{3}He and ^{7}Li) can proceed only in a very short time window – after the density of protons and neutrons drops below the certain threshold, the nucleosynthesis stops. The relationship between the expansion rate of the Universe (related to the total matter/radiation density) and the baryonic matter density (protons and neutrons) determines how much of the light elements have been produced in the early Universe. The measured primeval abundances show that the baryonic matter makes up only 0.04 of the critical cosmological density (the density required to make the Universe flat , while the total matter density in the Universe is found to be about 0.27[2].

Cosmic microwave background (CMB): The CMB was formed when the Universe became transparent to photons from the thermal radiation of the primordial plasma, i.e. after the recombination (formation of hydrogen and helium atoms) [17]. The temperature fluctuations in the CMB spectrum are directly related to the acoustic oscillations of the baryon-photon plasma. Gravitational force between baryonic matter concentrations in the plasma acts as an attractive force, while the radiation pressure, that builds up via Thomson scattering as the density increases, creates a repulsive force. These oscillations proceed in a gravitational potential set by dark matter, but dark matter itself does not oscillate as it decouples from the plasma at much earlier times. After the recombination, the photons continue to propagate freely and the temperature fluctuations in their spectrum correspond to baryon density perturbations at the time of decoupling. The perturbations, and consequently the CMB spectrum, depend on the matter/energy content of the early Universe. The expectation value of the square of the temperature fluctuation is given by

$$\left\langle \left(\frac{\delta T}{T} \right)^2 \right\rangle = \sum_{\ell} \frac{2\ell + 1}{4\pi} C_\ell, \tag{1.8}$$

where T is the black-body temperature of the CMB radiation, C_ℓ is the angular power spectrum and the different multipoles ℓ correspond to different angular scales (wavelengths of the oscillations) roughly as $\theta \sim \pi/\ell$. The angular power spectrum as a function of the angular scale is shown in Fig. 1.5. The observed values of C_ℓ can be compared to those calculated numerically given an ionization history and set of cosmological parameters. The first peak in the spectrum corresponds to one full compression of the sound wave and determines the size of the horizon at decoupling. The position of the peak is related to the comoving size of the sound horizon at the recombination r_s and the distance to the last scattering surface D_A as

$$\theta = \frac{r_s}{D_A}. \tag{1.9}$$

The parameters r_s and D_A are calculated given the properties of the primordial plasma (matter density) and the expansion history of the Universe, as well as its geometry, respectively, and

[2]The total matter/energy density is determined from various cosmological measurements, including CMB power spectrum, supernovae data and clustering of galaxies, see [15].

compared to the measured θ. Apart from providing certain constraints on the relative abundances of total and baryonic matter, the measured value $\theta \sim 0.6°$ (or $\ell \sim 220$) indicates the Universe is essentially flat [18]. The matter densities are measured from the relative heights of the acoustic peaks. Lower baryon densities imply symmetric oscillations around the equilibrium, since the gravitational potential is less affected the smaller the baryon contribution. Increasing the baryon density, relative to the dark-matter density, implies stronger compressions and weaker decompressions of the photon-baryon plasma, causing the first and the third power spectrum peak to be stronger than the second and the fourth. The baryonic and dark-matter densities measured by Planck are $\Omega_b h^2 = 0.02207 \pm 0.00033$ and $\Omega_{DM} h^2 = 0.1196 \pm 0.0031$, respectively[3] [18].

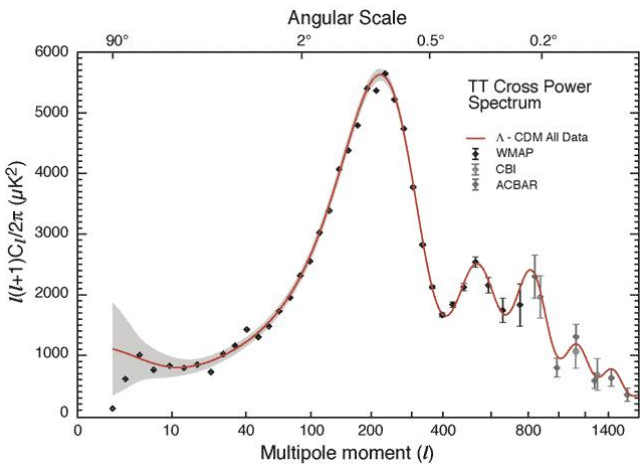

Figure 1.5: CMB temperature anisotropy (TT) power spectrum. The amplitudes of temperature perturbations, in terms of the angular power spectrum, are shown as a function of the angular size of the perturbations [19].

Structure formation: The structure formation proceeded by gravitational clustering induced by the initial density fluctuations in the gas (after the recombination). The size of the initial baryon density perturbations is measured from the CMB angular power spectrum – the first maximum in the spectrum corresponds to the largest wavelength of these density oscillations (Fig. 1.5). However, the gravitational clustering is a slow process and in order to build up all the observed structures in the present Universe, the initial density fluctuations would have to be much larger than the amplitude of fluctuations measured in the CMB data. The addition of a non-baryonic component, for which to the perturbation growth can start much earlier, may produce the perturbation amplitudes at the time of recombination which are large enough to allow for the present structures.

In conclusion, from a combination of astronomical and cosmological observations, the amount

[3] $\Omega_{b,\,DM}$ is the density fraction of the critical cosmological density of the flat Universe ($\Omega_c = 1$) and h is a dimensionless parameter related to the expansion of the Universe, $h = H^0/(100 \text{ km s}^{-1} \text{ Mpc}^{-1})$.

of dark matter is estimated to take up more than 80% of the total gravitationally attractive component in our Universe, with only $15\% - 20\%$ contained in the "ordinary" Standard Model matter.

1.3.2 WIMPs as dark-matter candidates

WIMPs, originally proposed by Steigman and Turner [20], are one of the most interesting DM candidates. They are electrically neutral particles with the weak-scale mass and interaction strength. If they are included in a thermal bath with other particles in the early-Universe, the Boltzmann equations (Eq. (1.10)-(1.11)) yield the number density of WIMPs which matches the number density inferred from cosmological observations (the so-called "WIMP miracle").

WIMPs (and other heavy particles) were created early in the Universe, before the primordial nucleosynthesis. As long as the Universe was dense and hot enough (compared to the WIMP mass), the annihilation of WIMPs into lighter particles and vice-versa proceeded at equal rates. The reaction rate per particle can be expressed as

$$\Gamma = n_w \sigma v,$$

where n_w is the number density of WIMPs, σ is the cross section and v is the relative velocity of two annihilating particles. While $\Gamma >> H(t)$, where $H(t)$ is the expansion rate of the Universe (the Hubble constant), the system can be described by equilibrium thermodynamics. As the Universe expands, and consequently cools down, the number density of WIMPs will decrease according to the Boltzmann equation as

$$\frac{dn_w}{dt} = -3Hn_w - \langle \sigma v \rangle \left[(n_w)^2 - (n_w^{eq})^2 \right], \tag{1.10}$$

where H is the Hubble constant, $\langle \sigma v \rangle$ is the thermal average of the annihilation cross section times the relative velocity and n_w^{eq} is the WIMP equilibrium density [21]. The rate of change of WIMP density in Eq. (1.10) depends on two factors: the expansion rate of the Universe (the first term) and the annihilation cross section of WIMPs into SM particles (the second term). For a non-relativistic WIMP (i.e. $m_w >> T$, with T being the temperature), its equilibrium density is given by the Maxwell-Boltzmann distribution

$$n_w^{eq} = g \left(\frac{m_w T}{2\pi} \right)^{2/4} e^{-m_w/T}, \tag{1.11}$$

where g denotes the number of degrees of freedom of a WIMP[4]. Fig. 1.6 shows the WIMP equilibrium density from Eq. (1.11) (solid line) as a function of temperature (or, equivalently, time). The evolution of WIMP equilibrium density can be divided into three phases, governed by Eqs. (1.10) and (1.11), and illustrated in Fig. 1.6.

[4]In the case of interest where WIMP is a spin-1 KK photon, g equals 3.

- While the temperature in the early Universe is much larger than the WIMP mass ($T >> m_w$), WIMPs are freely created and annihilated in pairs. Both pair creation and annihilation occur at the same rate.
- As the Universe cools down, light particles no longer have sufficient kinetic energy to produce heavier particles through interactions. WIMPs continue to annihilate, and their equilibrium density starts falling off until, eventually, all WIMPs annihilate (where the solid line in Fig. 1.6 crosses zero). However, there is another factor. Since the Universe's expansion dilutes the WIMP density, WIMP interaction rate drops down and they can no longer annihilate efficiently.
- At a certain temperature (which depends on the annihilation cross section and, to a smaller extent, the mass), the WIMP density becomes too low to support frequent annihilations. Consequently, WIMPs drop out of the thermal equilibrium. This is called the "freeze-out". WIMP abundance remains constant after the "freeze-out" and is known as the relic density (dashed line in Fig. 1.6).

A particle with a weak-scale interaction cross-section would "freeze-out" at the right time to reproduce the observed relic density (red lines in Fig. 1.6). A particle with larger interaction rate, e.g. electromagnetic- or strong-scale interaction cross-sections, would annihilate too efficiently and would produce smaller relic abundance. This observation makes WIMPs tantalising DM candidates.

1.4 Physics in extra dimensions

Many theories addressing the problems of the Standard Model propose adding extra spatial dimensions [25]. The idea originated in the 1920's when Kaluza and Klein independently explored the possibility of introducing additional dimensions. Their theory, known as the Kaluza-Klein (KK) mechanism, attempts to unify gravity with the strong and electroweak forces by extending Einstein's general relativity to a five-dimensional space-time. Although the theory has many appealing features, the attempt to convert it to a model of reality encountered many problems (e.g. the fermions must be introduced in an artificial way). Nevertheless, the principles of the KK theory are often embedded in more sophisticated theories and thus remain an important idea of theoretical physics.

The string theory is an example of a physical model with extra dimensions as a central ingredient. In addition to being able to correctly describe the Standard Model phenomenology, it successfully combines quantum field theory and general relativity, and, as such, is a candidate for a theory of everything. The extra dimensions are essential - consistent superstring theory requires 10 dimensions, while the non-supersymmetric theory is consistent only in 26 dimensional space-time. The extra dimensions are curled up into the Calabi-Yao shapes of the size $\sim 1/M_{Pl}$. Since this huge energy scale cannot be probed experimentally, the strings are impossible to be observed directly.

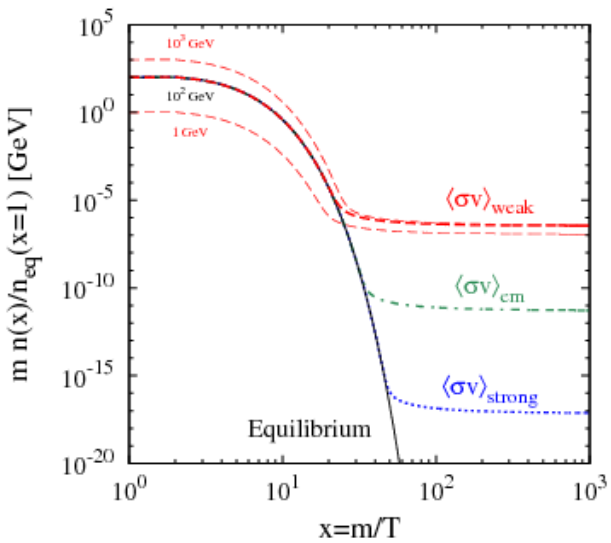

Figure 1.6: Evolution of WIMP abundance as a function of the temperature (time). The curves show the WIMP mass density, normalized to the initial equilibrium number density. Equilibrium density is shown with a solid line, while the dashed lines represent the relic density for different choices of annihilation cross section $\langle\sigma v\rangle$ and mass m. Evolution for $m = 100$ GeV is shown for weak interactions ($\langle\sigma v\rangle = 2 \times 10^{-26}$ cm^{3}s^{-1}, dashed red), electromagnetic interactions ($\langle\sigma v\rangle = 2 \times 10^{-21}$ cm^{3}s^{-1}, dot-dashed green), and strong interactions ($\langle\sigma v\rangle = 2 \times 10^{-15}$ cm^{3}s^{-1}, dotted blue). For the weak cross section the thin dashed curves show the WIMP mass dependence for $m = 10^3$ GeV (upper dashed curve) and $m = 1$ GeV (lower dashed curve). The solid black curve shows the evolution of the equilibrium abundance for $m = 100$ GeV [22].

However, there exist extra-dimensional theories that are both able to offer solutions to some of the SM problems and are experimentally observable. These include Universal Extra Dimensions (UED) proposed by Appelquist, Cheng and Dobrescu in 2000 [26] , ADD scenario of Large Extra Dimensions (LED) [27] and Randall-Sundrum models of Warped Extra Dimensions [28], to name just a few. In the Universal Extra Dimensions (UED) scenario, all the SM fields are allowed to propagate in additional Kaluza-Klein dimensions. Non-observation of the Kaluza-Klein excitations of SM particles sets the experimental upper limit on the size of extra dimensions to about $\sim$TeV^{-1} (corresponding to $\sim 10^{-18}$ m). Since the fundamental Planck scale remains high, the hierarchy problem is not addressed. On the other hand, UED provides a plausible dark matter candidate.

The Kaluza-Klein idea of compactification is explained in Sec. 1.4.1, followed by the description of the effects that flat extra dimensions have on gravity (Sec. 1.4.2). UED model is addressed in Sec. 1.4.3, while scenarios combining ideas of UED and LED are briefly discussed in Sec. 1.4.4. Information about ADD and RS models can be found in the appendix (A.2, A.3).

1.4.1 Kaluza-Klein theory

In Kaluza-Klein theory the extra spatial dimension is flat and compactified on a circle of radius R. The reason we do not observe this additional dimension is that the compactification radius is assumed to be small, i.e. $1/R$ is large compared to some currently accesible energy scale. Due to the finite size of the fifth dimension, the energy states propagating in it are quantised and form a tower of the, so called, Kaluza-Klein (KK) states. The particle wave functions satisfy

$$\Phi(x_\mu, y) = \Phi(x_\mu, y + n \cdot 2\pi R), \tag{1.12}$$

where x_μ refers to the usual four space-time coordinates, and y is the fifth dimension. Due to the periodicity along the y-coordinate, the fields can be expanded in a Fourier series as

$$\Phi(x_\mu, y) = \sum_{n=0,\pm1,\ldots} \phi_n(x_\mu) e^{iny/R}. \tag{1.13}$$

Applying five-dimensional Klein-Gordon equation to a scalar field of mass m_0 gives

$$\left(\partial_\mu^2 - \frac{\partial^2}{\partial y}\right) \Phi(x_\mu, y) + m_0^2 \Phi(x_\mu, y) = 0. \tag{1.14}$$

Substituting the Fourier expansion from Eq. (1.13) yields

$$\left(\partial_\mu^2 + \frac{n^2}{R^2}\right) \phi(x_\mu) + m_0^2 \phi(x_\mu) = 0, \tag{1.15}$$

from where it can easily be seen that the mass of the nth KK excitation is given by

$$m_n^2 = m_0^2 + \frac{n^2}{R^2}. \tag{1.16}$$

The 0th mode has just the mass m_0 and corresponds to the SM particle propagating only in our 3 spatial dimensions. $n > 0$ KK excitations get additional mass term $\sim n/R$ arising from their momentum component along the 4th spatial dimension. Once the energy scale larger than $\sim 1/R$ is reached, the tower of KK resonances can be directly observed.

1.4.2 Gravity in flat extra dimensions

Flat compactified extra spatial dimensions have interesting implications on gravity. Our 4D gravitational potential

$$V(r) = \frac{1}{M_{Pl}^2} \frac{m_1 m_2}{r}, \tag{1.17}$$

can be generalized to the $(4+N)$-dimensional space as

$$V(r) = \frac{1}{M_D^{N+2}} \frac{m_1 m_2}{r^{N+1}}, \tag{1.18}$$

where M_D is the fundamental Planck scale in the $(4+N)$-dimensional world. At distances $r << R$, where R is the size of N extra dimensions, Eq. (1.18) describes the fundamental $(4+N)$-dimensional gravitational potential. However, at distances much greater than the ED size, $r >> R$, the gravitational flux in ED can only go as far as R, and the potential in Eq. (1.18) is modified to

$$V(r) = \frac{1}{M_D^{N+2} \cdot R^N} \frac{m_1 m_2}{r}. \tag{1.19}$$

Comparing Eq. (1.17) to Eq. (1.18) we find the relation between the 4D Planck scale M_{Pl}, the fundamental Planck scale in $(4+N)$ dimensions M_D, and the radius of the extra dimensions R as

$$M_{Pl}^2 \sim M_D^{N+2} R^N. \tag{1.20}$$

The Eq. (1.20) is interesting since it can offer an explanation for the hierarchy problem. If the extra spatial dimensions are accesible only to the gravity, with other SM fields being localised on our 4D-brane, the ED could be as large as $R \sim eV^{-1} \sim 0.1$ mm[5]. For large enough R and/or N, the $(4+N)$-dim gravity in Eq. (1.18) could be operating at TeV scales, with the fundamental Planck mass of $M_D \sim$ TeV. At distances large compared to the size R, the effective 4D gravitational potential assumes our familiar $1/r$ form with the effective 4D M_{Pl} of $\sim 10^{16}$ TeV. The gravity is effectively "diluted" and its projection on our SM 4-dim brane is thus so much weaker in scale than the other forces. The idea of large extra dimensions (LED) accesible only to the gravity was originally proposed by Arkani-Hamed, Dimopulous and Dvali (ADD) (see Appendix A.2).

[5]Recent tests of the gravitational inverse-square law constrain the size of the gravity-only ED to be below $0.01 - 0.1$ mm [23], [24].

1.4.3 Universal Extra Dimensions

In UED model all the SM fields propagate in flat extra dimensions. The interesting point here is that bounds from the electroweak data on the size R of these universal extra dimensions are rather loose, allowing UED to be easily accesible at accelerators. In theories where only some of the SM fields propagate in the ED, the KK modes contribute at the tree level to the electroweak observables, which places a lower bound on the compactification scale 1/R of a few TeV. In UED, however, a key ingredient is the conservation of momentum in the extra dimension, resulting in Kaluza-Klein number conservation (at the tree level). This means that, in principle, only an even number of KK excitations can be coupled to a SM field, and there are no vertices involving only one odd-level KK mode. As a consequence, the SM fields do not mix with the first level KK excitations, and contributions to the electroweak precision observables arise only from loops involving two massive particles. In the case of one ED, the electroweak constraints allow KK excitations as light as a few hundred GeV. The corresponding compactification radius is, typically, much smaller than radii of the ADD dimensions where only gravity propagates.

Another appealing feature of the KK number conservation is that the lightest Kaluza-Klein particle (LKP) is stable. It is also electrically neutral, colorless and its abundance in the early universe agrees well with the measured dark matter density. It is thus a very good candidate for a WIMP dark matter, alternative to supersymmetric neutralinos.

Furthermore, problems with proton stability, arising in e.g. ADD model, do not appear in specific UED scenarios. Constraints on proton lifetime ($\tau \geq 10^{33}$ years [31]) place the upper bound on the gravity cut-off scale of $\sim 10^{16}$ GeV. When the Planck scale is lowered to $\sim$1 TeV in ADD, proton becomes unstable. While there are ways to avoid such issues in ADD, in six-dimensional UED Lorentz and gauge invariance naturally raise the baryon-number violating operators to a much higher scale than in the SM alone [32]. What is more, in six-dimensional UED the gauge anomalies cancel if there exist three generations of fermions [33].

UED is an effective theory with the ultra-violet cut-off scale denoted as Λ. Since the radiative corrections to the mass are naturally expected to lie at the cut-off scale, UED exhibits the, so called, little hierarchy problem [34]. Even though the compactification scale $1/R$ could lie around the weak scale, Λ is typically much larger. There exist possible solution to this problem in terms of extra-dimensional versions of Little Higgs or Twin Higgs models [34].

In its simplest scenario, called the minimal UED (mUED), where there is only one extra dimension where all the fields propagate, the hierarchy problem in not addressed. But if (4+1)-dim mUED space is embedded into a larger (5+N)-dim space and in N-dimensions only gravity is allowed to propagate (see Sec. 1.4.4), then the same ADD reasoning of lowering the Planck scale applies. However, this scenario has the phenomenology quite different form the one expected in mUED case (see Chapter 2). Minimal UED is discussed in more detail in Sec. 1.5, as the analysis in this thesis is optimised for this specific model.

1.4.4 UED with additional non-universal dimensions

In a non-minimal UED scenario there could be additional dimensions where only gravity propagates. The constraints on size of the extra dimensions where all the SM fields propagate are order of TeV^{-1}. However, if extra dimensions are to be used to solve the hierarchy problem, their size has to be as large as MeV^{-1} and up to eV^{-1}, depending on the number of ED accessible only to gravity. For example, there could be one or more TeV^{-1}-size extra dimensions in which both matter and gravity propagate, and several larger extra dimensions in which only gravity propagates. In this case first level excitations of quark and gluons can decay to a first level graviton and a SM particle and resulting phenomenology associated with the production of gravitons will be the same as in the ADD model.

In another scenario, the matter fields are restricted to a small TeV^{-1}-size region in the fifth dimension and only gravity propagates in large eV^{-1}-size extra dimensions. Since matter fields are restricted to the brane, the translational invariance is broken, and momentum conservation in the fifth dimension does not hold anymore. Thus the KK-number conservation does not apply in matter-gravity interactions, and the first level KK excitations of matter can decay by radiating gravitons. Since the mass splitting in the graviton tower is quite small (eV^{-1}), the resulting decay widths can be quite large. In the case when the gravitational decays of KK states dominate over decay channels induced by first level mass splittings, the KK excitations of quarks and gluons decay to SM quark and gluons plus gravitons. Since gravitons do not interact with the detector the experimental signature in this case will be jets plus missing transverse energy. In the case when the decays due to mass splitting between the first level KK excitations dominate, the quark and gluon KK excitations will decay all the way to the LKP, which then decays through gravitational interaction to a SM photon and a graviton. The characteristic signature in this case are two photons and missing energy in the event.

1.5 Minimal Universal Extra Dimensions

The minimal UED is the simplest scenario with only one extra dimension where all the SM fields propagate [30], [21]. It has only two free parameters: the compactification scale R^{-1} and the cut-off scale Λ. The scale Λ is defined as the scale where the effective 5-dimensional theory breaks down, i.e. where the 5-dimensional couplings become large and the theory is no longer perturbative. Without knowing the underlying fundamental theory, Λ can not be determined. However, upper limits on Λ can be set, for example, by using the unitarity bounds on heavy gluon scattering – the maximum number of KK excitations appearing in the effective 4D theory is typically found to be of $\mathcal{O}(10)$. The limit on the number of KK levels contributing to the scattering depends on the typical mass-splitting between the levels, therefore it is expressed with the parameter ΛR, i.e. $\Lambda R \sim \mathcal{O}(10)$.

Mass of a KK particle is a measure of its momentum in the extra dimension. Due to the kinematic terms along the 5th dimension (particle in a box), the KK fields obtain a tree-level

contribution to their mass (see Sec. 1.4.1)

$$m_n^2 = m_0^2 + \frac{n^2}{R^2}, \tag{1.21}$$

where m_0 denotes the mass of the corresponding SM partner. Assuming $R \sim \mathrm{TeV}^{-1}$, the masses of SM particles make a negligible contribution (with the possible exception for weak bosons and top quark), and KK masses are completely dominated by the right term in Eq. 1.21. This makes the KK spectrum highly degenerate at each level n. However, the degeneracy is lifted due to one-loop mass-corrections, which play an important role in the UED phenomenology.

By assuming the extra-dimensional momentum conservation, we would expect that the KK-number is a conserved quantity. For example, the momentum along ED carried by a KK particle can not just disappear by the particle decaying to two zero-mode SM states. However, the orbifolding, explained in the section 1.5.1 below, breaks the translational symmetry along the extra dimension, and thus leads to KK-number violating interactions. What remains, though, is a subgroup of KK-number conservation – KK-parity. It can be written as $P = (-1)^n$, where n denotes the level of a KK excitation. The KK-parity works in a similar way as the R-parity in supersymmetry (SUSY) – the level-one KK particles must be pair-produced at a collider. What makes UED different from SUSY, though, is that level-two KK states can also be singly produced in KK-number violating interactions.

1.5.1 Decomposition of the fields

In this section we derive a form of five-dimensional fields, assuming there is one finite extra dimension where all the Standard Model particles propagate. The compactification of the extra-dimension will be chosen so that the effective 4D SM phenomenology can be correctly reproduced. In the finite dimension of the size R the particle wave functions satisfy $\phi(x, y) = \phi(x, y + 2\pi R)$, where x refers to the usual four space-time coordinates, and y is the fourth spatial dimension. The fields can be expanded in a Fourier series along the y coordinate as

$$\phi(x, y) = \frac{1}{\sqrt{2\pi R}} \left[\phi_0(x) + \sqrt{2} \sum_{n \geq 1} \left(\phi_n^{(1)}(x) \cos(\frac{ny}{R}) + \phi_n^{(2)}(x) \sin(\frac{ny}{R}) \right) \right], \tag{1.22}$$

where $\phi_0(x)$, $\phi_0^{(1)}(x)$ and $\phi_0^{(2)}(x)$ are 4D fields. In the effective theory framework, $\phi_0(x)$ would correspond to the SM field, while $\phi_0^{(1)}(x)$ and $\phi_0^{(2)}(x)$ would be its KK excitations. If the field ϕ from Eq. 1.22 is now inserted, assuming it is a scalar, into the Lagrangian

$$\mathcal{L}_5(x, y) = \partial_M \phi \, \partial^M \phi = \partial_\mu \phi \, \partial^\mu \phi + (\partial_y \phi)^2 \tag{1.23}$$

and integrated over the fifth coordinate y, we obtain an effective Lagrangian

$$\mathcal{L}_{eff} = \partial_\mu \phi_0 \, \partial^\mu \phi_0 + \sum_{n\geq 1} \left[\partial_\mu \phi_n^{(1)} \, \partial^\mu \phi_n^{(1)} + \left(\frac{n}{R}\right)^2 (\phi_n^{(1)})^2 \right] \tag{1.24}$$

$$+ \sum_{n\geq 1} \left[\partial_\mu \phi_n^{(2)} \, \partial^\mu \phi_n^{(2)} + \left(\frac{n}{R}\right)^2 (\phi_n^{(2)})^2 \right]. \tag{1.25}$$

The zero mode stays massless, while KK excitations ϕ_n get mass equal to n/R. We can see that each KK level contains twice as many degrees of freedom as the zero one. Additional symmetries acting on the fifth coordinate can be imposed in order to eliminate these extra degrees of freedom. For example, the 5D fields can be made even or odd under the reflection $y \to -y$, i.e. $\phi(x,y) = \phi(x,-y)$ or $\phi(x,y) = -\phi(x,-y)$. This means the extra dimension is orbifolded - its compactification consists of projecting a circular extra dimension onto a line of length πR with two fixed points. For even fields it would result in the coefficients next to the sine, $\phi_n^{(2)}$, being set to zero, and for odd fields $\phi_n^{(1)}$ would be set to zero. The orbifolding is also important to eliminate extra degrees of freedom appearing at zero level. If we take 5D massless gauge vector field (A_μ, A_5) and do the same procedure as for the scalar field (Eq. 1.22 to Eq. 1.25), we find that the zero mode has five components $(A_0)_\mu$, $(A_0)_5$ and stays massless. For $n > 0$ KK excitations there exists a particular gauge choice in which the four fields $(A_n)_\mu$ become the components of a 4D massive gauge boson, and $(A_n)_5$ disappear from the theory (similar to the Goldstone bosons of the Higgs mechanism being absorbed into masses of the weak bosons). The $(A_0)_5$ field, however, remains and represents a massless gauge boson with the same interactions as the gauge fields. This field obviously has problematic phenomenological implications and needs to be eliminated. Again, by requiring that the A_μ components be even under the reflection in fifth dimension, $y \to -y$, the $(A_0)_5$ mode will drop out and the SM content will be correctly reproduced. We will take both scalar Higgs and gauge boson fields to be even under the orbifold symmetry, and thus their 5D wave functions will have the following KK decomposition:

$$(\phi, A_\mu) = \frac{1}{\sqrt{\pi R}} \left[\left(\phi_0, A_\mu^{(0)}\right) + \sqrt{2} \sum_{n\geq 1} \left(\phi_n, A_\mu^{(n)}\right) \cos\frac{ny}{R} \right]. \tag{1.26}$$

We can proceed in similar fashion for the fermions. A 5D fermion field can be expanded in a Fourier series in terms of the 4-component Dirac spinors as

$$\psi(x,y) = \frac{1}{\sqrt{2\pi R}} \left[\psi_0(x) + \sqrt{2} \sum_{n\geq 1} \left(\psi_n^{(2)}(x) \cos(\frac{ny}{R}) + \psi_n^{(2)}(x) \sin(\frac{ny}{R}) \right) \right]. \tag{1.27}$$

If $\psi(x,y)$ satisfies the 5D Dirac equation $\partial_M \Gamma^M \psi(x,y) = 0$, then

$$\partial_\mu \gamma^\mu \psi_0(x) = 0 \ , \quad \partial_\mu \gamma^\mu \psi_n^{1,2}(x) = \pm \frac{n}{R} \psi^{1,2}(x), \tag{1.28}$$

where $\Gamma^\mu = \gamma^\mu$, $\Gamma^5 = i\gamma_5 = \gamma^0\gamma^1\gamma^2\gamma^3$, and γ^μ the usual 4D Dirac matrices. The KK modes of 4D $\psi^{1,2}$ spinors thus have a mass of n/R. The problem with fermions arrises due to the fact that there is no chirality in five dimensions, i.e. a matrix equivalent to γ^5 in 4D , such that it anticommutes with all Γ^M and its square is identity, can not be constructed. Practically, this means that the 5D Lagrangian can not contain terms like $\psi\gamma^\mu\gamma_5\psi$ since they are not invariant under 5D Lorenz transformations. As a consequence, the left and right handed components of the zero mode ψ^0 can not be made to couple differently to the gauge fields as in the Standard Model. Therefore it is necessary to introduce two 5D fermion fields for each SM Dirac fermion: ψ, which has the quantum numbers of the left handed SM spinor, and ψ', with the quantum numbers of the right handed SM spinor. The SM fermion can then be seen as a combination of the left component of the ψ field zero mode, and the right component of the ψ' zero mode: $\psi^{SM} = P_L\psi_0 + P_R\psi'_0$, with the chirality projectors being $P_{L,R} = (1 \pm \gamma^5)/2$. The right handed components of ψ_0 and left handed components of ψ'_0 are again phenomenologically unacceptable massless degrees of freedom. The issue can yet again be solved by orbifolding – if we require ψ to be odd under the reflection of y coordinate (under which the spinor fields transform as $\psi(x,y) \to \gamma^5\psi(x,-y)$), and ψ' to be even, the decomposition of fermion fields can finally be written as

$$\psi(x) = \frac{1}{\sqrt{\pi R}}\left[\psi_{0L}(x) + \sqrt{2}\sum_{n\geq 1}\left(\psi^{(1)}_{nL}(x)\cos\frac{ny}{R} + \psi^{(2)}_{nR}(x)\sin\frac{ny}{R}\right)\right], \tag{1.29}$$

$$\psi'(x) = \frac{1}{\sqrt{\pi R}}\left[\psi'_{0R}(x) + \sqrt{2}\sum_{n\geq 1}\left(\psi'^{(1)}_{nR}(x)\cos\frac{ny}{R} + \psi'^{(2)}_{nL}(x)\sin\frac{ny}{R}\right)\right]. \tag{1.30}$$

All the ψ_n are vector-like fermions, while the zero modes are chiral, as desired.

1.5.2 Kaluza-Klein spectrum at one loop

At the tree level, the KK spectrum is highly degenerate (see Eq. 1.21). However, the radiative contributions to KK masses break the degeneracy, i.e. the mass splittings between the KK particles of the same level become larger [35]. This has important implications for the collider phenomenology. Larger mass splittings mean that heavier KK states can decay into lighter ones plus the SM particles, inside the detector volume. Exactly how much larger the mass splittings become, depends mainly on the cut-off scale Λ. Fermions recieve the following 1-loop

corrections [21]:

$$\delta(m_{Q^{(n)}}) = \frac{n}{16\pi^2 R}\left(6g_3^2 + \frac{27}{8}g_2^2 + \frac{1}{8}g_1^2\right)\ln \Lambda R \tag{1.31}$$

$$\delta(m_{u^{(n)}}) = \frac{n}{16\pi^2 R}\left(6g_3^2 + 2g_1^2\right)\ln \Lambda R \tag{1.32}$$

$$\delta(m_{d^{(n)}}) = \frac{n}{16\pi^2 R}\left(6g_3^2 + \frac{1}{2}g_1^2\right)\ln \Lambda R \tag{1.33}$$

$$\delta(m_{L^{(n)}}) = \frac{n}{16\pi^2 R}\left(\frac{27}{8}g_2^2 + \frac{9}{8}g_1^2\right)\ln \Lambda R \tag{1.34}$$

$$\delta(m_{\ell^{(n)}}) = \frac{n}{16\pi^2 R}\frac{9}{2}g_1^2 \ln \Lambda R, \tag{1.35}$$

where $\zeta(3) \simeq 1.2020$ is the third zeta function, g_3 is the strong, and g_1, g_2 are the electroweak coupling constants. SU(2) doublets (KK modes of left-handed SM fermions) are denoted with capital letters, while $u^{(n)}, d^{(n)}, \ell^{(n)}$ denote KK modes of right-handed SM fermions, SU(2) singlets (KK states themselves are massive Dirac fermions with both right- and left-handed polarizations). Similarly, one-loop corrections to masses of the spin-1 fields are given by

$$\delta(m^2_{g^{(n)}}) = \frac{g_3^2}{16\pi^2 R^2}\left(\frac{-3\zeta(3)}{2\pi^2} + 23n^2 \ln \Lambda R\right) \tag{1.36}$$

$$\delta(m^2_{W^{(n)}}) = \frac{g_2^2}{16\pi^2 R^2}\left(\frac{-5\zeta(3)}{2\pi^2} + 15n^2 \ln \Lambda R\right) \tag{1.37}$$

$$\delta(m^2_{B(n)}) = \frac{g_1^2}{16\pi^2 R^2}\left(\frac{-39\zeta(3)}{2\pi^2} - \frac{n^2}{3}\ln \Lambda R\right). \tag{1.38}$$

The mass spectrum of KK modes depends linearly on $1/R$ and only logarithmically on the cut-off scale Λ (see Fig. 1.7, left). For KK scalars and spin-1 particles the $\delta(m^2)$ mass-correction simply gets added to the tree-level mass in Eq. (1.21),

$$m_n^2 = m_0^2 + \frac{n^2}{R^2} + \delta(m^2), \tag{1.39}$$

while for KK fermions the correction is of the form [21]:

$$m_n^2 = m_0^2 + \left(\frac{n}{R} + \delta(m)\right)^2. \tag{1.40}$$

After the fifth components of KK gauge and Higgs fields get eaten by KK W- and Z-bosons, which acquire mass in the process, four scalars at each KK level remain – $H_n^0, H_n^\pm$ and A_n^0. Their

masses are given by [21]:

$$m^2_{H^0_n} = \frac{n^2}{R^2} + m_h^2 + \delta m^2_{Hn} \tag{1.41}$$

$$m^2_{H^\pm_n} = \frac{n^2}{R^2} + m_W^2 + \delta m^2_{Hn} \tag{1.42}$$

$$m^2_{A^0_n} = \frac{n^2}{R^2} + m_Z^2 + \delta m^2_{Hn}. \tag{1.43}$$

The radiative corrections $\delta(m^2_{H_n})$ are

$$\delta(m^2_{H_n}) = \frac{n^2}{16\pi^2 R^2}\left(3g_2^2 + \frac{3}{2}g_1^2 - 2\lambda_H\right)\ln \Lambda R + \bar{m}_H^2, \tag{1.44}$$

where λ_H is the Higgs quartic coupling and $\bar{m}_H^2$ is the mass term generated on the orbifold boundaries.

From the Eqs. (1.31) to (1.38) it can be seen that the strongly-interacting KK-states will receive larger radiative contributions to their mass than the electroweakly-interacting ones. Furthermore, SU(2) doublets will receive larger contributions than SU(2) singlet fields. KK gluon has the largest $\delta(m^2_{g^{(n)}})$ and is the heaviest particle in the spectrum. KK photon is the lightest KK particle (LKP) owing to the small and negative correction to its mass, see Eq. (1.38). In a particular choice of $\Lambda R = 20$, g_{KK} will receive a positive mass correction of about 30% compared to the tree level mass, q_{KK} will receive the correction of about 20%, W_{KK} and Z_{KK} only about 8%, with KK leptons and neutrinos receiving below 5% mass correction. The lightest particle is the level-1 photon, with approximately the tree-level mass of $1/R$. The typical mass spectrum at one loop is shown on the right hand side of Fig. 1.7.

As it is the case for SM electroweak bosons, $B^{(n)}$ and $W^{3(n)}$ fields mix to form the physical states. The mass matrix in the $B^{(n)}$, $W^{3(n)}$ basis is given by [21]:

$$\begin{pmatrix} \frac{n^2}{R^2} + \delta m^2_{B^{(n)}} + \frac{1}{4}g_1 v^2 & \frac{1}{4}g_1 g v^2 \\ \frac{1}{4}g_1 g v^2 & \frac{n^2}{R^2} + \delta m^2_{W^{(n)}} + \frac{1}{4}g v^2 \end{pmatrix},$$

where $v \simeq 174$ GeV is the Higgs vacuum expectation value. While for the zero-mode case the mixing angle is large ($\sin^2\theta_W \simeq 0.23$), for $n \geq 1$ levels the diagonal terms in the mass matrix above dominate, resulting in only a small degree of mixing ($\sin^2\theta_W \sim 10^{-3}$). Thus the level-1 mass eigenstate, called the "KK photon", is nearly identical to the state $B^{(1)}$ and couples to all fermions proportional to their hypercharges with the coupling g_1.

1.6 KK photon as a DM candidate

To be a WIMP candidate for dark matter, a particle should be electrically-neutral, non-baryonic and stable. Candidates for a mUED WIMP include first-level excitations of neutral electroweak

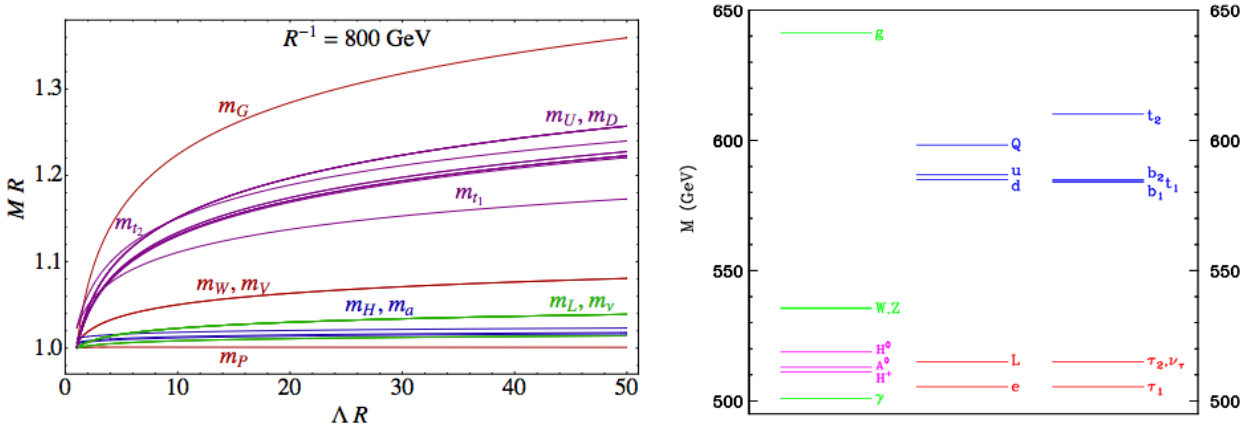

Figure 1.7: Left: Evolution of the $n = 1$ masses with the cutoff Λ at fixed $R^{-1} = 800$ GeV [36]. The vector bosons are shown in red ("P" stands for a photon), quarks in purple, leptons in green, while the blue color marks the scalars. Right: The spectrum of first level Kaluza-Klein states, including the effects of radiative corrections. A compactification radius of $R^{-1} = 500$ GeV, Higgs mass of 120 GeV and cut-off of $\Lambda R = 20$ have been used [29]. In both figures subscript "1" refers to SU(2) singlets and subscript "2" to SU(2) doublets.

gauge bosons (γ^1, Z^1) and neutrinos (ν^1). Due to the KK-parity conservation, the lightest level-1 KK state is stable. Since γ^1 receives negative radiative corrections to its mass (see previous section), it is the most likely LKP candidate. Alternatively, KK graviton could potentially also be the LKP as it receives negligible radiative corrections to its tree level $\sim R^{-1}$ mass. However, due to their very weak gravitational interactions, KK gravitons would annihilate much less efficiently and could produce a much larger relic density than the one observed. Thus, from the phenomenological point of view, γ^1 are the most likely WIMP candidates.

The relation between the annihilation cross section and the γ^1 mass is approximately given by [21]:

$$\langle \sigma v \rangle \simeq \frac{95 g_1^4}{324 \pi m_{\gamma^1}^2}, \tag{1.45}$$

where g_1 is the U(1) coupling constant. However, LKP can also co-annihilate with other UED particles, especially when the mass splittings between LKP and other light particles in the spectrum (such as KK leptons or Higgses, see Fig. 1.7) are small. Furthermore, the effect of level-2 KK particles also has to be taken into account when calculating the relic density. Annihilations of level-1 states through the exchange of an s-channel 2nd level KK particle near resonance can enhance the total cross section. Finally, level-2 particles can also be found in the final state [41]. These final-state level-2 particles then decay through loop-induced processes into SM particles (see Chapter 2 for more information on UED phenomenology). All these processes have to carefully be taken into account, as the final relic density (and consequently the preferred γ^1 mass) depends strongly on these factors. The relic density as a function of

the γ^1 mass is shown on the left-hand-side of Fig. 1.9[6]. Various contributions to the total (co)annihilation cross section are divided as follows:

- **$\gamma^1\gamma^1$ annihilations at the tree level (a0) and at one loop (a1), without considering channels with level-2 particles in the final state:** $\gamma^1\gamma^1$ annihilate predominantly to pairs of leptons and quarks (Fig. 1.8 left), with the annihilation fractions for $\gamma^1\gamma^1 \to \ell\ell$ being $\sim 19\%$ per generation, for $\gamma^1\gamma^1 \to t\bar{t}$ being $\sim 21\%$ and about 17% for other quark-antiquark pairs. The main channel at 1-loop level is $\gamma^1\gamma^1 \to h^2 \to t\bar{t}$, where the h^2 couples to SM particles through loop-induced diagrams. Including this channel slightly increases preferred LKP mass (a1) compared to tree-level only channels (a0).

- **Including all coannihilation channels at the tree level (b0) and at one loop (b1), without considering channels with level-2 particles in the final state:** Coannihilations of LKP with Higgs ($\gamma^1 H^1 \to t\bar{t}, b\bar{b}$) make one of the largest contributions. Many other channels, such as $\ell^1\bar{\ell}^1 \to X\bar{X}, H^1H^1 \to X\bar{X}$ etc., where ℓ^1 stands for e^1, μ^1, τ^1 and H^1 for any of the neutral or charged Higgses, each contribute $< 1\%$ to the total effective annihilation cross section. Coannihilations involving quarks are negligible. Since the coannihilation cross sections are typically weaker than the ones for $\gamma^1\gamma^1$ annihilation, the increase in the number of degrees of freedom effectively lowers the total (co)annihilation cross section. Due to their small mass splittings, the LKP and other next-to-LKPs freeze-out at approximately the same time. Next-to-LKPs subsequently decay to LKP, increasing the relic density (b0). Consequently, the preferred LKP mass shifts down by about 200 GeV. Adding the s-channel resonance of level-2 KK particles (mainly $\gamma^1 h^{1+} \to h^{2+} \to t\bar{b}$) increases significantly the annihilation cross section (Fig. 1.8 middle), thus shifting the preferred LKP mass back to about 800 GeV (b1).

- **Adding channels with level-2 particles in the final state, at the tree level (c0) and at one loop (c1):** The main contribution to final states including level-2 KK particles comes from coannihilation channels ($\gamma^1\ell^1 \to \gamma^2\ell$) that are enhanced by the exchange near resonance of the level-2 singlet lepton (Fig. 1.8 right). These channels make up together more than 50% of the (co)annihilation channels (see right-hand-side of Fig. 1.9). Other channels (including mainly γ^2, h^2, a^2 and $a^{\pm 2}$ in the final state) all contribute with small fractions to the total effective cross section. Due to the large increase in the total cross section, the relic density decreases by large amount, shifting the preferred LKP mass to above TeV level (c0, c1).

The relative contributions of various channels to the total effective (co)annihilation cross-section are shown on the right-hand-side of Fig. 1.9. After taking into account all these contributions, the preferred value for the LKP mass is found to be in the $1.3 - 1.5$ TeV range

[6]The relic density can be expressed as Ωh^2, where Ω is the DM density fraction and h is a dimensionless parameter related to the expansion of the Universe, $h = H^0/(100 \text{ km s}^{-1} \text{ Mpc}^{-1})$. The relic density measured by WMAP is $\Omega h^2 = 0.1120 \pm 0.0056$ [37] and by Planck $\Omega h^2 = 0.1199 \pm 0.0027$ [18].

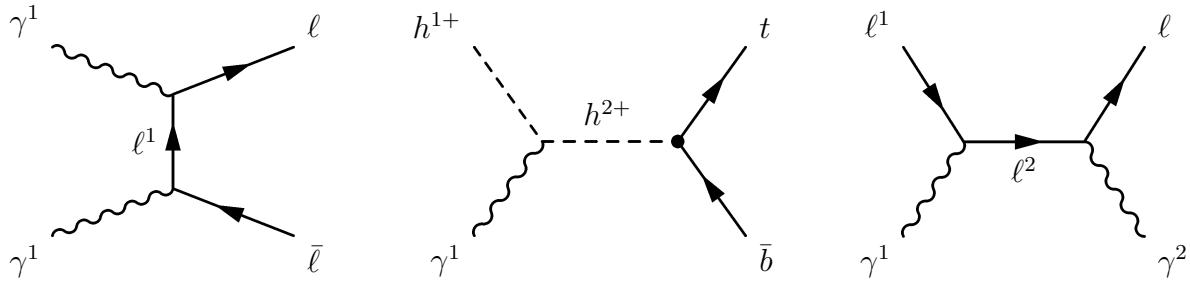

Figure 1.8: Examples of KK-photon (co)annihilations. From left to right: Annihilation of γ^1 to SM leptons, coannihilation of γ^1 and h^{1+} through a level-2 (near-)resonance charged Higgs (h^{2+}) into $t\bar{b}$ pair, and coannihilation of γ^1 with ℓ^1 through a level-2 (near-)resonance lepton (ℓ^2) in the final state with a level-2 photon γ^2 and a SM lepton. The blob in the middle diagram represents the KK-number-violating loop-induced decays of level-2 states into SM particles.

(where the c1-curve crosses the green band on the left-hand-side of Fig. 1.9). The value of the cut-off scale Λ affects the mass of the KK particles, and can consequently alter the (co)annihilation cross sections. The effect depends on the exact UED spectrum. Increasing ΛR to 50 is found to increase the preferred LKP mass by about 100 GeV.

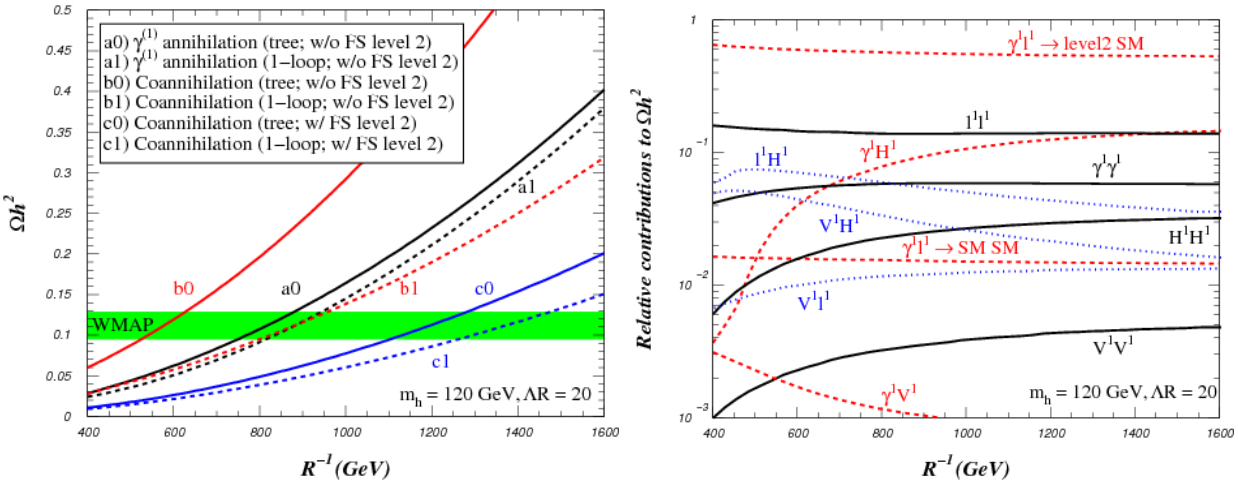

Figure 1.9: Left: The relic density (Ωh^2) as function of R^{-1} for Higgs mass of 120 GeV and $\Lambda R = 20$ including different processes as specified on the figure. Here 1-loop stands for one-loop couplings between KK level 2 and SM particles. The shaded region corresponds to the 3σ preferred region obtained by WMAP. Right: Relative contributions to the relic abundance at the LKP decoupling temperature as a function of R^{-1} for Higgs mass of 120 GeV and $\Lambda R = 20$. Here, summation over a class of initial states and all possible final states is performed with the exception of $\gamma^1\ell^1 \to$ level 2 SM which includes only processes with one level 2 particle in the final state and $\gamma^1\ell^1 \to$ SM SM which includes only SM particles in the final state. ℓ^1 stands for $e^1, \mu^1, \tau^1, \nu_i^1$, V^1 for W^1, Z^1 and H^1 for $a^1, h^{1\pm}, h^1$. All remaining channels contribute less than 1% [41].

1.7 Bounds on UED parameters

The physical range of the two free parameters in mUED – the cut-off scale Λ and the compactification scale R, can be derived from various theoretical considerations and experimental data. One way to put an upper bound on Λ is to look for a scale where the 4D gauge couplings become non-perturbative – the limit derived in this way is about $\Lambda R \sim 10$. However, a stronger limit can be placed by considering the vacuum stability constraint on the Higgs potential [38]. The stability of our vacuum depends on the sign of the quartic Higgs self-coupling λ – the coefficient next to the $|H|^4$ term in the Higgs potential. For negative λ the potential is unbounded from below and therefore unstable. Since λ is a running coupling, the electroweak vacuum stability bound is found by solving the renormalization group equation and requiring that the coupling remains non-negative even at high energies. The upper limit on the mUED cut-off scale Λ is the point where $\lambda(\Lambda)$ becomes zero:

$$\lambda(\mu = \Lambda_{\max}) = 0. \tag{1.46}$$

The limit found in [38] is shown in the Fig 1.10. While for 6D UED models, the values for the maximal Λ are quite low, the limit is relaxed for mUED case – for $M_{KK} \sim 1/R \sim$ TeV the upper limit on Λ is about 5 TeV.

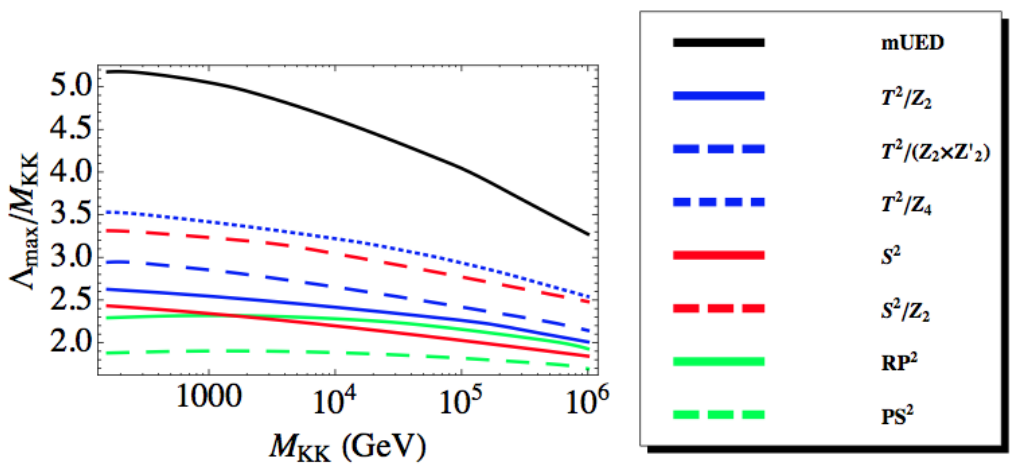

Figure 1.10: Left : Upper bounds on the UV cut-off Λ of the UED models as a function of M_{KK}, set by requiring the stability of the Higgs vacuum. Right: Color convention for types of the UED models. mUED is shown with a black line, while other colors correspond to different types of compactification for 6D UED models [38].

With the discovery of the Higgs particle, the bounds on the UED compactification radius R can be derived from measurements of Higgs properties. The contributions from loop diagrams including KK particles modify the Higgs production cross section and decay rates, which affect the Higgs signal strengths at the LHC. The electroweak precision data are another source of

	$\Lambda/M_{\rm KK}$ for $M_{\rm KK} \sim O(\text{TeV})$	Higgs signal strength	S and T parameters
mUED	5.0	610 GeV	680 GeV
T^2/Z_2	2.5	1060 GeV	1190 GeV
$T^2/(Z_2 \times Z_2')$	2.9	960 GeV	1080 GeV
T^2/Z_4	3.4	820 GeV	920 GeV
RP^2	2.3	1060 GeV	1220 GeV
S^2	2.3	1330 GeV	1490 GeV
S^2/Z_2	3.2	940 GeV	1050 GeV
PS	1.9	1240 GeV	1410 GeV

Table 1.2: Highest possible UV cut-off scales and lower bounds on the KK scale M_{KK} at the 95% CL for mUED and several other 6D UED models, as derived from the stability of Higgs vacuum (Λ), and Higgs measurements at the LHC and electroweak precision data (M_{KK}) [38].

experimental constraints on R. The electroweak S and T parameters proposed by Peskin and Takeuchi ([39], [40]), prove to be the most powerful in constraining the UED. The 95% C.L. lower bounds on the scale $M_{KK} \sim 1/R$ from the LHC Higgs measurements and from the S, T analysis are found in [38] to be 600 GeV and 700 GeV in mUED, while those in the 6D UED models are 800-1300 GeV and 900-1500 GeV, respectively (see Tab. 1.2).

If the lightest KK particle is stable, then the dark matter relic abundance provides a constraint on its mass, as well. The upper bounds on the LKP mass in some of the 6D UED models were found to be at the level of few 100 GeV, making tension with the values in Tab. 1.2. In mUED scenario, however, the mass splittings are such that the (co)-annihilations of level-1 KK states into second KK excitations play an important role. Due to the increase in the annihilation rate, the relic abundance is reduced, and preferred value for the LKP mass is raised to above-TeV level, 1300 GeV $\leq M_{KK} \leq$ 1500 GeV [41].

Another set of contraints is coming from collider searches at Tevatron and LHC. The D0 collaboration performed a search for KK particles in a final state with two muons of the same charge using 7.3 fb^{-1} of data collected in $p\bar{p}$ collisions at the center of mass energy of 1.96 TeV. They set a lower limit on the compactification scale of $R^{-1} > 260$ GeV within the minimal UED model [42]. The ATLAS collaboration set more stringent limits using 20 fb^{-1} of LHC data with proton-proton collisions at the center of mass energy of 8 TeV. Since UED signatures closely resemble supersymmetry signatures, some of ATLAS supersymmetry searches provided reinterpretation of their results within the mUED model. An example are searches with jets, missing transverse momentum and either two [43], or no leptons [44] in the final state. An analysis dedicated to mUED was performed in the di-muon final state [45] by the author of this thesis and served as a basis for this work. These ATLAS analyses placed lower limit on the compactification scale of about $R^{-1} > 800$ GeV. Somewhat weaker bounds on R^{-1} have been set in [46] by exploiting CMS limit on cross section for new physics resulting in resonant dilepton final states [47]. As already mentioned, level two KK states can decay through KK-number violating interactions to two zero mode SM particles, producing a resonant peak. The

ΛR	5	10	20	50
R^{-1} [GeV]	720	730	715	755

Table 1.3: 95% C.L. lower bounds on R^{-1} in mUED coming from dilepton-resonance searches, for different cut-off parameters ΛR [46].

limits correspond to $R^{-1} \gtrsim 715$ GeV (shown in Table 1.3) and to $M_{KK}^{(2)} \gtrsim 1.4$ TeV for the masses of the second Kaluza-Klein excitations.

A summary of the strongest limits in the mUED parameter space is shown in Fig. 1.11 (taken from [48]). Dark matter searches in direct-detection experiments are probing the more compressed part of the parameter space at low ΛR, while the collider searches probe higher ΛR with equal success. Both types of experimental constraints are approaching the KK mass scale preferred from the relic density point of view. Taking the electroweak vacuum stability into account, the phenomenologically interesting part of mUED parameter space seems to be just around the corner, with $\Lambda R \leq 5.5$ and $1/R \geq 1150$ GeV.

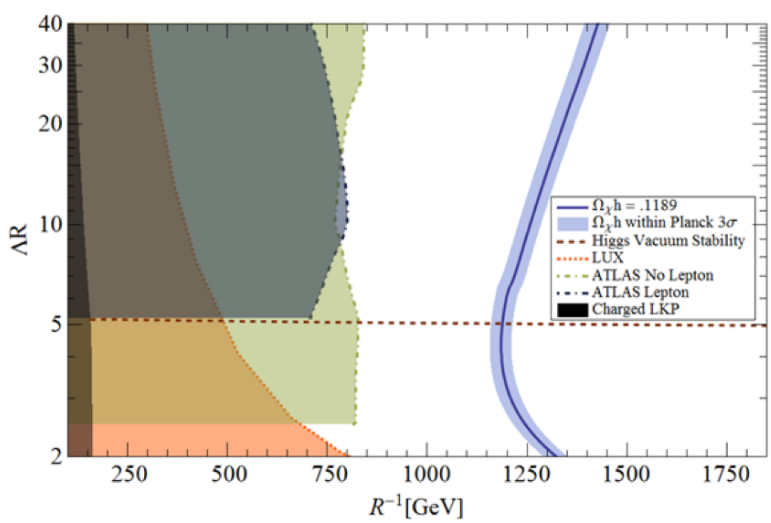

Figure 1.11: Limits on mUED parameters coming from a combination of sources: direct-detection dark-matter searches (LUX), collider searches (ATLAS), relic-density bounds (Planck) and the theoretical bound on Λ derived from the stability of the Higgs vacuum [48].

Chapter 2

Signature of mUED at the LHC

High energy proton-proton collisions offer a wide range of research opportunities in physics– from precision measurements of the Standard Model to potential discoveries of new physics, such as mUED. As protons are made up of quarks and gluons, which interact through the strong force, careful handeling of QCD calculations is essential in making precise predictions. Various perturbative and non-perturbative effects have to be taken into account correctly in order to achieve good understanding of different processes occuring proton-proton collisions, whether it is to understand how mUED signal looks in the detector, or to understand and control various backgrounds to mUED signal.

Cross section at the LHC and production channels of mUED are explained in Sec. 2.1.1. Typical mUED decay patterns and signatures are described in Sec. 2.2, while the treatment of different scales encountered when simulating the interactions at the LHC is summarized in Sec. 2.3.

2.1 Production at the LHC

The total production cross section for a process occurring in a proton-proton collision can be written as

$$\sigma_{\text{tot}}(\mu_F, \mu_R) = \int_0^1 dx_1 \int_0^1 dx_2 \sum_{ij} f_{i/p}(x_1, \mu_F) f_{j/p}(x_2, \mu_F) \hat{\sigma}_{ij}(x_1 p_1, x_2 p_2, \alpha_s(\mu_R^2), \mu_F, \mu_R), \quad (2.1)$$

where the $\hat{\sigma}_{ij}$ denotes the cross-section for the hard interaction of partons i, j, carrying x_1 and x_2 fractions of a proton momentum, respectively, and $\alpha_s(\mu_R^2)$ is the strong coupling constant evaluated at a particular renormalisation scale μ_R (see Sec. 1.1.1). All the non-perturbative QCD physics of the initial state is absorbed in the definition of the parton density functions (PDFs), $f_{i/p}(x_1, \mu_F)$ and $f_{j/p}(x_2, \mu_F)$, evaluated at the factorisation scale μ_F (see Sec. 2.1.1 below).

2.1.1 Parton density functions

Protons consist of three valence quarks (two up-type and one down-type quark), sea quarks (all the other quark and anti-quark flavors), and the gluons, collectively referred to as partons. The parton content of a proton is described with parton density functions (PDFs) $f_i(x_i, Q^2)$ – functions expressing the number density of a parton of the flavor i, carrying a longitudinal momentum fraction x_i of the total proton momentum, at a certain momentum transfer Q^2. When calculating the NLO contributions to a LO cross-section, we are faced with the the collinear divergencies occurring in the initial state radiation (the radiation off a parton "just" before it enters the interaction). To avoid the divergent contributions of the small-angle emissions, a minimum cutoff energy scale, called the factorisation scale (μ_F), is introduced. This scale "factorises" the short-range perturbative physics from long-range interactions occurring at small scales, $k_t \leq \mu_F$, where k_t is the transverse momentum of the emitted parton relative to its parent particle. The emissions and virtual corrections below the factorisation scale are absorbed in the definitions of the PDFs themselves, which then become functions of μ_F – $f_i(x_i, \mu_F; Q^2)$. Similar to the case of the running strong coupling constant, a universal set of PDFs, known at some reference scale μ_{F0}, can be evolved to any other scale μ_F by using DGLAP (Dokshitzer-Gribov-Lipatov-Altarelli-Parisi) equation, and used for any physics process (see Fig 2.1 for an example of a PDF set and the effect of evolution). In practice, the factorisation scale is often chosen to be equal to the momentum transfer involved, i.e. $\mu_F \sim \mu_R \sim Q^2$, so that the higher-order corrections to the leading-order cross section are small.

2.1.2 mUED production channels

The interactions between KK modes are equal to the Standard Model interactions, up to loop corrections. The tree-level KK-number conserving couplings are of the same strength as the corresponding Standard Model couplings. KK-number violating couplings (which still preserve the KK-parity) appear only at one-loop level. Therefore, the dominant mUED production channel at the LHC will be through strong interactions – typically two level-one gluons or quarks will be created in a proton-proton collision (see Fig. 2.2).

While level one states can be only pair-produced at colliders, level two states could be singly produced in KK-number violating interactions. Feynman diagrams for three types of level-two KK production are shown in Figure 2.3. The non-resonant KK-number preserving production of two second KK modes is possible through tree-level strong coupling. However, it suffers from phase-space suppression because of two heavy particles in the initial state. Resonant production of a second KK gluon is preferred from the point of view of required energy. However, it proceeds through one-loop suppressed KK-number violating coupling, and is further reduced due to the parton distribution functions at the LHC – $q\bar{q}$ is required in the initial state. Finally, a second KK mode quark or gluon can be produced in association with another zero mode. These non-resonant processes are again one-loop suppressed due to the KK-number violating coupling.

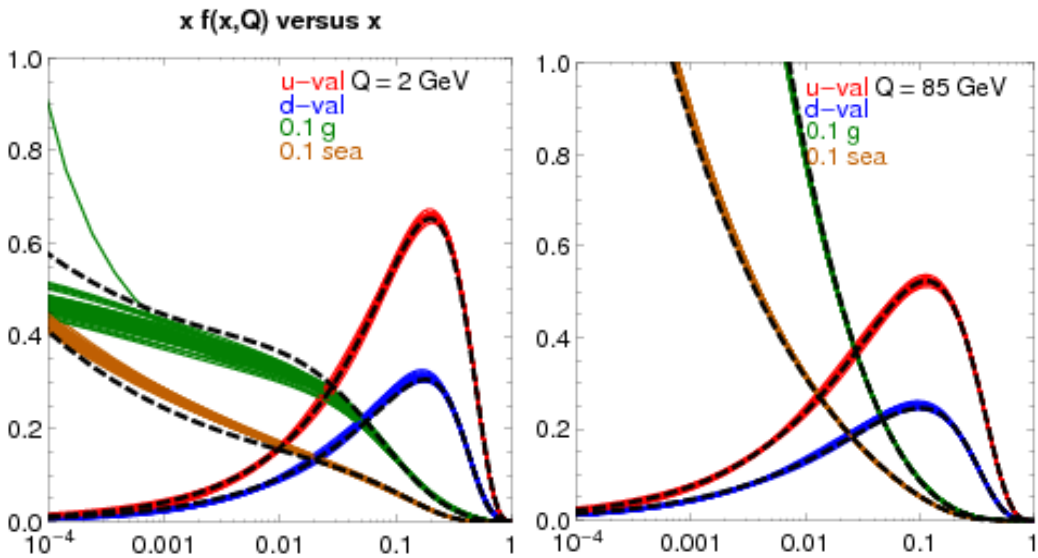

Figure 2.1: CT10 NNLO (solid color) and NLO (dashed) parton distribution functions at two scale choices ($Q = 2$ GeV and $Q = 85$ GeV): valence up(down)-quarks ($u(d)_{val}(x,Q) = (u(d) - \bar{(}u)(\bar{d}))(x,Q)$) are shown in red (blue), sea quarks ($q_{sea}(x,Q) = 2(\bar{(}u) + \bar{d} + \bar{s})(x,Q)$) in brown and gluons ($g(x,Q)$) are shown in green. The horizontal axis is proton-momentum fraction x, and vertical axis corresponds to $xf(x,Q)$. The colored band width corresponds to the uncertainty ranges on CT10 NNLO PDFs [50].

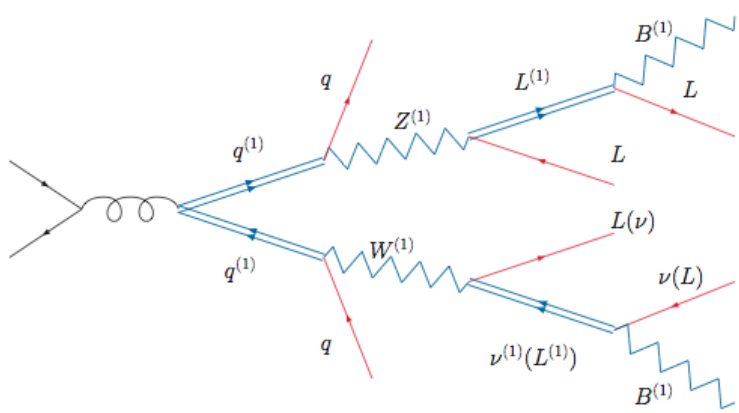

Figure 2.2: Production of two $n = 1$ KK quarks in a hadron collider. The KK quarks decay through KK-number conserving interactions down to the LKP – the KK-photon (denoted with $B^{(1)}$) [21].

Since the production of two level-1 quarks or gluons has the largest cross section, it is the target production-channel in this analysis. The cross sections depend on masses of KK-gluons and quarks, which are functions of the R^{-1} and Λ parameters, and vary from about 0.1 pb to about 10 pb for signal models considered in this analysis (see also Chapter 3).

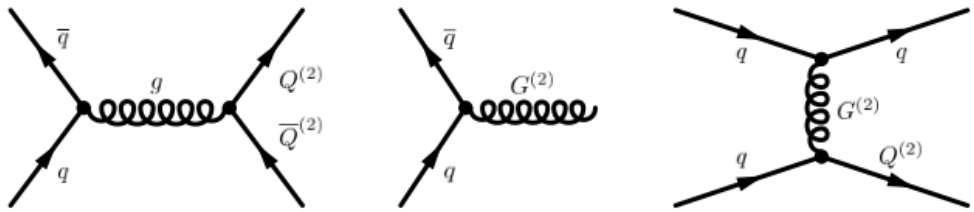

Figure 2.3: Examples of Feynman diagrams for KK-number preserving, KK-number violating direct, and KK-number violating associated production (from left to right). $Q^{(2)}$ and $G^{(2)}$ represent a second KK singlet or doublet quark and a second KK gluon mode, respectively [46].

2.2 Decay chains and signature of mUED

Colored KK particles produced in a pp collision typically decay to lighter KK states in cascades, radiating SM particles on the way. The decay chains end with the lightest KK particle (LKP), level-1 photon, which is stable due to the KK-parity conservation. As it does not interact with the detector, its presence in an event can only be inferred through momentum imbalance in the plane transverse to the collision direction. The typical decay pattern is the following (see Fig. 2.4):

- Gluon excitations decay to a quark pair, one quark being a KK level-one state, the other being a zero-mode SM quark.
- Singlet quark excitations decay through electroweak interaction directly to LKP: $q_1^1 \rightarrow q\,\gamma^1$, where the superscript "1" denotes a level-one KK excitation (SM states have no superscript) and subscript "1" stands for SU(2) singlets.
- SU(2) doublet KK quarks will predominantly decay to W^1 (with Br$\sim$0.65) or Z^1 (with Br$\sim$0.33): $q_2^1 \rightarrow q\,W^1(Z^1)$, where subscript "2" stands for SU(2) doublets.
- Due to the mass hierarchy (see Fig. 1.7), W^1 and Z^1 can not decay to quarks, and so they decay with almost 100% branching fraction to leptons:

$$W^1 \rightarrow q\,\bar{\nu}\,l^1\ ,\ q\,\bar{l}\,\nu^1 \tag{2.2}$$

$$Z^1 \rightarrow q\,\bar{l}\,l^1\ ,\ q\,\bar{\nu}\,\nu^1. \tag{2.3}$$

Due to typically small mixing between the SU(2) and U(1) eigenstates at $n \geq 1$ levels, the branching fractions of Z^1 decays to neutrinos versus charged leptons are roughly equal, and it will predominantly decay to left-handed fermions.

- Finally, leptons decay to the LKP, as this is the only kinematically allowed channel: $l^1 \to l\gamma^1$, $\nu^1 \to \nu\gamma^1$.
- Only about 2% of SU(2) quark doublets will decay directly to the LKP: $q^1 \to q\,\gamma^1$.

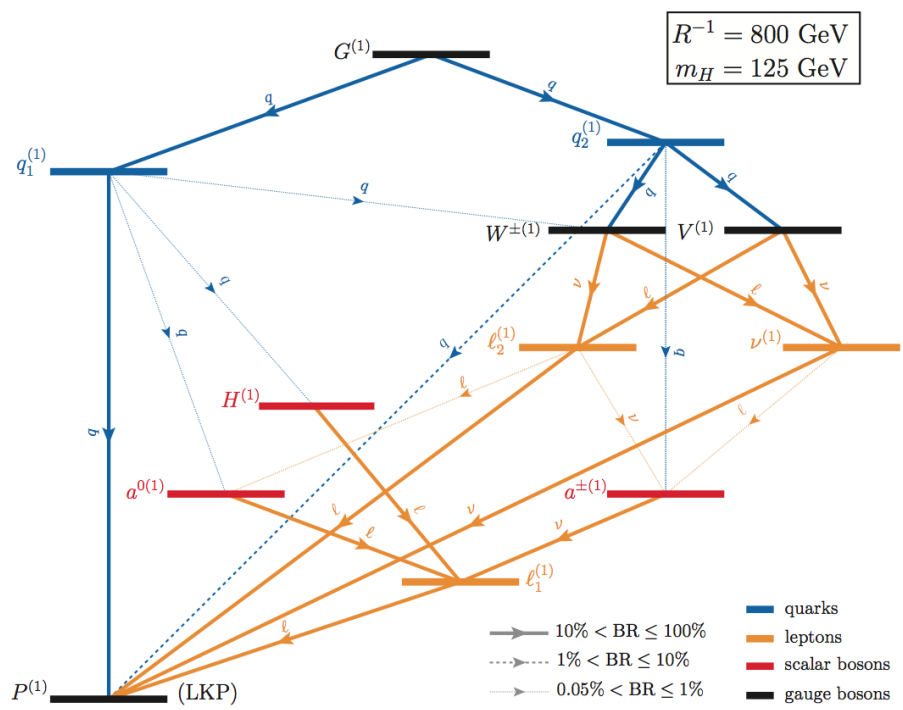

Figure 2.4: The principal decay channels of the $n = 1$ KK particles for $R^{-1} = 800$ GeV ($P^{(1)}$ stands for a KK photon) [36].

Due to almost 100% branching fraction of W^1 and Z^1 to leptons, mUED has lepton rich signatures. As lepton final states offer a relatively clean signature in hadron colliders, a two-lepton final state was chosen as a target signature for this analysis. Since the γ^1 does not interact with the detector, its presence can be inferred only through the momentum imbalance in the plane transverse to the beam direction – the missing transverse energy (E_T^{miss}).

In case level-2 KK particles are initially produced in the pp collision, the signature may differ. The decays of level-2 excitations proceed either through KK-number conserving interactions into one second and one zero mode or into two first KK modes, or through KK-number violating decays into two zero SM modes. The signature in this case may contain no LKPs, i.e. no E_T^{miss}, in the final state and is often characterised by SM dilepton resonances.

2.3 Simulation of proton-proton collisions

The big part of the challenge of the QCD predictions at the LHC is due to a given process often involving very different energy scales – from the ∼GeV scales involved at the inital-state proton's mass, up to ∼TeV momentum-transfers involved in production of a heavy particle, along with specific analysis requirements setting the scale of final state jets above a certain minimal transverse momentum. Physics processes occurring in the collisions are simulated using Monte Carlo (MC) event generators. Due to the presence of different scales involved in going from the initial hard interaction to the evolution of partons into the final state hadrons, the methods of calculation depend on the corresponding kinematic regime [51]. A pictorial representation of a typical hadron-collider event is shown in Fig. 2.5. Depending on the energy scale involved, it can be factorised into four well-defined phases:

- **High-Q^2 scattering:** Hard interaction of partons produces "interesting" physics events, e.g. new physics (represented by the red blob in Fig. 2.5). This interaction is known from the first principles, calculable in perturbation theory in the coupling constants and can be systematically improved by adding higher order terms. Matrix-element (ME) MC generators are used to simulate the hard scattering by calculating the Feynman diagrams up to a certain order for a process of interest (usually leading (LO) or next-to-leading order (NLO), depending on the generator and process). LO generators use only tree-level diagrams, but provide predictions for up to 6-8 (or more) additional partons produced in the hard scattering, along with the process of interest (e.g. W or Z production). On the other hand, NLO generators include usually only one additional parton produced in the hard interaction, but base their calculations on the tree-level as well as loop diagrams.

- **Parton shower:** QCD showering of the final- and initial-state partons (shown in red and blue in Fig. 2.5) is simulated with parton-shower (PS) MCs using an approximation to exact perturbation theory. QCD showering is physics known from the first principles, computationally, however, one runs into problems such as the divergences of soft and collinear parton emissions. Methods with Sudakov form-factors $\Delta(Q^2, t)$ (i.e. a probability of not-emitting a parton above some scale t) are generally used to evade the divergencies and evolve the parton showers from high scales where perturbation theory is applicable, down to the low energy (order of few Λ_{QCD}) where showering stops and hadronisation begins. The initial-state branching depends also on the way PDF is built up at the scale of the hard scattering.

- **Hadronisation:** Hadronisation involves the transition of partons into colorless hadrons (green blobs in Fig. 2.5). This is a non-perturbative process and there is no strong theoretical understanding of the phenomenon. Several phenological models exist and they generally rely on the assumption that the transition to hadrons is local in phase space, i.e. long-range correlations are highly suppressed. In the cluster model the partons are grouped into small-mass colorless clusters and then decayed into physical hadrons. The

color confinement potential of a quark-antiquark pair grows linearly with their distance ($V(R) \sim kr$, where $k \sim 0.2:\ \mathrm{GeV}^2$). In the string model this is simulated by stretching a string of uniform tension across the $q\bar{q}$ pair. When it becomes energetically favourable, the string will break in two by creating a new $q\bar{q}$ pair in the middle. The fragmentation of partons into hadrons is modeled using non-perturbative fragmentation functions: $D_Q^H(z, \mu^2)$ describes the probability of a quark Q fragmenting into a hadron H carrying fraction z of the quark's momentum, evaluated at the scale μ.

- **Underlying event:** Secondary hard or semi-hard interactions may occur between the remnants of the incoming protons (purple blob in Fig. 2.5). Here, again, there is no complete first-principles theory available, and different phenomenological models are employed and tuned to data.

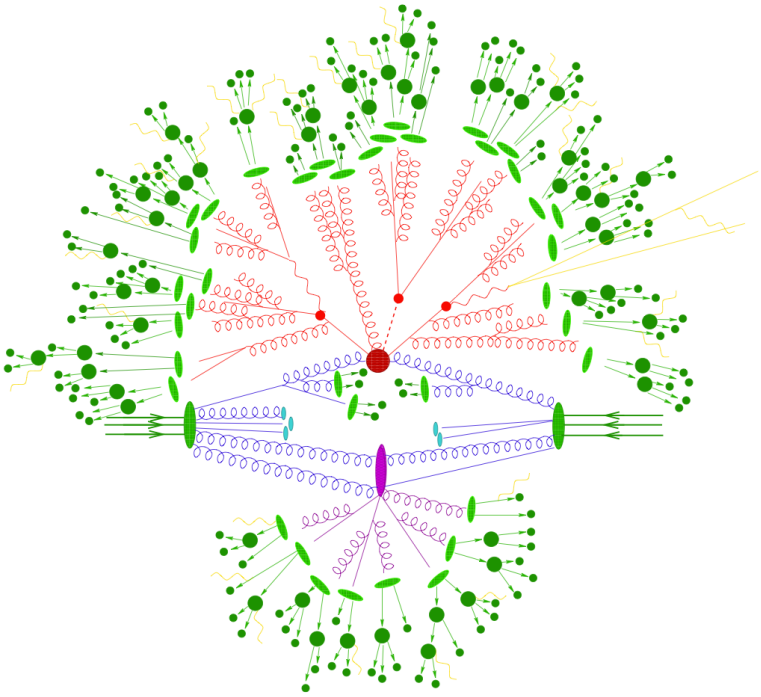

Figure 2.5: Pictorial representation of a typical proton-proton collision. Hard interaction of partons (red blob) is followed by the final state QCD radiation (red). Partons eventually hadronise (light green blobs) and hadrons decay (dark green blobs). Secondary QCD interactions (purple blob) take place between the proton remnants (figure adapted from [61]).

To obtain the optimal full-event simulation, the results from ME and PS have to be properly matched and any possible double counting of the events has to be avoided. Although parton-showers usually produce only soft and collinear parton emissions, occasionally a hard or large-angle parton can be emitted. Generally, if this parton produces a jet harder than a jet coming

from the initial hard interaction ME calculation, the event is rejected. This is the basis of MLM matching method. The exact procedure of the overlap removal depends on the merging scheme used. CKKW algorithm [57] is based on shower veto and event reweighting, rather than event rejection. A merging scale Q_{cut} is defined that separates the phase space between a regime of jet production, described by matrix elements, and a regime of jet evolution, described by parton showering. ME jet configurations are accepted or rejected according to reweighting in α_S and Sudakov form-factors. Each hard parton then undergoes a constrained showering starting from the scale where it parton appeared first, i.e. any new emission that would give rise to an extra jet is vetoed.

Various MC generators used in this thesis are presented in Chapter 3.

Chapter 3

The Large Hadron Collider and the ATLAS experiment

3.1 The Large Hadron Collider

The Large Hadron Collider (LHC) is the world's largest and most powerful particle accelerator designed to collide beams of protons at the centre-of-mass energy of 14 TeV. Its purpose is to explore physics at TeV scale and discover possible new phenomena beyond the Standard Model of particle physics. It is built at the European Organization for Nuclear Research (CERN) in Geneva, Switzerland. The main LHC ring, situated 100 m underground, has the radius of 27 km and accelerates two beams of protons in opposite directions. The beams collide at four experiments positioned on the ring: ATLAS, ALICE, CMS and LHC-b. ATLAS and CMS are multi-purpose detectors designed to measure precisely the Standard Model physics, as well as search for new phenomena. As their physics program is the same, they are complimentary to each other. ALICE is optimised to study the busy environment of heavy-ion (Pb nuclei) collisions. These collisions produce the conditions expected to resemble the state of our Universe a fraction of the second after the Big Bang. LHC-b, where b stands for beauty, is an experiment specialized for physics of b-hadrons. "B-physics" is important for understanding the matter-antimatter asymmetry of our Universe.

The source of protons at the LHC is a bottle of hydrogen. The hydrogen is passed through an electric field to strip off its electrons, and the protons are then taken through the acceleration process consisting of several steps. First, the protons are passed through a linear accelerator (Linac 2), which accelerates the protons to the energy of 50 MeV. Linac 2 consists of cillindrical conductors which are alternately charged positive or negative. As protons pass through them, they are pushed by the positive charge behind, and pulled by the negative charge ahead. The next step is Proton Synchrotron Booster (PSB), made up of four superimposed synchrotron rings, which pushes the protons up to 1.4 GeV. After PSB, the protons are injected into the Proton Synchrotron (PS) where they are accelerated by the conventional (room-temperature) electromagnets, and reach the energy of 25 GeV. Protons are then sent to the Super Proton

Synchrotron (SPS). With its 7 km in circumference, SPS is the second-largest machine in CERNs accelerator complex. It uses the conventional electromagnets to accelrate the protons to 450 GeV. Finally, the protons are injected into the LHC ring for the final acceleration. It takes 4 minutes and 20 seconds to fill each LHC ring, and 20 minutes for the protons to reach their maximum energy (in 2012) of 4 TeV. Under normal operating conditions, the beams circulated for many hours inside the LHC, colliding at the centre-of-mass energy of 8 TeV.

The LHC superconducting magnets operating at 1.9 K produce a magnetic field of 8.3 T needed to bend such a high energy beams and keep them in their orbit. There are 1232 dipole magnets (15 metres long) which bend the beams, and 392 quadrupole magnets (57 metres long) which focus the beams. The beams are organised in bunches containing up to 10^{11} protons each. At the nominal design, up to 2808 bunches with a 25 ns bunch spacing will collide in the LHC at the centre-of-mass energy of 14 TeV, producing the collision frequency of 40 MHz. During the 2012 data-taking the LHC was colliding 50 ns spaced bunches at the centre-of-mass energy of 8 TeV, with the number of bunches per beam reaching 1280. The 2012 8 TeV dataset is used in the analysis presented in this thesis.

3.2 The ATLAS detector

ATLAS (A Large Toroidal Lhc ApparatuS) is a general purpose detector designed to provide accurate measurements of particles and processes occurring in proton-proton (pp) and heavy-ion collisions [53]. The LHC is designed to collide bunches consisting of up to 10^{11} protons at a rate of 40 million times per second providing the instantaneous luminosity of $10^{34}\mathrm{cm}^{-2}\mathrm{s}^{-1}$, as well as to collide the heavy-ion nuclei at a design luminosity of $10^{27}\mathrm{cm}^{-2}\mathrm{s}^{-1}$. These conditions require high standards for the LHC detectors, in terms of interaction rates, radiation doses and particle multiplicities and energies. The detector requires fast, radiation-hard electronics and sensor elements, in addition to high detector granularity to reduce the influence of overlapping events. Furthermore, the cross section of "interesting" physics processes are many orders of magnitude smaller than the total inelastic-pp cross section of 80 mb, requiring large acceptance and good particle momentum resolutions and reconstruction efficiencies, as well as good coverage and performance of electromagnetic and hadronic calorimeters. Finally, highly efficient triggering on low transverse momentum objects with sufficient background rejection is required to achieve an acceptable trigger rate and high efficiency of collecting physics processes of interest.

3.2.1 Coordinate system

The ATLAS detector is shown schematically in Fig 3.1. It is forward-backward symmetric with respect to the interaction point. The origin of a right-handed coordinate system used to describe the detector is in the nominal interaction point of the colliding beams. The beam-line defines the z-axis and the x-y plane is transverse to the beam direction. The positive x-axis points to the center of the LHC ring, while the positive y-axis points upwards. In polar coordinates, the

azimuthal angle ϕ is measured in the transverse plane, around the beam axis, and the polar angle θ is defined as the angle from the z-axis. Since the pp collisions occur along the z-axis, one defines a rapidity $y = \frac{1}{2}\ln\frac{E+p_z}{E-p_z}$ which is invariant, up to a constant, under boosts along the z-axis, while the transverse quantities, such as p_x and p_y, remain invariant. For simplicity, in physics analyses a pseudorapidity defined as $\eta = -\ln\left(\tan\frac{\theta}{2}\right)$ is used instead of the true rapidity y. When a particle is "relativistic", i.e. $\beta \simeq 1$, which to a large extent is true for the LHC, the pseudorapidity η is a good approximation of the rapidity y. The distance ΔR between the objects is, therefore, defined as $\Delta R = \sqrt{\Delta\eta^2 + \Delta\phi^2}$.

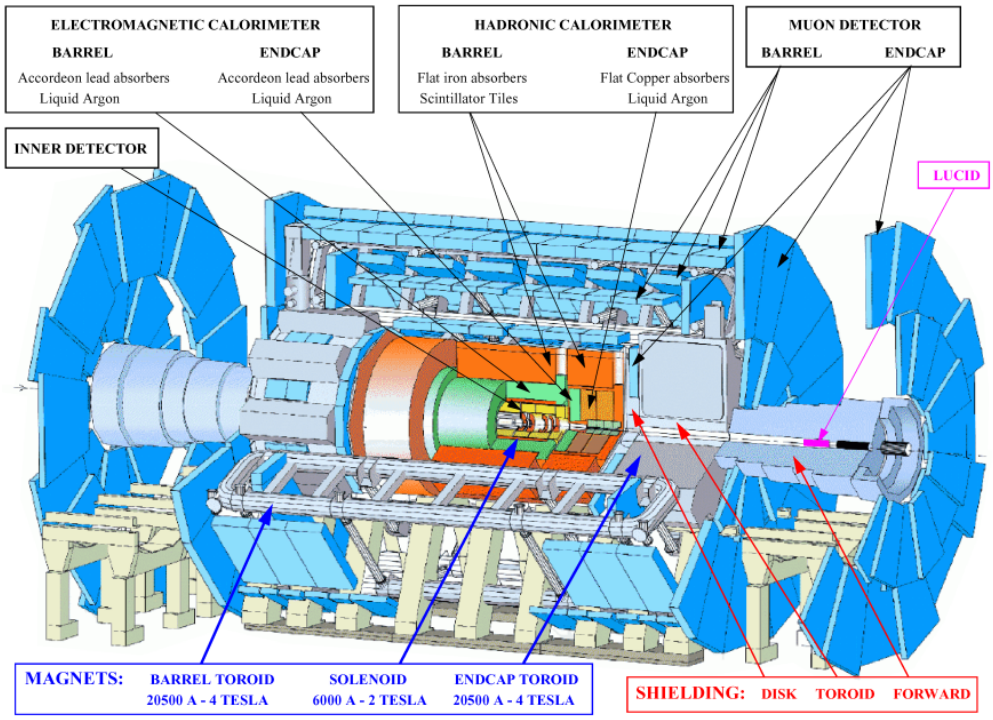

Figure 3.1: Overall layout of the ATLAS detector. The detector is 25 m high, 44 m long and weights approximately 7000 tonnes.

3.2.2 Magnet system

Charged particles' momenta are measured based on the deflection of their trajectory in a magnetic field. The ATLAS magnet system is composed of four large superconducting magnets (see Fig. 3.2) operating at temperatures of about 4.5 K. The central solenoid is runs 5.8 m parallel to the beam-line and has a diameter of 2.5 m. It encapsules the inner part of the detector and provides a 2 T homogenous magnetic field inside the coil which bends the particle trajectories in the ϕ direction. Three large toroidal magnets consist of eight independent coils each, arranged radially and symmetrically around the beam axis. The coils are located within the muon spectrometer and produce the magnetic fields of 3.9 T (4 T) in the barrel (end-cap) deflecting particles in the η direction. The barrel toroid extends radially from 9.4 m to 20.1 m and measures 25.3 m in length. The end-cap toroids are rotated by 22.5° with respect to the central barrel in order to provide higher overlap and optimise the bending power in the transition region. The advantage of the toroid is that it can cover larger volume as it requires less material (air core, no return yoke), with the down side being the non-uniform magnetic field.

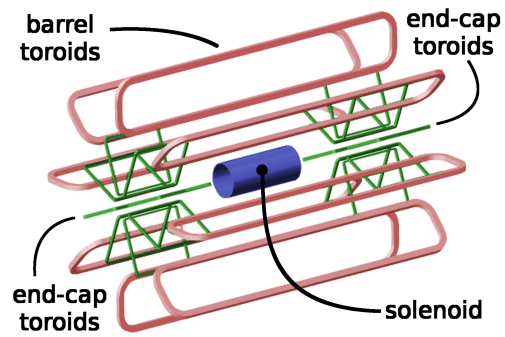

Figure 3.2: ATLAS magnet system: the central solenoid surrounds the inner detector and produces the magnetic field along the z-axis, while the large toroids dictate the detector size and provide the field along the ϕ direction.

3.2.3 Inner detector

The ATLAS Inner Detector (ID) provides efficient pattern recognition, excellent momentum and primary and secondary vertex measurements for charged tracks with $p_T > 0.5$ GeV in the pseudorapidity range $|\eta| < 2.5$, and electron identification for $|\eta| < 2.0$. It is contained within a cylindrical envelope of length ± 3.5 m and of radius 1.15 m, immersed in a 2 T magnetic field of the central solenoid. The ID consistes of three sub-detectors (see Fig. 3.3) – pixel detector and silicon microstrip tracker (SCT) providing the precision tracking up to $|\eta| < 2.5$, and Transition Radiation Tracker (TRT) covering up to $|\eta| < 2.0$.

The silicon pixel detector is the innermost subsystem consisting of three layers of rectangular pieces of silicon divided into pixels. It provides the highest granularity used for vertex reconstruction and is particularly important for the measurement of track impact parameters, defined as the minimum distance of the track to the primary vertex. The pixel layers are segmented in $R - \phi$ and z, with the intrinsic accuracies of 10 μm $(R - \phi)$ and 115 μm (z) in the barrel and 10 μm $(R - \phi)$ and 115 μm (R) in the endcap disks.

The SCT is composed of four layers of silicon microstrip modules in the barrel and nine

disks in the endcap. Each barrel layer consists of two sets of strips, where the set parallel to the beam direction measures the $R - \phi$ coordinate and the stereo strips with a 40 mrad tilt provide the z-coordinate. The endcap strips running radially determine the ϕ-position, while the R-coordinate is provided by a set of stereo strips at an angle of 40 mrad. The intrinsic accuracies are 17 μm $(R - \phi)$ and 580 μm (z) in the barrel and 17 μm $(R - \phi)$ 580 μm (R) in the disks.

The TRT consists of long 4 mm diameter straw (drift) tubes, providing only $R - \phi$ information, with an intrinsic accuracy of 130 μm per straw. It contributes significantly to the momentum measurement by providing 30 hits per track on average and over a longer track length, thus compensating for the lower precision per point compared to the silicon detectors. It also enhances the electron identification performance by generating and detecting the transition-radiation photons. Relativistic particles passing the boundary between the xenon-based gas mixture of the straw tubes and polyethylene radiator material filling the space between the tubes emit x-rays due to the change in dielectric constant of the medium. For the energy range of interest, this radiation is mainly present only for electrons, thus allowing for some distinction between electrons and hadrons.

The inner detector design momentum resolution and η coverage, along with the same parameters for other subdetectors, are shown in Tab. 3.1.

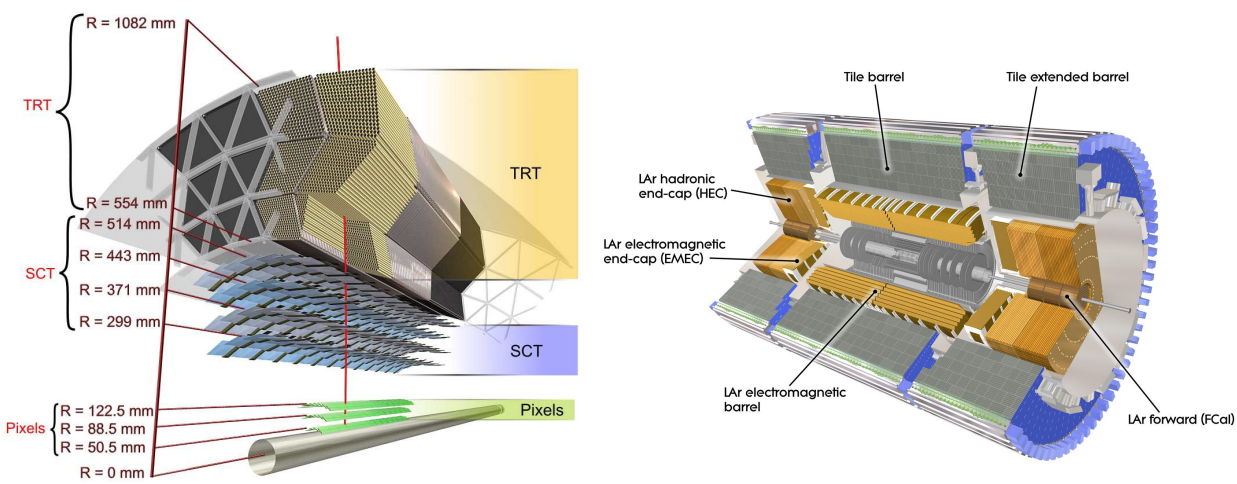

Figure 3.3: Left: The radial structure of the inner detector. Right: Layout of the ATLAS calorimeter system.

3.2.4 Calorimeters

ATLAS calorimeters consist of a number of sampling detectors dedicated to measurements of electromagnetic and hadronic activities. The calorimeters cover a pseudorapidity range up to

Detector component	**Design resolution**	η **coverage**	
		Measurement	Trigger
Tracking	$\sigma_{p_T}/p_T = 0.05\% \cdot p_T \oplus 1\%$	± 2.5	
EM calorimetry	$\sigma_E/E = 10\%/\sqrt{E} \oplus 0.7\%$	± 3.2	± 2.5
Hadronic calorimetry			
barrel/end-cap	$\sigma_E/E = 50\%/\sqrt{E} \oplus 3\%$	± 3.2	± 3.2
forward	$\sigma_E/E = 100\%/\sqrt{E} \oplus 10\%$	$3.1 < \|\eta\| < 4.9$	$3.1 < \|\eta\| < 4.9$
Muon spectrometer	$\sigma_{p_T}/p_T = 10\%$ at $p_T = 1$ TeV	± 2.7	± 2.4

Table 3.1: Design resolution and η coverage of ATLAS subdetector systems [53].

$|\eta| < 4.9$ and provide a full ϕ-symmetry and coverage around the beam pipe. They consist of several components using different techniques depending on the physics process of interest and the radiation environment of a particular η range. The active material of the calorimeters has thickness of about 10-11 interaction lengths (λ), which has been shown to be enough to provide good measurements for both missing transverse energy (E_T^{miss}) and high energy jets, as well to be sufficient for containing electromagnetic and hadronic showers and reducing the punch-through to muon system down to an acceptable level.

The ElectroMagnetic Calorimeter (EMCal) is a lead-Liquid Argon (LAr) detector with accordion-shape absorbers and electrodes. The geometry of LAr allows it to have several active layers in depth and azimuthal coverage without cracks. It consists of a barrel part extending to $|\eta| < 1.475$ and two end-cap components covering $1.375 < |\eta| < 3.2$. In the η-region matching that of the inner detector, LAr has fine granularity well suited for precision measurements of photons and electrons and is segmented in three sections in depth. The outer $|\eta|$ region has coarser granularity and two active layers in depth. A presampler detector, consisting of instrumented argon layer in $0 < |\eta| < 1.8$, provides a measurement of the energy lost in front of the EM calorimeters. The total thickness of EM calorimeter is > 22 (> 24) radiation lengths in the barrel (end-caps).

Hadronic calorimeters surround the EMCal and consist of three subsystems – tile calorimeter, LAr Hadronic End-cap Calorimeter (HEC) and LAr Forward Calorimeter (FCal). The tile calorimeter is a sampling calorimeter using steel as the absorber and scintillation tiles as the active material. It consists of the barrel covering $|\eta| < 1.0$ and the extended barrels covering the region $0.8 < |\eta| < 1.7$. Both components are segmented into three layers with a total depth of about 7.4 interaction lengths. Both HEC and FCal use liquid argon as the active detector medium due to its intrinsic linear behaviour, its stability of response over time and its intrinsic radiation-hardiness. The HEC is located directly behind the end-cap EM calorimeters and provides the coverage in $1.5 < |\eta| < 3.2$ range. It consists of two wheels per end-cap, each divided into two segments in depth, providing four layers with a total thickness of approximately 10 λ. The absorber material is copper. The FCal is located inside the inner radius of HEC wheels, and covers the region closest to the beam pipe in the range $3.1 < |\eta| < 4.9$. It consists of three modules, where the first is made of copper and optimised for electromagnetic

measurements, while the other two are made of tungsten and measure mainly the energy of hadronic interactions.

3.2.5 Muon spectrometer

The muon spectrometer is designed to detect charged particles exiting the calorimeters, predominantly composed of muons. It consists of high-precision tracking chambers measuring particle momenta up to ~ 3 TeV in the pseudorapidity range $|\eta| < 2.7$ and fast trigger chambers triggering on tracks up to $|\eta| < 2.4$. The magnetic field bending the particle trajectories is generated by large superconducting air-core toroid magnets located within the muon spectrometer (see Fig. 3.4).

The precision tracking is provided by Monitored Drift Tube (MDT) chambers covering pseudorapidity range $|\eta| < 2.7$ and Cathode-Strip Chambers (CSC) in the forward region ($2 < |\eta| < 2.7$). The MDT subsystem consists of three layers of chambers arranged in concentric cylindrical shells around the beam axis in the barrel region and installed in planes perpendicular to the beam in the end-caps. The chambers are composed of three to eight layers of drift tubes with an average resolution of about 35 μm per chamber in the bending plane. The CSCs are used in the innermost tracking layer due to their higher rate capability and time resolution. They are multiwire proportional chambers with cathode planes segmented into strips in orthogonal directions, allowing for both coordinates to be measured from the induced charge distribution. The resolution of a chamber is 40 μm in the bending plane (η) and about 5 mm in the transverse plane (ϕ). The performance goal of the muon system is the transverse momentum resolution of ~ 10 % for 1 TeV tracks, corresponding to a sagitta along the z direction of about 500 μm which has to be know to better than 50 μm. To achieve this goal, the precise positions of MDT wires and CSC strips are monitored with a high-precision optical alignement system.

The trigger system is composed of Resistive Plate Chambers (RPC) in the barrel ($|\eta| < 1.05$) and Thin Gap Chambers (TGC) in the end-cap ($1.05 < |\eta| < 2.4$). Both types of chambers deliver track information with the response time of less than 25 ns and are thus capable also of tagging the beam-crossing for the purpose of an event time calibration. The RPC consists of parallel electrode plates with gas-fileld gaps and provides a resolution of about 10 mm in both bending and non-bending planes. The TGCs operate on the same principle as multi-wire proportional chambers. Their characteristic is that the wire-to-cathode distance is smaller than the wire-to-wire distance to achieve a fast collecting time. The spatial resolution of TGC is $2 - 7$ mm for both coordinates. As the trigger chambers provide the track coordinate in both planes, the MDT measurement of the coordinate in the bending plane is complemented by the RPC measurement in the non-bending plane.

3.2.6 Trigger and data acquisition

The purpose of the trigger and data-acquisition system is to identify bunch crossings containing interesting events and to record the corresponding data on the permanent storage. While the

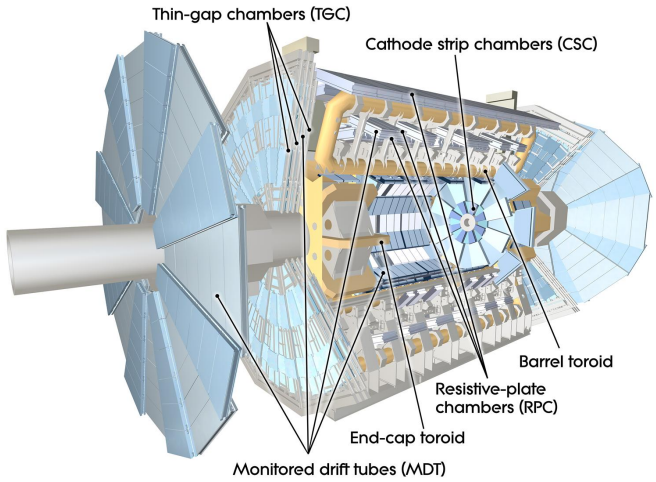

Figure 3.4: Cut view of the muon spectrometer showing positions of different chambers and magnet components.

interaction rate in 25 ns bunch crossings can be as high as 10^9 Hz, only about 100 Hz can be stored, requiring seven orders of magnitude reduction of the incoming event rate. The trigger system consists of three levels – L1, L2 and the event filter (see Fig. 3.5). L1 is hardware based trigger able to provide the decision $< 2.5\,\mu$s and reducing the rate down to about 75 kHz. L2 and event filter, collectively referred to as the high-level trigger (HLT), reduce the event rate down to 3.5 kHZ and 200 kHZ, with the processing time of approximately 40 ms and four seconds, respectively.

L1 trigger

The L1 trigger uses RPC and TGC information to look for high p_T muons, and reduced-granularity information from all the calorimeters to search for high p_T electrons/photons, jets, hadronically decaying τ-leptons, as well as large missing and total transverse energy. Results from L1 trigger are processed by the central trigger processor which implements the information about the trigger 'menu' – combinations of trigger selections that need to satisfied in order to accept the event. All the information from the detector is stored in the pipeline until the L1 decision is made. L1 trigger is also responsible for providing the correct identification of the bunch-crossing containing the object of interest.

- **Calorimeter trigger:** The L1 Calorimeter trigger (L1Calo) trigger decision is based on the multiplicity of trigger objects passing some threshold criteria or flags indicating which thresholds were passed in case of the global variables. It uses the reduced-granularity calorimeter information in form of the trigger towers – sums of cell energies within a $\Delta\eta \times \Delta\phi$ region of typically 0.1×0.1 size. The cluster processor module selects electron/photon

and τ-lepton candidates with E_T above some threshold by identifying 2×2 clusters of trigger towers, and satisfying, if required, certain isolation criteria [1]. The jet/energy module adds 2×2 trigger towers from the EM calorimeter to 2×2 towers from the hadronic calorimeters and uses them to identify jets and to produce global sums of scalar and missing transverse energy. The electron/photon and τ triggers cover up to $|\eta| = 2.5$ which corresponds to the pseudorapidity range of the precision tracking in the inner detector and the EM calorimeter. The jet trigger covers up to $|\eta| = 3.2$, while the E_T^{miss} and total transverse-energy triggers include also the forward calorimetry up to $|\eta| = 4.5$ in order to provide the adequate E_T^{miss} performance.

- **Muon trigger:** The L1 muon trigger is based on requiring a coincidence of hits in RPC or TGC stations within a road of the particle. The centre of the road is defined as a straight (infinite momentum) path connecting the interaction point with the hit in the pivot plane of a station [2]. Corresponding hits within the road width are then searched for in the other stations. The road width is a function of the p_T threshold to be applied to the object, and the higher the p_T threshold, the smaller the road width is. There are a total of six p_T thresholds, three in the approximately $6 - 9$ GeV range, and three in the $9 - 35$ GeV range.

High-level trigger

The HLT algorithms use the full granularity and precision of muon chambers and calorimeters, as well as the data from the inner detector. More precise information on energy deposits improves the resolution of the threshold cuts, while the track information from the inner detector significantly enhances the particle identification, e.g. enables the distinction between photons and electrons.

The L2 selection is seeded by Regions-of-Interest (RoI's), i.e. $\eta - \phi$ regions of the detector containing interesting features, as defined by the L1 trigger. The event data from the readout electronics is moved to the data acquisition system (DAQ) and buffered at the L1 trigger rate. The data required for the L2 decision, typically corresponding to RoI's, is transmitted to the trigger as requested. Feature extraction algorithms attempt to reconstruct objects, e.g. tracks or calorimeter clusters, and a hypothesis algorithm determines whether the identified feature satisfies the criteria, such as shower-shape, track-cluster match or E_T threshold.

For the events fulfilling the L2 criteria the event-building is performed. These fully-built events are then processed by the event filter which uses standard ATLAS offline event reconstruction and analysis procedures to make the final decision of keeping or discarding the event. The data corresponding to the events passing the HLT decision are recorded on the permanent storage for the subsequent offline analysis.

[1] The isolation implies that the particle should have a minimum angular separation from any significant energy deposit in the same trigger.

[2] The pivot planes of RPC and TGC are defined in the second and third stations, respectively.

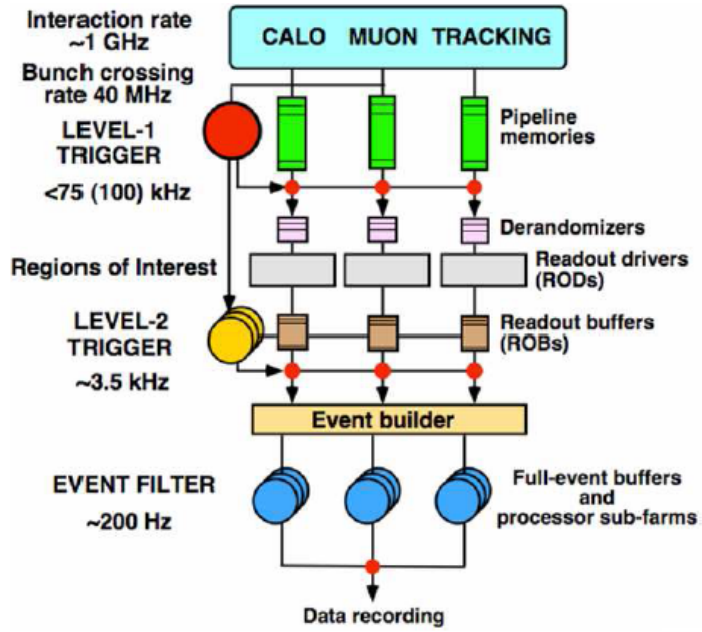

Figure 3.5: A schematic view of ATLAS trigger and data acquisition system.

3.3 Luminosity

The amount of data collected by the ATLAS detector during some period of time is quantified by the integrated luminosity L, which is related to the total number of events recorded during that time N and the cross section σ as

$$L = \int \mathcal{L} dt = \int \frac{N}{\sigma} dt, \tag{3.1}$$

where $\mathcal{L}$ is the instantaneous luminosity measured at a specific time. The instantaneous luminosity in a circular pp collider can be expressed as

$$\mathcal{L} = \frac{\mu_{vis} n_b f_r}{\sigma_{vis}^{inel}}, \tag{3.2}$$

where μ_{vis} is the average number of visible inelastic interactions per bunch crossing, σ_{vis}^{inel} is the visible pp inelastic cross section, and f_r and n_b are the revolution frequency and the number of bunches crossing at the interaction point, respectively. The interaction rate μ_{vis} is an experimentally observable quantity and is measured based on number of hits or events per bunch crossing in several ATLAS detector subsytems used for luminosity measurements. The Beam Conditions Monitor (BCM) consists of four small diamond sensors at $|\eta| = 4.2$, arranged around the beampipe on each side of the interaction point (IP), at a distance of $z = \pm 184$ cm from the nominal IP. LUCID is a Cherenkov detector consisting of aluminium tubes filled with

C_4F_{10} gas surrounding the beampipe on each side of the IP at a distance of 17 m, and covering the pseudorapidity range $5.6 < |\eta| < 6.0$. Further luminosity measurements are provided by measuring average particle rates over longer time scales using components of the ATLAS calorimeter system – the tile calorimeter and the forward calorimeter.

The visible cross section σ_{vis}^{inel} is a calibration constant and is determined for each luminosity detector by inferring the absolute luminosity scale from direct measurements of the beam parameters. The delivered luminosity can be expressed in terms of the accelerator parameters as

$$\mathcal{L} = \frac{n_b f_r n_1 n_2}{2\pi \Sigma_x \Sigma_y}, \tag{3.3}$$

where n_1 and n_2 are the number of protons per bunch (bunch populations), as determined in an independent measurement. Σ_x and Σ_y characterise the horizontal and vertical beam profiles and are measured in dedicated beam-separation scans, also known as van der Meer (vdM) scans, in which the beams are separated by steps of a known distance. After measuring the luminosity delivered in the vdM scan and the visible interaction rate μ_{vis} in each luminosity detector, the visible cross section σ_{vis}^{inel} can be determined from Eq. (3.2).

The uncertainties on the integrated luminosity values used in ATLAS physics analyses arise from various effects, such as the choice of the algorithm used by the luminosity detectors to measure the μ_{vis}, uncertainties on the measurement of σ_{vis}^{inel}, including the determination of bunch populations (n_1, n_2), and the stability of extrapolating the result of a few vdM calibrations occurring in 2012 to the entire 2012 dataset. The total luminosity uncertainty amounted to $\pm 2.8\%$ for the 2012 data-taking.

The number of colliding bunches in ATLAS and the peak instantaneous luminosity as a function of time in 2010, 2011 and 2012 are shown in Fig. 3.6. The number of colliding bunches in 2012 reached a peak value of 1380, with up to $1.7 \cdot 10^{11}$ protons in a bunch. The maximum instantaneous luminosity in 2012 corresponded to 7.7×10^{33} cm^2 s^1.

In total, the ATLAS detector recorded 20.3 fb^{-1} of pp collisions at 8 TeV in 2012, while the LHC delivered 22.8 fb^{-1} (see Fig. 3.7). The analysis presented in this thesis uses the whole 2012 dataset. Due to the choice of a trigger (see Chapter 5), the available luminosity is slightly reduced, and the integrated luminosity used in the analysis amounts to total of 20.1 fb^{-1}.

3.4 Pile-up

During the high-luminosity running conditions at the LHC, additional proton-proton interactions occur in the same time-window as the hard-scatter triggered event. These additional interactions are called pile-up (PU) events and consist of soft particles produced in inelastic QCD interactions. There are two types of additional interactions: in-time pile-up, which consists of interactions in the same bunch crossing as the triggered event, and out-of-time pile-up, which causes signal modulation in the calorimeter from interactions in surrounding bunch crossings. The variables often used to characterise the amount of pile-up are the number of primary

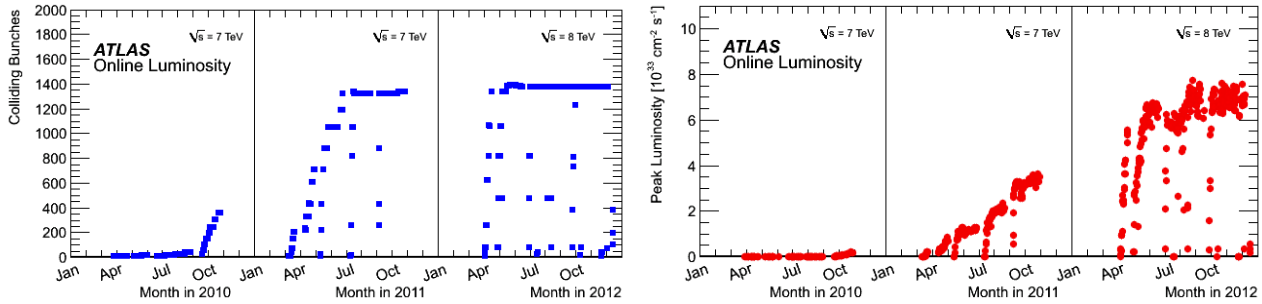

Figure 3.6: The number of colliding bunches and the peak instantaneous luminosity delivered to ATLAS per day versus time during the p-p runs of 2010, 2011 and 2012 [52].

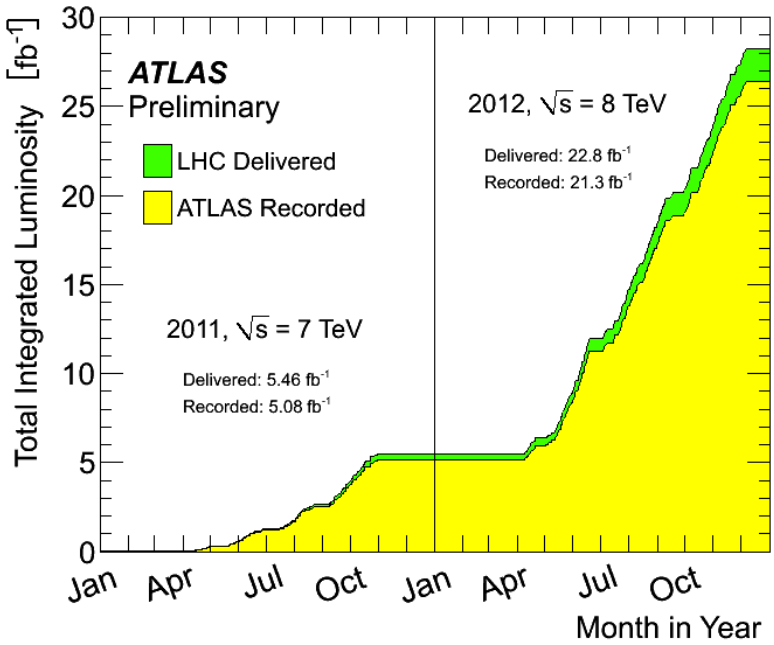

Figure 3.7: Total integrated luminosity versus time delivered to (green), and recorded by ATLAS (yellow) during stable beams and for pp collisions at 7 and 8 TeV centre-of-mass energy in 2011 and 2012. The delivered luminosity accounts for the luminosity delivered from the start of stable beams until the LHC requests ATLAS to put the detector in a safe standby mode to allow a beam dump or beam studies [52]. The recorded luminosity is generally smaller due to DAQ inefficiencies.

vertices N_{PV}, sensitive to in-time PU, and the average number of inelastic pp interactions per bunch crossing $\langle\mu\rangle$, which gives an estimation of the out-of-time pile-up.

The primary vertices are formed by associating the reconstructed charged-particle tracks to primary interaction points compatible with the beam-spot constrains. Figure 3.8 is showing an example of a high pile-up event in 2012 run. Out of 25 reconstructed primary vertices, the one with the highest energy associated to it is considered as the source of the hard-scatter event – in this case it corresponds to a Z$\rightarrow \mu\mu$ candidate.

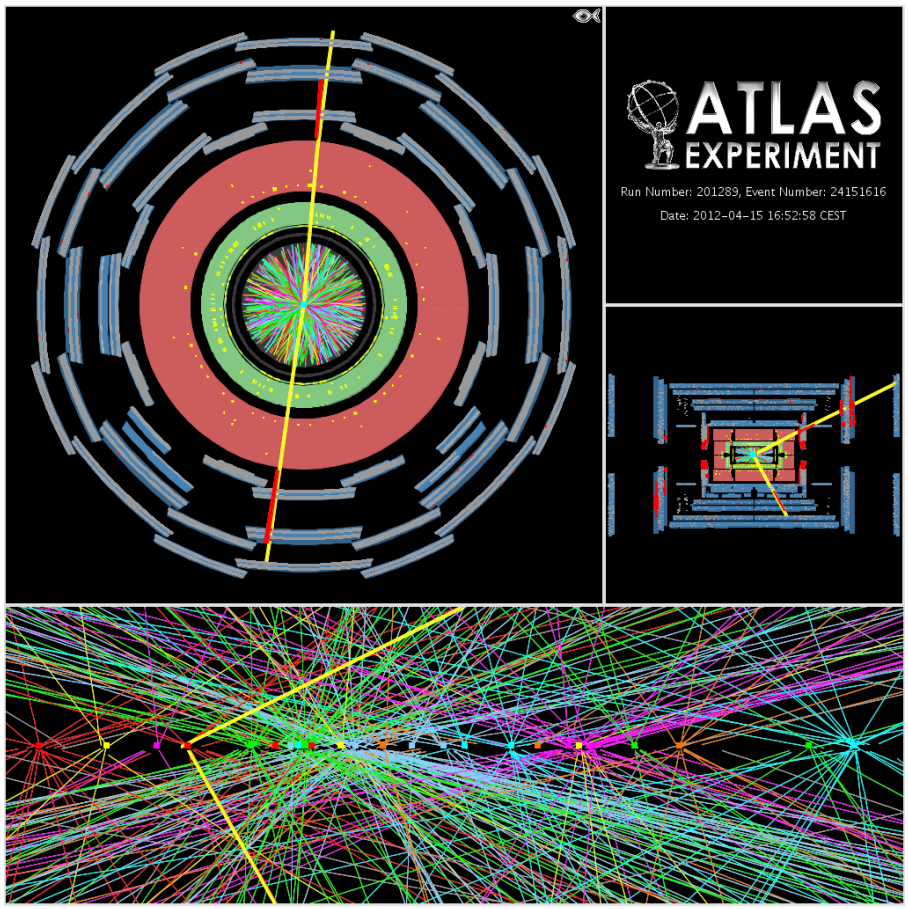

Figure 3.8: A candidate Z boson event in the dimuon decay with 25 reconstructed vertices. This event was recorded on April 15th 2012 and demonstrates the high pile-up environment in 2012 running. The vertices shown are reconstructed using tracks with p_T greater than 0.4 GeV [52].

The mean number of interactions per bunch crossing, $\langle\mu\rangle$, is related to the instantaneous luminosity L as:

$$\langle\mu\rangle = \frac{L \times \sigma_{inel.}}{N_{bunch} \times f_{LHC}} \tag{3.4}$$

where $\sigma_{inel.}$ is the total inelastic pp cross-section (about 73 mb) and $N_{bunch} \times f_{LHC}$ is the average frequency of bunch crossings in the LHC [54]. The average pile-up activity in 2012 corresponded to $\langle\mu\rangle \sim 20.7$ interactions per bunch crossing. Figure 3.9 is showing the luminosity weighted $\langle\mu\rangle$ distribution for the 2011 and 2012 data. As can be seen, in 2012 the amount of pile-up significantly increased compared to 2011 data.

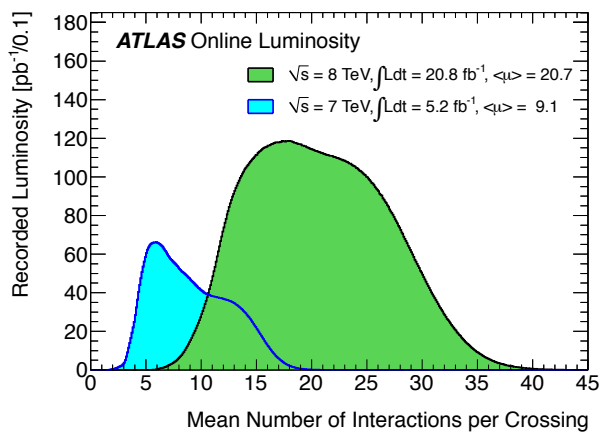

Figure 3.9: Luminosity-weighted distribution of the average number of interactions per crossing for the 2011 and 2012 data. The average number of interactions per crossing corresponds to the mean of the poisson distribution of the number of interactions per each bunch-crossing. It is calculated as $\mu = (L \times \sigma_{inel.}) / (N_{bunch} \times f_{LHC})$ [52].

The pile-up effects need to be taken into account when reconstructing the data, as the pile-up may affect the energy scale and resolution of objects reconstructed in the calorimeters, as well as the tracking efficiency. Reconstruction and calibration of jets are particularly sensitive to the effects of pile-up, mainly due to the fact that the particles associated to a jet tend to extend across a wide area of the detector. The larger the area, the more likely it becomes that particles from pile-up interactions overlap with the jet and affect its kinematics. Furthermore, pile-up produces additional jets in an event, in the form of both genuine QCD particle jets from individual additional interactions and stochastic fluctuations of soft activity from several interactions. Various methods of pile-up suppresion are developped in ATLAS, some of which will be addressed in Chapter 4.

3.5 Monte Carlo and detector simulation

Monte Carlo (MC) simulation is used to model the events in pp collisions, including the primary hard scattering, particle decays and subsequent evolution of the parton shower and the hadronisation. The physical principles of the simulation have been presented in Chapter 2, while this section lists Monte Carlo generators used in the analysis and summarises their main features.

The events generated with an appropriate MC generator are passed through the ATLAS detector simulation GEANT4 [56], which simulates the interaction of final state particles with the detector material. All Monte Carlo events describing the hard process of interest are overlaid with additional inelastic events generated to simulate the effect of pile-up. The amount of pile-up is usually characterised by the average number of interactions per crossing $\langle\mu\rangle$. The distribution of $\langle\mu\rangle$ observed in the 2012 data and the one employed for the MC production used in this thesis are shown in Fig. 3.10. The MC samples are reweighted so that the $\langle\mu\rangle$ distribution of the sample matches the corresponding distribution in the data. After the detector simulation the events are reconstructed and analysed with the same algorithms as used on the real collision data. All the Monte Carlo samples used in this analysis are part of the ATLAS official production.

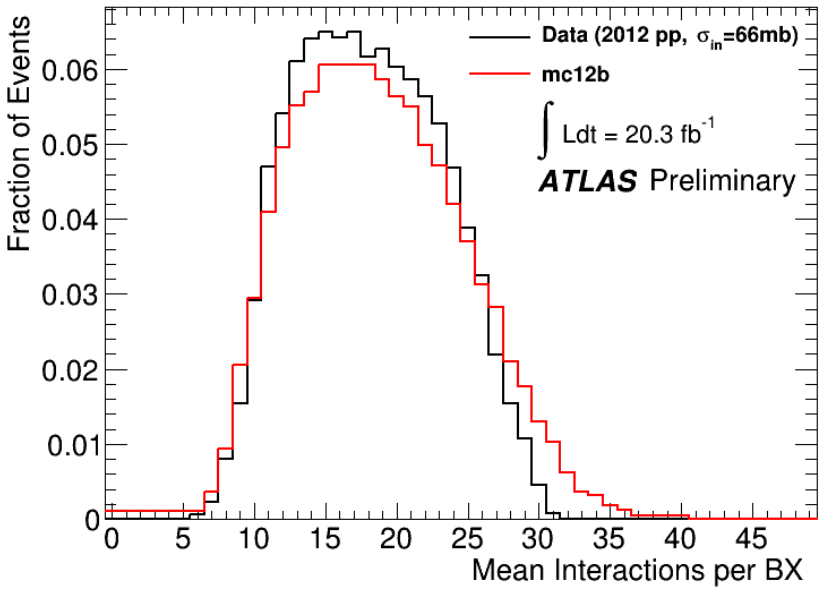

Figure 3.10: Luminosity weighted distribution of the mean number of interactions per bunch-crossing (BX) in the 2012 data and Monte Carlo. The MC distribution has been generated at the end of 2012 *pp* data-taking based on the observed data distribution, and has been used for post-data-taking Monte Carlo production campaign. The data luminosity distribution has been converted to mean number of interactions per beam crossing using an inelastic cross-section of 66 mb. This value was found to give the best Monte Carlo description of luminosity sensitive quantities in the data such as the vertex multiplicity distribution. [52].

3.5.1 Monte Carlo samples

Monte Carlo generators used to simulate the parton-shower (PS) are PYTHIA [58] and HERWIG [59]. In addition to parton-shower and hadronisation description, PYTHIA provides particle decays and underlying event simulation as well, while HERWIG is paired with JIMMY [60] which takes care of secondary multi-parton interactions. The main difference between the two is the choice of the scale variable t in Sudakov form-factor used to evolve the shower from a high scale Q down to an infrared cut-off $Q_0 \sim 1$ GeV. HERWIG uses angular ordering, i.e. each subsequent emission is characterised by an angle smaller that the angle of previous emission. This is, in fact, a true quantum interference effect – any radiation outside of the cone of emitting particles will average out when integrated over the full azimuth. PYTHIA uses transverse momentum ordering of the shower, i.e. harder emissions come first, and events which do not respect the angular ordering are removed. HERWIG uses the cluster model for hadronisation, while PYTHIA implements the string model.

SHERPA [61] is a complete event generator framework which includes its own matrix-element (ME) generator (at the leading order), parton-shower, hadronisation package etc. Showering is ordered in virtuality (the amount by which the particle is off its mass shell) and angular ordering is respected as well. Cluster model is used for hadronisation. Matching between the ME and PS is performed by CKKW algorithm. Sherpa is used for the simulation of W and Z productions in association with jets and up to 4 additional partons are included in the matrix-element calculation.

ALPGEN [62] and MadGraph5 [63] are leading-order (LO) ME generators, and can be interfaced with either HERWIG or PYTHIA for the simulation of showering processes. Both use the MLM matching scheme. ALPGEN builds up amplitudes by recursively reusing simpler ones and is therefore efficient at high multiplicities. MadGraph obtains formulae from direct evaluation of Feynman diagrams making it easy to include new physics processes. Top quark pair production in association with vector bosons is generated with MadGraph, and ALPGEN is used for Drell-Yan pocess simulation.

MC@NLO [65] and POWHEG [66] are next-to-leading-orded (NLO) event generators. Matching with PS is more complicated in NLO case due to the fact that virtual corrections (loop diagrams) and diagrams involving a real parton emission at NLO are separately divergent and cancel out only when combined together. In other words, final states coming form virtual and real NLO contributions can not be showered separately, as is the case for fixed order LO generators, since the weights next to a parton shower spectrum would diverge. MC@NLO employs a Monte Carlo counterterm (obtained by expanding PS MC to NLO) designed to separately cancel out divergencies in virtual and real NLO emissions. Since the counterterm is MC dependent, MC@NLO has soo far been matched only to HERWIG shower. POWHEG uses a MC-independent method for matching and has been interfaced with both HERWIG and PYTHIA. The NLO precission in MC emissions is achieved by replacinig the Born-level contribution with the NLO cross section integrated in the extra parton phase space. The Sudakov form factor is then modified in order to avoid double counting and obtain a correct NLO differ-

ential cross section. The $t\bar{t}$, single-top and di-boson productions are simulated with POWHEG interfaced with Pythia. Additional diboson samples used for the evaluation of systematic uncertainties have been simulated with aMC@NLO [70]. It is a recently developed framework which uses MadGraph5 to generate matrix elements up to NLO precission and in an automated way. It also calculates automatically the MC counter term, and has thus been matched with both HERWIG and PYTHIA.

The parton-distribution function (PDF) set used for ALPGEN, MadGraph and AcerMC samples is CTEQ6L1 [79], while CT10 [80] PDF set is used for the MC@NLO, SHERPA and POWHEG samples. The theoretical cross sections for W+jets and Z+jets are calculated with DYNNLO [81] with the MSTW2008NNLO [82] PDF set. The diboson cross sections are obtained from MCFM [76]. The $t\bar{t}$ cross section is calculated with HATHOR 1.2 [72] using MSTW2008NNLO PDFs. The single-top cross sections are computed at NLO+NLL accuracy [73, 74, 75] and the $t\bar{t} + W/Z$ cross sections, at NLO accuracy [77, 78]. To correct the absolute normalisation of processes calculated at LO to their full NLO cross-section, the overall normalisation factor (k-factor) is applied to LO MC samples.

All the background MC samples used in this analysis are shown in Tab. 3.2.

Signal Monte Carlo

The mUED signal is generated using HERWIG++ event generator [83]. It is a general-purpose Monte Carlo generator, building upon a structure of the HERWIG program, and including the calculation of the matrix-element (at LO), underlying event, parton-shower and hadronisation. The simulation of BSM physics is implemented by specifying the Feynman rules and mass spectrum of the model. The full set of radiative corrections is taken into account to give a realistic spectrum of the mUED. The list of possible two- and three-body decays of mUED particles is generated automatically and the corresponding matrix-elements are calculated taking into account full spin correlations. The cross sections are calculated at the leading order, and CTEQ6L1 PDF set is used.

A grid of signal samples is generated for various values of ΛR and R^{-1} parameters, with the Higgs mass is set to 125 GeV. Samples are generated for $700 < R^{-1} < 1300$ GeV in steps of 100 GeV, and $\Lambda R = \{2, 3, 5, 10, 20, 40\}$. The signal grid is more finely segmented for $\Lambda R \leq 5$ as this is theoretically most interesting part of the phase space. The values $R^{-1} < 700$ GeV are not simulated, since this region has already been excluded (see Chapter 1). As the sensitivity reach is not expected to extend beyond $R^{-1} > 1100$ GeV, the grid is somewhat coarser in this region, with only $\Lambda R = \{3, 10, 40\}$ points being generated.

The mass splittings between the heaviest KK level one state, the KK gluon (g_1), and the lightest KK particle, the level 1 photon (γ_1), are shown in Fig. 3.11 for $\Lambda R = \{3, 10, 40\}$ points. The relative mass splittings defined as $\Delta M/M = (M_{g_1} - M_{\gamma_1})/M_{g_1}$ are approximately constant for a particular value of ΛR, and correspond to about 10%, 18%, 20% and 25% for $\Lambda R = 3$, 10, 20 and 40, respectively. The cross sections for all the generated points are included in the Appendix B.1 and vary from about 0.1 pb to about 10 pb. The dependency of cross

sections on the values of ΛR and R^{-1} is illustrated on the right hand side of Fig. 3.11.

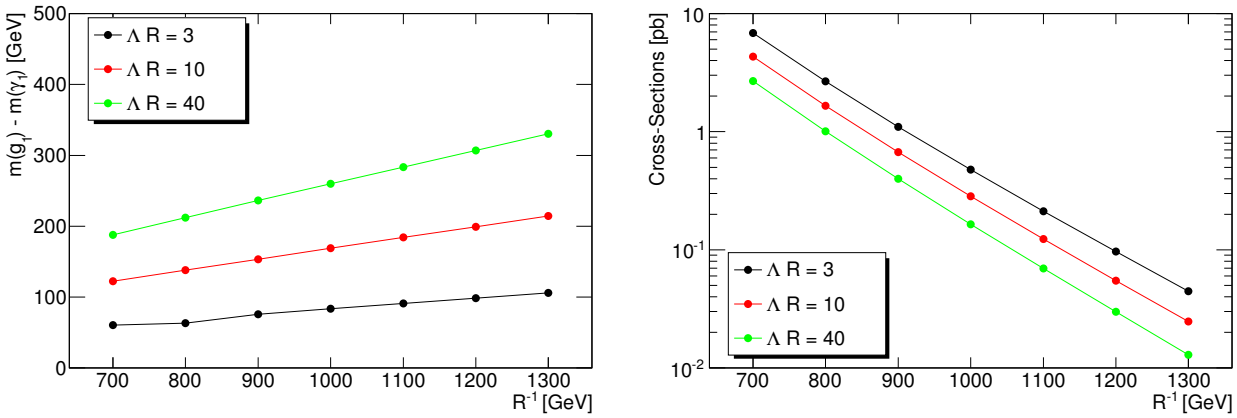

Figure 3.11: The mass difference between KK-gluon and KK-photon (left) and the total production cross-section (right) as a function of the compactification radius R^{-1}.

Physics process	Generator	Cross section [pb]	Cross section order	PDF
$W(\rightarrow \ell\nu)$ + jets	SHERPA 1.4.1 [61]	1.22×10^4	NNLO [71]	CT10
$Z/\gamma^*(\rightarrow \ell\ell)$ + jets ($m_{\ell\ell} > 40$ GeV)	SHERPA 1.4.1	1.24×10^3	NNLO[71]	CT10
$Z/\gamma^*(\rightarrow \ell\ell)$ + jets ($10 < m_{\ell\ell} < 60$ GeV)	ALPGEN 2.14 [62]	4.37×10^3	NNLO[71]	CTEQ6L1
WW	POWHEG-BOX 1.0 [67],[68],[69]	5.80	NLO [76]	CT10
WZ	POWHEG-BOX 1.0	3.68	NLO [76]	CT10
ZZ	POWHEG-BOX 1.0	0.99	NLO [76]	CT10
$t\bar{t}$ ($\rightarrow \ell\nu$ + X)	POWHEG-BOX 1.0	137.38	NLO+NLL [72]	CT10
Single-top (t-chan $\rightarrow \ell$)	AcerMC 3.8 [64]	28.43	NLO+NLL [73]	CTEQ6L1
Single-top (s-chan $\rightarrow \ell$)	POWHEG	1.82	NLO+NLL [74]	CTEQ6L1
Single-top+W (Wt-chan $\rightarrow \ell\ell$)	POWHEG-BOX 1.0	2.35	NLO+NLL [75]	CTEQ6L1
Single-top+Z (Wt-chan $\rightarrow \ell\ell$)	MadGraph5 [63]	0.004	NLO	CTEQ6L1
Single-top+Z (s-chan $\rightarrow \ell\ell$)	MadGraph5	0.031	NLO	CTEQ6L1
$t\bar{t} + W$	MadGraph5	0.233	NLO [77]	CTEQ6L1
$t\bar{t} + Z$	MadGraph5	0.206	NLO [78]	CTEQ6L1
$t\bar{t} + WW$	MadGraph5	0. 00092	LO	MSTW2008LO

Table 3.2: Simulated background event samples used in the analysis, along with their production cross sections and PDFs. The notation LO×K indicates that the process is calculated at leading-order and corrected by a factor derived from the ratio of NLO to LO cross sections for a closely related process.

Chapter 4

Object reconstruction and selection

4.1 Track and primary vertex reconstruction

Charged-particle tracks reconstructed in the Inner Detector are used in numerous ways in the definition of physics objects. They are used as an input to the reconstruction of muons and electrons, and are important ingredient for the calculation of lepton isolation, identification of b-quark jets, as well as for the pile-up suppression in jets. A sequence of algorithms is used in track reconstruction [84]. The inside-out algorithm is seeded by hits in the silicon detectors (SCT) to which subsequent hits away from the interaction point are added. It is the baseline algorithm for the reconstruction of primary charged particles defined as particles with a lifetime longer than 3×10^{-11} s, either directly produced in a pp interaction or coming from subsequent decays or interactions of particles with lifetimes shorter than 3×10^{-11} s. The tracks reconstructed in this way are required to have $p_T > 400$ MeV. Back-tracking reconstruction algorithm is designed to reconstruct secondary particles, the particles produced in the interactions of primaries. It starts from segments reconstructed in TRT and extends them inward by adding hits from SCT. A second inside-out algorithm with looser requirements on pattern recognition is executed after the back-tracking in order to recover tracks with $p_T > 150$ MeV (low p_T tracking).

The reconstruction of primary vertices proceeds in two steps – the primary vertex finding algorithm associates reconstructed tracks to the vertex candidates, while the vertex fitting algorithm is used to reconstruct the vertex position [85]. The iterative vertex finding procedure starts with finding a vertex seed by looking for the global maximum in the distribution of z coordinates of preselected tracks compatible with originating from the interaction region. The vertex fitting algorithm takes as an input the seed position and the tracks around it and performs a χ^2 based fit [86] to decide which tracks belong to the vertex, and which are incompatible with the vertex position and therefore can be used to seed a new vertex. The effect of pile-up on primary vertex reconstruction is shown on the right-hand-side of Fig. 4.1. The relation between N_{PV} and $< \mu >$ is linear up to high values of pile-up. The probability to reconstruct multiple close-by interactions as a single vertex increases at higher values of $< \mu >$ causing some non-linearities.

The distance of the closest approach of a track to the primary vertex is called the track impact parameter (IP). Transverse and longitudinal IPs are defied as (see Fig. 4.1 right):

- **Transverse IP:** Distance between the point of the closest approach of a track and the primary vertex in the transverse detector plane: d_0^{PV}. Transverse IP significance is denoted by $d_0^{PV}/\sigma(d_0^{PV})$.
- **Longitudinal IP:** The z-coordinate (along the beam axis) of the transverse IP is denoted as z_0^{PV}, and also used as $|z_0^{PV} \times \sin(\theta)|$, where θ is the polar angle of the track.

The IP variables are used to asses the compatibility of a given track to be coming from the primary vertex. Examples of usage include b-jet tagging algorithms (see Sec. 4.5) and rejection of non-prompt leptons (see Sec. 5.4).

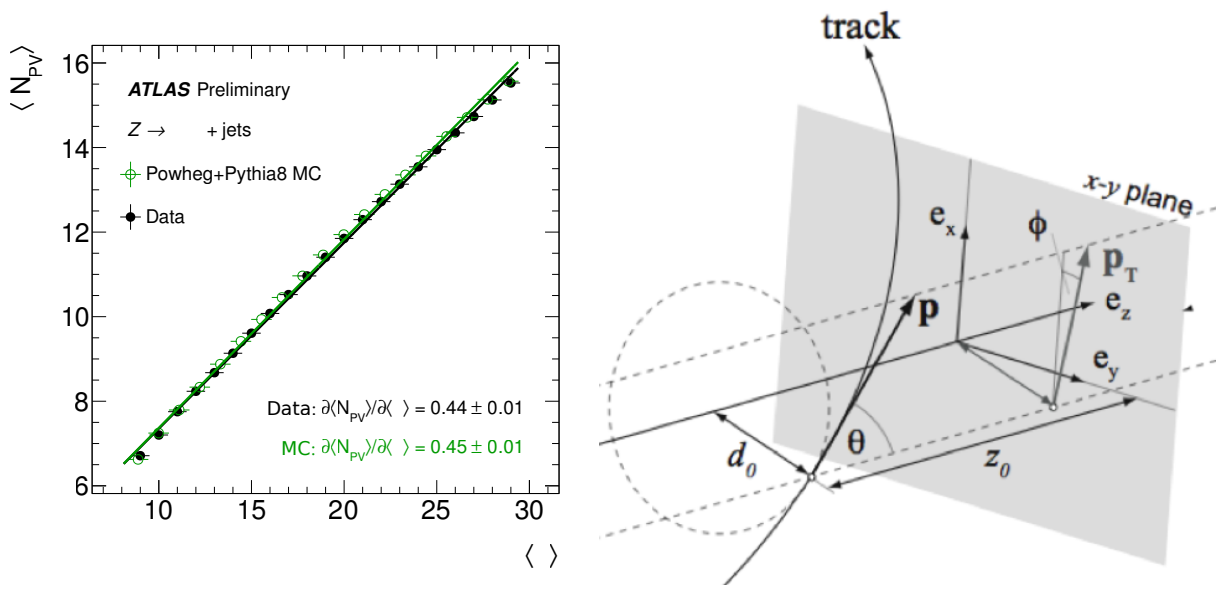

Figure 4.1: Left: Mean N_{PV} as a function of $< \mu >$ for Z+jet events in data and MC. Resulting gradients of linear fits are also shown [97]. Right: Definition of track impact parameters. Track d_0^{PV} (z_0^{PV}) are the distances of the closest approach to the PV in the transverse plane (along the z-axis). ϕ_0 is the azimuthal angle at the closest approach, and θ is the polar angle of the track.

4.2 Muons

4.2.1 Muon reconstruction and identification

Muons traverse all subdetector systems before reaching the muon spectrometer (MS). In addition to the MS system, the inner detector (ID) and the calorimeter information are used in the

reconstruction of muons as well. Two types of muons, based on the reconstruction procedure, are used in this analysis.

Combined (CB) muons: Tracks are reconstructed independently in the ID and MS, and then combined into a single track. Several algorithms for combining the ID and MS measurements are available in ATLAS. The algorithm used in this thesis is called Staco (denoted as "Chain 1" in Fig. 4.2). Pairs of tracks with a χ^2 of the MS-ID combination below certain threshold are retained and a statistical combination of inner and outer track vectors and covariance matrices is performed to obtain the full track parameters.

Segment tagged (ST) muons: Tracks reconstructed in ID are extrapolated to MS and assigned to a muon if they can be matched to at least one segment[1] in MDT or CSC chambers. Using this type of muons, in addition to CB ones, is useful for increasing the acceptance in cases in which a muon passes only one layer of MS station due to either low p_T or becuase it falls into a region with reduced MS acceptance.

A set of requirements on minimal number of hits in the pixel, SCT and TRT sub-detectors is applied to the ID tracks to ensure only the good quality tracks are used for muon reconstruction. Muon reconstruction efficiency is measured in an unbiased way with a tag-and-probe method using $Z \to \mu\mu$ (for muons with $p_T > 10$ GeV) and $J/\Psi \to \mu\mu$ (for muons with $4 < p_T < 20$ GeV) events [87],[88]. The tag muon is required to be a CB muon, while the probe muon is a reconstructed track forming, among other requirements, an invariant mass with the tag muon within a suitable Z or J/Ψ mass window. The reconstruction efficiency of CB+ST muons is found to be above 99% for almost all detector regions and uniform in p_T (Fig. 4.2). A steep increase of the efficiency is observed at low p_T since a minimum momentum of approximately 3 GeV is required for a muon to traverse the calorimeter material and cross at least two layers of MS stations before being bent back by the magnetic field. The plateau is reached for $p_T > 6$ GeV which sets the lower p_T threshold for muons used in the analysis. As can be seen from the right-hand-side of Fig. 4.2, the use of segment-tagged muons allows for recovery of the efficiency especially in the region $1.1 < \eta < 1.3$ in which part of the MS chambers were not installed. The same tag-and-probe procedure is applied to both data and MC, and the results are found to be in good agreement, in general well within 1% (see the lower panels in Fig. 4.2). Efficiency scale factors (SF) are defined as a ratio of the efficiency as measured in the data over the efficiency measurement in the MC simulation and are applied to MC samples in the analysis.

Additional handle in identifying prompt muons is track- and calorimeter-based isolation. Isolation variables provide a measure of activity inside a narrow cone around the muon, either by summing up momenta of tracks in the ID, or by summing up the energy of the calorimeter clusters. Prompt muons coming from decays of particles produced in the initial hard-scatter (e.g. Z- or W-bosons) are generally more isolated than muons coming from e.g. hadron decays inside jets. The isolation definition and performance will be discussed in Chapter 5.

[1]Segment is part of a track reconstructed within a single MDT/CSC chamber.

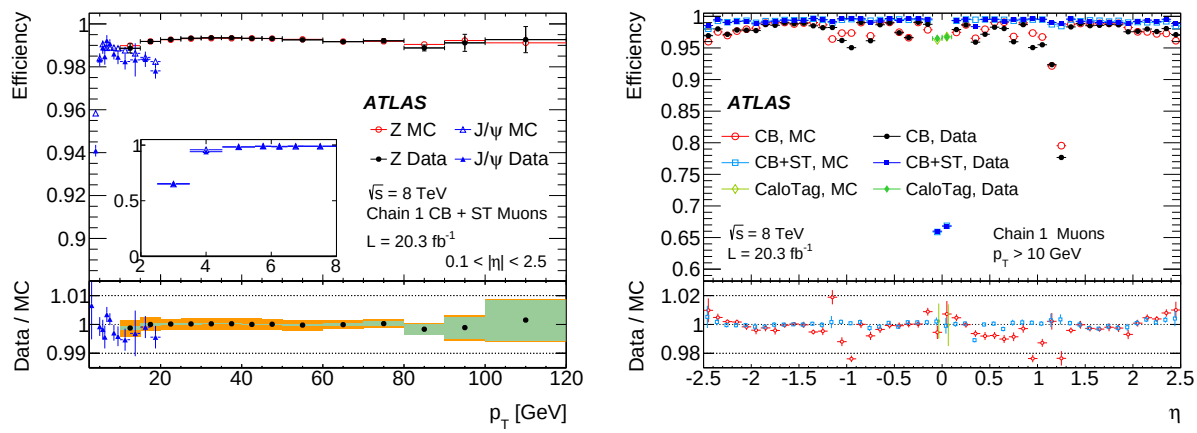

Figure 4.2: Left: Reconstruction efficiency for CB+ST muons as a function of the p_T of the muon, for muons with $0.1 < |\eta| < 2.5$. The results obtained with both $Z \to \mu\mu$ and $J/\Psi \to \mu\mu$ events are shown. The insert shows the zoom-up of the efficiencies in the low p_T region. The panel at the bottom shows the ratio between the measured and predicted efficiencies. The green areas denote the pure statistical uncertainty, while the orange areas also include systematic uncertainties. Right: Muon reconstruction efficiency as a function of eta measured in $Z \to \mu\mu$ events for muons with $p_T > 10$ GeV and different muon reconstruction types. The error bars on the efficiencies indicate the statistical uncertainty. The panel at the bottom shows the ratio between the measured and predicted efficiencies. The error bars on the ratios are the combination of statistical and systematic uncertainties [87].

4.2.2 Muon momentum scale and resolution

Additional corrections are applied to the MC simulation in order to reproduce the muon momentum scale and resolution in experimental data up to a high level of precision. Both scale and resolution are calibrated using dimuon resonances, $Z \to \mu\mu$ and $J/\Psi \to \mu\mu$. Corrected momentum scale can be expressed with the formula

$$p_T^{\mathrm{Corr}} = p_T^{\mathrm{MC}} + s_0 + s_1 \cdot p_T,$$

where s_0 and s_1 are functions of ϕ and η. The difference in scale between data and MC arising from the imperfect knowledge of the magnetic field and of the radial dimensions of the detector is reflected in the multiplicative momentum scale factor s_1, while the difference in the energy loss of muons passing through the material in front of MS is taken into account by the constant factor s_0. Fractional muon resolution can be parametrised as

$$\frac{\sigma(p_T)}{p_T} = r_0/p_T \oplus r_1 \oplus r_2 \cdot p_T,$$

where $\oplus$ denotes a sum in quadrature, and coefficients r are functions of ϕ and η. The first coefficient (r_0) is related to the energy loss in the calorimeter material, the second term independent of p_T accounts for multiple scatering, local magnetic field inhomogenities and local

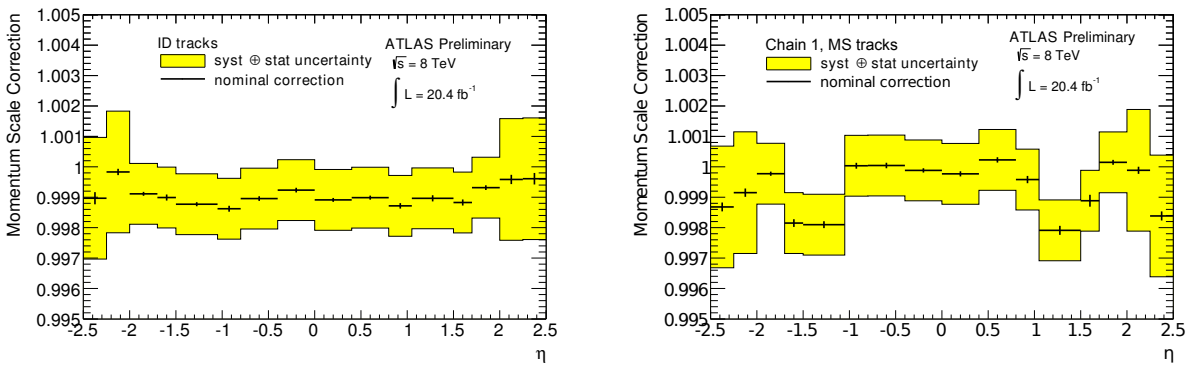

Figure 4.3: MC momentum scale corrections in ID (left) and MS (right) derived from $Z \to \mu\mu$ data for Staco muons. The systematic uncertainty on the correction is shown in yellow [89].

radial displacements, while the third coefficient (r_2) is related to the intrisic resolution and residual misalignement. Scale (s_0, s_1) and resolution (r_0, r_1, r_2) parameters are obtained by using a MC template fitting technique, where binned likelihood fit is used to match the best template to the data mass spectrum. The measurement is performed independently for MS and ID (in case of ID s_0 and r_0 are set to zero) and the corrections are later propagated to CB muons. The scale corrections are found to be below 0.1% for ID, regardless of p_T and η, and mostly below 0.1% for MS (Fig. 4.3). Only a small dependency on the muon p_T (coming from the energy loss corrections) is found for the muon momentum scale in MS. The effect is visible only at small momenta and is covered by the applied systematic uncertainty. Depending on the p_T region, total resolution corrections are found to be below 10% and 15% for ID and MS, respectively. The scale and resolution corrections, based on the measured s and r parameters, are applied to ID, MS and combined muon momenta in MC samples.

4.3 Electrons

4.3.1 Electron reconstruction and identification

Reconstruction: Central electrons are reconstructed using the information from the EM calorimeter and the ID (extending up to $|\eta| < 2.5$) [90]. EM clusters, seeded by energy deposits with total transverse energy $E_T > 2.5$ GeV, are associated with the reconstructed tracks in the ID. The matched track is refitted by taking into account radiative losses (bremsstrahlung) of the electrons. There are 4 contributions to the total energy of the reconstructed electron-candidate: the estimated energy deposit in the material in front of the EM calorimeter, measured energy of the cluster in the EM, the estimated energy deposit outside the cluster (lateral leakage), and the estimated energy deposit beyond the EM calorimeter (longitudinal leakage). The (η, ϕ) coordinates of the electron candidate

are taken from the matched track at the interaction vertex.

Identification: The reconstructed electron candidates are subjected to further identification criteria with the aim of rejecting background electrons: jets misidentified as electrons, non-prompt electrons from hadron decays and electrons from photon conversions. Three sets of identification criteria are defined, in the order of increasing background-rejection power: Loose[2], Medium and Tight. The Loose selection uses shower-shape variables in different layers of the EM calorimeter, hadronic leakage information and imposes additional criteria on track quality (in pixel and silicon detectors) and on track-cluster matching. In addition to applying all of the Loose requirements (and tightening some), Medium selection requires a hit in the innermost layer of the pixel detector (to reject electrons from photon conversions), constrains transverse impact parameter to be less than 5 mm, and uses the information from TRT. Finally, in addition to the Medium selection with generally tightened requirements, Tight identification applies a requirement on the ratio of the EM cluster energy to the track momentum and rejects electron candidates matched to reconstructed photon conversions. Medium electrons are used for the main part of this analysis.

As for muons, an important additional handle in identifying prompt electrons is the isolation. It will be discussed in Chapter 5.

Electron reconstruction and identification efficiency

Electron reconstruction and identification efficiencies are evaluated in $Z \to ee$ and $J/\Psi \to ee$ data with the tag-and-probe method for electrons with $E_T > 7$ GeV. The efficiency of the initial cluster reconstruction is estimated in MC simulation to be $\sim 97\%$ for soft electrons at E_T=7 GeV, and approximately 100% for electrons above 20 GeV. The efficiency of the reconstruction algorithm, which matches clusters with tracks to form the electron candidates, is evaluated with respect to the sample containing reconstructed clusters. The measured reconstruction efficiency is found to be above 96% for most of the E_T and η range [91]. The identification efficiency of Loose, Medium and Tight criteria is evaluated with respect to reconstructed electrons having a good quality track pointing to an EM cluster. The efficiencies for Medium electrons start from about 80% for electrons with $E_T < 30$ GeV, and increase up above 90% for electrons with $E_T > 50$ GeV. The combined reconstruction and identification efficiencies as functions of E_T and η are shown in Fig. 4.4.

Similarly to muons, data-MC efficiency scale factors are derived for electrons starting at E_T=7 GeV and applied to MC samples in the analysis (see bottom panels in Fig. 4.4).

[2]The electron identification criteria, denoted here as Loose, Medium and Tight for simplicity, correspond to Loose++, Medium++ and Tight++ ATLAS menu employed for 2012 data.

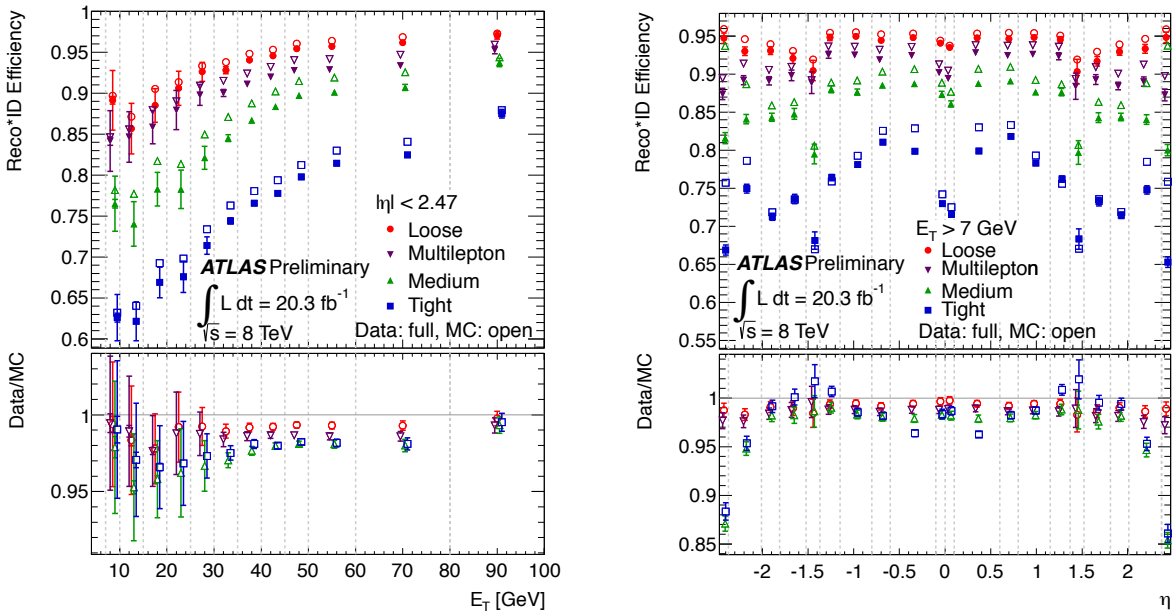

Figure 4.4: Measured combined reconstruction and identification efficiency as a function of E_T (left) and η (right) for Loose, Medium and Tight and Multilepton identification criteria, compared to MC expectation for electrons from $Z \to ee$ decay. The lower panel shows the data-to-MC efficiency ratios [91].

4.3.2 Electron calibration

The energy response of electrons is calibrated in several steps using a combination of MC-based and data-driven methods [92]. The EM clusters are calibrated to the original electron energy in simulated MC in order to correct for the energy lost in the material upstream of the calorimeter, the energy deposited in the cells neighbouring the cluster ϕ and η, and the energy lost beyond the LAr calorimeter. The MC based electron response calibration is applied to the cluster energies reconstructed in both data and MC.

The difference in response between data and simulation is corrected for by applying energy scale and resolution correction factors derived from $Z \to ee$ events. The energy scale mis-calibration is parametrized as

$$E^{\text{data}} = E^{\text{MC}}(1 + \alpha), \tag{4.1}$$

where α is a function of η. The relative energy resolution of EM objects can be parametrized as

$$\frac{\sigma}{E} = r_1/\sqrt{E} \oplus r_2/E \oplus r_3,$$

where $\oplus$ denotes a sum in quadrature, and coefficients r_1, r_2, r_3 are functions of η. The first term denotes the calorimeter intrinsic resolution (the sampling term). It contributes mostly at low energy and is measured to be about $10\%/\sqrt{E[\text{GeV}]}$ in independent test-beam studies [93]. The second term is the noise term and receives contributions from the pile-up and the electronic noise. The constant term r_3 absorbes the potential mis-modelling of the sampling and electronics noise terms, the asymptotic resolution at high energy, and the effect of passive material upstream of the calorimeter. Since the sampling term is already known, electron resolution corrections are derived by using the following parametrisation:

$$\left(\frac{\sigma_E}{E}\right)^{\text{data}} = \left(\frac{\sigma_E}{E}\right)^{\text{MC}} \oplus c.$$

The energy scale (α) and resolution (c) correction factors are derived by fitting the invariant mass MC templates to the data in $Z \to ee$ events. The scale corrections are found to be about 1% in the central region, and up to about 4% in the endcap (see Fig. **??** left). E_T-dependent corrections $\Delta\alpha$ on the η-dependent scale correction α are measured in $J/\Psi \to ee$ and $Z \to ee$ events and are found to be below 1% (see Fig. 4.5 right). The resolution corrections are about 0.8% in the barrel, and about 1% on average in the endcap. The resolution for electrons with low energy is improved by combining the track momentum in ID and cluster energy measurements. The effect is assessed on the $J/\Psi \to ee$ data, where the invariant mass resolution is found to be improved by 20%.

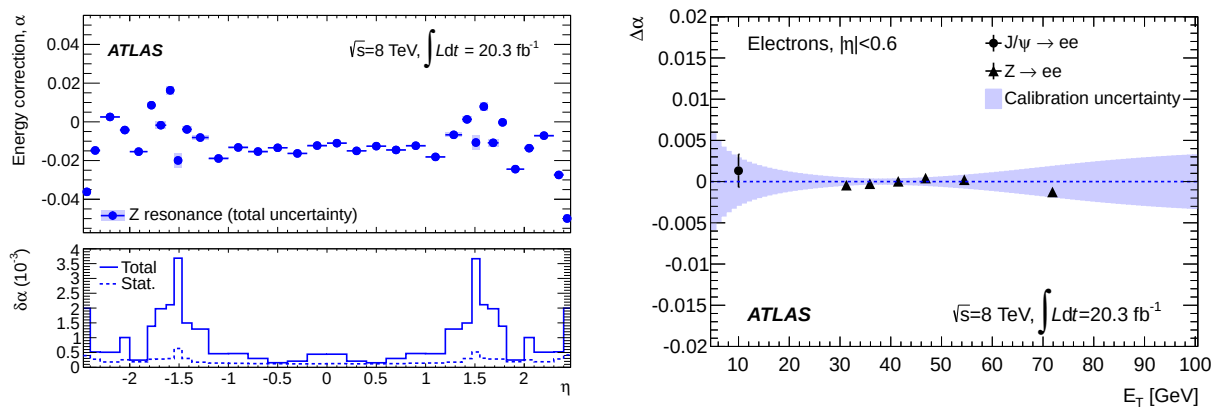

Figure 4.5: Left: Energy scale corrections α, defined as in Eq. 4.1, and derived from $Z \to ee$ events using the template method, as a function of η. The error bands include statistical and systematic uncertainties. Bottom panel is showing statistical and total energy scale uncertainties, $\delta\alpha$, as a function of η. Right: Energy scale factors $\Delta\alpha$ as a function of electron E_T obtained from $J/\Psi \to ee$ and $Z \to ee$ measurements. The band represents the calibration systematic uncertainty [92].

4.4 Jets

4.4.1 Jet reconstruction

Jets are reconstructed using the anti-k_t jet clustering algorithm [94]. The input to the algorithm are topological (topo) clusters – the objects formed by grouping together calorimeter cells with energy significantly above the measured noise [95]. The clustering of objects is based on sequential combination and proceeds by identifying the smallest of the distances between all pairs of objects (d_{ij}) and between all objects and the beam (d_{iB}). The two distance parameters are defined as

$$d_{ij} = \min\left(\frac{1}{k_{ti}^2}, \frac{1}{k_{tj}^2}\right)\frac{\Delta R_{ij}^2}{R^2}, \quad d_{iB} = \frac{1}{k_{ti}^2}, \tag{4.2}$$

where k_{ti} is the transverse momentum of an object i, and $\Delta R_{ij}^2 = (y_i^2 - y_j^2) + (\phi_i^2 - \phi_j^2)$ is the distance between objects i and j calculated with the rapidity y. The radius parameter R (jet cone size) is set to 0.4. If d_{ij} is the smallest distance, objects i and j are combined. If d_{iB} is the smallest, i is called a jet and removed form the list of input objects. Jet momenta are constructed by adding up zero-mass four-vectors of all the clusters belonging to a jet. The characteristic of the anti-k_t algorithm is that soft particles will tend to cluster with hard ones, rather then among themselves. If there are no other hard particles within a $2R$ distance around the first hard particle, the resulting jet will have a perfectly conical shape of radius R. If two hard particles are found within a $R < \Delta R_{ij} < 2R$ distance, two jets will be formed, but it is not possible for both to be perfectly conical. In other words, the key feature of the algorithm is that the soft particles do not modify the shape of the jet, while hard particles do.

4.4.2 Jet calibration

The hadronic shower consists of electro-magnetic (EM) energy (mainly $\pi^0 \to \gamma\gamma$), non-EM energy (from either charged-particle deposits, e.g. $\pi^{\pm}$, or the invisible energy in the form of nuclear breakup/excitations) and escaped energy (e.g. neutrinos). The topo-clusters are initially reconstructed at the EM scale and the hadronic part is taken into account later in the form of local cluster weighting (LCW) method [95]. Hadronic calibration accounts for the invisible and escaped energy, deposits in non-instrumented regions and signal losses due to noise-threshold effects. Clusters are classified as being of electromagnetic or hadronic origin, primarily based on the measured energy density and the longitudinal shower depth. The corrections to the hadronic clusters are applied based on simulations of charged and neutral particles. The main contribution to the non-compensating nature of the hadronic calorimeters comes from the "invisible energy", i.e. breakup of the nuclei and nuclear excitations. The full ATLAS jet calibration procedure [96], [97] proceeds in several steps and is schematically shown in Fig. 4.6.

Pile-up correction

Jets formed from the topo-clusters are first corrected for energy from additional proton-proton collisions in the same bunch crossing (in-time pile-up) and from past and future bunch-crossings (out-of-time pile-up). The pile-up corrections include both event-by-event average energy subtraction (offset) from a reconstructed jet energy and jet-by-jet specific corrections. The different contributions to the total pile-up (PU) correction are applied in the form:

$$p_T^{jet,corr} = p_T^{jet} - \rho \cdot A - \alpha(N_{PV} - 1) - \beta\langle\mu\rangle, \tag{4.3}$$

where ρ denotes the median of the event p_T density, A is the transverse jet area, N_{PV} number of primary vertices and $\langle\mu\rangle$ average number of interactions per bunch crossing. The median p_T density is defined as

$$\rho = \text{median}\left\{\frac{p_{T,i}^{\text{jet}}}{A_i^{\text{jet}}}\right\},$$

where the index i enumerates the jets and calorimeter topo-clusters (no lower p_T cut is used) found when clustering the event with the k_t algorithm. The jet-by-jet correction $\rho \cdot A$ is based on the assumption that the pile-up activity can be treated as a uniform, diffuse background, whose contribution to the jet-energy is proportional to the jet-area A. The median p_T density ρ provides an estimate of the global pile-up activity, while the jet area provides an estimate of a jet's sensitivity to pile-up. Plot on the left-hand-side of Fig. 4.7 is showing the mean jet-multiplicity as a function of $\langle\mu\rangle$ before and after the jet-area correction. After the correction, pile-up jet p_T is shifted below the reconstruction threshold, resulting in the mean number of jets becoming approximately constant with increasing $\langle\mu\rangle$.

Additional residual corrections proportional to N_{PV} (sensitive to in-time PU) and $\langle\mu\rangle$ (sensitive to out-of-time PU) are derived by comparison to truth particle jets in simulated dijet events. Fig. 4.8 shows this dependence for both the N_{PV} and the $\langle\mu\rangle$ term, along with a fit

with a logarithmic functional form. The fits are evaluated at 25 GeV to obtain the nominal correction coefficients α and β in Eq. (4.3), while the p_T dependency of the corrections is taken as a source of systematic uncertainty. Plot on the right-hand-side of Fig. 4.7 is showing the dependence of the reconstructed jet p_T on N_{PV} for a fixed $\langle\mu\rangle$. After subtracting $\rho \cdot A$, the residual correction due to N_{PV} and $\langle\mu\rangle$ is quite small.

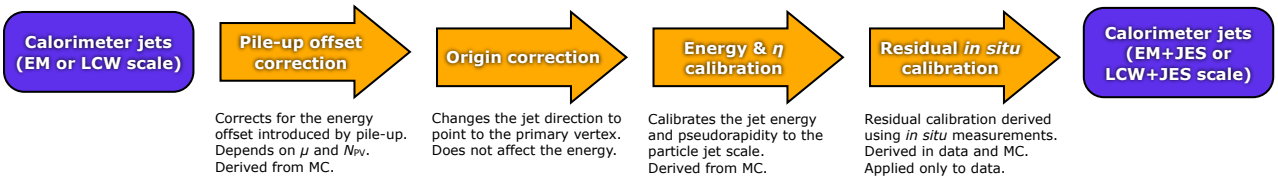

Figure 4.6: ATLAS jet calibration scheme [96].

Jet energy scale corrections

Further calibrations, referred to as jet energy scale (JES) corrections, relate the reconstructed jet energy to the truth jet energy and result in the LCW+JES calibrated jets. The first JES correction is derived from MC by applying the inverse of the average energy response, $R = E_{jet}^{LCW}/E_{jet}^{truth}$, of jets in energy and η bins. Further corrections are derived using data-driven (in situ) methods that exploit the p_T balance between jet p_T and p_T of a well-calibrated reference object:

$$\left[p_T^{\text{jet}}/p_T^{\text{ref}}\right]_{\text{data}} / \left[p_T^{\text{jet}}/p_T^{\text{ref}}\right]_{\text{MC}} . \tag{4.4}$$

Several techniques are used – direct p_T balance between a photon or a Z-boson and a jet, and balance between a system of low-p_T jets and a high p_T-jet. The JES calibration for forward jets is performed by exploiting the p_T-balance with the central jets for which the scale can be determined more precisely (the procedure known as η-intercalibration). The Z+jets, γ+jets and multi-jet balance techniques are combined to obtain the final in situ JES calibration shown in Fig. 4.9.

Jet vertex fraction

Pile-up subtraction based on jet areas removes larger part of pile-up jets by shifting their p_T below threshold. However, some pile-up jets still remain due to localized fluctuations in pile-up activity. Jet vertex fraction (JVF) is a variable that uses tracks to associate jets to the hard-scatter interaction (see Fig. 4.10 left) and is used to further reject any remaining LCW+JES calibrated jets originating from PU activity. Sum of p_T of tracks that are matched to a jet and pointing to the primary hard-scatter vertex is divided by the total summed p_T of all tracks matched to the jet. By requiring a minimum JVF (usually about 0.25), number of PU jets passing the final selection can be further reduced (see right-hand-side of Fig. 4.10). The

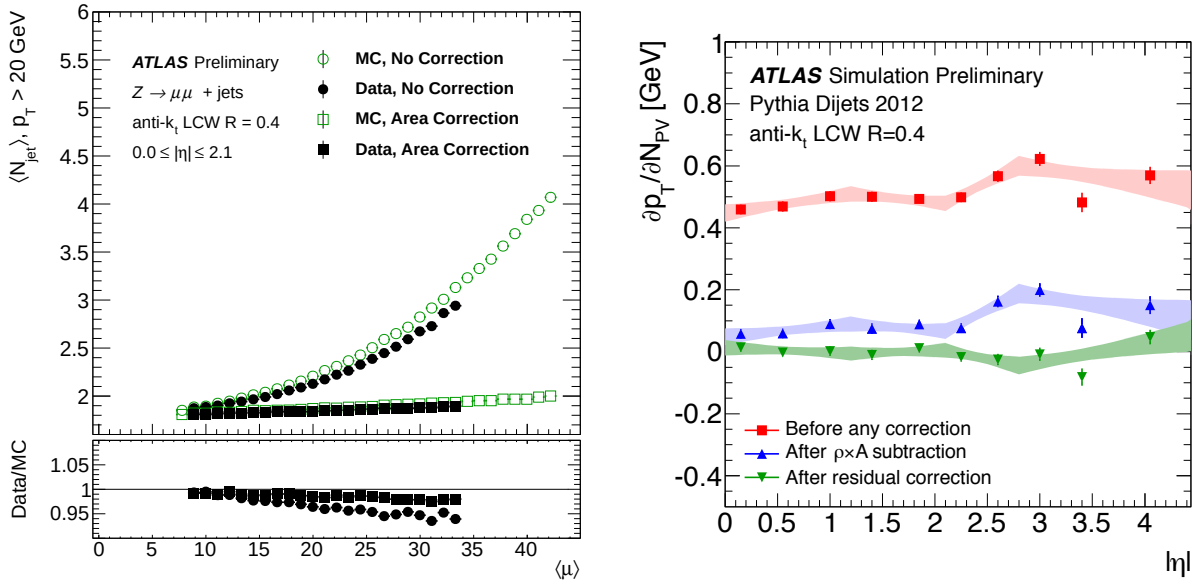

Figure 4.7: Left: The mean jet multiplicity against $\langle\mu\rangle$ in Z+jet events for jets with p_T >20 GeV and $|\eta| < 2.1$. Right: Dependence of the reconstructed jet p_T on in-time pile-up at various correction stages: before any correction, after $\rho \cdot A$ subtraction, and after the residual N_{PV} and $\langle\mu\rangle$ corrections. The error bands show the 68% confidence intervals of the fitted corrections [97].

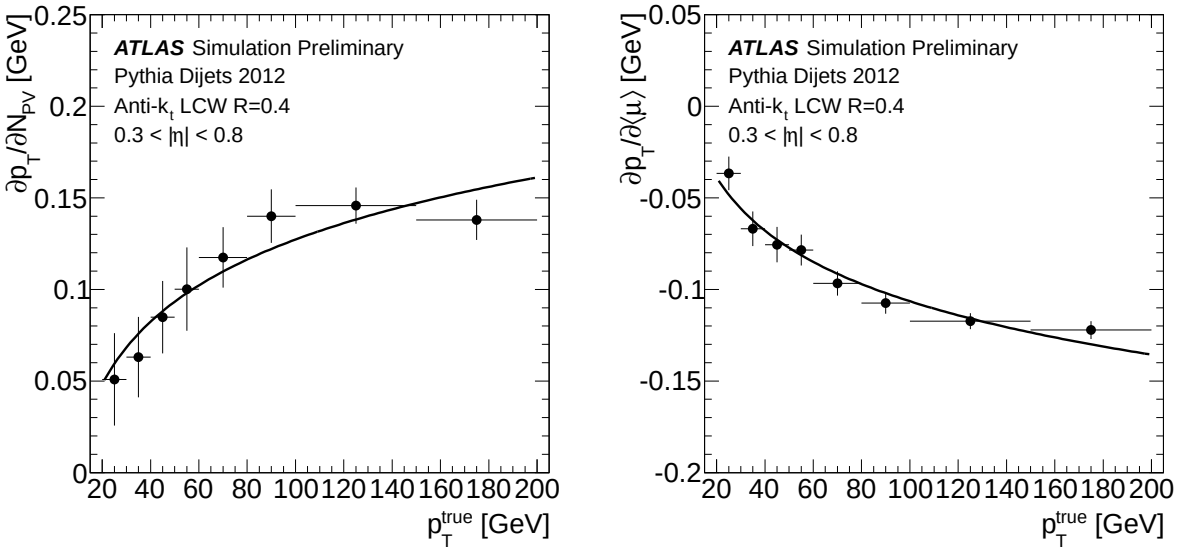

Figure 4.8: Dependence of the coefficients of the residual pile-up correction (α and β in Eq. (4.3)) on the p_T of matched truth particle jets in simulated dijet events. The points are consistent with a logarithmic functional form [97].

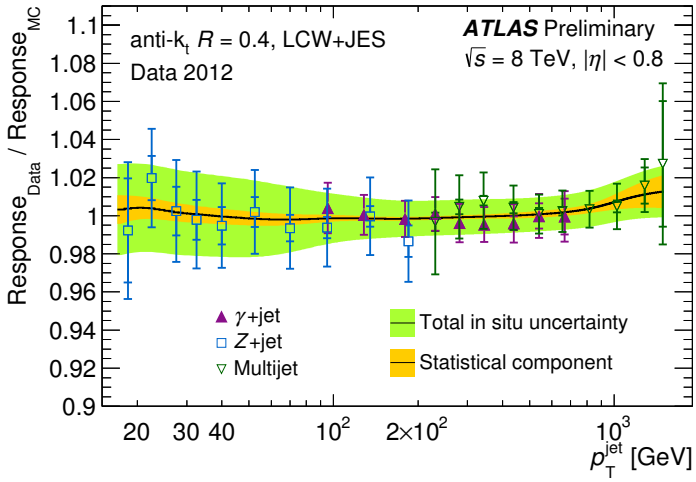

Figure 4.9: Jet response ratio of the data to the MC simulation as a function of p_T for three in situ techniques combined to determine the in situ energy scale correction: Z+jet (squares), γ+jet (full triangles) and multijet (empty triangles). The error bars indicate the statistical and the total uncertainties (adding in quadrature statistical and systematic uncertainties). The outer band indicates the total uncertainty resulting from the combination of in situ techniques, while the inner dark band shows the fraction purely from statistical uncertainties.

JVF cut is applied only to jets with p_T <50 GeV, as higher p_T jets are less sensitive to the PU. The uncertainty associated with applying the JVF cut is assessed by comparing the efficiencies with which hard-scatter jets in Z+jets events in MC (ϵ_{MC}^{nom}) and data (ϵ_{data}^{nom}) are selected when applying a nominal JVF cut. For observed ϵ_{MC}^{nom} and ϵ_{data}^{nom}, such value of the JVF threshold is found that gives the new MC efficiency of $\epsilon_{MC}^{nom} \pm (\epsilon_{MC}^{nom} - \epsilon_{data}^{nom})$. The JVF uncertainty is then formed by rerunning the analysis with these up and down variations of the JVF threshold value. For the $|\text{JVF}| > 0.25$ requirement used in this analysis, the JVF threshold is varied down to 0.21 and up to 0.28.

Jet energy scale uncertainties

Jet energy scale uncertainties coming from each of the energy calibrations mentioned above are considered separately, and result in a set of parameters describing the uncertainty on JES:

- **PU uncertainties:** Four sources of uncertainties related to the PU subtraction are considered – uncertainties due to $\langle\mu\rangle$ and N_{PV} offset subtraction, uncertainty in the determination of the median p_T density ρ due to topology dependency, and the uncertainty on the initial p_T term (Eq. 4.3), which itself depends on $\langle\mu\rangle$ and N_{PV}. The total combined PU uncertainty is shown in Fig. 4.11.

- **Uncertainties from in-situ methods:** The uncertainties associated with these methods include the uncertainties arising from detector description (e.g. electron or photon

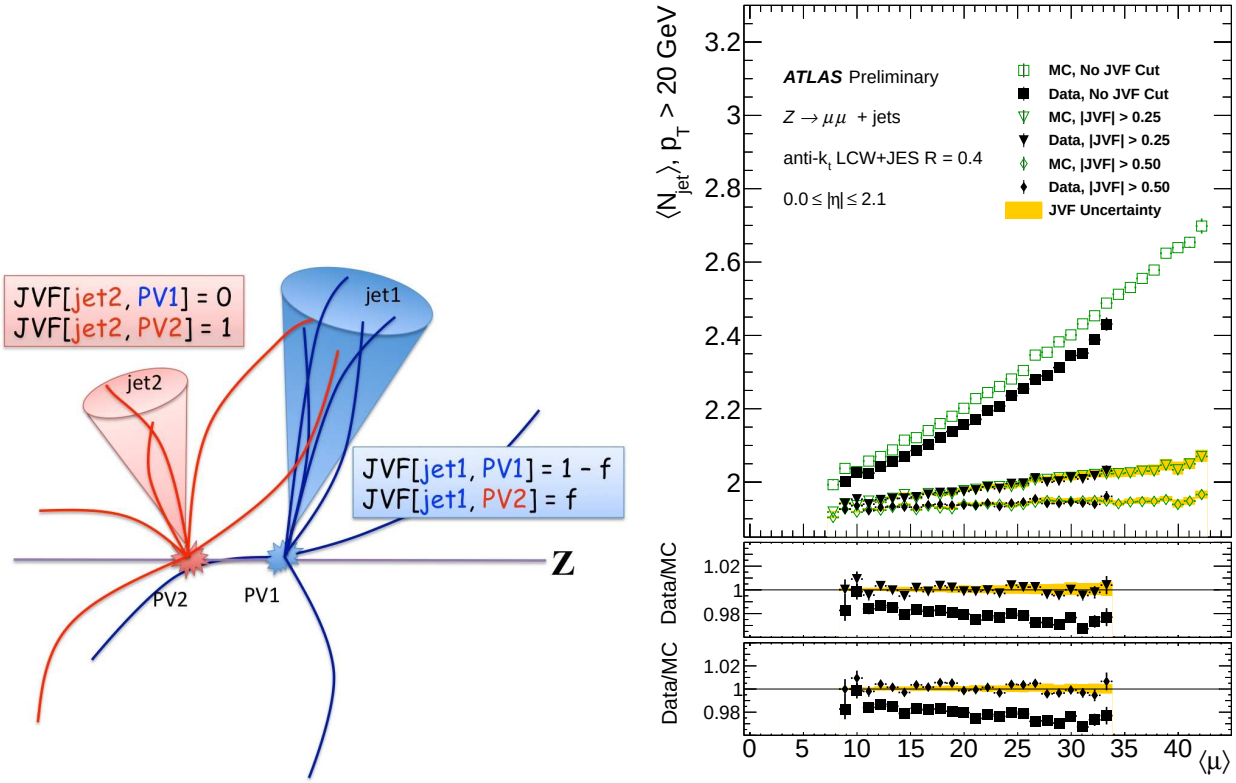

Figure 4.10: Left: Schematic representation of the JVF principle. Right: The mean multiplicity of jets with $|\eta| < 2.1$ versus $\langle \mu \rangle$ in Z+jet events before and after applying |JVF| cuts to any jets (at the fully calibrated LCW+JES scale) with p_T <50 GeV . The upper ratio plot shows before and after an application of a |JVF| cut of 0.25 and the lower ratio plots show the same for a cut of 0.50 [97].

energy scale), physics modelling (e.g. contribution of particles outside the jet cone) and statistics. A correlation matrix of more than 50 sources is created, and the dominant 5 eigenvectors are taken as separate components. The remaining eigenvectors are added in quadrature to form a residual 6th component. The total JES uncertainty due to in-situ measurements is shown in Fig. 4.11. It is separated into two components – absolute in-situ JES refers to the combination of uncertainties from Z+jets, γ+jets and multi-jet balance techniques, while relative in-situ JES denotes the uncertainties due to the η-intercalibration procedure.

- **Single hadron response:** The JES corrections can also be extracted from single hadron response measurements based on MC simulation and extrapolated test-beam results. In this method jets are treated as a superposition of energy deposits of single particles. The uncertainty of up to 2% is applied only to very high p_T jets ($p_T > 2$ TeV) for which the in-situ techniques are limited in statistics.

- **Flavor response and composition:** Z+jets and γ+jets samples used for in-situ measurements contain a large fraction of quark-initiated jets, while samples used in physics analyses may have different jet flavor composition. An uncertainty to cover the fragmentation differences between quark and gluon initiated jets is derived by studying the two types of jet response in MC. The difference in the response between light-quark and gluon initiated jets is found to amount up to about 2% for lower jet momenta and decrease to less than 0.5% at higher jet p_T. Analysis-dependent systematic uncertainty increasing linearly with the gluon content of a sample under study is applied to account for such potential shifts in the gluon-jet energy scale. Additional uncertainty is applied to account for possible different flavour compositions in the data and MC. The magnitudes of the two flavour uncertainty components in a dijet sample are shown in Fig. 4.11.

- **Uncertainties for jets with heavy flavour:** The uncertainty in the calorimeter response to b-jets is estimated in a combination of MC and data–driven techniques. The derived additional uncertainty of 1.5% – 3% is applied to jets in the analysis that have been b-tagged (instead of the light-quark and gluon flavour composition uncertainty outlined in the previous paragraph).

- **Non-closure uncertainties:** The *in situ* jet-energy scale corrections (Eq. 4.4), as well as the corresponding uncertainties, have been derived using Pythia MC generator as a nominal sample. As the jet response may be different in other simulation configurations, the ratio of miscalibration (deviation of the jet response from unity) of a different MC sample to the nominal one is taken as an additional uncertainty. The uncertainty is found to be negligible in the central region and to amount to a maximum of 3.5% in the transition region between the endcap and forward calorimeters ($|\eta| \simeq 3.2$).

The total relative JES uncertainty, as well as a breakdown to individual components (except the b-jet scale uncertainty), as a function of jet p_T and η is shown in Fig. 4.11. The total

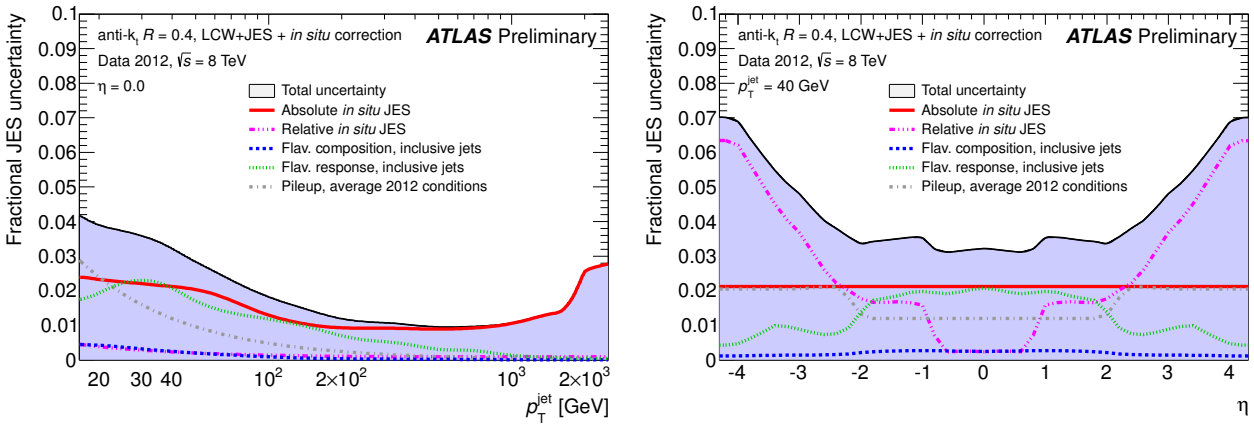

Figure 4.11: Fractional jet energy scale systematic uncertainty components as a function of p_T for jets at $|\eta| = 0.0$ (left) and as a function of η for jets at $p_T = 40$ GeV (right). The total uncertainty (all components summed in quadrature) is shown as a filled blue region topped by a solid black line. Average 2012 pileup conditions were used, and topology dependent components were taken from inclusive dijet samples [52].

uncertainty is below 4% in the whole p_T range and drops below 2% for jets $200 < p_T < 1000$ GeV. The uncertainty is larger than 4% for forward jets with $|\eta| > 2$ due to the uncertainties on the η-intercalibration procedure.

Jet energy resolution

The jet energy resolution (JER) has been measured in the data and MC with two methods: dijet balance and bisector technique [98]. The first method relies on the approximate scalar balance between the transverse momenta of the two leading jets and measures the sensitivity of this balance to the presence of extra jets. In the bisector technique the vector sum of the leading jets' transverse momenta is projected on the coordinate system where one axis is along the bisection of the $\Delta\phi$ angle between the two jets and the other is orthogonal to it. The fractional JER (defined as $\sigma(p_T)/p_T$) as a function of p_T is shown in Fig. 4.12. The measured values in data and MC are in good agreement, within 10%. The systematic uncertainties on JER include the variation in resolution when varying the $\Delta\phi$ threshold between two jets in the dijet balance method, the variation in JER due to the soft radiation correction modelling, uncertainties due to JES and pile-up effects. The total systematic uncertainty on JER is less than 7% for the whole jet p_T range.

4.5 b-jet tagging

The process of identifying jets originating from b-quark fragmentation is called b-tagging. It provides an important handle in distinguishing processes containing one or more b-jets in the

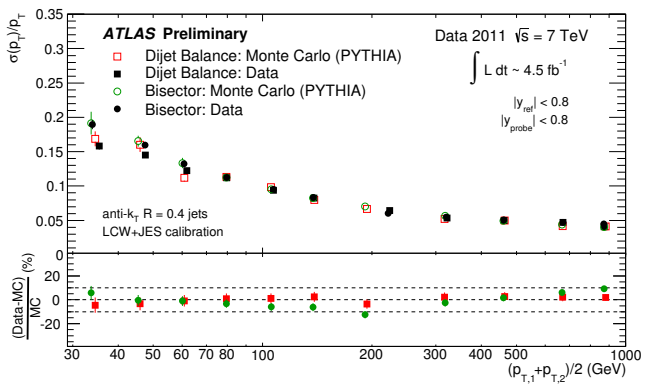

Figure 4.12: Fractional jet energy resolution as a function of the average jet p_T measured with the di-jet balance (squares) and bisector (circles) in situ methods. The bottom plot shows the relative difference between data results (black) and Monte Carlo simulation for each method. The dotted lines indicate a relative difference of 10%. Only statistical errors are shown [52].

final state, such as e.g. $t\bar{t}$, from processes producing predominantly light-flavor (u, d, s) jets (e.g. QCD jet production). Thanks to the relatively long lifetime of b-hadrons ($\sim$1.5 ps), leading to a few millimeters flight path in the detector, the main distinguishing feature of b-jets is the presence of a secondary decay vertex inside a b-jet cone. The ATLAS detector gains most of its b-jet identification power through 3-component Inner Detector, which provides high resolution tracking and vertexing.

A number of b-tagging algorithms have been developed in ATLAS [99]. The impact parameter-based algorithms ("JetProb" and "IP3D") combine the transverse and longitudinal impact-parameter significances to form a discriminating variable. The transverse impact parameter d_0 is defined as the distance of closest approach of the track to the primary vertex point in $r\phi$ projection (see Fig 4.13). The z coordinate of this point is referred to as the longitudinal impact parameter z_0 (or, strictly speaking, $|z_0|\sin\theta$, where θ is the polar angle of the track). Considering the significance of an impact parameter $(d_0/\sigma_{d_0}, z_0/\sigma_{z_0})$ gives more weight to tracks measured more precisely. Adding the sign to the significance additionally increases the power of the discriminating variable, as the tracks of b/c hadrons tend to have a positive sign (the sign of the impact parameter is positive if the track extrapolation crosses the jet direction in front of the primary vertex, and negative otherwise). Secondary vertex-based algorithms (e.g. "SV1") use tracks to build an inclusive vertex formed by the decay products of a b-hadron. "SV1" algorithm combines three of the vertex properties into a likelihood ratio: the invariant mass of all tracks associated to the vertex, the ratio of the sum of the energies of the tracks in the vertex to the sum of the energies of all tracks in the jet, and the number of two-track vertices. "JetFitter" algorithm exploits the topology of weak b- and c-hadron decays inside the jet, as well as information about an approximated flight path of the b-hadron. In the analysis presented in this thesis, MV1 b-tagging algorithm is used. It is based on a neural network

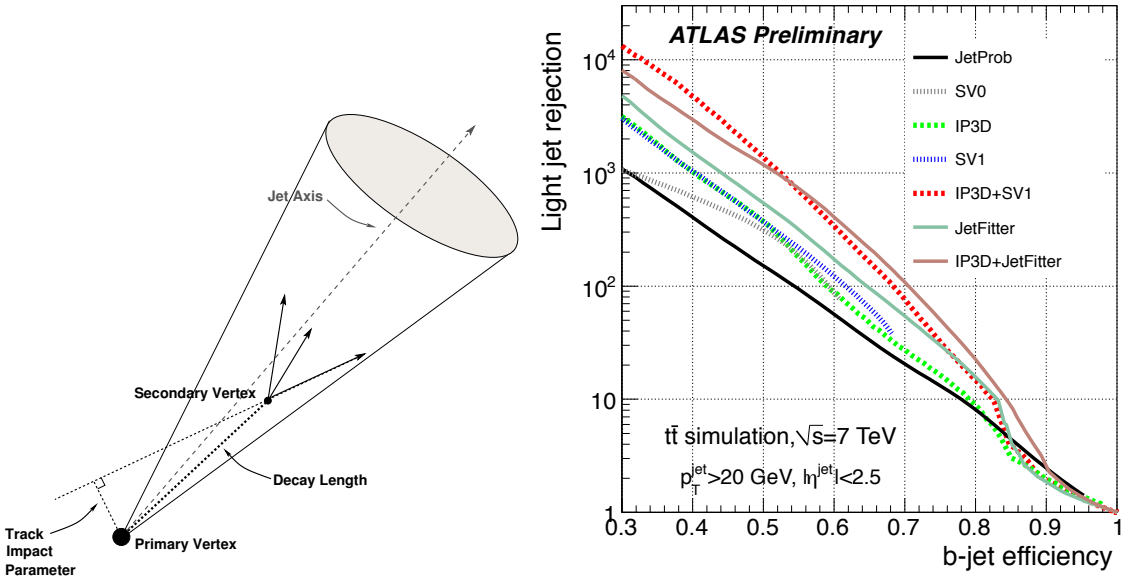

Figure 4.13: Left: Illustration of variables used in b-tagging. Right: Light-jet rejection as a function of the b-jet tagging efficiency for different b-tagging algorithms, based on simulated $t\bar{t}$ events [99].

b-jet efficiency [%]	purity [%]	RF(c)	RF(τ)	RF(light)
80.00	85.41	3.08	5.49	25.18

Table 4.1: The purity and charm-, τ- and light-jet rejection factors for MV1 algorithm at 80% b-jet tagging efficiency point.

using as an input the output weights of different algorithms: "JetFitter+IP3D", "IP3D" and "SV1". The performance of individual algorithms in terms of b-jet tagging efficiency and light jet rejection factor is shown on the right hand side of Figure 4.13. The tagging efficiency is the fraction of jets labeled as b-jets that are properly tagged, while the rejection is the reciprocal of the fraction of jets that are labeled as light jets and are tagged incorrectly by the algorithm. The labeling procedure is based on the flavor of true quarks in MC simulation. The MV1 algorithm has improved performance in terms of tagging efficiency and rejection, compared to the individual components (see Ref. [100]). The 80% efficiency point is used in this analysis, for which the purity, as well as charm-, τ- and light-jet rejection, are shown in Table 4.1.

4.5.1 b-tagging calibration

The calibration of b-tagging algorithms includes the measurement of the mis-tag rates and b-tagging efficiency and is expressed in the form of p_T-dependent scale factor $\kappa_{\epsilon_b}^{\text{data/sim}}$, defined as:

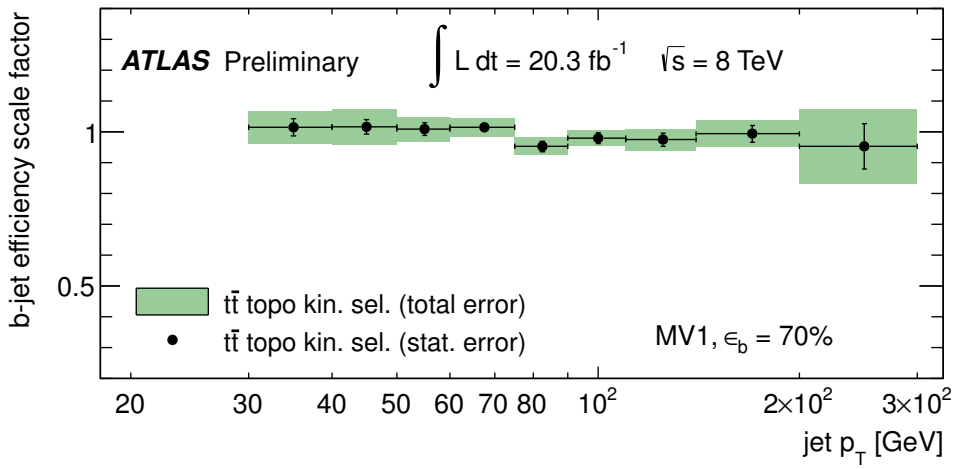

Figure 4.14: Right: The b-tag efficiency data-to-simulation scale factor for the MV1 tagging algorithm at 70% efficiency on 8 TeV data, using a tag and probe method based on kinematic selection on $t\bar{t}$ dilepton sample with two jets in the final state [52].

$$\kappa_{\epsilon_b}^{\text{data/sim}} = \frac{\epsilon_b^{\text{data}}(p_T)}{\epsilon_b^{\text{sim}}(p_T)} \tag{4.5}$$

Several independent methods of calibration are combined to obtain the final data-MC scale factors [101], [102]. "System8" and $t\bar{t}$-based calibrations have been used for b-jets in this analysis. "System8" method relies on solving a set of 8 equations to numerically calculate the b-tagging efficiency. It uses muons from leptonic decays of b-quarks to measure the b-jet content of a given sample. Similarly, the $t\bar{t}$-based method uses the fact that $t\bar{t}$ events, in most of the cases, contain exactly 2 b-jets. A number of sources of systematic uncertainties was considered when deriving the scale factors. The uncertainties depend on the method, and include the uncertainties on B-hadron decay modelling (e.g. semileptonic branching fractions), b-fragmentation fractions (i.e. production fractions of particular B-hadron species), choice of MC generator and parton shower, jet-energy scale and resolution, to name a few. The scale factors, along with their systematic and statistical uncertainties, for MV1 algorithm obtained with the $t\bar{t}$-based method are shown in Figure 4.14. The total systematic uncertainty is less than 5% in most of the b-jet p_T range. Charm-jet scale factors have been measured using a sample of D^+ mesons, reconstructed within a jet in the $D^+ \to D^0(\to K^-\pi^+)\pi^+$ final state [103]. The mistag rate of b-tagging algorithms has been performed using methods similar to the impact parameter-based tagging algorithms [104]. While secondary vertices in b-jets tend to have positive decay length (positive track impact parameters), the light jets tend to have the negative sign of these variables. The invariant mass spectrum of tracks associated with reconstructed secondary vertices is another useful variable to separate light and heavy-flavour jets.

4.6 Missing transverse energy

4.6.1 E_T^{miss} reconstruction and calibration

In a hadron collider the exact energy of the colliding partons is unknown, therefore the total energy of the event is unknown, too. However, the momentum conservation law can be applied to the transverse plane - as there is no initial momentum perpendicular to the beam axis, the net transverse momentum produced in the collision has to add up to zero. Any transverse momentum imbalance is called the missing transverse energy (E_T^{miss}) and is attributed to non-interacting particles, such as neutrinos or new-physics weakly interacting particles.

E_T^{miss} is reconstructed from energy deposits in the calorimeters and reconstructed muons. It is calculated as the negative sum of all calibrated reconstructed objects in the event, in addition to the energy deposits and tracks which are not associated to any object (the soft E_T^{miss}-term) in the followng order [105], [106]:

$$E_{x(y)}^{miss} = E_{x(y)}^{miss,e} + E_{x(y)}^{miss,\gamma} + E_{x(y)}^{miss,\tau} + E_{x(y)}^{miss,jets} + E_{x(y)}^{miss,SoftTerm} + E_{x(y)}^{miss,\mu}. \tag{4.6}$$

All the objects in Equation 4.6 have their respective calibrations applied, e.g. the jets are corrected for the pile-up and are calibrated with the LCW+JES scheme (see section 4.4.2). The p_T threshold for electrons, photons and muons entering the E_T^{miss} caculation is set to 10 GeV, while the jet threshold is 20 GeV. Taus do not enter the calculation directly, but are included in either the jet or the soft term. To suppress any noise contribution, the soft term is calculated from the topological clusters with LCW technique. The soft term includes both the contribution from soft jets (p_T <20 GeV) and from topoclusters/tracks not associated to high p_T-objects.

All E_T^{miss} terms in Equation 4.6 are in principle affected by the pile-up, but the most susceptible ones are the jets and the soft term. The pile-up supression applied to the jet-term is the same as the method used for jets in the analysis (see Section 4.4.2) – both the jet-area and the jet-vertex-fraction (JVF) based suppressions are applied. However, no pile-up correction for soft term is used in this analysis. When studying processes with large genuine E_T^{miss}, e.g. $t\bar{t}$ or SUSY/UED, the soft term brings only minor contribution to the total E_T^{miss} (as opposed to e.g. the jet term). As a result, the total E_T^{miss} is not particularly sensitive to the PU effects in the soft term. Left hand side of the Fig. 4.15[3] is showing the E_T^{miss} distirbution in data and MC in a sample of $Z \to \mu\mu$ events. No genuine E_T^{miss} is expected in $Z \to \ell\ell$ processes, apart from a small contribution from the semi-leptonic decays of heavy-flavour hadrons in jets. It can be seen that, even without soft term PU correction, E_T^{miss} is quite well described in the whole range, with the tail of the distribution being compatible with backgrounds like $t\bar{t}$ and dibosons producing the real E_T^{miss}.

[3]Several techniques for the PU suppression in the soft E_T^{miss} term exist. Similar to the JVF, the STVF is defined as the fraction of momenta of tracks matched to the soft term which are associated with the hard scattering vertex.

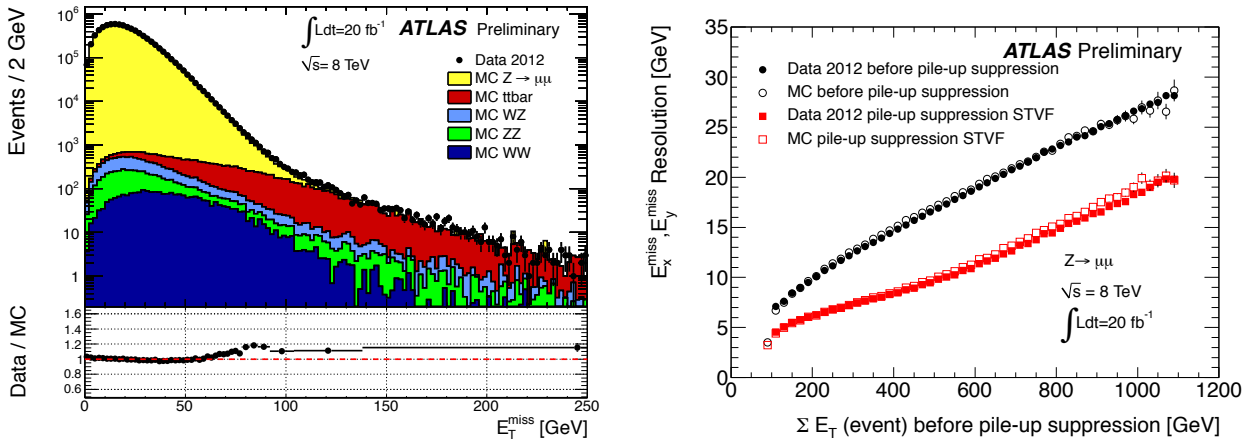

Figure 4.15: Left: Distribution of E_T^{miss} as measured in a data sample of $Z \to \mu\mu$ events without any pile-up suppression. The expectation from MC simulation is superimposed and normalized to data, after each MC sample is weighted with its corresponding cross-section. The lower parts of the figure shows the ratio of data over MC. Right: E_x^{miss} and E_y^{miss} resolution as a function of the total transverse energy in the event calculated by summing the p_T of muons and the total transverse energy in the calorimeter in data. Resolution in data and MC simulation are compared in $Z \to \mu\mu$ events before and after pile-up suppression with STVF [105].

4.6.2 E_T^{miss} resolution

The performance of E_T^{miss} can be evaluated by studying its resolution as a function of the total transverse energy in the event ($\sum E_T$). As no genuine E_T^{miss} is expected in $Z \to \ell\ell$ processes, the resolution can be evaluated by directly measuring the E_x^{miss} and E_y^{miss} components in the $Z \to \ell\ell$ data, and assuming their true values are zero. The E_x^{miss} and E_y^{miss} resolution as a function of the $\sum E_T$ is shown on the right hand side of Fig. 4.15. As can be seen, excellent agreement between the data and the MC simulation is observed, both before and after the pile-up suppression. Without the PU correction, the E_T^{miss} resolution follows an aproximately stochastic behaviour with the $\sum E_T$ described by the function $\sigma \sim \sqrt{\sum E_T}$.

4.6.3 E_T^{miss} systematic uncertainties

The overall systematic uncertainty on the E_T^{miss} measurement is evaluated by combining the uncertainties on reconstructed objects entering the E_T^{miss} calculation (Eq. 4.6). Additionally, scale and resolution uncertainties on the soft term need to be added. The soft-term scale uncertainty is evaluated in $Z \to \mu\mu$ events with no jets p_T >20 GeV in the final state by looking at the projection of E_T^{miss} onto the Z boson transverse direction. The average deviation from unity of the data-MC ratio of this variable is taken as the measure of the systematic uncertainty. The resolution uncertainty is assesed in the similar way, by looking at the E_x^{miss} and E_y^{miss} components in the same data sample. Uncertainties of 8% and 2.5% have been

assigned to the scale and the resolution of the soft term, respectively.

4.7 Selection of objects for the analysis and event cleaning

The selection of final-state objects used for the analysis proceeds in several steps. First the baseline (or preselected) muons, electrons and jets are defined among the objects identified and calibrated as outlined in Sec. 4.2 to 4.4. Baseline muons (electrons) are required to have p_T above 6(7) GeV and $|\eta| < 2.4$ ($|\eta_{\text{cluster}}| < 2.47$). Jets are required to have $p_T > 20$ GeV and $|\eta| < 2.5$. Any overlap between the baseline objects in an event is removed. If a jet and an electron are found to be within $\Delta R < 0.2$, where $\Delta R = \sqrt{(\Delta\eta)^2 + (\Delta\phi)^2}$, the jet is removed in favour of the electron. If the distance between a jet and an electron is $0.2 < \Delta R < 0.4$, the electron is removed, and the jet is kept. Finally, the angular separation between baseline muons and jets is required to be larger than 0.4 ($\Delta R > 0.4$), otherwise the muon is discarded.

At this point events containing badly reconstructed objects or objects arising from non-collision sources are vetoed in order to ensure a good quality of the selected data sample. A baseline muon is considered to be badly reconstructed if $\frac{\sigma(q/p)}{q/p} > 0.2$, where q is the charge of the muon. Cosmic muons are identified based on track impact parameters: if $|z_0^{PV}| > 1$ mm or $|d_0^{PV}| > 0.2$ mm the muon is considered cosmic. Events containing badly reconstructed or cosmic muons are rejected. As the transition region between the barrel and the endcaps of the LAr calorimeter contains a relatively large amount of inactive material, any events with a baseline electron falling in this region ($1.37 < |\eta| < 1.52$) are vetoed. Quality of baseline jets is assessed by considering various variables related to the deposited energy fractions in different parts of the calorimeters and to pulse shapes used to reconstruct the cell energy. A set of VeryLoose criteria [95] are applied in order to identify jets coming from non-collision events (e.g. beam halo) or detector effects (e.g. calorimeter noise). Events containing at least one VeryLoose bad jet are vetoed.

After the overlap removal and event cleaning, further selection criteria are imposed on the baseline objects in order to select the final signal objects. Signal leptons are required to be well isolated – requirements are imposed on various track- and calo-based isolation variables, as well as on the longitudinal and transverse track impact parameters [4]. The p_T threshold for signal jets is raised to 25 GeV in order to reduce the contamination from the pile-up jets. Furthermore, any jets with $|\eta| < 2.4$ and $p_T < 50$ GeV are required to have $|\text{JVF}| > 0.25$. No JVF criteria are applied on jets with $p_T > 50$ GeV, nor on b-tagged jets, as a probability of pile-up jets satisfying either of these criteria is negligible. The object selection criteria are summarised in Tab. 4.2.

[4] The isolation definition and optimisation are described in detail in Chapter 5.

	Muons	**Electrons**	**Jets**
Baseline objects			
algorithm/quality	Staco, CB or ST	Medium quality	Anti-k_t, $R = 0.4$
p_T [GeV]	> 6	> 7	> 20
$\|\eta\|$	< 2.4	< 2.47	< 2.5
remove object if	$\Delta R^{\mu,jet} < 0.4$	$0.2 < \Delta R^{e,jet} < 0.4$	$\Delta R^{e,jet} < 0.2$
remove event if	$\frac{\sigma(q/p)}{q/p} > 0.2$ or cosmic	$1.37 < \|\eta\| < 1.52$	VeryLoose
Signal objects			
p_T [GeV]	> 6	> 7	> 25
isolation (leptons)	Medium Iso (if $p_T < 25$ GeV) Standard Iso (if $p_T > 25$ GeV)		-
PU suppression (jets)	-	-	|JVF| >0.25 (if $p_T < 50$ GeV and $\|\eta\| < 2.4$)
B-jets	MV1 algo at 80% efficiency, $p_T > 25$ GeV, $\|\eta\| < 2.5$		

Table 4.2: Summary of selection criteria for leptons and jets used in the analysis. Baseline objects are identified and calibrated as described in Sec. 4.2 to 4.4. On top of the baseline quality requirements, additional criteria are applied to select the signal objects.

Chapter 5

Analysis overview and selection optimisations

As described in Chapter 2, mUED signal is characterised by lepton-rich final states. Due to KK quarks being heavier than the weak bosons, W^1 and Z^1 will mainly decay to leptons. mUED decay chains end with a γ^1, which is stable and does not interact with the detector, therefore relatively large E_T^{miss} is another characteristic of mUED events. Since leptons provide a relatively clean signature in the hadron collider, a two-lepton final state, in association with E_T^{miss}, is chosen for this analysis.

The analysis is designed as a number counting experiment. The signal region is defined so as to maximise the signal-to-background ratio. The compatibility of the Standard-Model expectation is tested against the data in the signal ragion. Any deviation from the SM-only prediction could mean a presence of a new signal.

The detailed characteristics of the target signal are described in Sec. 5.1, followed by the overview of the Standard Model backgrounds in Sec. 5.2. The trigger strategy and lepton-isolation optimisation procedure are introduced in Sec. 5.3 and 5.4, respectively. Finally, the event-selection optimisation (resulting in the signal-region definition) is described in Sec. 5.5. Various background estimation techniques are described later in Chapter 6.

5.1 Target signature

The two-lepton final state mainly occurs when one of the KK quarks/gluons decays hadronically, while the other decays to two leptons through a neutral KK vector boson (Z^1) (see Figure 5.1). If decaying to charged leptons, the Z^1 will produce two opposite-sign and same-flavor leptons (OSSF leptons) – two muons or two electrons[1]. Final states with two leptons of

[1]For convenience, both particle and its anti-particle are referred to with the same name, with the difference being made by specifying the charge (e.g. positrons are referred to as "positively charged electrons"). Furthermore, the word "leptons" denotes only muons or electrons, unless specified otherwise.

opposite flavor (OF, e.g. electron-muon pair), or two leptons of the same sign (SS, e.g. two positively charged leptons) can be produced if both of the initial-state KK quarks/gluons decay leptonically through intermediate W^1 or Z^1. Since the probability for both of the initial g^1 decaying leptonically is about 50% smaller than for the mixed hadronic-leptonic decays, the signal acceptance is larger by roughly a factor of two in the OSSF final states. Additionally, the background arising from the top-quark pair production is larger approximately by a factor of two in the electron-muon channel, resulting in much smaller sensitivity compared to the same-flavor channels.

As mUED signal points with $\Lambda R \sim 5$ are theoretically favoured (see Section 1.7), the main feature of signal leptons is their small transverse momentum. The sensitivity of the analysis is thus increased by placing an upper bound on the lepton momenta. Transverse momenta of jets appearing in the decay chain depend on the signal point and decay pattern, but for small ΛR-models the jet momenta will typically be rather small as well. As it is very difficult to differentiate a signal containing only soft leptons and jets in the final state from the SM backgrounds, the sensitivity of the analysis is increased by selecting events where the whole KK system is recoiled against a high p_T jet coming from the initial state radiation.

Finally, mUED events will contain relatively large missing transverse energy due to two weakly-interacting KK photons appearing at the end of the decay chain. By placing a high-p_T threshold on the leading jet, in combination with the requirement of large E_T^{miss}, boosted KK events are naturally selected and signal-to-background ratio is increased.

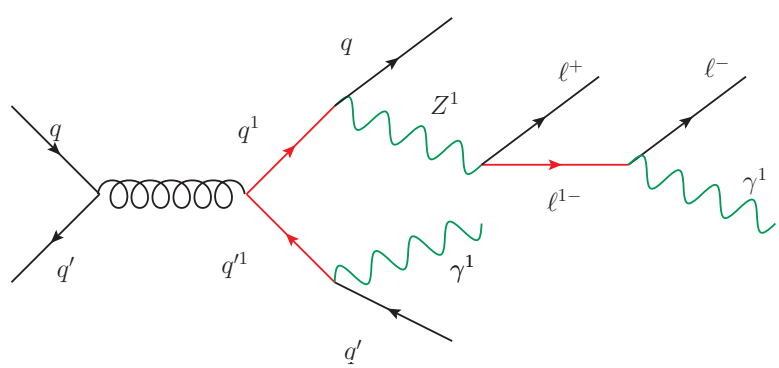

Figure 5.1: Dominant decay pattern contributing to the two-lepton final state.

To summarise, the target signal is characterised by two soft same-flavor, opposite-sign leptons, high-p_T leading jet and large E_T^{miss} from an escaping LKP. For highly compressed points ($\Lambda R \leq 5$) the leading jet is mainly an ISR jet, while for the models with larger mass splitting the leading jet can also come from one of the initial KK gluons decaying hadronically.

5.2 Standard Model backgrounds

Two main types of backgrounds in the analysis are processes with either two prompt (real) leptons (to-quark and weak-boson backgrounds) or with a combination of a prompt and a non-prompt (fake) lepton.

Top-quark backgrounds: The dominant prompt-lepton background in this analysis is coming from dileptonic decays of $t\bar{t}$ events (see Figure 5.2). Top and anti-top quarks decay to a W-boson and a b-jet with nearly 100% branching fraction. If both W-bosons decay leptonically, the final state will contain two leptons of the opposite sign plus a missing transverse energy produced by the two neutrinos. Similar topology, but with smaller cross-section, arrises also in decays of a singly-produced top quark in association with a W-boson (see Figure 5.3 left). Top-quark pair production in association with vector bosons results in, again, similar final states, but with yet smaller cross sections.

Since top-quark events always contain b-jet(s), while signal produces mainly light-quark jets, this type of background can efficiently be reduced by vetoing events with a b-jet in the final state. Event-shape variables, such as effective mass (m_{eff}) or ratio of E_T^{miss} to m_{eff} (see Sec. 5.5.2), can further help in discriminating signal from background.

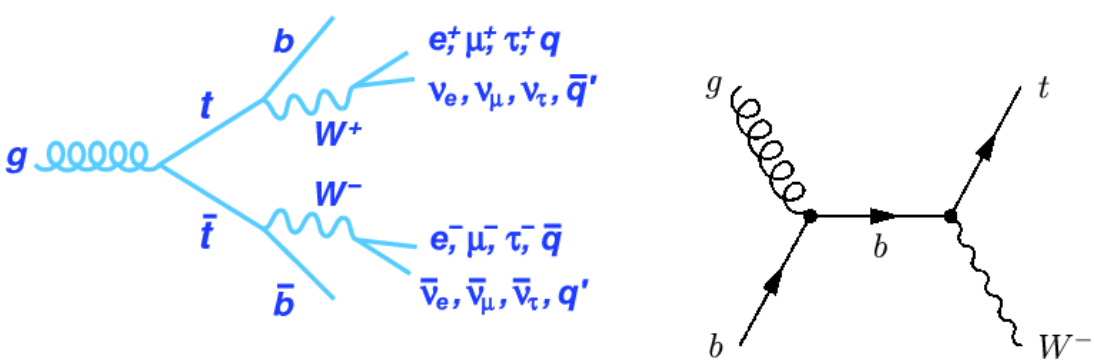

Figure 5.2: Top-quark pair production (left) and singly produced top quark in association with a W-boson.

Weak-boson backgrounds: Two charged leptons and large missing transverse energy can occur in leptonic decays of weakly produced vector-boson pairs (WW, WZ, or ZZ). The dominant contribution is coming from WW production (Fig. 5.3 left), with both bosons decaying leptonically and jets being produced in initial- and/or final-state radiation. Similar topologies can arrise also from WZ and ZZ decays (Fig. 5.3 middle). Drell-Yan and Z-boson productions in association with jets constitute a minor background in this category (Fig. 5.3 right). As events with a Z-boson decaying to two charged leptons (muons or electrons) have no genuine missing transverse energy, large E_T^{miss} in these events arrises due to mis-measurements of jet momenta. Alternatively, genuine E_T^{miss} is present in

cases where Z-boson decays to tau leptons, which, in turn, decay leptonically, producing two charged leptons and two neutrinos. $Z \to \tau\tau$ is the dominant contribution to Z+jets background in this analysis.

Weak-boson backgrounds are mainly suppressed by requiring high E_T^{miss}. Furthermore, Z+jets and DY backgrounds are brought to a negligible level by requiring that transverse mass (see Sec. 5.5.2) is above some minimum value. WW and WZ processes represent irreducible backgrounds to the analysis.

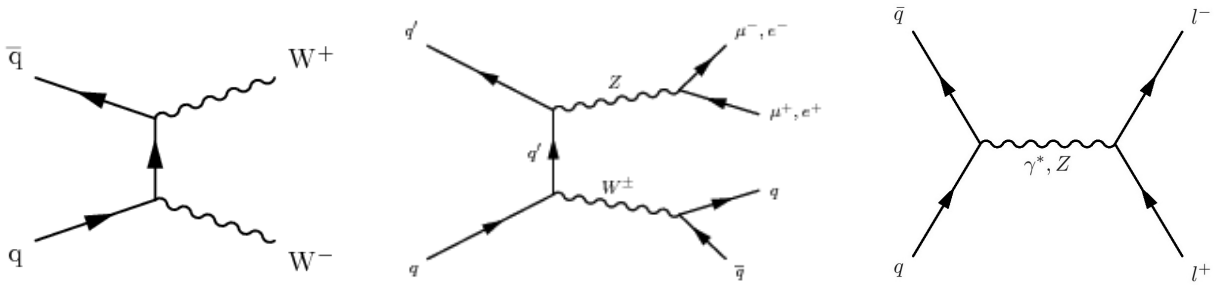

Figure 5.3: Production of a W-boson pair (left), a W- and Z-boson pair (middle) and Drell-Yan process (right).

Fake lepton background: This background consists of events with one prompt and one fake lepton. The dominant processes contributing to this category are semileptonic $t\bar{t}$ decays and W+jets production (Fig. 5.4). The misidentified lepton in $t\bar{t}$ decays in majority of cases is a product of leptonically decaying heavy-flavor hadrons present in b-jets. In W+jets events light-flavor jets also contribute as a source of misidentified leptons. Single-top production in S- and T-channels makes a minor contribution to this category.

Main discrimination variable between fake and real leptons is the isolation – a measure of activity in the calorimeters or in the inner detector inside a narrow cone around the lepton. Isolation study is described in Sec. 5.4.

5.3 Trigger

The dataset used for the analysis is collected with the missing transverse energy trigger. The trigger with the lowest E_T^{miss} threshold available throughout 2012 data-taking period has the minimum E_T^{miss} requirement set to 80 GeV at the event filter level (EF, see Sec 3.2.6)[2]. The L1 and L2 thresholds are set to 40 GeV and 45 GeV, respectively. The online calculation of

[2]The trigger is called EF_xe80_tclcw_loose where "xe80" denotes that the E_T^{miss} requirement on the EF level is set to 80 GeV, and "loose" (or alternatively "medium", "tight", etc.) refers to E_T^{miss} thresholds at L1 and L2, with "loose" denoting a trigger with lower threshold, i.e. higher efficiency.

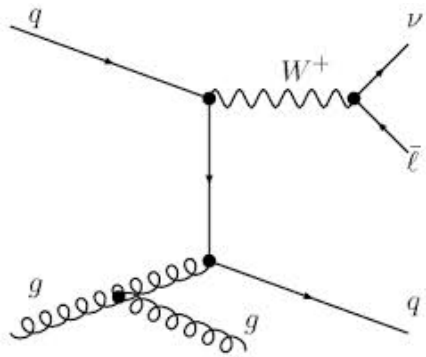

Figure 5.4: Production of a W-boson in association with jets.

E_T^{miss} is based on topological clusters with local cluster weighting ("tclcw", see Sec. 4.4.2) and contribution from muons is not taken into account.

The turn-on curve and the efficiency on the plateau of the $E_T^{\text{miss}} > 80$ GeV trigger are derived with respect to a reference single-muon trigger (with the EF threshold set at $p_T^{\mu} > 25$ GeV[3]) as a function of the offline E_T^{miss}, for both data and MC simulation of the Z+jets process. Since the online (trigger) E_T^{miss} calculation does not include the muon contribution, the turn-on curve is plotted versus offline E_T^{miss} calculated both without (Fig. 5.5) and with (Fig. 5.6) the muon term (offline E_T^{miss} used in the analysis includes the muon contribution). It can be seen that, although the shape of the turn-on curve depends on the offline E_T^{miss} definition, the point where it reaches the plateau, and the efficiency on the plateau, are independent of the offline E_T^{miss} being used. Since the trigger behaviour depends on the kinematics of the event as well, the turn-on curves are shown for two different values of jet requirements: the presence of at least one jet with $p_T > 60$ GeV or $p_T > 180$ GeV is imposed.

For both jet requirements, and regardless of the offline E_T^{miss} definition, the trigger reaches the plateau at $E_T^{\text{miss}} > 150$ GeV and is 100% efficient, for both data and MC. Thus the baseline E_T^{miss} threshold for the analysis is set to 150 GeV. Above 150 GeV the trigger is expected to collect both data and MC events with 100% efficiency in an unbiased way.

5.4 Isolation optimisation for leptons

After the basic lepton identification criteria described in Chapter 4, and refered to as the baseline selection, various isolation criteria are further imposed to select the signal leptons. Isolation is an important handle for discriminating prompt from non-prompt leptons. The former are referred to as real leptons (originating in e.g. W- or Z-boson decays, or decays of mUED particles) and are expected to be well separated from other tracks and/or energy deposits in the detector. The later are referred to also as the fake leptons and are generally

[3] EF_mu24i_tight

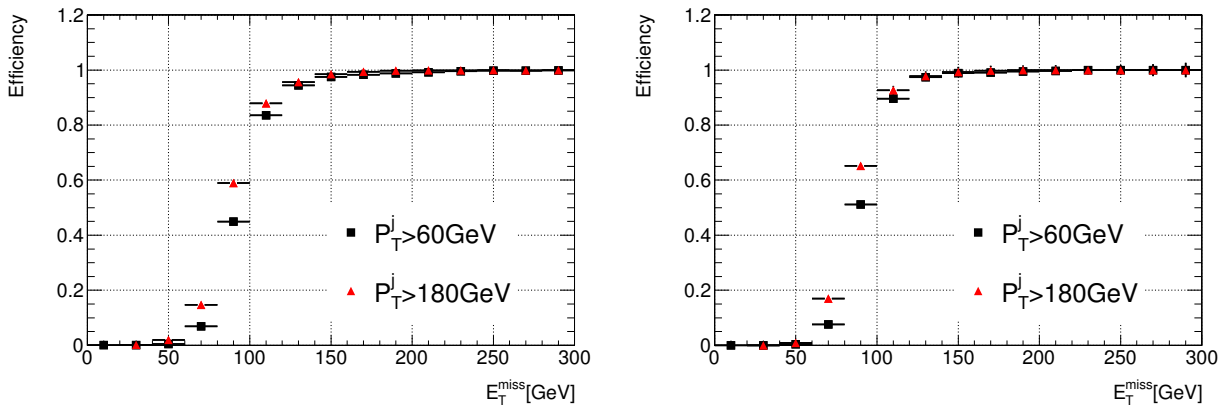

Figure 5.5: Efficiency of the $E_T^{\text{miss}} > 80$ GeV trigger for data (left) and Z+jets MC (right) with respect to the single-muon trigger, shown as a function of the offline E_T^{miss} calculated without the muon term, for two different leading jet selections.

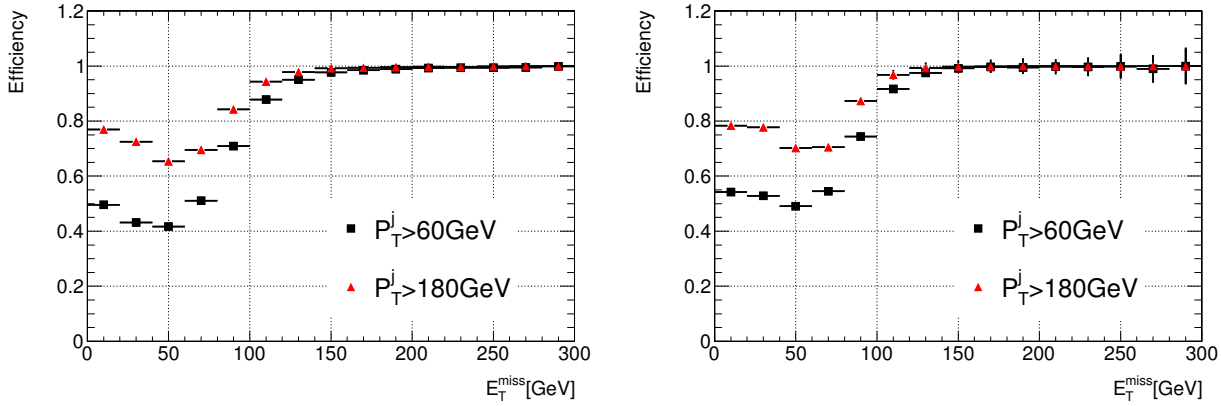

Figure 5.6: Efficiency of the $E_T^{\text{miss}} > 80$ GeV trigger for data (left) and Z+jets MC (right) with respect to the single-muon trigger, shown as a function of the offline E_T^{miss} calculated including the muon term, for two different leading jet selections.

expected to be surrounded by more of calorimetric activity and/or inner-detector tracks. The fake leptons can be divided into two (three) categories in the case of muons (electrons):

- **Leptons from hadron decays within jets:** Leptonic decays of hadrons (such as $b \to c\,\ell\,\nu$ and $c \to s\,\ell\,\nu$, where b- and c-quarks are contained inside the hadron) often produce relatively soft leptons which, being inside a jet, are usually surrounded by large hadronic activity. If, however, most of the hadron's energy is transfered to the lepton, and other hadronic particles in the jet are soft, the lepton may appear as isolated and be reconstructed as a prompt lepton. Most of the fake muons come from this category.

- **Various objects mis-reconstructed as leptons:** Charged hadrons, jets and muons may be mis-reconstructed as electrons if they leave enough energy in the EM calorimeter and/or they emit a photon before the EM calorimeter. Similarly, energetic charged hadrons may leave the dense calorimeter material reaching the muon chambers (also known as punch-through particles), and may be falsely identified as muons.

- **Conversions:** A photon undergoes an asymmetric conversion into an electron-positron pair, where one of the two picks up most of the original photon's energy and is reconstructed as an independent object in the electromagnetic calorimeter. Electrons from Dalitz decays are also considered as non-prompt.

Soft lepton regions are much more likely to be populated by a significant fraction of fake leptons. As mUED signal is characterised by soft leptons, it is important to identify the isolation definition with the optimal power of discrimination between real and fake leptons. Muons and electrons from hadron decays inside jets give the largest contribution to this analysis, among the three categories listed above. A dedicated isolation optimisation is performed in order to identify the isolation variables and their working points with the optimal performance.

5.4.1 Isolation variables

The isolation variables are based on the amount of energy flow around a lepton candidate measured by the calorimeter and the tracking. The following variables are considered:

- **Track Isolation**: ptCone30 (ptCone20) is the sum of the transverse momenta of tracks with $p_T > 400$ MeV found within a cone of radius $\Delta R = 0.3$ (0.2) around the lepton.

- **Calorimeter Isolation**: etCone30, (etCone20) is the sum of the transverse energy of topological clusters calibrated at the electromagnetic scale within the cone of radius $\Delta R = 0.3$ (0.2) around a lepton. The $\mathsf{etCone30}^{\mathsf{corr}}$ is the energy sum after applying N_{PV}-dependent correction in order to correct energy increase due to in-time pileup [4].

[4] $\mathsf{etCone30}^{\mathsf{corr}} = \mathsf{etCone30} - a \times N_{\mathrm{PV}}$, where the term a is 0.02015 (0.01794) in data (MC). It is determined based on observation that the dependency of etCone30 variable is approximately linear as a function of N_{PV}. The slope a is determined from a fit with a linear function.

In addition to the track and calorimeter based isolation variables, impact parameter (IP) constraints are also found to be useful for identifying prompt leptons. Leptons coming from hadron decays will have their track impact parameter – the distance of the closest approach of a track to the primary vertex – generally larger than the prompt-lepton IP, as non-prompt leptons are originating in secondary vertices. Both the transverse and the longitudinal IP (see Chapter 4) are considered in the optimisation.

5.4.2 Optimisation procedure

Several types of track- and calorimeter-based isolations, as well as IP parameters, are scanned in order to find values with best performance with respect to real lepton efficiency and fake lepton rejection. The optimal choice of isolation may change depending on the lepton p_T, since the relative amount of activity around the lepton with respect to its p_T will change. Furthermore, as harder leptons are less affected by the fake lepton contamination, the isolation criteria may be relaxed at higher p_T in favor of increasing the lepton acceptance. For this reason the study is done in bins of lepton p_T, with the focus being on soft leptons in $p_T < 25$ GeV region.

The isolation performance is quantified by two variables: real- and fake-lepton efficiencies. Real (fake) lepton efficiency is defined as the ratio of the number of real (fake) leptons passing the isolation criteria over the total number of real (fake) leptons in the sample, satisfying the baseline identification requirements (see Sec. 4.2 and Sec. 4.3):

$$\epsilon_{\text{real/fake}} = \frac{N^{\text{isolated}}_{\text{real/fake}}}{N^{\text{baseline}}_{\text{real/fake}}}.$$

The isolation-optimisation study is performed using Powheg+Pythia $t\bar{t}$ Monte Caro simulation. The $t\bar{t}$ events contain two b-jets and therefore provide large enough statistics of fake leptons originating from heavy-flavour decays, which are also the dominant source of fake leptons in the analysis (see Chapter 6). Leptons are classified as real or fake according to the MC truth information. Different thresholds on relative/absolute pt(et)Cones, as well as on the IP-based variables, are tested and each time ϵ_{real} and ϵ_{fake} are calculated.

Figures 5.7 and 5.9 are showing fake versus real muon and electron efficiencies for different threshold-values of track and calorimeter based isolations in three lepton-p_T bins. Both absolute and relative (with respect to the p_T) cone isolations were considered. Track isolation is found to perform better than the calo-based one, for both muons and electrons, in terms of keeping the real lepton efficiency as high as possible, while rejecting as many fakes as possible. In the case of muons, it can clearly be seen that the absolute ptCone20 isolation is the best choice for hard leptons ($p_T > 25$ GeV), while for soft leptons ($p_T < 25$ GeV) relative ptCone30 isolation performs the best. The performance of different isolation criteria for high p_T electrons is quite comparable, while for soft electrons relative ptCone30 isolation is again found to perform the best.

Similarly, figures 5.8 and 5.10 are showing fake versus real muon and electron efficiencies for

different values of the IP variables. These variables primarily reject leptons from heavy-flavour decays while keeping the real lepton efficiencies high.

5.4.3 Optimisation results and performance

Based on this study an optimal working point for each variable was chosen and three types of isolation criteria were defined: `LooseIso`, `MediumIso` and `TightIso` (see Tabs. 5.1 and 5.2). As the name suggests, the `LooseIso` imposes looser criteria thus keeping real lepton efficiency higher, while tighter criteria contained in `TightIso` definition reject more of non-prompt leptons. The Tabs. 5.1 and 5.2 also show the isolation definition existing prior to this study, referred to as the standard isolation (StdIso), which had been optimised for high-p_T leptons.

		LooseIso	**MediumIso**	**TightIso**	**StdIso**
Track iso.	**ptCone30**$/p_T$	< 0.12	< 0.12	< 0.12	**ptCone20** < 1.8 GeV
Calo iso.	**etCone30**$^{\text{corr}}/p_T$	–	–	< 0.12	–
Transv. IP	$\lvert d_0^{PV}/\sigma(d_0^{PV})\rvert$	–	< 3	< 3	–
Longit. IP	$\lvert z_0^{PV} \times \sin(\theta)\rvert$	< 0.4 mm	< 0.4 mm	< 0.4 mm	–

Table 5.1: Four different isolation criteria for muons. MediumIso is used for muons with $p_T < 25$ GeV, while for $p_T > 25$ GeV StdIso is used.

		LooseIso	**MediumIso**	**TightIso**	**StdIso**
Identification Criteria		Medium[5]	Medium	Tight	Tight
Track iso.	**ptCone30**$/p_T$	< 0.16	< 0.16	< 0.16	**ptCone20**$/p_T < 0.1$
Calo iso.	**etCone30**$^{\text{Corr}}/p_T$	-	-	< 0.18	–
Transv. IP	$\lvert d_0^{PV}/\sigma(d_0^{PV})\rvert$	–	< 5	< 5	$\lvert d_0^{PV}\rvert$ <2 mm
Longit. IP	$\lvert z_0^{PV} \times \sin(\theta)\rvert$	< 0.4 mm	< 0.4 mm	< 0.4 mm	$\lvert z_0^{PV}\rvert$ <1 mm

Table 5.2: Four different isolation criteria for electrons. MediumIso is used for electrons with $p_T < 25$ GeV, while for $p_T > 25$ GeV StdIso is used.

The performance of four types of isolation definitions (`LooseIso`, `MediumIso`, `TightIso` and `StdIso`) in terms of fake and real lepton efficiencies is shown in Figs. 5.11 and 5.12 as a function of the lepton p_T. Based on the balance between fake lepton rejection and real lepton efficiency, the following choice of isolation for this analysis has been made:

[5]The Medium and Tight electron identification criteria in this table correspond to Medium++ and Tight++ ATLAS menu employed for 2012 data.

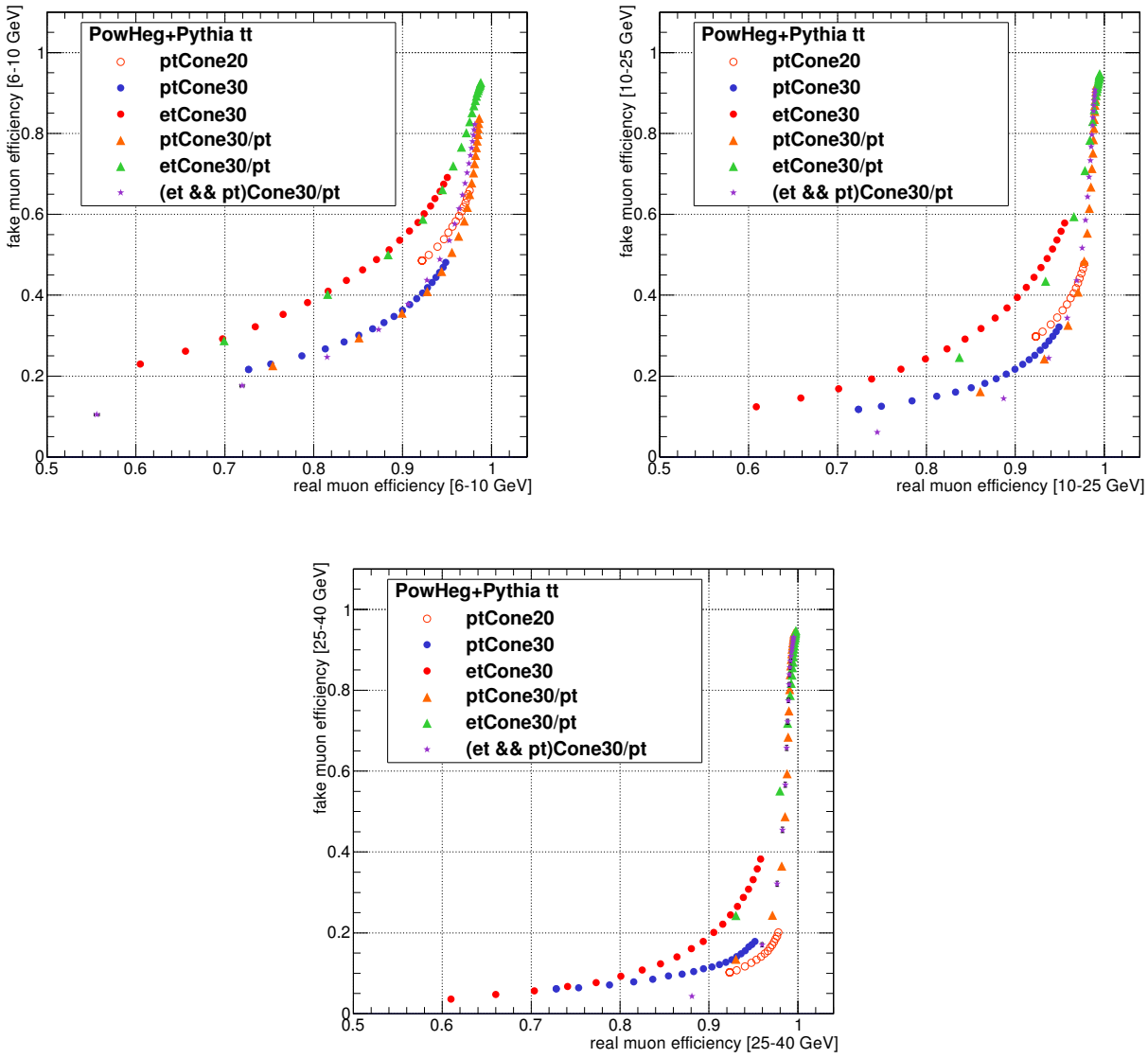

Figure 5.7: Real versus fake muon efficiencies for different values of track- and calorimeter-based isolations in three p_T bins. The efficiencies are evaluated with respect to the baseline muons. The threshold values on the relative cone isolations start from 0.06 (left-most point) and go up with the steps of 0.06. The values of the absolute cone isolations start from 0.24 GeV (left-most point) and go up with the steps of 0.12 GeV.

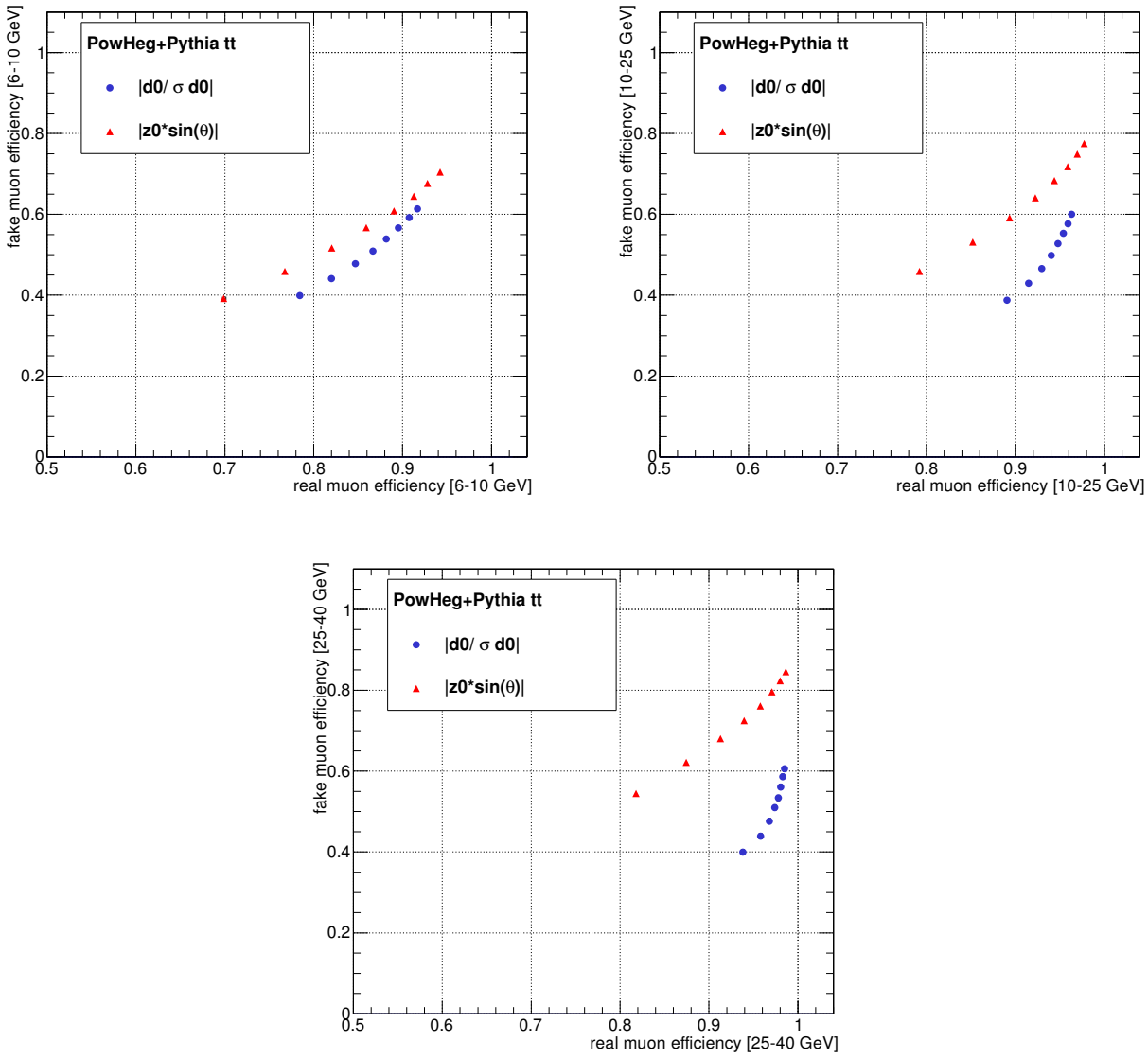

Figure 5.8: Real versus fake muon efficiencies for different values of the impact-parameter based variables in three p_T bins. The efficiencies are evaluated with respect to the baseline muons. The threshold values on the d_0^{PV} significance start from 2.2 (left-most point) and go up with the steps of 0.4. The threshold values on the $|z_0^{PV} \times \sin(\theta)|$ start from 0.08 mm (left-most point) and go up with the steps of 0.02 mm.

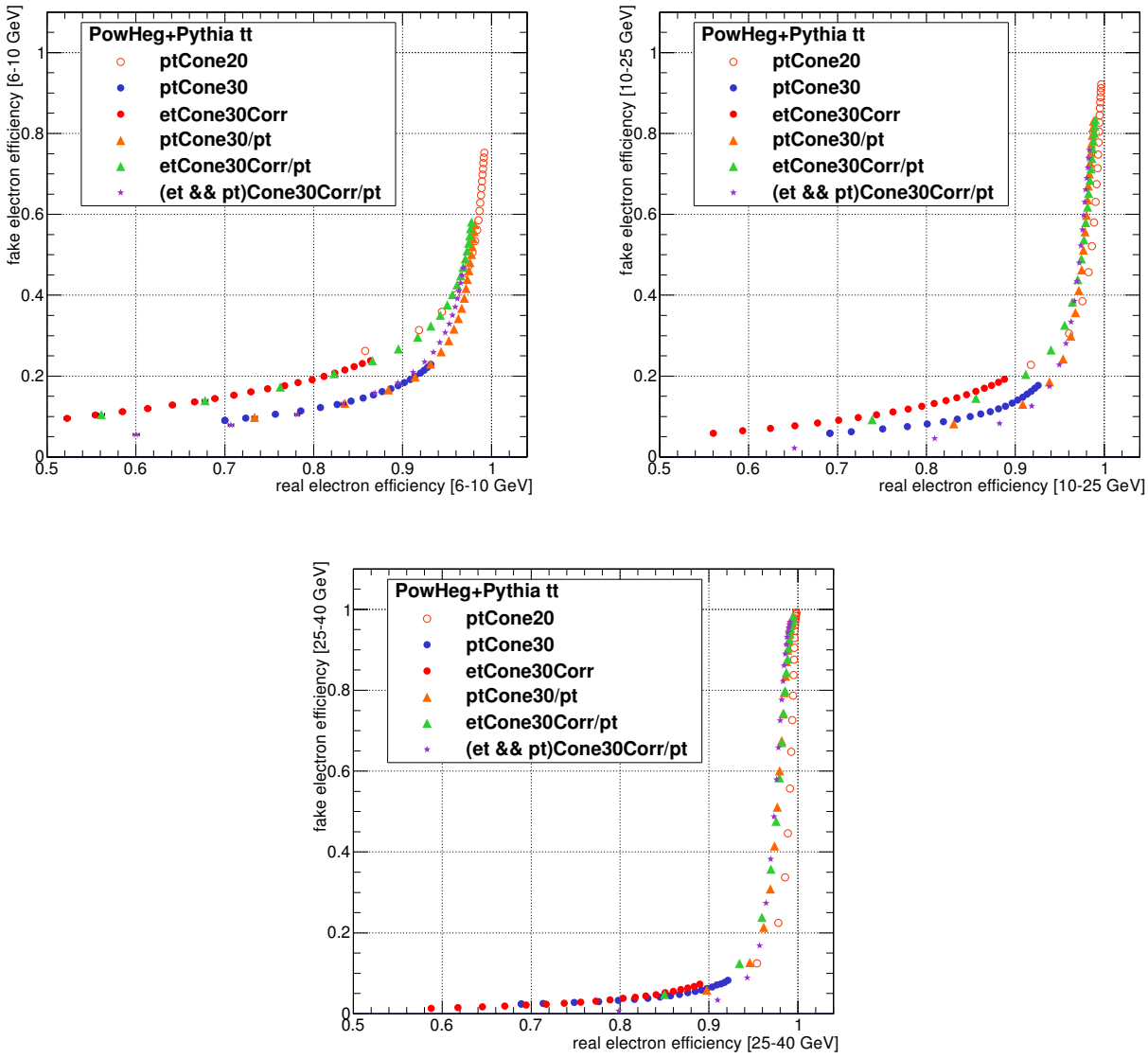

Figure 5.9: Real versus fake electron efficiencies for different values of track- and calorimeter-based isolations in three p_T bins. The efficiencies are evaluated with respect to the baseline electrons. The threshold values on the relative cone isolations start from 0.06 (left-most point) and go up with the steps of 0.06. The values of the absolute cone isolations start from 0.24 GeV (left-most point) and go up with the steps of 0.12 GeV.

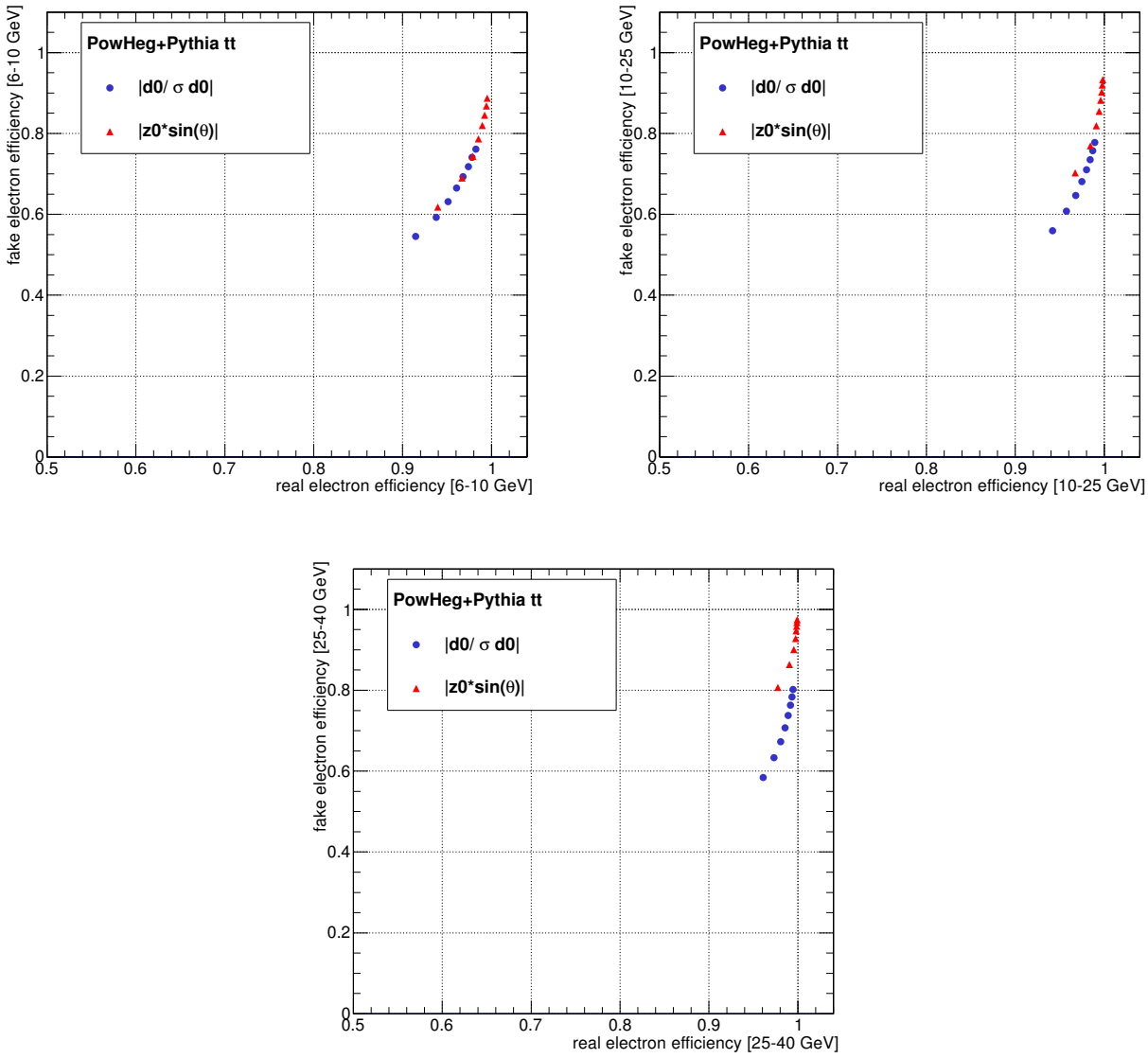

Figure 5.10: Real versus fake electron efficiencies for different values of the impact-parameter based variables in three p_T bins. The efficiencies are evaluated with respect to the baseline electrons. The threshold values on the d_0^{PV} significance start from 4.2 (left-most point) and go up with the steps of 0.8. The threshold values on the $|z_0^{PV} \times \sin(\theta)|$ start from 0.22 mm (left-most point) and go up with the steps of 0.06 mm.

- **MediumIso** for leptons $p_T < 25$ GeV
- **StdIso** for leptons $p_T > 25$ GeV

The improvement in terms of fake lepton rejection can clearly be seen for low p_T muons – the fake efficiency is reduced from the level of 50%-70% (StdIso) down to the level of 20%-30% (MediumIso) for very soft muons ($p_T < 15$ GeV). The 50% reduction of the fake muon efficiency in the whole $p_T < 25$ GeV range is of significant importance for controlling the fake-muon background. For hard muons ($p_T > 25$ GeV) the standard isolation performs better both in terms of fake lepton rejection and real lepton efficiency. Similar observation can be made for the electron case – the medium isolation results in about 30% reduction of the fake electron efficiency, with respect to the standard isolation. The improvement with MediumIso is more visible when looking at real electron efficiencies - for electrons $p_T < 15$ GeV the efficiency is increased from 75%-80% (StdIso) to 90% (MediumIso) level. Keeping the signal lepton efficiencies high is another important factor for enhancing the sensitivity to new physics signals producing soft leptons. Even though the plateau of the real electron efficiency when using StdIso is only at 85% level (mainly due to tightness of Tight identification criteria), due to harmonisation efforts among soft and hard lepton analyses [6], the decision to use the standard isolation for electrons with $p_T > 25$ GeV was made.

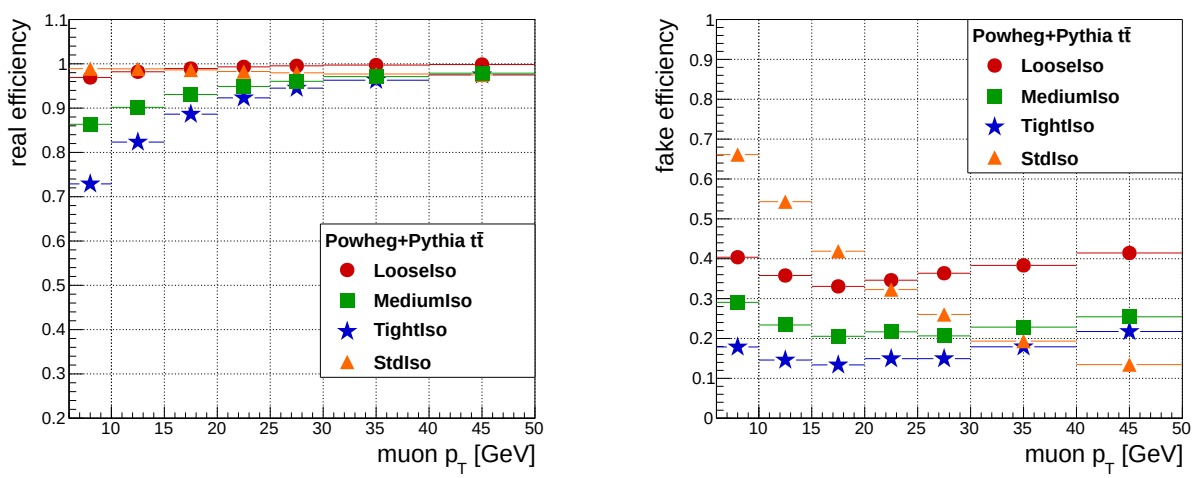

Figure 5.11: Muon real and fake efficiencies for different isolation criteria as functions of the lepton p_T. Truth information in $t\bar{t}$ MC is used to classify leptons as real or fake. No kinematic selection is imposed. Statistical uncertainty is included, but smaller than the marker size.

[6] Since soft and hard lepton analyses are joined in one publication, it is desirable to keep the basic object definitions and general flow of the analysis the same for the sake of simplicity, unless there is a strong physical reason not to.

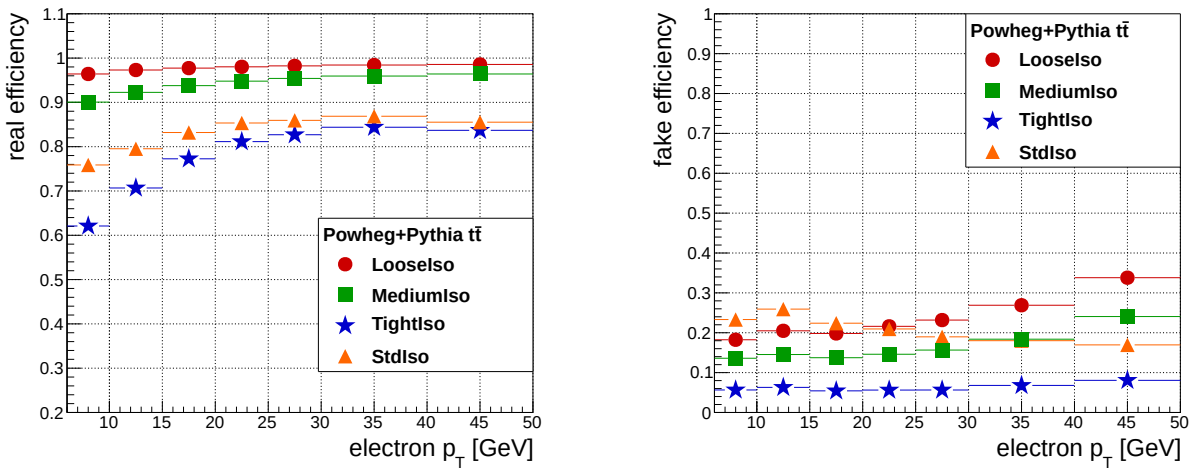

Figure 5.12: Electron real and fake efficiencies for different isolation criteria as functions of the lepton p_T. Truth information in $t\bar{t}$ MC is used to classify leptons as real or fake. No kinematic selection is imposed. Statistical uncertainty is included, but smaller than the marker size.

In order to verify the choice of isolation, sensitivity to the mUED signal was tested in a simplified way. Firstly, only $t\bar{t}$ MC was taken as a background source – it is assumed that the $t\bar{t}$ process is the dominant source of both real- and fake-leptons in the analysis. Secondly, the event selection was briefly optimised to enhance the signal over background ratio using the simple significance formula, $S/\sqrt{B + (0.3B)^2}$, where B corresponds to the number of $t\bar{t}$ events predicted by the Monte Carlo simulation, and the uncertainty on the MC $t\bar{t}$ estimate is taken to be 30%. This uncertainty of 30% was assumed to cover all experimental uncertainties that will be addressed exactly later in the analysis, as well as the potential difference between the MC and semi-data driven $t\bar{t}$ predictions. The preliminary signal region was defined as:

- Lepton selection: $N^{\text{lep}} \geq 2$ (of the same flavor), $6 < p_T^{\text{lep}} < 25$ GeV
- Jet selection: $N^{\text{jet}} \geq 2$, $p_T^{\text{jet}} > 25$ GeV, $p_T^{\text{leading jet}} > 100$ GeV
- Missing energy selection: $E_T^{\text{miss}} > 200$ GeV, $E_T^{\text{miss}}/m_{\text{eff}} > 0.3$

This signal-region-like selection was used to asses the impact of different isolation criteria on the amount of background events and signal efficiency. The signal region was later carefully re-optimised (see Sec. 5.5 below) by properly taking into account all the backgrounds and other effects. The result is shown in Figures 5.13 and 5.14. When going from MediumIso to StdIso the sensitivity increases for both dimuon and dielectron channels. In both channels the 95% CL exclusion reach is extended by about 100 GeV in 1/R. The improvement is the result of two effects – better rejection of fake leptons while keeping the prompt-lepton efficiency as high as possible.

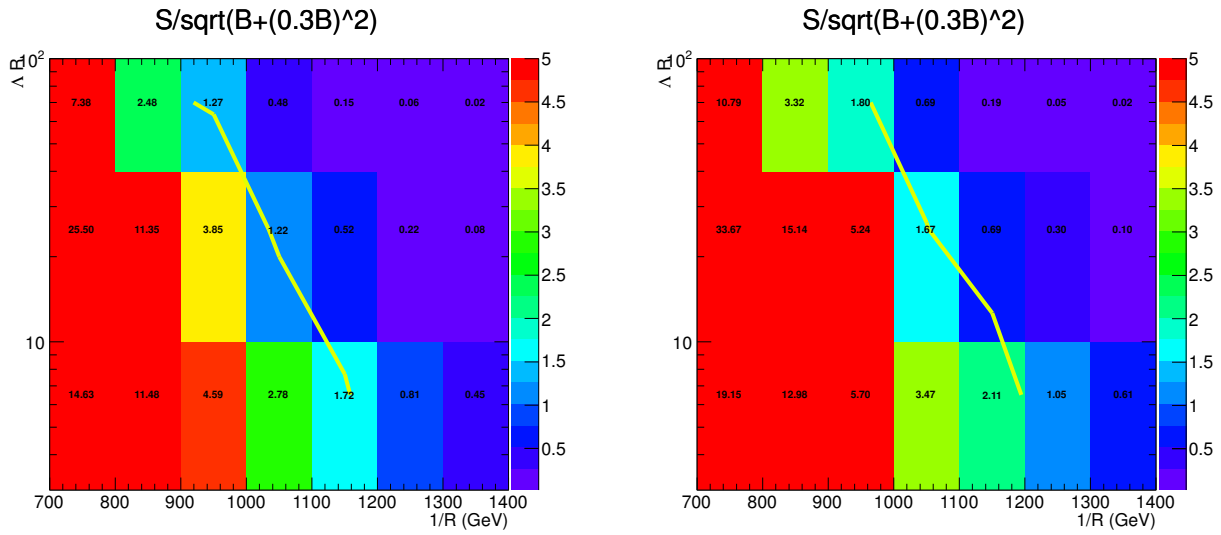

Figure 5.13: The sensitivity with the preliminary signal-region-like selection in the dimuon channel as a function of the muon isolation. The numbers in the plot are showing the significance at each signal point and the yellow line indicates the exclusion reach at 95% CL. The $t\bar{t}$ MC sample was considered as the only source of background. Left: StdIso. Right: MediumIso. Improvement in going form the StdIso to MediumIso can clearly be seen.

5.5 Signal region optimisation

The kinematic selection for the signal region was optimised so as to reject the Standard Model backgrounds as much as possible, while keeping the signal acceptance as high as possible. All the SM backgrounds considered in the main analysis have been taken into account while performing the optimisation. Monte Carlo simulations have been used for all the processes: top-quark pair production ($t\bar{t}$), singly-produced top-quark (single top), top-quark pair production in association with vector bosons ($t\bar{t}$+V), Z-boson production in association with jets (Z+jets), production of two vector bosons (dibosons), Drell-Yan process (DY) and the fake-lepton background. To avoid the effects of statistical fluctuations due to a limited number of generated MC events, the optimisation was performed by requiring a minimum of 5 background events in the signal region and by requiring the MC statistical error on signal models close to the sensitive region to be less than 50%. The total background systematic uncertainty was assumed to be 30%.

5.5.1 Figure of merit

The expected sensitivity in the final result is calculated with the full analysis setup (taking into account exact systematic and statistical uncertainties) using a CLs approach [115]. As this

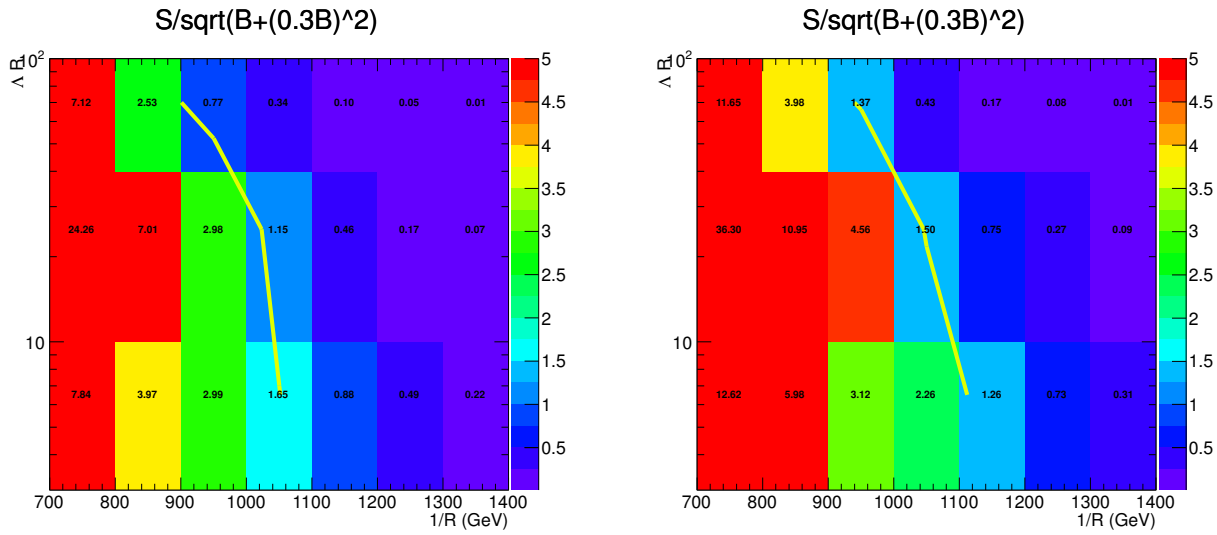

Figure 5.14: The sensitivity with the preliminary signal-region-like selection in the dielectron channel as a function of the electron isolation. The numbers in the plot are showing the significance at each signal point and the yellow line indicates the exclusion reach at 95% CL. The $t\bar{t}$ MC sample was considered as the only source of background. Left: StdIso. Right: MediumIso. Improvement in going form the StdIso to MediumIso can clearly be seen.

procedure takes time, and is intensive from the computing point of view, a simplified approach is used when computing the sensitivity with the purpose of optimising the signal region selection.

Both signal (n_S) and background (n_B) number of events in the signal region are expected to follow a Poisson probability with mean μ_S and μ_B, respectively. Consequently, the total number of observed events (n_{obs}) is also a Poisson-distributed variable with the mean $\mu_{obs} = \mu_S + \mu_B$. When computing the expected sensitivity, μ_S and μ_B, are taken from a MC simulation (or, alternatively, data-driven estimation, see above), and n_{obs} is assumed to be equal to μ_B.Sensitivity to a particular signal model yielding n_S number of events is characterised by a Z-score value (or significance) – number of standard deviations in a 1-sided Gaussian significance level. It can be calculated by using the inverse of the error function as

$$Z = \sqrt{2}\mathrm{erf}^{-1}(1 - p), \tag{5.1}$$

where p is the p-value of the s+b hypothesis [107] - a probability to obtain a result at least as extreme as the observed one (n_{obs}), under the assumption of s+b hypothesis. Small p-value characterises small compatibility of observed data with the hypothesis being tested. The signal model is considered excluded if p-value equals to 5% (95% confidence level (CL) exclusion). This, in turn, corresponds to a Z-score value of 1.64. To compute the significance in equation 5.1, the calculated p-value is multiplied by a factor two – by doing this we approximate the CLs procedure and obtain a more realistic (and conservative) result.

5.5.2 Kinematic variables

Several kinematic variables are defined to help isolate specific background processes or enhance the signal over background ratio in the signal region.

Transverse mass The transverse mass (m_T) is defined as,

$$m_T = \sqrt{2 \cdot p_T^{\ell} \cdot E_T^{\text{miss}} \cdot (1 - \cos(\Delta\phi(\ell, E_T^{\text{miss}})))},$$

where the leading lepton p_T and ϕ are used unless otherwise specified. It is used to characterise the mass of a leptonically decaying W boson – the m_T distribution of W-events exhibits a Jacobian peak at 80 GeV. Since no information on longitudinal components of neutrino momenta is available, only the transverse information is used in the calculation. On the other hand, multi-jet events containing fake leptons will typically have small transverse mass, so applying a lower bound on m_T can be effective in reducing this type of background.

Effective mass The scalar sum of transverse momenta of jets, leptons and E_T^{miss} in the event is called the 'effective mass', m_{eff}:

$$m_{\text{eff}} = \sum p_T^{\text{jet}} + p_T^{\ell_1} + p_T^{\ell_2} + E_T^{\text{miss}}, \tag{5.2}$$

where the sum goes over all the signal jets ($p_T > 25$ GeV) present. The effective mass m_{eff} often has good relation to the mass of initially produced heavy particles and can be good discriminating variable between signal and backgrounds, especially if signal is characterised by greater number of jets.

Minimum ΔR between a lepton and jets The minimum angular separation between a lepton and jets is calculated as

$$\Delta R_{\text{min}}^{j,\ell} = \min\left[\sqrt{\Delta\phi(\text{jet}_i,\text{lep}_2)^2 + \Delta\eta(\text{jet}_i,\text{lep}_2)^2}\right], \tag{5.3}$$

where the subscript i goes over all jets with $p_T > 20$ GeV in the event and lep_2 referrs to the second leading lepton in the event. The $\Delta R_{\text{min}}^{j,\ell}$variable is calculated with the subleading lepton, unless noted otherwise. As fake leptons (e.g. decay products of heavy-flavor hadrons in a jet) tend to be close to a jet, placing a lower threshold on $\Delta R_{\text{min}}^{j,\ell}$ may reduce this type of background. Alternatively, as prompt lepton identification efficiency is sensitive to the hadronic activity inside a cone around the lepton, requiring a minimum $\Delta R_{\text{min}}^{j,\ell}$ separation reduces the dependency of the prompt lepton efficiency on the jet activity in the event.

The distributions of m_T, m_{eff} and $\Delta R^{j,\ell}_{\text{min}}$ are shown in Fig. 5.15 for all the SM backgrounds and three mUED signal benchmark points. The signal points are characterised by two parameters (R^{-1} [GeV] and ΛR) which are quoted in parentheses inside the legends of these and all subsequent figures. It can be seen that the fake lepton background tends to have low values of m_T and $\Delta R^{j,\ell}_{\text{min}}$, while m_{eff} shows discrimination power between the signal and the $t\bar{t}$ background. Additionally, large portion of Z+jets background can be rejected by imposing a minimum requirement on m_T.

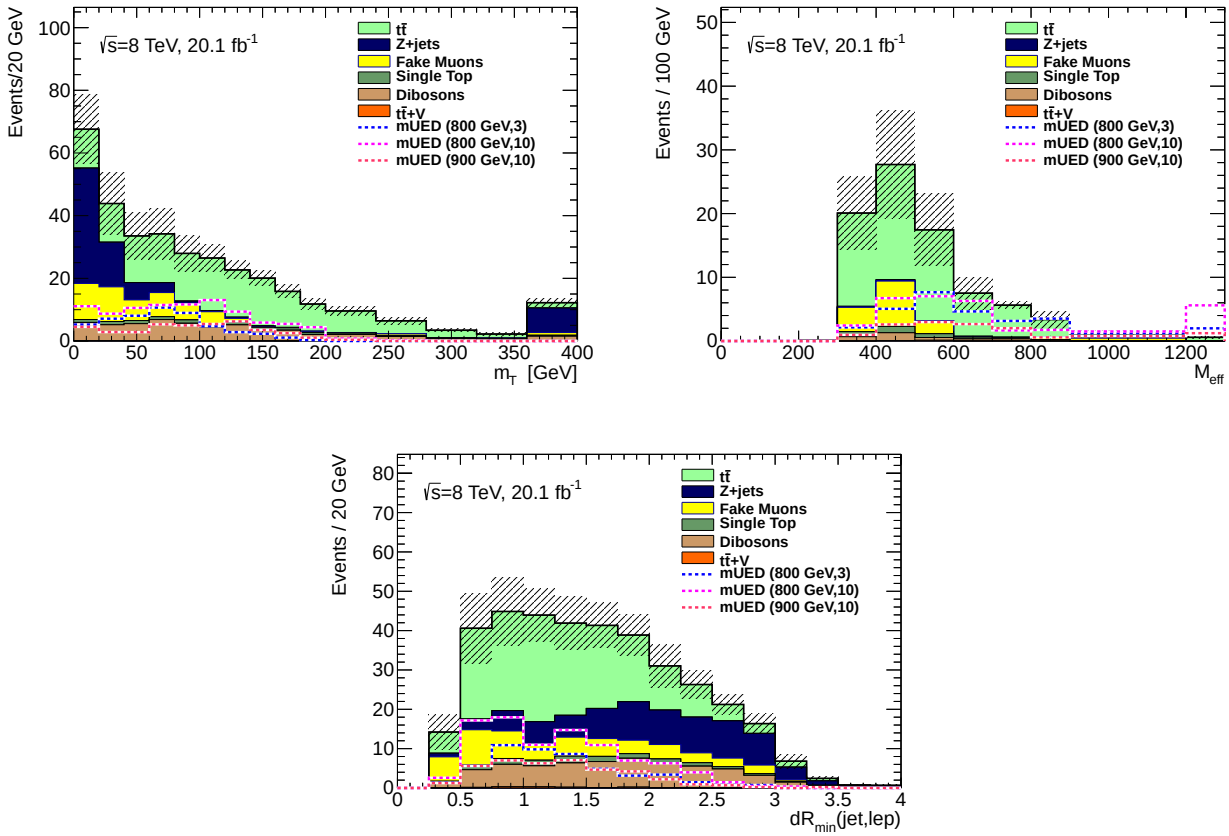

Figure 5.15: Distributions of m_T, M_{eff} and $\Delta R^{j,\ell}_{\text{min}}$ in the dimuon channel for backgrounds and three mUED signal models close to the final signal-region selection (see Tab. 5.3). For m_T and $\Delta R^{j,\ell}_{\text{min}}$ distributions the following selection is made: all the baseline selection requirements (see Sec. 5.5.3) except $\Delta R^{j,\ell}_{\text{min}} > 1$, on top of which $p_{\text{T}}^{\text{1st-jet}}$ >80 GeV and no b-jets among 3 leading jets are requirements added. For m_{eff} distribution $p_T^{\mu_1} < 25$ GeV and $m_T > 40$ GeV are added on top of the baseline selection. Fake lepton background is estimated with the data-driven method (see Sec. 6.1) and pure MC-based prediction is shown for all other backgrounds. The errors are statistical only.

5.5.3 Selection optimisation scan

The selection optimisation starts from a set of baseline requirements defined based on the target signal characteristics and several experimental constraints:

- exactly 2 OSSF leptons, $p_T^{\mu} > 6$ GeV, $p_T^{e} > 7$ GeV
- $E_T^{\text{miss}} > 150$ GeV
- $N_{\text{jets}}(p_T^{\text{jet}} > 25\text{GeV}) \geq 2$
- $M_{\ell\ell} > 15$ GeV; $|M_{\ell\ell} - M_Z| > 10$ GeV
- $\Delta R_{\text{min}}^{j,\ell} > 1$

Exactly two muons or electrons are required with the minimum p_T needed for a reliable reconstruction (Sec. 4.2 and Sec. 4.3). The E_T^{miss} threshold is set to 150 GeV which corresponds to the E_T^{miss} trigger plateau, and so eliminates any possible bias due to the trigger. At least two jets with $p_T > 25$ GeV are required since the signal is expected to produce several moderate-p_T jets. The threshold of 25 GeV corresponds to the lowest p_T required to reconstruct and calibrate jets reliably, avoiding the pile-up effects. The lower bound on the di-lepton invariant mass is placed at 15 GeV to avoid the low-mass resonances, as well as the lack of generated MC events for low-mass DY and Z+jets processes. The veto on the invariant mass within 10 GeV of the Z-boson mass is very efficient in eliminating large part of the background due to Z-boson production. The minimum $\Delta R_{\text{min}}^{j,\ell}$ requirement is placed at one to avoid any topology dependency of prompt and fake lepton efficiencies (as discussed in Sec. 6.1).

On top of the baseline selection, various threshold values of other kinematic variables have been scanned to find the optimal operating points (see Tab. 5.3).

Variable	Considered thresholds	Optimal threshold
E_T^{miss}	$>$ 160, 170, 180, 190 GeV	$>$ 180 GeV
$p_T^{j_1}$	$>$ 60, 80, 100 GeV	$>$ 80 GeV
$p_T^{j_2}$	$>$ 25, 35, 40 GeV	$>$ 25 GeV
$p_T^{j_3}$	no requirement, $>$ 25, 35 GeV	no requirement
$N_{\text{b-jets}}$	no requirement, b-jet veto	b-jet veto
$E_T^{\text{miss}}/\ m_{\text{eff}}$	$>$ 0, 0.3	$>$ 0.3
$p_T^{\ell_1,\ell_2}$	no requirement, $<$ 20, 25, 30 GeV	$<$ 25 GeV
$M_{\mu\mu}$	no requirement, $<$ 40, 60, 80, 110 GeV	$<$ 60 GeV
$m_T^{\ell_1}$	$>$ 0, 20, 40, 50, 60, 80, 100 GeV	$>$ 40 GeV
$m_T^{\ell_2}$	$>$ 0, 20, 40, 50, 60, 80, 100 GeV	$>$ 0 GeV

Table 5.3: The list of the kinematic variables used in the optimisation procedure, along with the considered and optimal threshold values.

The optimisation was first performed in the dimuon channel, and then the same selection was applied to the dielectron channel. The distributions of the variables listed in Tab. 5.3 are shown in Figs. 5.16 and 5.17 for all the SM backgrounds and three mUED signal benchmark points.

From Figure 5.16 it can be seen that the signal concentrates on low values of muon p_T and $M_{\mu\mu}$. By applying $p_T^{\mu_1,\mu_2} < 25$ GeV the total background is reduced by about 90%, while the signal acceptance remains constant for $\Lambda R \sim 5$ points and gets smaller by up to 80% for large mass-splitting ($\Lambda R \sim 40$) models (see Tab. 5.5). By additionally applying an upper bound on the dilepton invariant mass of 60 GeV, the signal acceptance remains unchanged, while some of the backgrounds can be further suppressed.

Figure 5.17 is showing E_T^{miss} and number of b-jets distributions. As expected, the background falls-off quickly towards higher E_T^{miss} values, while the signal spectrum is much flatter, with higher E_T^{miss} thresholds always resulting in the increased sensitivity. Thus the E_T^{miss} requirement was placed as high as possible, while still retaining the minimum of five background events in the signal region. Number of b-jets distribution shows that the signal peaks at 0 b-jets, while the dominant $t\bar{t}$ background naturally peaks at higher b-jet multiplicities. Even though the presence of only two jets is explicitly imposed, when calculating $N_{\text{b-jets}}$ the three leading jets are considered in order to increase the efficiency of tagging $t\bar{t}$ events – if the leading jet is an ISR jet (in most cases it would be a gluon-jet), the two b-jets from top-quark decays are expected to be the 2nd and 3rd most energetic jets in the event. By placing a b-jet veto in the signal region, $t\bar{t}$ background is reduced by a large factor ($\sim 85\%$, see Tab. 5.4), while the signal acceptance is kept high.

Number-of-jets distribution (Figure 5.16 bottom left) for signal points with larger mass-splitting (ΛR $\sim$ 10) peaks at 3 jets, but smaller mass-splitting signal points (ΛR $\sim$ 3) have rather flat distribution. No requirement on 3rd jet was imposed to keep the good acceptance for small ΛR points. Finally, the ratio of E_T^{miss} to m_{eff} is found to be a useful discriminant between the background and the signal (Figure 5.16 bottom right). The signal has higher contribution of E_T^{miss} to the total effective mass than most of the backgrounds processes. Placing the lower threshold on $E_T^{\text{miss}}/m_{\text{eff}}$ at 0.3 was found to increase the sensitivity for small mass-splitting mUED models.

During the optimisation procedure, the sensitivity is assessed by looking at the expected significance in the 1/R – ΛR plane. Figure 5.18 is showing the increase in the expected sensitivity achieved when gradually applying the signal-region defining requirements. Figure 5.19 is showing the expected sensitivity with the final signal-region selection in the dimuon (left) and the dielectron (right) channels. The sensitivity in the dielectron channel is much smaller than the dimuon-channel sensitivity. The reason is lower reconstruction and identification efficiencies of soft electrons, with respect to muons. As no significant improvement is expected even with the combination of the two channels, the analysis was performed in the dimuon channel only. The number of background, data and signal events remaining after applying each of the signal-region selection requirements are shown in Tab. 5.4 and 5.5.

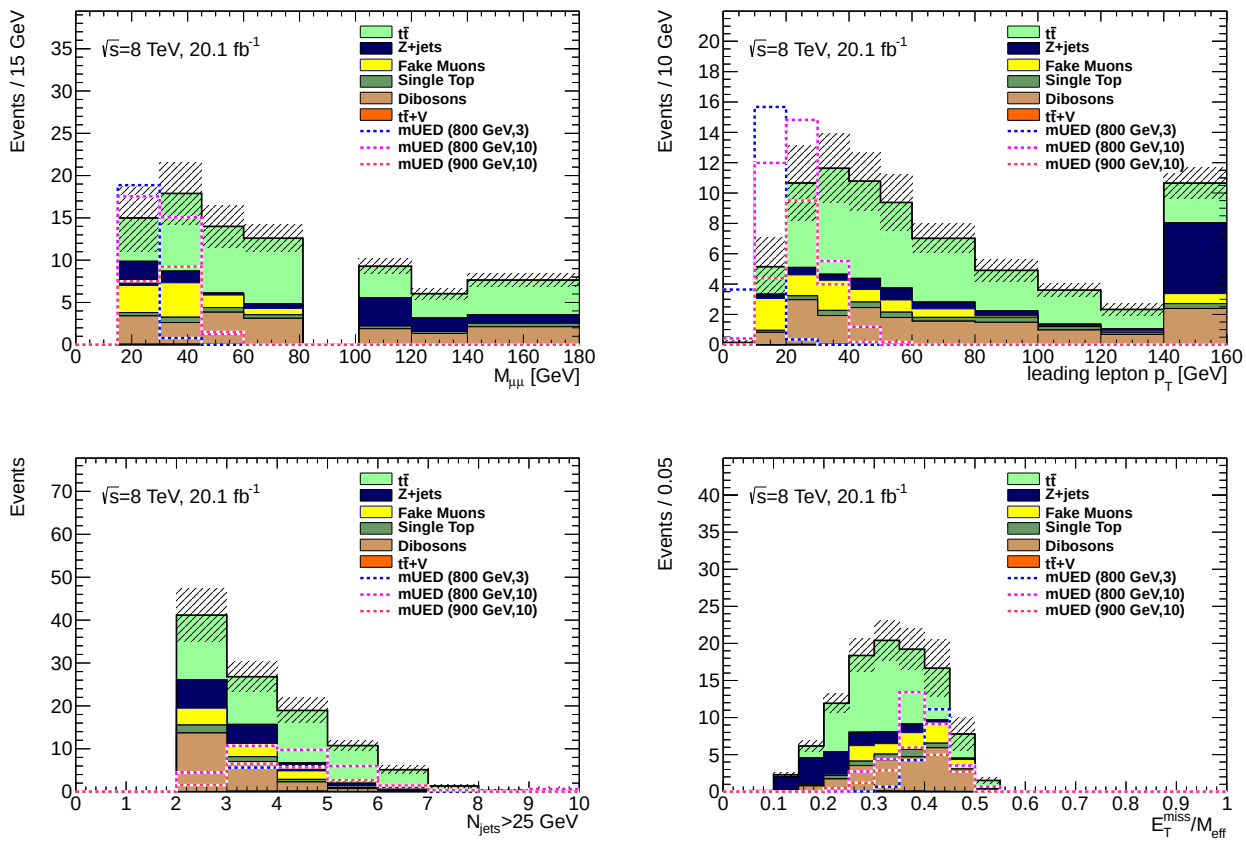

Figure 5.16: Distributions of (from top left) di-muon invariant mass, leading muon p_T, number of jets with p_T >25 GeV and $E_T^{\text{miss}}/\ m_{\text{eff}}$ in the dimuon channel for backgrounds and three mUED signal models close to the final signal-region selection (see Tab. 5.3). In addition to applying the baseline selection, the following selection is added: E_T^{miss} >180 GeV, $p_{\text{T}}^{\text{1st-jet}}$ >80 GeV, $m_T^{\mu 1}$ >40 GeV and no b-jets among 3 leading jets. Fake lepton background is estimated with the data-driven method (see Sec. 6.1) and pure MC-based prediction is shown for all other backgrounds. The errors are statistical only.

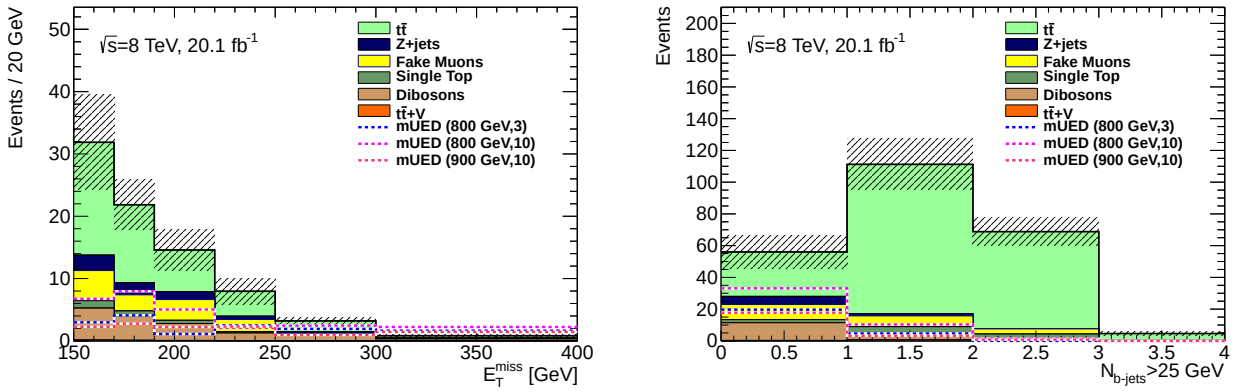

Figure 5.17: Distributions of E_T^{miss} and number of b-jets in the dimuon channel for backgrounds and three mUED signal models close to the final signal-region selection (see Tab. 5.3). In addition to applying the baseline selection, the following selection is added: $p_T^{\mu_2} < 25$ GeV, $p_{\text{T}}^{\text{1st-jet}} > 80$ GeV, $m_T^{\mu 1} > 40$ GeV. Additionally, no b-jets among 3 leading jets was required for the E_T^{miss} plot (left), and requirement on E_T^{miss} was tightened to $E_T^{\text{miss}} > 180$ GeV for $N_{\text{B-jets}}$ distribution (right). Fake lepton background is estimated with the data-driven method (see Sec. 6.1) and pure MC-based prediction is shown for all other backgrounds. The errors are statistical only.

	Backgrounds					
Selection	$t\bar{t}$	t	Dibosons	Fake lep.	Z+DY	$t\bar{t}$+V
trigger + OS μ	10580±20.94	1079.4±2.79	1144.67±8.224	0±97.66	229680±472.8	69.7574±0.6528
$E_T^{\text{miss}} > 180$ GeV	548±4.8	60.9±0.67	103±2.5	86.6±8.7	105±5.1	7.12±0.21
$N_{\text{jets}}(p_T > 25) \geq 2$	502.1±4.6	51.8±0.62	66.6±2	68.2±7.8	74.5±4.2	7±0.2
$p_{T,\text{jet1}} > 80$ GeV	479.7±4.5	50±0.61	64.9±2	64.7±7.6	73.8±4.2	6.82±0.2
$M_{\mu\mu} > 15$, $\lvert M_{\mu\mu} - M_Z \rvert > 10$	410.1±4.1	43.3±0.56	44.4±1.7	56.3±6.8	52.9±2.1	5.2±0.18
$\Delta R_{\text{min}}^{j,\ell} > 1$	267.5±3.3	30.8±0.48	35.9±1.5	33.7±5.4	46.5±1.9	3.13±0.14
$p_T^{\mu 1} < 25$ GeV	22.83±0.99	1.88±0.12	2.73±0.41	12.2±3.1	1.48±0.41	0.235±0.036
b-veto	3.331±0.38	0.339±0.051	2.43±0.39	6.35±2	1.46±0.41	0.0183±0.0084
$M_{\mu\mu} < 60$	2.931±0.36	0.308±0.049	1.95±0.33	6.09±1.9	1.46±0.41	0.0183±0.0084
$m_T^{\mu 1} > 40$ GeV	2.336±0.32	0.252±0.044	1.49±0.28	2.89±1.4	0.493±0.25	0.0153±0.0081
$E_T^{\text{miss}}/m_{\text{eff}} > 0.3$	1.795±0.28	0.238±0.042	1.37±0.27	2.34±1.2	0.278±0.2	0.00499±0.005

Table 5.4: Number of different background events remaining in the dimuon channel after the selection requirements are added one by one. The errors are statistical only. The $t\bar{t}$ sample is normalised to the data (see Sec. 6.2), fake lepton background is estimated by the data-driven method (see Sec. 6.1) and pure MC-based prediction is shown for other backgrounds.

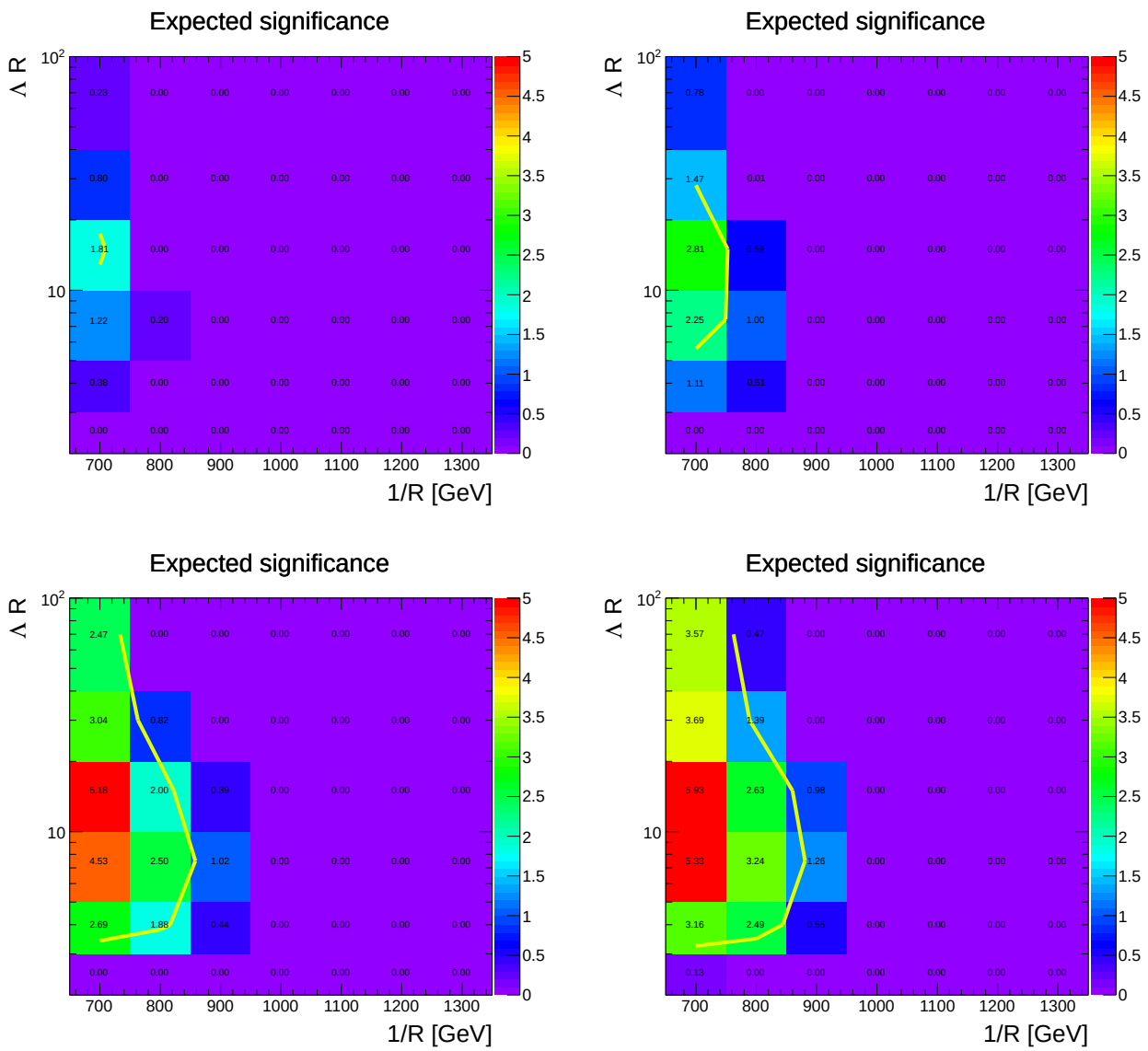

Figure 5.18: The increase in the expected significance in the dimuon channel when going closer to the signal region. In all four plots $p_T^{\mu_1,\mu_2} < 25$ GeV and $p_T^{1\mathrm{st-jet}} > 80$ GeV are applied in addition to the baseline selection. Further requirements are added on top of the previous selection: E_T^{miss} is raised to 180 GeV in the top right plot, b-jet veto is imposed additionally in the bottom left plot, and $m_T > 40$ GeV and $M_{\ell\ell} < 60$ GeV are added in the bottom right case. The yellow line connects the points with significance of 1.64, i.e. it corresponds to the expected 95% CL exclusion reach.

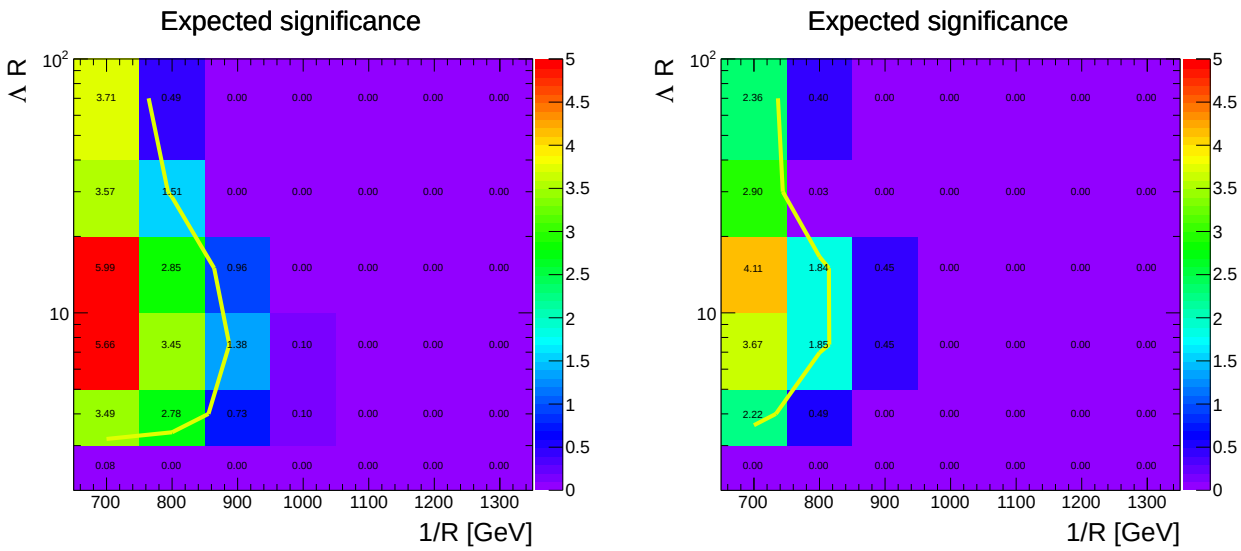

Figure 5.19: Expected significance in the signal region (see right-most column of the Tab. 5.3) of the dimuon (left) and dielectron (right) channels. The yellow line connects the points with significance of 1.64, i.e. it corresponds to the expected 95% CL exclusion reach.

	Background	Data	Signal $(R^{-1}, \Lambda R)$		
Selection	Total exp.	Obs.	(800,3)	(800,10)	(800,40)
trigger + OS μ	242554±483.3	214053±462.7	240±11	346±13	352±11
E_T^{miss} >180 GeV	911.12±11	888±30	101±7.3	109±7.3	112±6
$N_{\text{jets}}(p_T > 25) \geq 2$	770.32±10	773±28	89±6.9	108±7.3	110±6
$p_{T,\text{jet1}} > 80$ GeV	740±10	739±27	87.7±6.8	106±7.2	106±5.9
$M_{\mu\mu}$ >15, $\lvert M_{\mu\mu} - M_Z \rvert$ >10	612±8.4	611±25	48.2±5.1	91±6.7	96.8±5.6
$\Delta R_{\text{min}}^{j,\ell}$ >1	418±6.8	397±20	32±4.2	59.5±5.4	56.7±4.2
$p_T^{\mu 1}$ <25 GeV	41.3±3.3	0±0	32±4.2	33.7±4	11.4±1.8
b-veto	13.9±2.1	0±0	24.4±3.6	25.8±3.4	7.83±1.5
$M_{\mu\mu}$ <60	12.8±2	0±0	24.4±3.6	25.8±3.4	7.83±1.5
$m_T^{\mu 1}$ >40 GeV	7.48±1.4	0±0	19.7±3.3	20.8±3.1	6.84±1.4
$E_T^{\text{miss}}/m_{\text{eff}}$ >0.3	6.03±1.3	0±0	19.6±3.3	20.2±3	6.17±1.3

Table 5.5: Number of total background events, data and signal events remaining in the dimuon channel after the selection requirements are added one by one. The errors are statistical only. The data are blinded after $\Delta R_{\text{min}}^{j,\ell} > 1$ requirement.

Chapter 6

Background estimation

Three different background prediction methods are used to estimate the contribution of the Standard Model backgrounds to the signal region.

The fake muon background is one of the dominant processes contributing to the signal region and is estimated in a fully data-driven way by the, so called, matrix method. Another major background, the top-quark pair production is estimated with a semi data-driven method. The shapes of various kinematic distributions are taken from the Monte Carlo simulation, and it is expected that Monte Carlo describes these well. The overal normalisation of the $t\bar{t}$ MC is derived with the profile-likelihood fit to the data in the dedicated control region. The matrix method is explained in Sec. 6.1, while the overal procedure of the background fit and the choice of the control and validation regions are presented in 6.2. The details of the fit are described in the next Chapter 7.

Other minor backgrounds (dibosons, single-top production in association with W- or Z-boson, $t\bar{t}$ production in association with weak bosons, Z+jets and Drell-Yan processes) are estimated by using purely Monte Carlo-based predictions.

6.1 Fake muon background

6.1.1 Matrix-method

The fake lepton background is estimated in a fully data-driven way, by the, so called, matrix method. The method is based on inverting the lepton isolation and looking into both the number of signal leptons (the ones passing the required isolation and denoted as N_T, where "T" stands for tight) and into the number of leptons which pass the baseline quality criteria, but fail the final isolation requirement (denoted as N_L, where "L" stands for loose). In a given event sample, the following formulae describe the obtained number of tight and loose leptons:

$$N_T = r \cdot N_{\text{real}}^{\text{baseline}} + f \cdot N_{\text{fake}}^{\text{baseline}}, \tag{6.1}$$

$$N_L = (1-r) \cdot N_{\text{real}}^{\text{baseline}} + (1-f) \cdot N_{\text{fake}}^{\text{baseline}}, \tag{6.2}$$

where r and f are the probabilities of real and fake leptons, respectively, to pass the isolation requirement:

$$r = \frac{N_{\text{real}}^{\text{tight}}}{N_{\text{real}}^{\text{baseline}}}, \qquad f = \frac{N_{\text{fake}}^{\text{tight}}}{N_{\text{fake}}^{\text{baseline}}} \ . \tag{6.3}$$

In other words, the number of observed tight leptons is given by the number of fake baseline leptons times the probability of fake leptons passing the isolation criteria, plus the same for real leptons, and vice-versa for the number of observed loose leptons in the event. The Eq. 6.1 and 6.2 work in the case where there is only one lepton in the event. In the case of two leptons, the possibilities of having events with two real (N_{RR}), one real and one fake (N_{RF}, N_{FR}), and two fake (N_{FF}) baseline leptons have to be considered. Then the Eq. 6.1 and 6.2 can be extended and written in the form of a matrix:

$$\begin{pmatrix} N_{TT} \\ N_{TL} \\ N_{LT} \\ N_{LL} \end{pmatrix} = \Lambda \times \begin{pmatrix} N_{RR} \\ N_{RF} \\ N_{FR} \\ N_{FF} \end{pmatrix}, \tag{6.4}$$

where Λ is defined as:

$$\Lambda = \begin{pmatrix} r_1 r_2 & r_1 f_2 & f_1 r_2 & f_1 f_2 \\ r_1(1-r_2) & r_1(1-f_2) & f_1(1-r_2) & f_1(1-f_2) \\ (1-r_1)r_2 & (1-r_1)f_2 & (1-f_1)r_2 & (1-f_1)f_2 \\ (1-r_1)(1-r_2) & (1-r_1)(1-f_2) & (1-f_1)(1-r_2) & (1-f_1)(1-f_2) \end{pmatrix}. \tag{6.5}$$

The number of tight-tight (N_{TT}), loose-tight (N_{TL}, N_{LT}) and loose-loose (N_{LL}) events is the information easily accesible in the data. The real (r_1, r_2) and fake (f_1, f_2) efficiencies are the key ingredients and are measured in the data, as described in the Sec. 6.1.2 and 6.1.3. Finally, the numbers of real and fake leptons ($N_{RR}, N_{RF}, N_{FR}, N_{FF}$) in the sample are the unknowns which can be calculated by inverting the matrix Λ in the Eq. 6.4.

In the simplified case of one-lepton events, the Eq. 6.1 to 6.3 can be combined to form the set of equations:

$$\begin{pmatrix} N_{\text{T}} \\ N_{\text{L}} \end{pmatrix} = \begin{pmatrix} 1 & 1 \\ 1/r - 1 & 1/f - 1 \end{pmatrix} \begin{pmatrix} N_{\text{real}}^{\text{tight}} \\ N_{\text{fake}}^{\text{tight}} \end{pmatrix}. \tag{6.6}$$

$N_{\text{fake}}^{\text{tight}}$ ($N_{\text{real}}^{\text{tight}}$) denote the number of fake (real) leptons passing the isolation requirement and are the variables of interest. Eq. 6.6 can be solved to obtain the solution for $N_{\text{fake}}^{\text{tight}}$:

$$N_{\text{fake}}^{\text{tight}} = \frac{f}{r-f}\left[rN_L - (1-r)N_T\right]. \tag{6.7}$$

If this equation is applied to one event per time, the values for N_L and N_T can have the value of either 0 or 1. The result for $N_{\text{fake}}^{\text{tight}}$ will give an event weight which quantifies whether the event is more fake-lepton-like or real-lepton-like. If there is a tight lepton in the event (N_T=1 and N_L=0), the weight will be negative (under the assumption that the fake-lepton efficiencies are smaller that-real lepton ones), and vice-versa. By multiplying each data event by such a weight, the final number of fake-lepton events can be estimated in any region. For the dilepton case the event weights derived from Eq. 6.4 are more complex, but the procedure is identical. The fake (f) and real (r) efficiencies are measured in the data QCD and $Z \to \mu\mu$ + jets samples, respectively, in several p_T and $|\eta|$ bins, and used as an input for the matrix method.

6.1.2 Fake muon isolation efficiency

The fake muon efficiency (also referred to as the fake rate) is measured in the data in a control region enriched in QCD (dijet and multijet) events. The QCD dominated region is selected by the following requirements:

- presence of one preselected (baseline) lepton, before any isolation requirements
- ≥ 1 jet with p_T >60 GeV
- $m_T < 40$ GeV
- $E_T^{\text{miss}} < 30$ GeV

By requiring the presence of at least one jet with $p_T > 60$ GeV and a baseline muon, we are expected to pick up dijet (or multijet) events where the other jet (or some jet) is misreconstructed as a muon. As the majority of events at low m_T and E_T^{miss} values are coming from the QCD jet production, relatively high purity of the sample is expected, with the leptons being mainly fakes, i.e. decay products of hadrons composing a jet. Any contamination of the dijet control sample coming from the processes involving real leptons is taken into account by using the MC simulation (Z+jet and W+jet).

A combination of single muon triggers is used to efficiently collect QCD events containing soft muons: EF_mu6, EF_mu15, EF_mu24_tight, with muon p_T thresholds set at 6, 15 and 24 GeV, respectively. As the rate of these low p_T triggers is very high, the triggers were prescaled, i.e. only a fraction of the data triggered was actually recorded. The prescale values varied

during the data taking, but roughly corresponded to ~ 3000, ~ 1000 and ~ 10 for EF_mu6, EF_mu15, EF_mu24_tight, respectively, where a prescale factor of e.g. 10 means that only every 10th event that has fired the trigger was eventually recorded. When normalising the MC to the appropriate data luminosity, the luminosity recorded with a particular trigger was correctly taken into account, depending on the muon p_T value and the trigger that has fired.

The fake muon efficiency is extracted as the ratio of the number of isolated muons over the total number of baseline muons in the sample:

$$f = \frac{N^T_{data} - N^T_{MC}}{N^T_{data} - N^T_{MC} + N^L_{data} - N^L_{MC}}, \tag{6.8}$$

where N^T and N^L denote the number of muons which pass the isolation requirement and those which do not pass the isolation, respectively, and N_{MC} denotes contribution of Z+jets and W+jets events as obtained from MC. Fig. 6.1 is showing the muon p_T distributions of the denominator and the numerator of the above equation, for the MedIso. At low muon p_T there is a significant excess of the data over the Z and W contributions corresponding to QCD events containing fake muons. In $p_T < 25$ GeV range, the contamination from Z and W processes is negligible. At higher momenta ($p_T > 50$ GeV), the contribution from processes containing real leptons becomes dominant and the fake rates can not be extracted reliably. Therefore, the f was extracted only up to $p_T = 50$ GeV, while for muons above that range the value from the last p_T bin ($40 < p_T < 50$ GeV) is used. Since the contribution of fake muons at high p_T is very small, using this approximation is not expected to introduce any visible effects.

The fake rates as a function of the muon p_T are shown in Fig. 6.2. Left-hand-side plot is showing the result for both types of isolation used in the analysis: MedIso for muons $p_T < 25$ GeV and StdIso for muons $p_T > 25$ GeV. The p_T behaviour is consistent with what was observed when studying the isolation efficiency on $t\bar{t}$ MC (see Sec. 5.4). MedIso is clearly better for soft muons, while for hard muons the two isolation definitions perform similarly, with StdIso showing more stable behaviour at high p_T values due to the isolation requirement which is constant with the muon p_T (see Table 5.1).

For the final result, the fake rates are measured in 11 bins in muon p_T and 4 bins in η (see right-hand-side of Fig. 6.2). The p_T bin size is 5 GeV up to p_T=25 GeV, 2 GeV for $25 < p_T < 35$ GeV and finally 5 GeV and 10 GeV in size for the last two bins. The bin size depends on the statistics available for that particular p_T range. Muons at higher η show up to 10% higher fake rates than for muons in the central region. Overall, the fake rates are between 22% and 42% for all the p_T and η bins.

Systematic uncertainties

Two types of systematic uncertainties on the fake efficiencies, in addition to the statistical uncertainty, are taken into account: the uncertainty on the amount of contamination from real muon processes and the flavor uncertainty. These are described in the following.

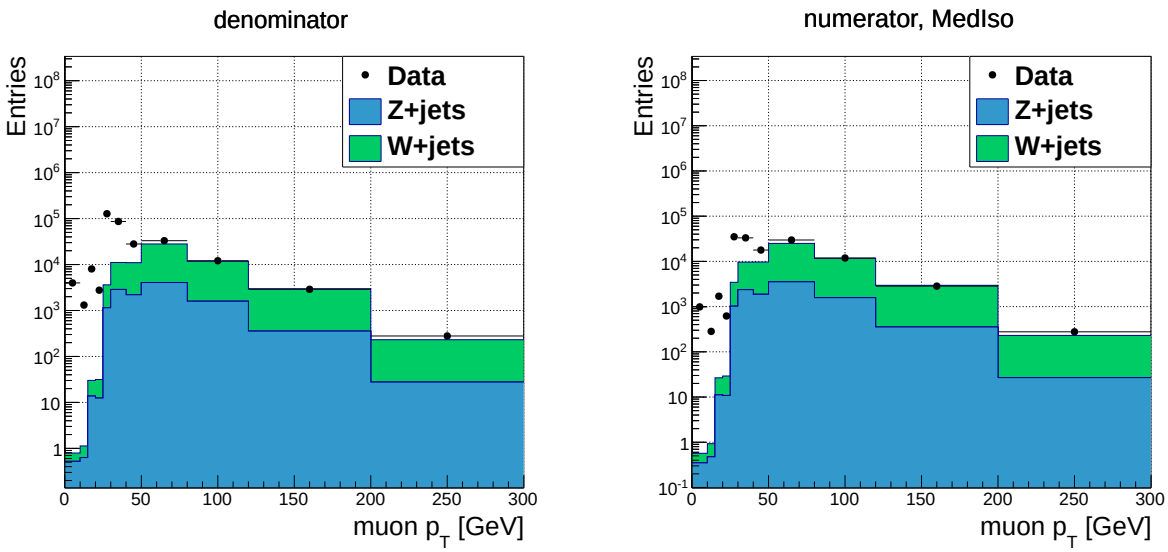

Figure 6.1: Muon p_T distributions in the QCD control region used to measure the fake rates. Contamination coming from processes involving real leptons (Z+jets and W+jets) is subtracted using the MC simulation. A distribution of the denominator of Eq. (6.8) is shown on the left, while the numerator for the MedIso (used for muons $p_T < 25$ GeV) is shown on the right. The up and down fluctuations of the number of data entries in the first four bins are caused by varying luminosity of the trigger used to collect muons in a particular p_T bin.

Uncertainty on the amount of contamination from real muon processes: The measurement of the fake efficiencies is affected by the amount of contamination in the QCD control region from processes involving real leptons. The uncertainty on the amount of contamination is assessed by assigning a 20% uncertainty on the cross sections of Z+jets and W+jets MC samples. The fake rates are extracted after varying the cross sections up and down by 20%, and the difference from the nominal value is taken as the uncertainty.

Flavor uncertainty: The fake efficiencies can vary depending on the origin of a fake muon – whether it was produced in decays of heavy-flavor (HF) or light-flavor (LF) hadrons inside jets. Ideally, the fake rates should be measured in a data sample with a flavor composition similar to the flavor composition of fake muons in the signal region. The origin of fakes in the SR, based on MC simulation, is shown in Tab. 6.1. The majority of fake muon events is coming from W+jet process (about 70%) and the rest from top-quark processes (mostly $t\bar{t}$ with negligible contribution of single-top $s-$ and $t-$ channels). Fake muons in both W and top-quark events are dominantly coming from the HF jets ($\simeq$ 80%), but there is also a smaller contribution from muons originating in light-flavour jets. On the other hand, the flavor composition of jets producing fake leptons in the data QCD sample could not be extracted in a reliable way. Since the fake muon background is one of the dominant contributions to the SR, a conservative

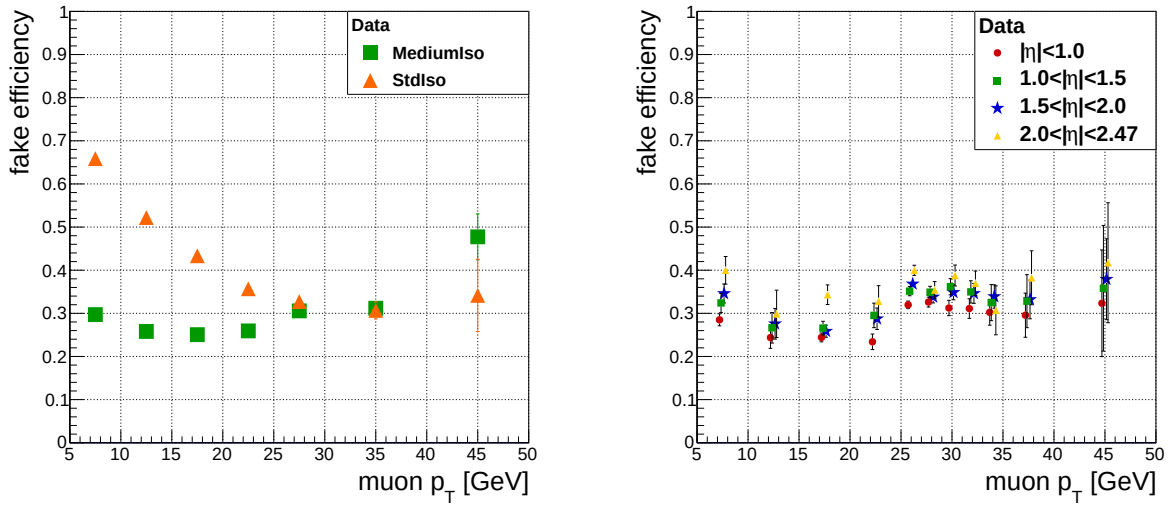

Figure 6.2: Fake efficiencies as a function of muon p_T, as measured in the data dijet sample. The results for two types of isolation definitions used in the analysis are shown on the left, without any η binning. Plot on the right is showing the final result binned in p_T and η used in the analysis, where MedIso is applied to muons up to p_T=25 GeV, and StdIso is applied above 25 GeV. The points in the same p_T bin are slightly horizontally displaced for easier visibility. The error bars in both plots include statistical uncertainty and systematic uncertainty on the MC cross section added in quadrature.

MC process	N events in SR	HF origin	LF origin
W+jets	1.5±0.6	$\sim$ 80%	$\sim$ 20%
single top + $t\bar{t}$	0.7±0.2	>85%	<15%

Table 6.1: Origin and flavor composition of fake muon events in the signal region, as obtained from the MC simulation. The errors are statistical only.

approach has been taken – the full maximum difference observed in MC between HF and LF fake rates, amounting to 30%, was taken as an overal flavor uncertainty and assigned to muon fake rates measured in the data, regardless of the p_T and η bin. The study leading to the estimation of 30% flavor uncertainty is described in the following paragraph.

The flavor dependency of the fake efficiencies is measured in two $t\bar{t}$ MC samples with different parton shower algorithms - Powheg+Pythia and Powheg+Jimmy (Herwig). The MC truth information is used to classify the origin of fake muons into two categories: HF origin including b- and c-jets, and LF origin coming from light-flavor and gluon jets. The definition of a fake efficiency is the same as when estimating the fake efficiencies from the data – the ratio of the number of fake muons passing the isolation condition over the total number of fake baseline muons in the sample. Fig. 6.3 is showing the fake efficiencies in $t\bar{t}$ MC samples as

a function of the muon p_T. Both parton shower schemes, PYTHIA and HERWIG, show very similar p_T dependency of the fake rates, with the discrepancy being larger in the LF case. It can be seen, however, that the absolute values, as well as the p_T behaviour, differ between HF and LF fakes. Furthermore, the relative difference between HF and LF fake rates is different for the two parton showers. Figure 6.4 shows the ratio of HF fake rates to LF fake rates, as a function of the muon p_T, for both parton showers. In the low p_T region, PYTHIA predicts between 10% and 30% larger heavy-flavor fake rates, while HERWIG shows 10% - 20% smaller heavy- compared to light-flavor fake rates. The reason for this discrepancy between the two parton showers was not investigated further. Instead, a maximum difference observed in the low p_T region (amounting to 30%) is taken as an overal conservative flavor uncertainty.

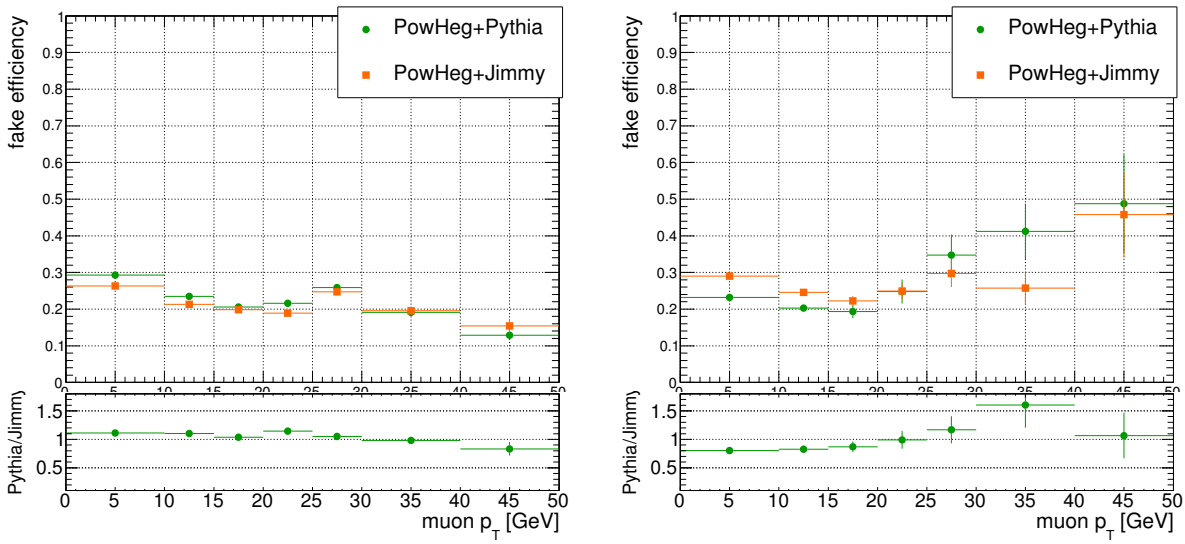

Figure 6.3: Fake efficiencies of muons coming from heavy flavor (left) and light flavor (right) hadrons in two $t\bar{t}$ MC samples, as a function of the muon p_T. MedIso is applied to muons up to p_T=25 GeV, and StdIso is applied above 25 GeV.

6.1.3 Real muon isolation efficiency

The isolation efficiency of prompt muons is measured with the rag-and-probe method in the data using two types of samples: $Z \to \mu\mu$ and $t\bar{t} \to \mu\mu$ events. By requiring the lepton invariant mass within the Z mass window, a high purity $Z \to \mu\mu$ sample is selected in the data, from which the lepton efficiencies are easily extracted. However, the isolation efficiencies may be process-dependent, i.e. the probability of a lepton passing the isolation criteria can depend also on the kinematics of the event. For this reason, it is preferable to measure the efficiencies in a physics process that is also the dominant background in the analysis (being $t\bar{t}$ in this case), and thus take into account the topology-dependent effects.

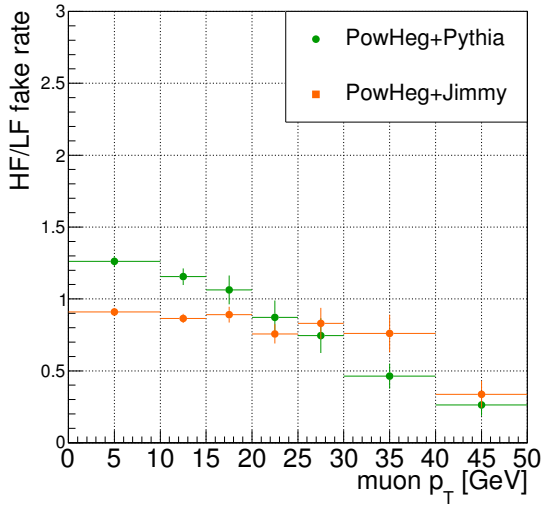

Figure 6.4: Ratio of muon HF fake rates to LF fake rates as a function of the muon p_T. The 30% difference between HF and LF rates observed in PYTHIA in the first p_T bin is taken as an overal flavor uncertainty on the fake muon efficiencies measured in the data.

The selection criteria are shown in the table 6.2. Events are required to have at least two baseline leptons, and at least one lepton is required to pass the isolation criteria. In addition to the same single-muon prescaled triggers used to collect QCD events in Sec. 6.1.2 (EF_mu6, EF_mu15, EF_mu24_tight), a dilepton trigger EF_e12Tvh_medium1_mu8[1], which remained unprescaled during the whole data-taking, was added to increase the available luminosity. $Z \to \mu\mu$ events are selected by requiring the muon invariant mass to be between 80 and 100 GeV (see Fig. 6.5), while for the $t\bar{t}$-enriched sample the invariant mass is required to be outside the Z-mass window and the presence of at least one b-tagged jet is imposed.

The tag-and-probe method relies on having at least one well isolated muon with $p_T > 25$ GeV, called the tag muon. The other muon is called the probe and is tested whether it passes the isolation requirement. The real efficiency is extracted as:

$$r_{Z/t\bar{t}} = \frac{N^{\mu}_{\text{isolated}}}{N^{\mu}_{\text{baseline}}},$$

where the subscript indicates a data sample in which the efficiency is measured. An average

[1]The Tvh specification for the electron part of the trigger refers to different quality criteria for the trigger-level electrons: "T" indicates higher E_T threshold at L1, with respect to HLT threshold, "v" denotes the variable E_T threshold at L1 as a function of $|\eta|$, and "h" means the electromagnetic shower energy deposit in the hadronic calorimeter is required to be below 1 GeV.

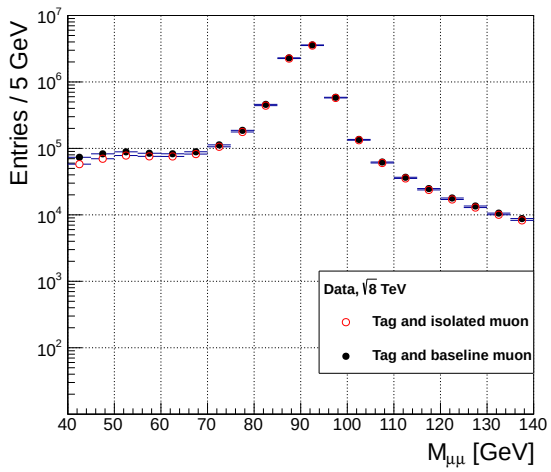

Figure 6.5: Dimuon invariant mass for the $Z \to \mu\mu$ data sample selected as shown in Tab. 6.2. Real muon efficiencies are measured in the events contained inside the Z-boson mass window, $80 < M_{\mu\mu} < 100$ GeV. The red points are events where the probe muon is isolated (numerator), while the black points denote all the events with both isolated and non-isolated probe-muons (denominator).

real efficiency is calculated as a weighted mean of the r_Z and $r_{t\bar{t}}$,

$$r = \frac{\frac{r_Z}{\delta_Z^2} + \frac{r_{t\bar{t}}}{\delta_{t\bar{t}}^2}}{1/\delta_Z^2 + 1/\delta_{t\bar{t}}^2},$$

where δ_Z and $\delta_{t\bar{t}}$ denote the statistical uncertainties in Z and $t\bar{t}$ measurements, respectively. The maximum difference between the average value and the values of the two components is symmetrized, and taken as a systematic uncertainty,

$$\delta_{\text{syst}} = MAX[|r - r_Z|, |r - r_{t\bar{t}}|].$$

The systematic and statistical uncertainties are added up in quadrature to obtain the total uncertainty on the real efficiencies,

$$\Delta = \sqrt{\delta_{\text{stat}}^2 + \delta_{\text{syst}}^2},$$

where δ_{stat} is defined by

$$\delta_{\text{stat}} = \frac{1}{1/\sqrt{\delta_Z^2 + 1/\delta_{t\bar{t}}^2}}.$$

Real efficiency as a function of a muon p_T measured in Z events is shown for data and MC in Fig. 6.6. The agreement between the data and MC is very good, within 1%.

	$N_{lep}^{baseline}$	$p_T^{\text{tag lepton}}$	$N_{\text{jets}}^{p_T>80}$	$N_{b-jets}^{p_T>25}$	$M_{\mu\mu}$ [GeV]
Z	≥ 2	> 25 GeV	≥ 1	$= 0$	$80 < M_{\mu\mu} < 100$
$t\bar{t}$				≥ 1	$M_{\mu\mu} < 80$ or $M_{\mu\mu} > 100$

Table 6.2: Selection criteria for the two data samples used for the real muon isolation efficiency measurement.

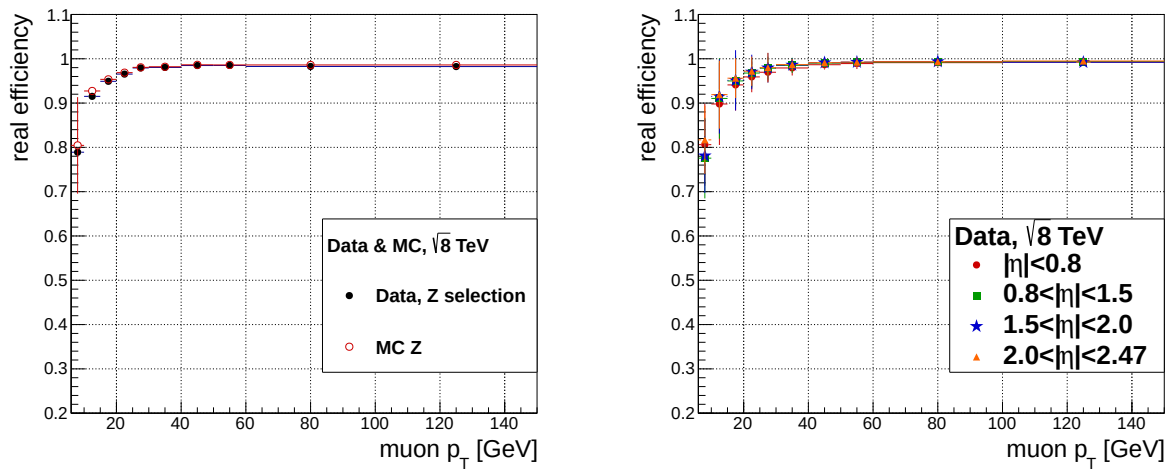

Figure 6.6: Left: Real efficiencies as a function of muon p_T, as measured in a Z sample in the data and simulation. The errors shown are statistical only. Right: Statistically weighted mean of prompt muon efficiencies measured in Z and $t\bar{t}$ data. The errors correspond to statistical and systematic uncertainties added up in quadrature, and are fully dominated by the systematic component.

Kinematic dependency of the real efficiency

Further kinematic dependency of the real muon efficiency is studied using $t\bar{t}$ MC simulation (POWHEG+PYTHIA). Besides p_T and η, two additional variables are considered for the parametrisation of the efficiency: minimum ΔR distance between a muon and a jet in the event ($\Delta R_{\text{min}}^{j,\ell}$), and p_T of the jet closest to the muon. The real efficiencies as a function of $\Delta R_{\text{min}}^{j,\ell}$ are shown in Fig. 6.7. On the left-hand-side plot they are further parametrised as a function of the muon p_T, while on the right-hand-side the parametrisation is done with respect to p_T of the closest jet.

It can be seen that there is a drop in the efficiency for smaller $\Delta R_{\text{min}}^{j,\ell}$, while the plateau is reached around $\Delta R_{\text{min}}^{j,\ell}$=1 for all lepton p_T bins. This is expected, since the closer a muon is to a jet, the more hadronic activity is present in its proximity, thus causing it to be less isolated. This, in turn, reduces the isolation efficiency. In a jetty environment muons are more likely to be close to jets and the real efficiencies are more likely to be affected than in, e.g.,

rather clean Z+jets environment from which the efficiencies are extracted. To avoid this effect, a $\Delta R^{j,\ell}_{\rm min} > 1$ requirement is imposed in the analysis. Apart from removing the dependency of the real muon efficiency on $\Delta R^{j,\ell}_{\rm min}$, this requirement is useful for further rejecting the fake lepton background. Fig. 6.8 shows the $\Delta R^{j,\ell}_{\rm min}$ distribution for fake and real muons, in two p_T bins. The distributions are normalised to the unit area. A clear difference in shapes of $\Delta R^{j,\ell}_{\rm min}$ distributions can be seen between fake and real muons. A requirement of $\Delta R^{j,\ell}_{\rm min} > 1$ is optimal for keeping the acceptance of real muons high, while rejecting a large portion of fake muons.

As shown in right-hand side of Fig. 6.7, no dependency of the real muon efficiency on the p_T of the closest jet is observed, and therefore no parametrisation is attempted.

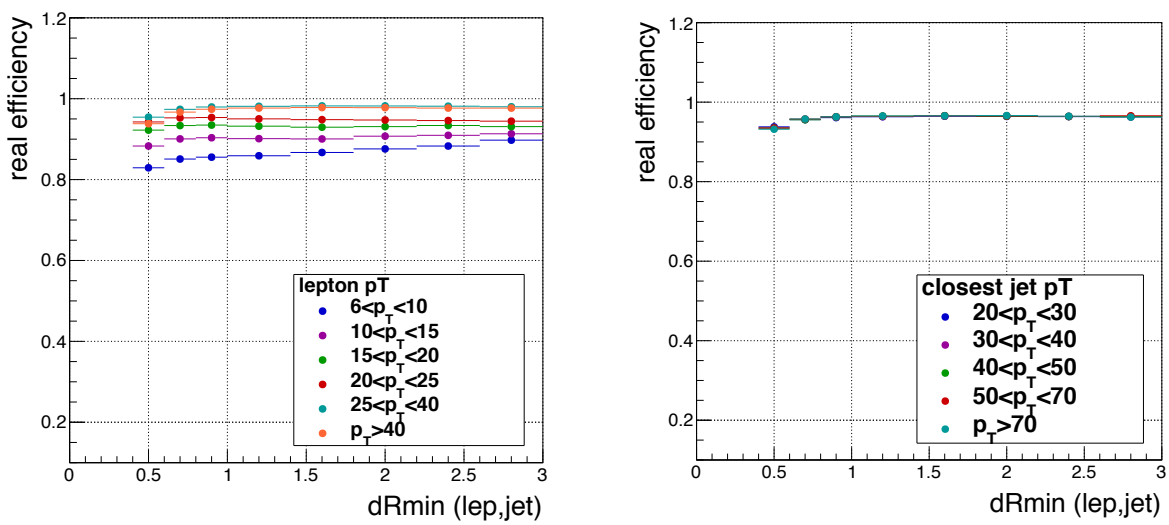

Figure 6.7: Real muon isolation efficiencies in $t\bar{t}$ MC as a function of a minimum ΔR distance to a jet. The efficiencies are additionally parametrized as a function of muon p_T (left), and p_T of a jet closest to the muon (right).

6.1.4 Validation of the fake muon background estimation

The results obtained with the matrix method described above are verified in a dedicated validation region. The validation region is defined with the following selection:

- exactly 2 SS muons, $p_T^{\mu} > 6$ GeV
- $M_{\mu\mu} > 15$ GeV; $|M_{\mu\mu} - M_Z| > 10$ GeV
- $E_T^{\rm miss} > 0$ GeV
- $N_{\rm jets}^{p_T>25} \geq 2$

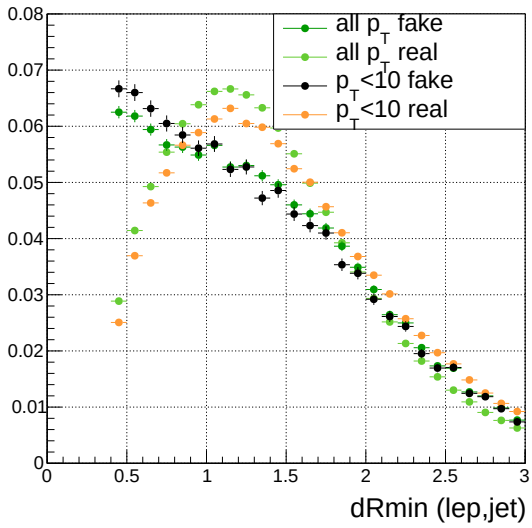

Figure 6.8: $\Delta R^{j,\ell}_{\rm min}$ distributions for fake and real muons in $t\bar{t}$ MC, shown in two muon p_T bins: inclusive in all muon p_T (green), and for soft muons with $p_T < 10$ GeV (orange and black). The distributions are normalised to the unit area.

- $p_{\rm T}^{\rm 1st-jet} > 80$ GeV
- no b-jet among 3 leading jets

As the standard model processes producing two prompt muons of the same sign are quite rare (the contributions consist of dibosons and single-top or $t\bar{t}$ -pair production in association with weak bosons), the SS region will be dominated by fake muons. The jet and b-jet requirements are the same as in the signal region. To gain more statistics, no selection on $E_T^{\rm miss}$ was imposed. As the analysis data is collected with the $E_T^{\rm miss}$ trigger having the plateau at $E_T^{\rm miss} > 150$ GeV, using the region $E_T^{\rm miss} < 150$ GeV implies looking at the trigger turn-on curve. Even so, the agreement of the expectation with the data is reasonably good, as can be seen from the Figure 6.9. Shapes of various important distributions – $E_T^{\rm miss}$, leading jet p_T, muon p_Ts, $M_{\mu\mu}$ and $E_T^{\rm miss}/m_{\rm eff}$ – are well described with the fake muon contribution obtained by the matrix method. A small discrepancy is observed in the sub-leading muon $p_T > 30$ GeV region, but, as the signal muons have $p_T < 25$ GeV, the signal region estimate is not expected to be affected by this discrepancy.

The large error band is mostly due to the 30% flavor uncertainty (see Sec. 6.1.2). The statistical and systematic uncertainties due to MC subtraction of prompt lepton contamination in QCD control region give up to 30%-50% of systematic error per bin. After adding the additional 30% flavor uncertainty, the error band becomes larger than 50%.

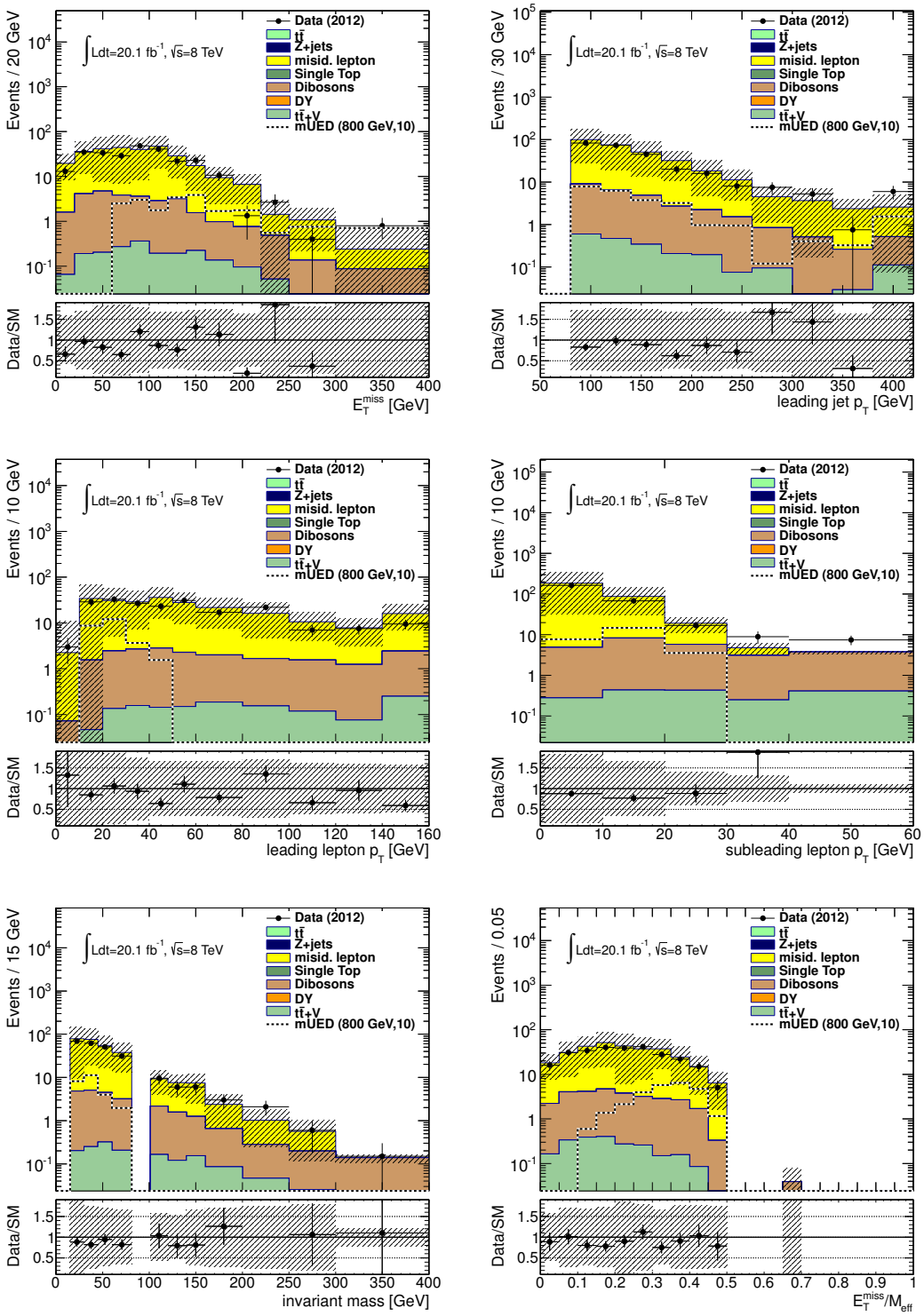

Figure 6.9: Distributions of (from top left) E_T^{miss}, the leading jet p_{T}, the leading and sub-leading muon p_{T}, $M_{\mu\mu}$ and $E_T^{\text{miss}}/m_{\text{eff}}$ in the fake-muon background validation region. The $t\bar{t}$ MC is normalised to the data, and the fake-muon estimation is performed with the matrix-method. The uncertainty band includes MC statistical, b-tagging, JES, JVF, JER, lepton energy scale/resolution, E_{T}^{miss} scale/resolution and matrix method related uncertainties.

6.2 $t\bar{t}$ background

The $t\bar{t}$ background estimation is semi-data-driven as it relies on the shape from the Monte Carlo simulation to extrapolate the expected $t\bar{t}$ yield from the control to the signal region, but derives the normalisation from the data. The $t\bar{t}$ normalisation factor is extracted from a control region by performing a fit based on the profile log-likelihood method. The details of the fit are described in Chapter 7, while in this section the overal procedure is introduced and the choice of control and validation regions is motivated.

6.2.1 $t\bar{t}$ control region

The $t\bar{t}$ control region (TCR) has to fulfil several requirements. It should have high purity of $t\bar{t}$ events, i.e. the contamination from other SM processes should be as low as possible in order to ensure a reliable extraction of the $t\bar{t}$ normalisation factor. Furthermore, the control region has to be orthogonal to the signal region, and the signal contribution should be negligible. Finally, as the $t\bar{t}$ normalisation factor may be different in different parts of the phase space (depending on how well the MC simulation describes the data in a particular kinematic regime), the control region should be as close as possible to the signal region. In practice, the control region is defined by inverting the signal-region defining requirement on one or more kinematic variables. Since the mUED signal is characterised by soft leptons, the natural choice are the muon p_T and $M_{\ell\ell}$ variables. By defining the $t\bar{t}$ control region in $p_T^{\mu_1} > 25$ GeV and $M_{\mu\mu} > 60$ GeV, both the orthogonality to the SR and low signal contamination requirements are satisfied. To increase the purity of the $t\bar{t}$ process, the b-tagging condition is also inverted – the presence of at least one b-jet among the 3 leading jets is imposed. To gain more statistics in the CR, the requirement on $E_T^{\text{miss}}/m_{\text{eff}}$ is removed. All the other selection is exactly the same as for the signal region. The control region defined in this way has about 140 events, $t\bar{t}$ purity is $\sim 85\%$ and signal contamination is smaller than 1%.

To ensure a reliable extrapolation from the control to the signal region along these three variables – leading muon p_T, $M_{\ell\ell}$ and the b-tagging requirement – the agreement between the data and the MC distributions of these variables is assessed in a region with looser selection:

- exactly 2 OS muons, $p_T^{\mu} > 6$ GeV
- $M_{\mu\mu} > 15$ GeV; $|M_{\mu\mu} - M_Z| > 10$ GeV
- $E_T^{\text{miss}} > 150$ GeV
- $N_{\text{jets}}^{p_T>25} \geq 2$
- $p_{\text{T}}^{\text{1st-jet}} > 80$ GeV

The distributions of the extrapolation variables, along with E_T^{miss} and $E_T^{\text{miss}}/m_{\text{eff}}$ distributions, are shown in Fig. 6.10. The distributions are showing good agreement between the

data and the SM prediction, both concerning the shapes and normalisation. In these plots, the $t\bar{t}$ normalisation factor, as derived in Chapter , has already been applied. Any discrepancies are contained within the uncertainty band which includes the following contributions: MC statistical, b-tagging, JES, JVF, JER, lepton energy scale/resolution, E_{T}^{miss} scale/resolution and fake muon background related uncertainties.

6.2.2 $t\bar{t}$ validation regions

After the $t\bar{t}$ normalisation factor is extracted, the result of the fit is checked in several validation regions. The validation regions are defined somewhere "in between" the control and the signal regions. The validation regions are also orthogonal to the signal region, but, as they are closer in phase space, the contamination from the signal and other SM processes may be larger than in the $t\bar{t}$ CR. To validate the extrapolation along each of the three variables inverted in the control region, there is one validation region defined for each variable, with the requirement on the variable in question being the same as in the signal region.

The definitions of control, validation and signal regions are summarised in the Tab. 6.3 and pictorially represented in the Fig. 6.11.

	SR	TCR	VR1	VR2	VR3
N_μ	$== 2$				
$p_T^{\mu_1}$ [GeV]	[6, 25]	> 25	> 25	> 25	[6, 25]
$p_T^{\mu_2}$ [GeV]	[6, 25]	> 6			
$p_T^{\ell_3}$ [GeV]	< 6 (muon), < 7 (electron)				
$M_{\mu\mu}$ [GeV]	> 15; $\lvert M_{\mu\mu} - M_Z \rvert > 10$				
$M_{\mu\mu}$ [GeV]	< 60	> 60	< 60	> 60	–
$\Delta R_{\mathrm{min}}^{j,\ell}$	> 1.0				
$m_T^{\mu 1}$ [GeV]	> 40				
$N_{\mathrm{jets}}^{p_T>25}$	≥ 2				
$p_T^{j_1}$ [GeV]	> 80				
$p_T^{j_2}$ [GeV]	> 25				
$N_{\text{b-jets}}$ (among 3 leading)	veto	>=1 b-jet	–	veto	>=1 b-jet
E_T^{miss} [GeV]	> 180				
$E_T^{\mathrm{miss}}/m_{\mathrm{eff}}$ [GeV]	> 0.3	–			

Table 6.3: Overview of the selection criteria for signal, control and validation regions.

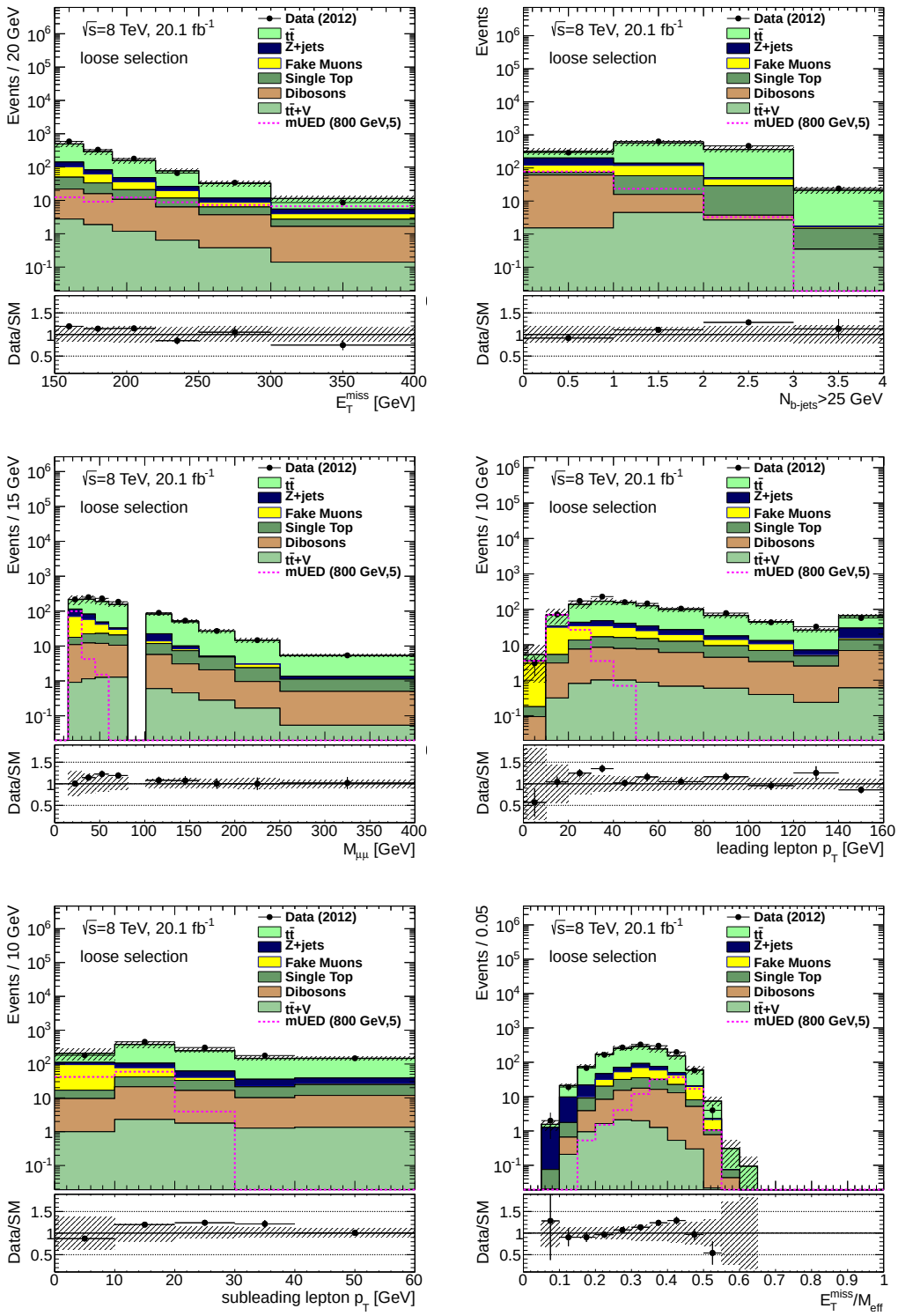

Figure 6.10: Distributions of (from top left) E_T^{miss}, $N_{\text{b-jets}}$, $M_{\mu\mu}$, $p_T^{1\text{st }\mu}$, $p_T^{2\text{nd }\mu}$ and $E_T^{\text{miss}}/m_{\text{eff}}$ in the data and Monte Carlo after loose selection (see text for the definition). The $t\bar{t}$ MC is normalised to the data, and the data-driven estimation is performed for the fake muon background. The uncertainty band includes MC statistical, b-tagging, JES, JVF, JER, lepton energy scale/resolution, E_{T}^{miss} scale/resolution and fake muon background related uncertainties.

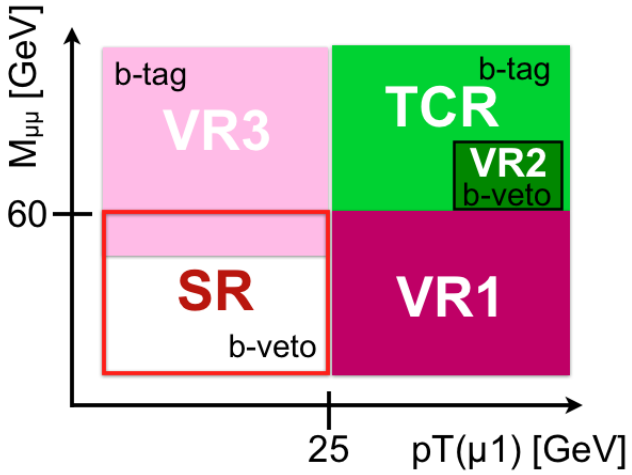

Figure 6.11: Pictorial representation of signal, control and validation regions definitions.

Chapter 7

Fit method for the background and signal estimation

The profile likelihood fit is performed to estimate the background and possible signal contribution to the signal region (SR) [108], [110],[109]. A probability-density function (PDF) is built for signal and background processes by filling the histograms in a phase-space of interest using the MC simulation. The PDF contains the unconstrained free parameters for background and signal components which are used to adjust the relative contributions of signal and background in all the regions. Dedicated control region (CR), where the signal contamination is expected to be negligible, is used to constrain the background. The overall shape of PDF remains unchanged in the fit, and is used to give the relative ratio of number of events in the SR to the one in the CR. The CR and SR are orthogonal to each other which ensures the statistical independence of the regions, and it is thus possible to combine them in one simultaneous fit. All systematic and statistical uncertainties are treated as nuisance parameters and are constrained by Gaussian distributions, unless stated otherwise. Several validation regions are used as a cross-check of the fit result and do not constrain the background.

The likelihood function is introduced in Sec. 7.1, followed by the analysis-specific setup in Sec. 7.2. The test statistic and limit-setting procedure are described in Sec. 7.3 and Sec. 7.4, respectively, while the three possible fit configurations are explained in Sec. 7.5. Various systematic uncertainties affecting the analysis and their treatment are described in Sec. 7.6.

7.1 The likelihood function

The behaviour of background and signal events is modelled by building a probability-density function (PDF). A PDF $F(\vec{x}, \vec{\mu})$ gives the probability density of a distribution of variables $\vec{x}$ where $\vec{\mu}$ are the parameters of the model describing this distribution. Generally, to describe signal and background contributions in some region of phase space a sum of their PDFs can be written as:

$$F(x) = \mu S(x) + B(x), \tag{7.1}$$

where S(x) corresponds to the PDF of the nominal signal model, while B(x) represents the background. The parameter of interest is, usually, μ (also called the signal strength), with $\mu = 0$ corresponding to the background only hypothesis, and $\mu = 1$ being the nominal signal hypothesis. In order to constrain the background, measurement is made in a control region where signal contribution is expected to be negligible.

Practically, the PDF is built by combining distributions of signal and background events using the MC simulation. The PDF essentially consists of a collection of histograms defined over some region of phase space where the content of each bin can be thought of as a counting experiment. The signal and control regions are defined to be mutually exclusive, allowing them to be modeled independently by using the Poisson probabilities. In order to test the data against the signal + background hypothesis in some region of interest, a profile log likelihood ratio approach (PLL) is used [111],[114].

The likelihood function is defined as the product of Poisson distributions for the signal and control regions, and of additional distributions that implement the constraints on systematic uncertainties. It can be written as

$$L(\mathbf{n}, \boldsymbol{\theta^0} | \mu, \mathbf{b}, \boldsymbol{\theta}) = P_{SR} \times P_{CR} \times P_{Sys} \tag{7.2}$$

$$= \prod_{j=1}^{N^S} \frac{(\lambda_j^S)^{n_j^S}}{n_j^S!} e^{-\lambda_j^S} \times \prod_{i=1}^{N^C} \frac{(\lambda_i^C)^{n_i^C}}{n_i^C!} e^{-\lambda_i^C} \times \mathrm{P_{Sys}}(\boldsymbol{\theta^0}, \boldsymbol{\theta}), \tag{7.3}$$

where N^S (N^C) is the number of bins (or measurements) in the signal (control) regions and $\boldsymbol{\theta}$ are nuisance parameters that parametrise systematic uncertainties. The $P_{Sys}(\boldsymbol{\theta^0}, \boldsymbol{\theta})$ of independent nuisance parameters is a product of their respective PDFs, typically Gaussian distributions. Where appropriate, e.g. for MC statistical uncertainties, the nuisance parameters are constrained by a Poisson term. The nominal values are denoted as $\boldsymbol{\theta^0}$, around which $\boldsymbol{\theta}$ can be varied. The $\boldsymbol{\theta^0}$ are taken to be zero, and $\boldsymbol{\theta} = \pm 1$ corresponds to one sigma deviations from the nominal value. These one sigma deviations, i.e. the width of the constraining Gaussian functions, are obtained by auxiliary measurements outside this analysis. All the systematic uncertainties are constrained and propagated into the fit and its uncertainty through the functions $P_{Sys}(\boldsymbol{\theta^0}, \boldsymbol{\theta})$. The presence of the nuisance parameters broadens the likelihood function which represents the loss of information about μ due to the systematic uncertainties.

The Poisson expectations for signal $\lambda^S(\mu, \mathbf{b}, \boldsymbol{\theta})$ and control $\lambda^C(\mu, \mathbf{b}, \boldsymbol{\theta})$ regions are functions that depend on the background normalisation factors contained in $\mathbf{b}$, nuisance parameters $\boldsymbol{\theta}$ and the signal strength μ. They can be written in terms of the transfer factors $\mathbf{c}$ as

$$\lambda^i(\mu, \mathbf{b}, \boldsymbol{\theta}) = \mu \cdot \mathbf{c_{s,i}}(\boldsymbol{\theta}) \cdot \mathbf{s} + \sum_{\mathbf{j}} \mathbf{c_{j,i}}(\boldsymbol{\theta}) \cdot \mathbf{b_j}, \tag{7.4}$$

where index i denotes the region, index j sums over all considered backgrounds and $\mathbf{b}$ ($\mathbf{s}$) refers to the number of background (signal) events as determined in its respective control region. The transfer factors $c_{j,i}(\boldsymbol{\theta})$ are used to extrapolate the prediction from the dedicated control region of the process to all other regions of interest (signal, validation). They are obtained from the MC simulation as

$$c_{j,i} = \frac{MC(j,i)}{MC(j,j)} \times \left(1 + \sum_k \Delta_{j,i;k}\theta_k\right). \tag{7.5}$$

The effect of any nuisance parameter $\boldsymbol{\theta}$ on the expected number of events is taken care of through these transfer factors. The quantities $\Delta_{j,i;k}$ denote the size of a given systematic uncertainty on the expectation value in a region i for a process j, given its $\boldsymbol{\theta}$. For example, a 10% uncertainty on the expected number of events for a one sigma deviation would be expressed as $\Delta_{j,i;k}$=0.10. It can be seen from Eq.(7.5) that the uncertainties that change the MC normalisation in CR and SR equally, will tend to cancel out. This is true if the kinematic selection chosen for the control region is representative of the background event topology in the signal region. What remains is just the relative change in systematic uncertainty between the control and signal (validation) regions. The systematic uncertainties for which such cancelation is not appropriate (e.g. MC statistical uncertainty or the cross-section uncertainties), the full systematic uncertainty has been explicitly implemented, in both the signal and control regions.

7.2 The fit setup

In this analysis one bin per signal and control region is used, the likelihood function from the Eq. (7.3) therefore simplifying to

$$L(n, \boldsymbol{\theta^0}|\mu, \mathbf{b}, \boldsymbol{\theta}) = \frac{(\lambda^{\mathbf{S}})^{\mathbf{n}}}{\mathbf{n}!}\mathbf{e}^{-\lambda^{\mathbf{S}}} \times \frac{(\lambda^{\mathbf{C}})^{\mathbf{m}}}{\mathbf{m}!}\mathbf{e}^{-\lambda^{\mathbf{C}}} \times \mathbf{P_{Sys}}(\boldsymbol{\theta^0}, \boldsymbol{\theta}), \tag{7.6}$$

where λ^S (λ^C) are the Poisson expectations of the total background, and possibly signal, in the signal (control) region. Only the dominant $t\bar{t}$ background is fitted to the data, other backgrounds have their normalisations fixed by other methods. Factor $P_{\text{Sys}}(\boldsymbol{\theta^0}, \boldsymbol{\theta})$ contains all the systematic nuisance parameters of the Gaussian form and a Poisson-constrained nuisance parameter due to the MC statistical uncertainty. The Poisson statistical error is applied on the sum of all the MC contributions in a given region.

The following different types of components are included in the fit:

- **$t\bar{t}$-background:** The $t\bar{t}$ MC sample is assigned a floating normalisation parameter, denoted by $\mu_{t\bar{t}}$, whose initial value is set to one.
- **Fake muon background:** The event yield of this background in each region is taken from the matrix-method estimate. The central value is allowed to vary within the uncertainties of this estimate.

- **Other backgrounds:** Other minor backgrounds have their contributions taken form the MC simulation. No normalisation parameter is assigned to them, but the fit is allowed to vary their estimates within the uncertainties assigned to each background.

- **Signal:** When performing the exclusion fit (see the section below), signal MC samples are included as well, along with signal-specific nuisance parameters. The signal contribution is adjusted by fitting a floating normalisation parameter, μ_{Sig}, in analogy to $\mu_{t\bar{t}}$.

7.3 Test statistic

The test statistic is defined as the negative of the profile log likelihood ratio (PLL), with the likelihood L being defined as in Eq. (7.6):

$$\Lambda(\mu) \equiv \Lambda(\mu, \mathbf{n}, \boldsymbol{\theta^0}) = -\mathbf{2} \ln \frac{\mathbf{L}(\mathbf{n}, \boldsymbol{\theta^0} | \mu, \hat{\hat{\mathbf{b}}}, \hat{\hat{\boldsymbol{\theta}}})}{\mathbf{L}(\mathbf{n}, \boldsymbol{\theta^0} | \hat{\mu}, \hat{\mathbf{b}}, \hat{\boldsymbol{\theta}})}. \tag{7.7}$$

Here $\hat{\hat{\mathbf{b}}}$ and $\hat{\hat{\boldsymbol{\theta}}}$ denote the values of $\mathbf{b}$ and $\boldsymbol{\theta}$ that maximize L for a specific μ (the value of μ that is being tested), while $\hat{\mu}$, $\hat{\mathbf{b}}$ and $\hat{\boldsymbol{\theta}}$ in the denominator maximize the unconditional likelihood function. The ratio of conditional to unconditional likelihood functions will always be between zero and one, $(0 \leq L(\mu)/L(\hat{\mu}) \leq 1)$, with values close to one implying good agreement between the data and the hypothesised value μ. Conversely, small values of the test statistic $\Lambda(\mu)$ imply the good agreement, whereas higher values of $\Lambda(\mu)$ correspond to increasing incompatibility between the data and μ. Since only the signal hypotheses leading to a positive number of observed events are considered, the test statistic is constrained to the case $\mu \geq 0$:

$$q_\mu \equiv \begin{cases} -2 \ln \frac{L(\mu, \hat{\hat{\boldsymbol{\theta}}}(\mu))}{L(\hat{\mu}, \hat{\boldsymbol{\theta}})} & \text{if } \hat{\mu} \geq 0 \\ -2 \ln \frac{L(\mu, \hat{\hat{\boldsymbol{\theta}}}(\mu))}{L(0, \hat{\hat{\boldsymbol{\theta}}}(0))} & \text{if } \hat{\mu} < 0. \end{cases} \tag{7.8}$$

When conducting an experiment, two types of hypothesis tests can be performed – testing the data against the background-only hypothesis can lead to a discovery of a new signal, provided the background-only hypothesis is rejected, whereas the background-plus-signal hypothesis is tested against the background-only hypothesis for the purpose of setting limits on parameters of a signal model.

When testing the background-only hypothesis, i.e. $\mu = 0$ case, the test statistic of Eq.(7.8) becomes

$$q_0 \equiv \begin{cases} -2 \ln \frac{L(0, \hat{\hat{\boldsymbol{\theta}}}(0))}{L(\hat{\mu}, \hat{\boldsymbol{\theta}})} & \text{if } \hat{\mu} \geq 0 \\ 0 & \text{if } \hat{\mu} < 0. \end{cases} \tag{7.9}$$

Rejecting the $\mu = 0$ hypothesis leads to a discovery of a new signal. For the purpose of setting the upper limits on the signal strength parameter, the test statistic is defined as

$$q_\mu \equiv \begin{cases} -2\ln\frac{L(\mu,\hat{\hat{\boldsymbol{\theta}}}(\mu))}{L(\hat{\mu},\hat{\boldsymbol{\theta}})} & \text{if } 0 \leq \hat{\mu} \leq \mu \\ -2\ln\frac{L(\mu,\hat{\hat{\boldsymbol{\theta}}}(\mu))}{L(0,\hat{\hat{\boldsymbol{\theta}}}(0))} & \text{if } \hat{\mu} < 0 \\ 0 & \text{if } \hat{\mu} > \mu. \end{cases} \tag{7.10}$$

where q_μ is set to 0 for the $\hat{\mu} > \mu$ case since the data with $\hat{\mu} > \mu$ are not considered as less compatible with μ than the data obtained.

7.4 Limit-setting procedure

To quantify the level of disagreement between between the observed data and the hypothesis being tested, a p-value for a hypothesised μ is computed as

$$p_\mu = \int_{q_{\mu,\text{obs}}}^{\infty} f(q_\mu|\mu)\mathrm{d}q_\mu, \tag{7.11}$$

where $q_{\mu,\text{obs}}$ is the value of the statistic observed in the data, and $f(q_\mu|\mu)$ denotes the probability density function of q_μ under the assumption of the signal strength μ. When quantifying the sensitivity of the experiment, a median of the alternate hypothesis ($q_{\mu',\text{med}}$) is used in Eq.(7.11) instead of the observed one ($q_{\mu,\text{obs}}$), as shown on the left-hand side of Fig. 7.1. The distribution of q_μ can be found either by building pseudo experiments or by using the asymptotic formulae. According to theorems due to Wilks [112] and Wald [113], for sufficiently large data samples and the case of a single parameter of interest, the test statistic takes an asymptotic form

$$q_\mu \equiv \begin{cases} \frac{\hat{\mu}^2}{\sigma^2} & \text{if } \hat{\mu} \geq 0 \\ 0 & \text{if } \hat{\mu} < 0 \end{cases} \tag{7.12}$$

for the discovery, and

$$q_\mu \equiv \begin{cases} \frac{(\mu-\hat{\mu})^2}{\sigma^2} & \text{if } 0 \leq \hat{\mu} \leq \mu \\ \frac{\mu^2}{\sigma^2} - \frac{2\mu\hat{\mu}}{\sigma^2} & \text{if } \hat{\mu} < 0 \\ 0 & \text{if } \hat{\mu} > \mu \end{cases} \tag{7.13}$$

for setting the upper limits, i.e. the distribution of the test statistics approaches a chi-square distribution for one degree of freedom.

When setting the upper limits on new-physics signal models, a CL_S procedure is used [115]. The CL_S value is defined as

$$\mathrm{CL}_S = \frac{P(q \geq q_{\mathrm{obs}}|s+b)}{P(q \geq q_{\mathrm{obs}}|b)} = \frac{p_{s+b}}{1-p_b}. \tag{7.14}$$

A signal model is considered excluded at 95% confidence level (CL) if the value of $\mathrm{CL_S}$ is found to be less than 0.05. This procedure ensures that models to which the experiment has essentially no sensitivity (e.g. signals with very small S/B ratios) will not be rejected. As can be visualised from the right-hand side plot of Fig. 7.1, if $f(q|s+b)$ and $f(q|b)$ distributions significantly overlap, requiring simply $p_{s+b} < 0.05$ will result in the exclusion of a signal model to which the experiment has little or no sensitivity. On the other hand, when $f(q|s+b)$ and $f(q|b)$ are sufficiently well separated, the $\mathrm{CL_S}$ value approaches that of a p_{s+b}.

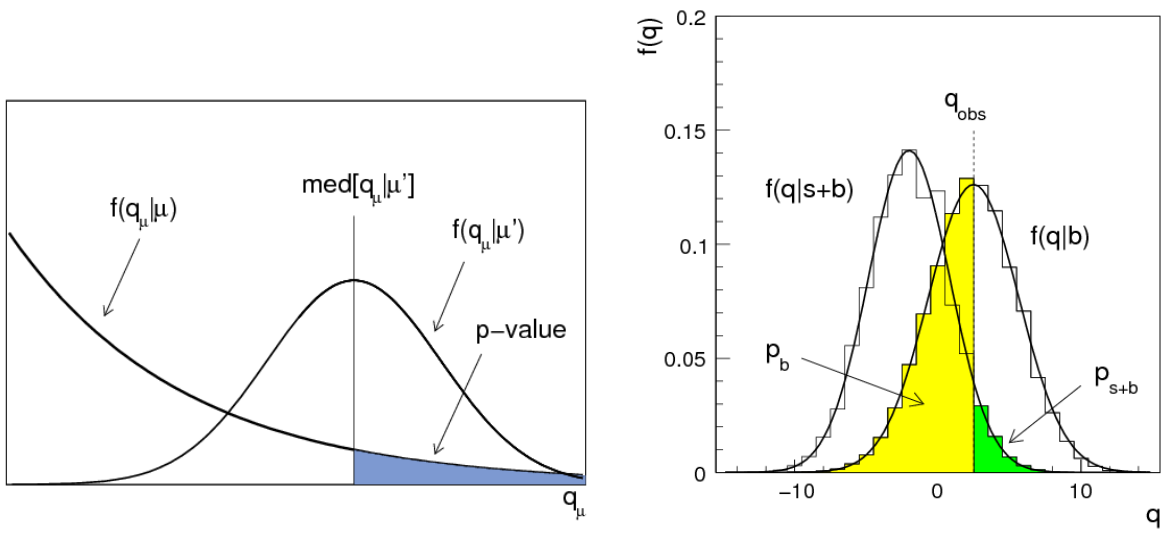

Figure 7.1: Left: Illustration of the p-value corresponding to the median of q_μ assuming a strength parameter μ', used to characterise the sensitivity of an experiment. Right: The distributions $f(q)$ of the statistic q under the s+b and b-only hypotheses. When the two distributions significantly overlap, the experiment has little or no sensitivity to the considered signal model. In such cases the $\mathrm{CL_S}$ method ensures the signal will not be falsely rejected. Figures adapted from [114].

7.5 The fit configurations

The fit can be run in three different configurations, depending on the purpose of the study:

- **Background-only mode:** Only the $t\bar{t}$-CR is used in the fit and all the SM background components are included. No signal contribution is considered in any of the regions and, consequently, all the signal-related nuisance parameters are turned off. The only floating

parameter is $\mu_{t\bar{t}}$ and its best-fit value is used to extrapolate the result of the background-only fit to the signal and validation regions.

- **Exclusion mode:** Both $t\bar{t}$-CR and SR are used in the fit. A signal sample of interest is included, in addition to all the background samples. The signal and $t\bar{t}$ normalisation parameters, μ_{Sig} and $\mu_{t\bar{t}}$, are simultaneously fitted to the data. Depending on the possible signal contamination in the TCR, fitted $\mu_{t\bar{t}}$ may differ from the $\mu_{t\bar{t}}$ value obtained in the background-only fit. All the signal-specific nuisance parameters, are turned on. The exclusion fit is used when setting limits on particular signal models.

- **Discovery mode:** Both CR and SR are used in the fit, but the signal contribution is neglected in the CR. Even if the background-only assumption in the CR is false, this will lead to a conservative p-value for the discovery since the background will be over-estimated. The number of signal events in the SR is set to one, and $\mu_{t\bar{t}}$ and μ_{Sig} are simultaneously fitted to the data. Fitting μ_{Sig} in this way effectively corresponds to fitting the number of potential signal events in the signal region. Since there are no model-dependent assumptions for the signal, all the signal-related nuisance parameters are set to zero. The discovery fit is used when calculating the discovery p-value and setting the model-independent upper limits.

7.6 Systematic uncertainties

Systematic uncertainties have an impact on the expected event yields in the signal and control regions and on the normalisation factors $\mu_{t\bar{t}}$, used to derive the $t\bar{t}$ background yield in the signal region, and μ_{Sig}, used to quantify possible signal contribution.

The widths of Gaussian distributions which constrain the nuisance parameters are given by the size of the respective uncertainties as determined from auxiliary measurements, e.g. measurements of the jet-energy scale (JES). The effect on the number of events per region is obtained by varying the uncertainty-related parameters, e.g. JES parameters, by one sigma up and down from their nominal value. The relative variation in number of events is then translated into the Gaussian-constraint parameters $\boldsymbol{\theta}$. Some systematic uncertainties are treated as correlated over all regions and samples (mainly the detector-related uncertainties) and are implemented by assigning one joint nuisance parameter to all the samples. Other uncertainties (e.g. theoretical uncertainties) are treated as uncorrelated, and separate nuisance parameter is assigned to each process.

The uncertainties are implemented in two different ways based on their origin and purpose:

- **Shape uncertainties:** This type of uncertainties is assumed to affect only the shapes of nominal distributions. They are implemented as the uncertainties on the transfer factor (see Eq.(7.5)):

$$\mathrm{TF} = \frac{\text{Number of events in SR (VR), MC}}{\text{Number of events in TCR, MC}}, \tag{7.15}$$

i.e. only the relative change in systematic uncertainty between the control and the signal (validation) regions has an effect. The overall normalisation of the $t\bar{t}$ MC, and consequently the error on the normalisation, is derived from the fit to the data in the TCR. The systematic uncertainties, on the other hand, affect only the shapes of various distributions used in the extrapolation, but not the normalisation itself. The shape uncertainties include most of the experimental and $t\bar{t}$-theoretical uncertainties.

- **Normalisation uncertainties:** These uncertainties affect the overall normalisation of the sample in question and do not cancel out when extrapolating from the control to the signal (validation) region. To this category fall mostly the uncertainties on minor bakcgrounds (e.g. cross section and theory), as these do not have their normalisations derived from the data.

The optimal values and errors of the nuisance (and free) parameters, as well as their correlations, are determined simultaneously when the PDF is fitted to the data. Since the fit to the data is minimally constrained (there is only one bin in the CR, and one free parameter - $t\bar{t}$ normalisation factor - to be adjusted), the nuisance parameters are essentially simply propagating the effect of the uncertainties to the signal and the validation regions.

The uncertainties are divided into two categories – experimental and theoretical. The are described in detail, along with their implementations, in the following two sections.

7.6.1 Experimental uncertainties

A number of experimental uncertainties affect the measurement and are applied to all background and signal MC samples in the analysis. These are mainly the detector-related uncertainties which include the effects on object identification efficiencies and energy and/or momentum measurement. Each uncertainty is associated with a nuisance parameter in the fit, and there are a total of 17 detector-related nuisance parameters.

- **Jet uncertainties:** Jet energy scale (JES) and resolution (JER) uncertainties are assumed to affect the shape of spectrum in a correlated way in all the regions considered in the analysis. They are implemented as the uncertainties on the MC transfer factors. Only the reduced set of seven JES parameters is used, along with the JVF uncertainty. The rest of the original 17 JES parametrs (see Sec. 4.4) are found to have negligible impact and are left out in order to simplify the fit.

- **E_T^{miss} uncertainties:** The effects of lepton- and jet-energy scale and resolution uncertainties are propagated to the E_T^{miss} calculation and taken care-off by the corresponding jet and lepton nuisance parametes. Two additional sources of uncertainty which affect

the value of E_T^{miss} are energy scale and resolution of E_T^{miss} soft terms. These are introduced as two additional nuisance parameters and treated in the same way as jet-related uncertainties described above.

- **B-tagging:** The total uncertainty associated with b-tagging of jets includes the uncertainties on b-jet tag efficiency and c- and light-jet mis-tag rates. The uncertainties are uncorrelated between the three flavors and added as a separate nuisance parameters. The three nuisance aprameters are then correlated for all the samples and regions and treated in the same way as JES (JER) uncertainties, i.e. as a shape systematic.

- **Pile-up:** The uncertainty on pile-up reweighting is also considerd as a shape-systematic and applied in the same way as the uncertainties above.

- **Lepton uncertainties:** Lepton identification efficiency, and energy scale and resolution uncertainties are correlated over all the regions and samples in the analysis and treated in the same way as the uncertainties above. The muon energy resolution uncertainty is divided into two parts, one corresonding to the inner detector and one to the muon system, in addition to the uncertainty on the muon energy scale. Electron uncertainties are described by four nuisance parameters for the energy scale and one for the energy resolution.

- **Trigger:** The uncertainty on the trigger plateau-efficiency of 5% is applied as an uncertainty on the overall normalisation. It is correlated for all the samples and in all the regions.

- **Luminosity:** Luminosity uncertainty of 2.8% is correlated for all the samples and in all the regions. It affects the overall normalisation.

In order to improve the fit stability and enable the fit to run faster, experimental uncertainties found to have a negligible effect are left out of the fit. An uncertainty is considered negligible if it is smaller than 2% on the total estimate in all the regions of interest (CR,SR,VR), and if its effect is smaller than 2% on the $t\bar{t}$ background in all the regions. All the lepton related uncertainties, except the lepton efficiency, along with already mentioned JES parameters, were found to have such minor impact. Eight nuisance parameters related to lepton energy scales and resolutions and 10 JES parameters are therefore left out of the final fit.

7.6.2 Theoretical uncertainties

Various theoretical uncertainties are related to calculations included in MC simulations and can impact both shapes and overall yields of distributions, as well as cross-sections. Their sources and implementation for backgrounds and signal are explained below.

Theoretical uncertainties on backgrounds

All the uncertainties related to $t\bar{t}$ are applied as shape uncertainties, i.e. implemented on the $t\bar{t}$ transfer factor. No cross-section uncertainty is considered for the $t\bar{t}$ sample as it has its normalisation fixed by the data. As there is no dedicated control region available for minor backgrounds with MC-based estimates, the theoretical uncertainties on these backgrounds, including the cross-section one, are applied as uncertainties on the overal normalisation. The following uncertainties are considered in the analysis:

- **Renormalisation and factorisation scales:** Additional samples are produced for which the renormalisation (μ_R) and factorisation (μ_F) scales are independently varied up and down by a factor of two. In case of MadGraph, a single parameter controlling the factorization and renormalization scales of the hard scatter is varied. This uncertainty is expectd to be small for NLO generators (Powheg), and larger for LO generators (Sherpa, Madgraph).

- **Parton density function (PDF):** PDF uncertainty includes both the variation of eigenvector parameters within the default PDF set (intra) and comparison with different PDF set (inter variation).

  - CT10 eigenvector and MSTW2008lo68c for samples using CT10 PDF.
  - CTEQ61 eigenvector and MSTW2008lo68c for samples using CTEQ6L1 PDF.

  The differences due to intra- and inter-variations are added up in quadrature to obtain the total PDF uncertainty.

- **Initial and final state radiation:** The uncertainty on the amount of ISR and FSR is evaluated by comparing two Pythia samples generated with ISR/FSR tunes containing more and less parton showering.

- **Finite number of partons in the matrix element:** This uncertainty is applied to Sherpa and Madgraph samples and covers the effect of only finite number of partons being included in the ME calculation. It is evaluated by comparing a MC sample with nominal number of partons simulated to a MC sample with one less parton.

- **Matching of matrix-element with parton-shower:** In MadGraph interfaced to Pythia the scale for the first emission in MLM matching (α_S) and the minimum k_T jet measure between partons are varied.

- **Matrix-element generator:** To asses the dependency on the ME generator, the nominal Powheg sample is compared to Alpgen for $t\bar{t}$ and for the diboson process Powheg is compared to aMC@NLO sample.

- **Parton shower modelling:** The effect of the PS-algorithm choice on the final state is assesed by comparing the nominal Pythia sample to a sample with Herwig PS interfaced to the same ME generator.

- **Interference with $t\bar{t}$:** This uncertainty is specific to NLO single top generators [116]. At NLO level top quark produced in asocciation with W boson can also have a b-quark radiated from an internal t-quark line. This final state is the same as for $t\bar{t}$ production and, when the top propagator is on-shell, the two processes overlap. $t\bar{t}$ contribution can be subtracted from the single-top NLO generation in two ways:

  - **Diagram removal (DR):** In this approach all the doubly resonant diagrams in the NLO Wt produciton are simply removed from the calculation.
  - **Diagram subtraction (DS):** Here the doubly resonant diagrams are kept, but the NLO Wt cross section is modified by implementing a suitably designed subtraction term.

  DR sample is used as a nominal sample, and to assess whether the overlap has been successfully eliminated, it is compared to a DS one.

As the number of uncertainties per background process is large, and the fit does not have the power to constrain them due to the data being fitted only in one CR (especially so for the minor backgrounds), a reduced set of nuisance parameters was used to ensure the fit stability and fast running. Cross-section and PDF uncertainties are assigned one nuisance parameter per background. Then the envelope of the remaining uncertainties listed above is calculated for each background process, i.e. the largest upward and downward deviations from the nominal value are taken as the total theoretical uncertainty and asocciated with one nuisance parameter in the fit. The exceptions are Z renormalisation/factorisation scale variations and $t\bar{t}$ ME and PS uncertainties. These are not included in the envelope, but are associated with separate nuisance parameters. All the theoretical uncertainties considered in the analysis, along with associated nuisance parameters, are listed in Table 7.1.

Theoretical uncertainties on signal

Two types of theoretical uncertainties are considered for the signal samples:

- **Uncertainty on the cross-section:** The nominal cross-section is calculated with Herwig++ at LO level. A conservative uncertainty of 25% is applied to all the signal points.

- **Uncertainty on the acceptance:** Theory uncertainties affect shapes of kinematic variables, and thus can also affect the acceptance of the signal. In particular, the uncertainty on the modelling of initial state radiation (ISR) plays an important role for small mass-splitting signal models relying on an ISR jet. The uncertainties on the acceptance are assesed by generating additional MadGraph5+Pythia samples for which the following two

Parameter	Uncertainty
	$t\bar{t}$
tt_PowAlp	MC generator : POWHEG+JIMMY vs ALPGEN+JIMMY
tt_pythjim	Parton shower : POWHEG+PYTHIA vs POWHEG+JIMMY
PDFttbar	PDF
topTheo	Envelope : ISR/FSR, μ_R and μ_F
	$t\bar{t}$+ W/Z, $t\bar{t}$+ WW
ttbarWZXsec	Cross-section (22 % for ttbar+W/Z)
ttbarWWXsec	Cross-section (50 % for ttbar+WW)
PDFttbarV	PDF
ttbarVTheo	Envelope: FSR, α_S, ME-PS matching scale, μ_R & μ_F, and number of ME partons
	Single top
SingleTopWXsec	Cross-section (6.8 % for Wt)
SingleTopZXsec	Cross-section (50 % for $Z + t$)
PDFsingletop	PDF
SingleTopTheo	Envelope: ISR/FSR, interference and parton shower (PYTHIA vs HERWIG)
	Z + jets
ktfacZ,qfacZ	μ_R and μ_F
PDFZjets	PDF
ZTheoNpart	Number of ME partons
	Dibosons
DibosonsWWZZsec	Cross-section (5 % for WW/ZZ)
DibosonsWZXsec	Cross-section (7 % for WZ)
PDFdibosons	PDF
dbTheo	Envelope : μ_R and μ_F, PS (PYTHIA vs HERWIG), MC (POWHEG vs aMC@NLO)

Table 7.1: Summary of theoretical uncertainties considered in the analysis and nuisance parameters associated to them. Cross-section and PDF uncertainties have a separate nuisance parameter associated, while most of the other uncertainties are contained within the envelope and assigned one nuisance parameter with "*Theo" in the name. The parameters correspond to the names used in the tables showing contributions from various systematic uncertainties.

parameters are varied up and down in turn by a factor two: the MadGraph scale used to determine the event-by-event renormalisation and factorisation scale and the MadGraph parameter used to determine the scale for QCD radiation. The reason to use MadGraph instead of Herwig++ (which is used for the nominal sample) is that it would be computationally challenging to generate all the samples of the full mUED model in Herwig++ for each of the theory-systematic variations. In MadGraph, only the main production and decay process was simulated and the derived uncertainty was applied to the full nominal sample:

$$\begin{array}{lll} pp \rightarrow & g^1 D^1 & \\ & g^1 & \rightarrow U^1 \bar{u} \rightarrow \gamma^1 u \bar{u} \\ & D^1 & \rightarrow Z^1 d \rightarrow \mu^1_L \mu^- d \rightarrow \gamma^1 \mu^+ \mu^- d. \end{array}$$

The uncertainties due to the two MadGraph variations are added up in quadrature. The values range from only 2%-5% for the larger mass splittings ($\Lambda R \sim 40$) up to 8%-23% for the most compressed signal models ($\Lambda R \sim 2$). Smaller dependency was observed on the 1/R parameter as well – as lower 1/R, for the same values of ΛR, implies somewhat smaller mass splittings, models with lower 1/R tend to have somewhat larger uncertainty.

The cross-section and acceptance uncertainties are added-up in quadrature, assigned one nuisance parameter and applied as the uncertainty on the overal normalisation.

Chapter 8

Results

In this chapter the final results of the analysis are presented. In Sec. 8.1 the result of the background-only fit (introduced in Chapter 6) is shown, which provides the final background estimates and the impact of the systematic uncertainties in the signal region. After the validation of the fit, the background estimate is compared to the observed number of data events. No significant excess above the SM expectation is observed. Upper limit at 95% confidence level (CL) on the number of non-SM events in the signal region is derived in Sec. 8.2. The results are further interpreted in terms of upper limits on the parameters of the mUED model. Finally, the combination of the results from the soft-dimuon analysis presented in this thesis and from ATLAS hard-dilepton analysis is also shown.

8.1 Background-only fit

The background-only fit is performed in order to derive the $t\bar{t}$ normalisation factor from the control region with high purity of $t\bar{t}$ events. No signal contamination is taken into account in this setup. Other backgrounds are allowed to vary in the fit within their respective uncertainties. The $t\bar{t}$ normalisation is a free parameter, and is fitted to

$$\mu_{t\bar{t}} = 0.69 \pm 0.10.$$

The background yields before and after the fit and number of observed events in the CR, as well as $\mu_{t\bar{t}}$, are shown in the Tab. 8.1. Here the event yields labeled as "expected" in the lower part of the table denote the nominal MC prediction for backgrounds containing prompt muons, and the nominal data-driven prediction for the fake muon background. "Fitted" yields in the upper part of the table refer to the numbers after the fit – $t\bar{t}$ background has been scaled down by 0.69 and there are some minor changes in the nominal yields for other backgrounds. The agreement between the observed data and the total background after the fit is very good, by construction.

The dimuon invariant mass before and after the fit is shown in Fig. 8.1, where the $M_{\mu\mu} > 60$ GeV corresponds to TCR. Good agreement in the full $M_{\mu\mu}$ range is observed on the right-

	TCR
Observed events	138
Total fitted SM events	138.06 ± 11.80
Fitted $t\bar{t}$ events	114.42 ± 14.61
Fitted Z+jets events	2.70 ± 1.49
Fitted single-top events	14.73 ± 4.93
Fitted dibosons events	3.37 ± 1.63
Fitted $t\bar{t}$+V events	1.35 ± 0.39
Fitted fake muon events	$1.48^{+5.80}_{-1.48}$
Total exp. SM events	189.96 ± 12.34
MC exp. $t\bar{t}$ events	166.36 ± 8.32
MC exp. Z+jets events	2.69 ± 1.50
MC exp. single-top events	14.67 ± 4.96
MC exp. dibosons events	3.38 ± 1.65
MC exp. $t\bar{t}$+V events	1.35 ± 0.39
Data-driven exp. fake muon events	$1.50^{+5.87}_{-1.50}$
$\boldsymbol{\mu_{t\bar{t}}}$	0.69 ± 0.10

Table 8.1: Background-only fit results for the $t\bar{t}$ control region. The lower part of the table gives the nominal MC (data-driven) expectations before the fit, for comparison. Z+jets background includes the Drell-Yan contribution.

hand-side of the figure, after the $t\bar{t}$ background is scaled down by $\sim 30\%$. This relatively large deviation of $\mu_{t\bar{t}}$ from unity is due to the fact that the $t\bar{t}$ MC is too hard at large values of E_T^{miss}. As can be seen from the ratio plot of the upper left distribution in Fig. 6.10, there appears to be a slight downward slope when going towards higher E_T^{miss} values. However, this discrepancy between the data and the background expectation after the fit is covered by the uncertainty band. Furthermore, E_T^{miss} is not used for the extrapolation from TCR to SR, i.e. both TCR and SR have the E_T^{miss} threshold set to 180 GeV. Thus the $t\bar{t}$ estimation in the SR is not expected to be affected by this issue. The E_T^{miss} distribution in TCR before and after the fit is shown in Fig. 8.2, and very good agreement between the data and the SM expectation is observed after the fit.

The uncertainties on yields in the Tab. 8.1 include only the uncertainties affecting the overal normalisation (see Sec. 7.6). The shape uncertainties are implemented on the MC transfer factor and, thus, show up only when extrapolating the result to the signal or the validation regions. Tab. 8.2 shows the breakdown of the uncertainty on the total background estimate in the control region (only the uncertainties larger than 1% are listed). The dominant uncertainty is coming from the $t\bar{t}$ normalisation factor, $\mu_{t\bar{t}}$, followed by the trigger efficiency uncertainty and

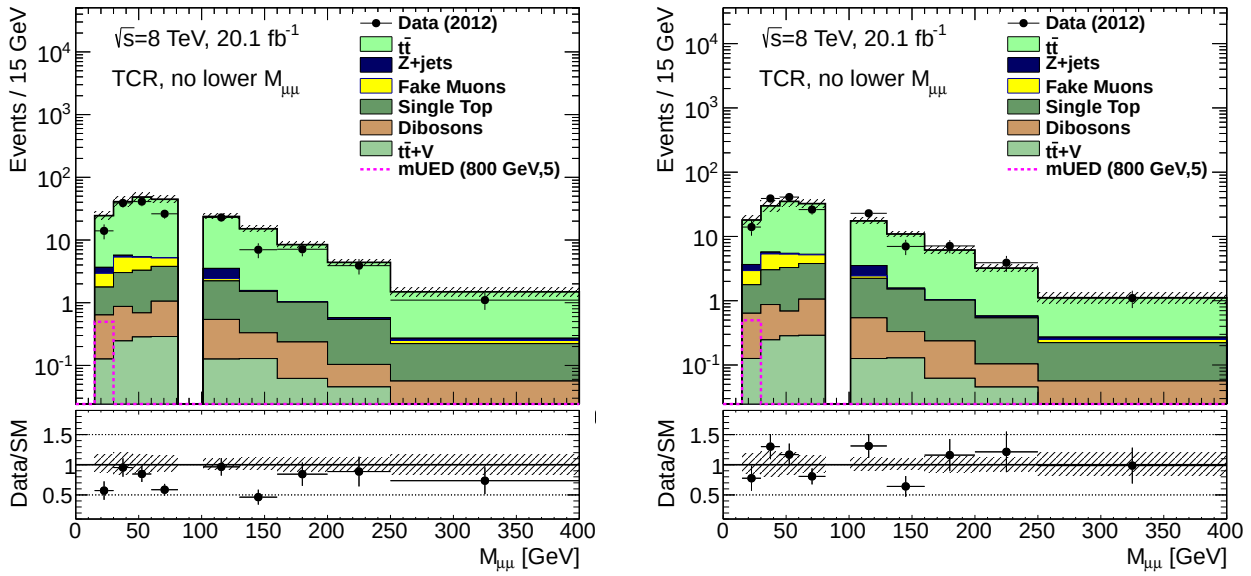

Figure 8.1: $M_{\mu\mu}$ distribution before (left) and after (right) the fit in the $t\bar{t}$ control region, but without the $M_{\mu\mu} > 60$ GeV requirement. Good agreement in the whole $M_{\mu\mu}$ range is observed on the right-hand-side, after the normalisation factor of 0.69 is applied to the $t\bar{t}$ MC. The error band includes MC statistical, b-tagging, JES, JV, JER, lepton energy scale/resolution, E_{T}^{miss} scale/resolution and fake estimation uncertainties.

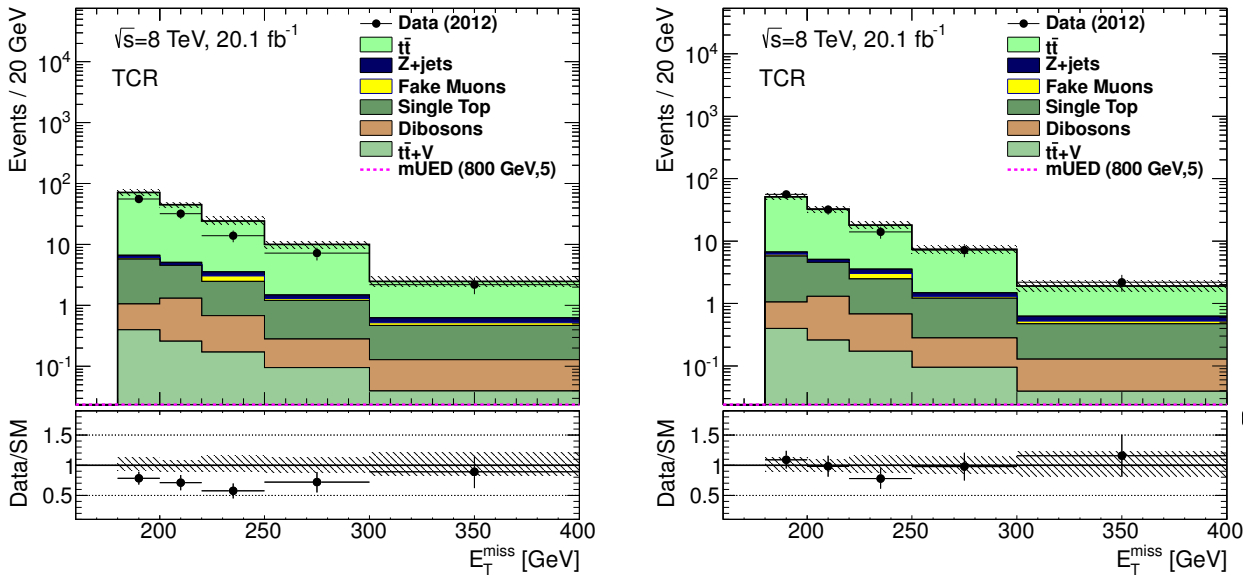

Figure 8.2: E_T^{miss} distribution before (left) and after (right) the fit in the $t\bar{t}$ control region. Good agreement is observed on the right-hand-side, after the normalisation factor of 0.69 is applied to the $t\bar{t}$ MC. The error band includes MC statistical, b-tagging, JES, JV, JER, lepton energy scale/resolution, E_{T}^{miss} scale/resolution and fake muon background uncertainties.

the uncertainty on the fake muon prediction. The sizes of individual uncertainties are derived by setting all other floating nuisance parameters to constant, except the parameter of interest, and then propagating the uncertainty due to this parameter only. Due to possible correlations between the single floating parameters, the squared sum of the individual uncertainties does not necessarily match the total uncertainty.

8.1.1 Extrapolation to the validation regions

The validation regions, defined to be kinematically close to the signal region, but orthogonal to both the control and signal regions, are used to check the agreement between the data and the SM prediction after the background-only fit. The validation regions are not used in the fit to constrain any of the backgrounds, the result of the background-only fit in the TCR is simply propagated to the VRs. Both normalisation and shape systematic uncertainties contribute to the systematic uncertainties in the validation regions. Tab. 8.3 shows the expected and fitted numbers of events in the validation regions[1]. The data and the total background estimate agree well after the fit, especially in VR1 and VR2. Fig. 8.3 is showing E_T^{miss} and $M_{\mu\mu}$ distributions in the three validation regions, after the fit. The agreement with the observed data is good, mostly within the uncertainty band.

[1]Dominant systematic uncertainties affectnig the validation regions can be found in the Appendix B.

Systematic uncertainties (background-only fit)	CRT
Total background expectation	138.06
Total statistical ($\sqrt{N_{\text{exp}}}$)	± 11.75
Total background systematic	± 11.80 [8.55%]
$\mu_{t\bar{t}}$	± 16.11 [11.7%]
Trigger efficiency	± 6.79 [4.9%]
Fake muons prediction	± 5.80 [4.2%]
Single-top: theory envelope	± 4.38 [3.2%]
Single-top: PDF	± 1.90 [1.4%]
Dibosons: theory envelope	± 1.61 [1.2%]

Table 8.2: Breakdown of the dominant systematic uncertainties on the background estimate in the $t\bar{t}$ control region. The individual uncertainties can be correlated, and do not necessarily add up quadratically to the total background uncertainty. The percentages show the size of the uncertainty relative to the total expected background.

	VR1	VR2	VR3
Observed events	119	40	31
Total fitted SM events	116.67 ± 21.78	47.08 ± 9.51	21.55 ± 7.46
Fitted $t\bar{t}$ events	81.00 ± 13.12	20.57 ± 6.01	15.93 ± 3.27
Fitted Z+jets events	5.21 ± 2.53	9.61 ± 4.30	$0.02^{+0.03}_{-0.02}$
Fitted single-top events	7.23 ± 2.82	2.41 ± 0.92	1.22 ± 0.49
Fitted dibosons events	9.72 ± 3.60	13.50 ± 4.97	0.19 ± 0.13
Fitted $t\bar{t}$+V events	0.84 ± 0.26	0.31 ± 0.14	0.17 ± 0.07
Fitted fake muon events	$12.66^{+17.25}_{-12.66}$	$0.69^{+1.74}_{-0.69}$	$4.03^{+6.74}_{-4.03}$
Total exp. SM events	153.43 ± 22.95	56.42 ± 11.60	28.78 ± 7.83
MC exp. $t\bar{t}$ events	117.77 ± 13.16	29.90 ± 8.02	23.16 ± 3.91
MC exp. Z+jets events	5.22 ± 2.55	9.59 ± 4.32	$0.02^{+0.03}_{-0.02}$
MC exp. single-top events	7.20 ± 2.83	2.40 ± 0.92	1.21 ± 0.49
MC exp. dibosons events	9.74 ± 3.63	13.52 ± 5.00	0.19 ± 0.13
MC exp. $t\bar{t}$+V events	0.84 ± 0.26	0.31 ± 0.14	0.17 ± 0.07
Data-driven exp. fake muon events	$12.66^{+17.25}_{-12.66}$	$0.69^{+1.74}_{-0.69}$	$4.03^{+6.74}_{-4.03}$

Table 8.3: Background-only fit results for the vaildation regions. The lower part of the table gives the nominal MC (data-driven) expectations before the fit, for comparison. Z+jets background includes the Drell-Yan contribution.

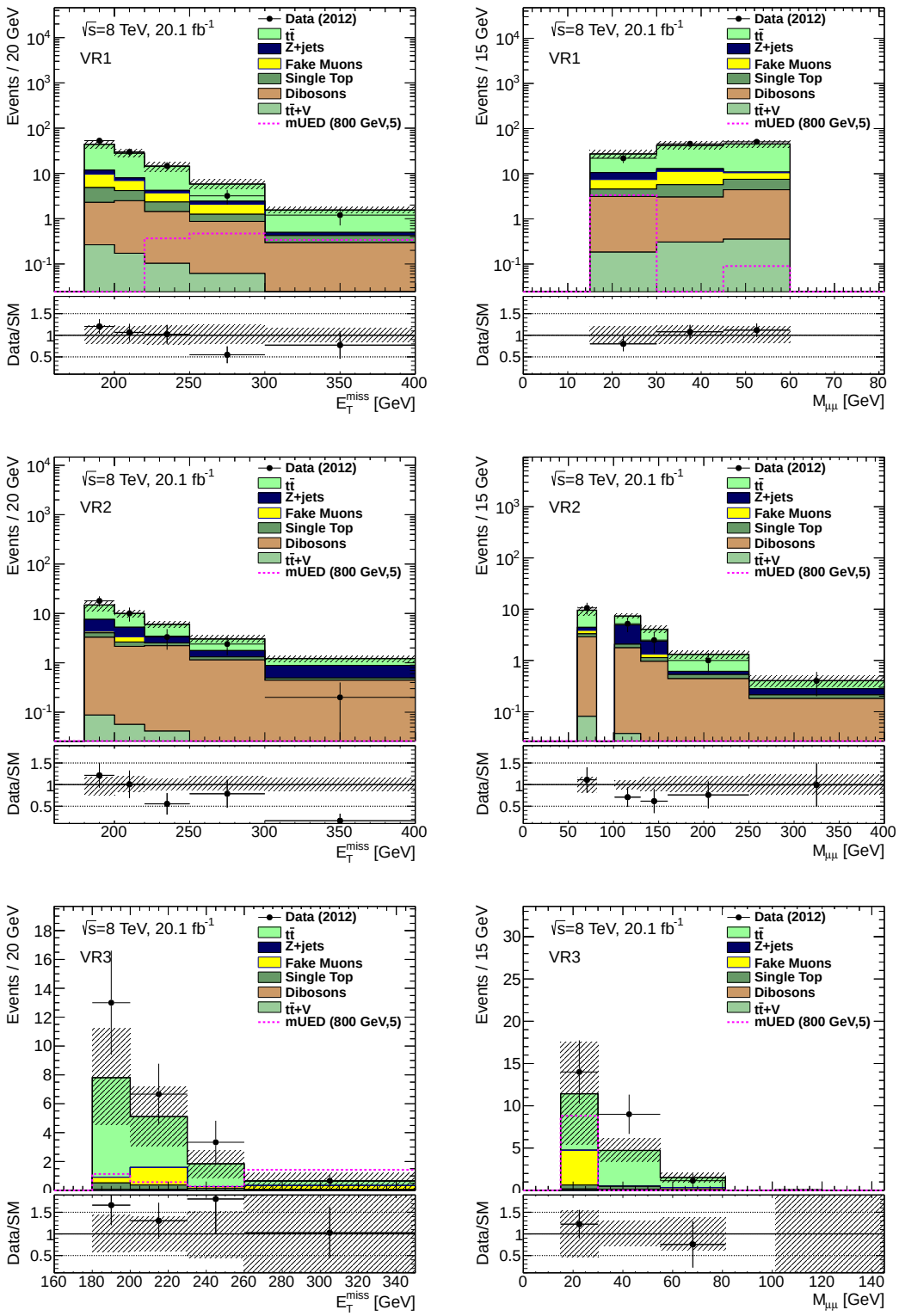

Figure 8.3: Distributions of E_T^{miss} (left) and $M_{\mu\mu}$ (right) after the fit in the three validation regions. The error band includes MC statistical, b-tagging, JES, JVF, JER, lepton energy scale/resolution, E_{T}^{miss} scale/resolution and fake muon background uncertainties.

	SR
Observed events	6
Total fitted SM events	6.02 ± 2.61
Fitted $t\bar{t}$ events	1.79 ± 0.78
Fitted Z+jets events	0.28 ± 0.19
Fitted single-top events	0.24 ± 0.14
Fitted dibosons events	1.37 ± 0.53
Fitted $t\bar{t}$+V events	0.00 ± 0.00
Fitted fake muon events	$2.34^{+2.38}_{-2.34}$
Total exp. SM events	6.83 ± 2.75
MC exp. $t\bar{t}$ events	2.60 ± 1.09
MC exp. Z+jets events	0.28 ± 0.20
MC exp. single-top events	0.24 ± 0.14
MC exp. dibosons events	1.37 ± 0.54
MC exp. $t\bar{t}$+V events	0.00 ± 0.00
Data-driven exp. fake muon events	$2.34^{+2.38}_{-2.34}$

Table 8.4: Background-only fit results for the signal region. The lower part of the table gives the nominal MC (data-driven) expectations before the fit, for comparison. Z+jets background includes the Drell-Yan contribution.

8.1.2 Result in the signal region

After the validation, the result of the background-only fit is extrapolated to the signal region. As in the case of validation regions, the signal region is not used in the fit to constrain the data. The fitted background estimate is 6.02 ± 2.61, while 6 events are observed, resulting in an excellent agreement between the data and the Standard Model expectation. Tab. 8.4 shows the expected and fitted number of background events in the signal region.

The breakdown of the uncertainty on the total background estimation to various components is shown in the Tab. 8.5. The dominant source of the uncertainty is due to the error on the fake muon estimation, amounting to almost 40% versus the total background prediction. The error on the fake muon estimation is dominated by systematic uncertainties (about 60% with respect to the nominal prediction in the SR), while the statistical component amounts to about 47% versus the nominal fake muon prediction. All other uncertainty sources in the signal region have less than 10% impact on the final estimate. The total statistical uncertainty in the third row of Tab. 8.5 is computed as the square root of the number of expected events. It is shown to illustrate the relative impact of the Poisson uncertainty with respect to the total background uncertainty.

Fig. 8.4 is showing the after-fit values of individual nuisance parameters in the background-

Systematic uncertainties (background-only fit)	SR
Total background expectation	6.02
Total statistical ($\sqrt{N_{\text{exp}}}$)	± 2.45
Total background systematic	± 2.61 [43.33%]
Fake muons prediction	± 2.38 [39.5%]
$t\bar{t}$: Powheg vs. Alpgen	± 0.51 [8.5%]
MC statistics	± 0.43 [7.2%]
$t\bar{t}$: theory envelope	± 0.31 [5.2%]
JES: flavor composition	± 0.31 [5.1%]
Dibosons: theory envelope	± 0.30 [5.0%]
$t\bar{t}$: Pythia vs. Herwig/Jimmy	± 0.27 [4.4%]
$\mu_{t\bar{t}}$	± 0.25 [4.2%]
JES: EffectiveNP2	± 0.22 [3.7%]
B-tagging: b-tag efficiency	± 0.22 [3.7%]
B-tagging: light-jet mistag efficiency	± 0.22 [3.7%]
JES: flavor response	± 0.21 [3.4%]
JES: b-jets	± 0.21 [3.4%]
Trigger efficiency	± 0.18 [3.0%]
JES: EtaIntercalibrationModelling	± 0.13 [2.2%]
Single-top: theory envelope	± 0.13 [2.1%]
Lepton efficiency	± 0.11 [1.8%]
Z+jets: renormalisation scale	± 0.09 [1.5%]
Jets: resolution	± 0.09 [1.5%]
E_T^{miss}: scale	± 0.08 [1.3%]
JES: EffectiveNP1	± 0.08 [1.3%]
Z+jets: ME partons	± 0.07 [1.2%]
JES: PileupRhoTopology	± 0.07 [1.2%]
Dibosons: PDF	± 0.06 [0.93%]
WW/ZZ: cross-section	± 0.06 [0.93%]
Z+jets: factorisation scale	± 0.04 [0.64%]
B-tagging: c-jet mistag efficiency	± 0.04 [0.61%]
Single-top: PDF	± 0.03 [0.54%]
Z+jets: PDF	± 0.02 [0.32%]
$t\bar{t}$: PDF	± 0.02 [0.29%]
WZ: cross section	± 0.02 [0.28%]
Single-top+W: cross section	± 0.02 [0.27%]
Pileup	± 0.01 [0.25%]
E_T^{miss}: resolution	± 0.01 [0.24%]

Table 8.5: Breakdown of the dominant systematic uncertainties on the background estimate in the signal region. The individual uncertainties can be correlated, and do not necessarily add up quadratically to the total background uncertainty. The percentages show the size of the uncertainty relative to the total expected background. The uncertainties amounting to less than 0.2% are not shown.

only fit. The input value of the parameters to the fit is zero, with ± 1 shifts corresponding to $\pm 1\sigma$ sizes of the uncertainties. In principle, if the fit is over-constrained, the nuisance parameters could be shifted from their central values ("pulled"), meaning that the fit could find better agreement with the observed data if the distributions were shifted in the direction of the uncertainty in question. Similarly, some uncertainty could be constrained to be smaller that its input value (i.e. smaller than ± 1) if these variations were found to be too large and not consistent with the data. As can be seen on Fig. 8.4, the after-fit values are still centered at zero with error bars still having ± 1 size, i.e. there is no pulling nor constraining of the nuisance parameters. This is expected, since the fit has only one bin to constrain one background and there is simply not enough information to constrain any of the nuisance parameters.

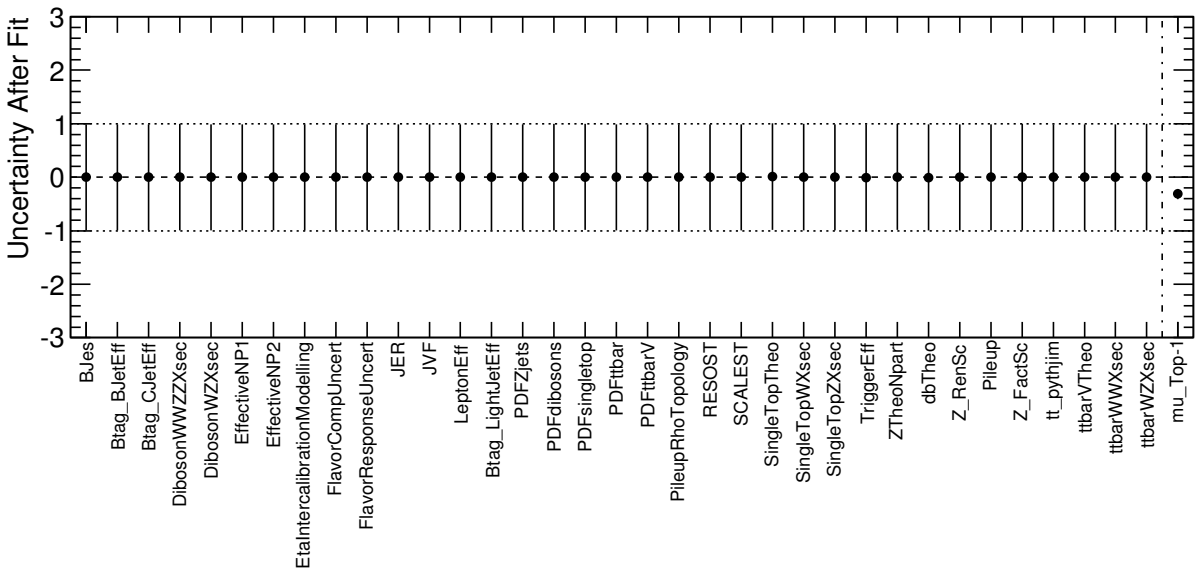

Figure 8.4: Nuisance parameters values and their errors in the signal region after the background-only fit.

E_T^{miss} and the sub-leading muon p_T distributions in the signal region are shown in Fig. 8.5, while Fig. 8.6 is showing the $M_{\mu\mu}$ and the leading muon p_T distributions after all the signal region selections have been applied, except the requirement on the variable shown. Good agreement between the data and the Standard Model expectation can be seen for all the distributions.

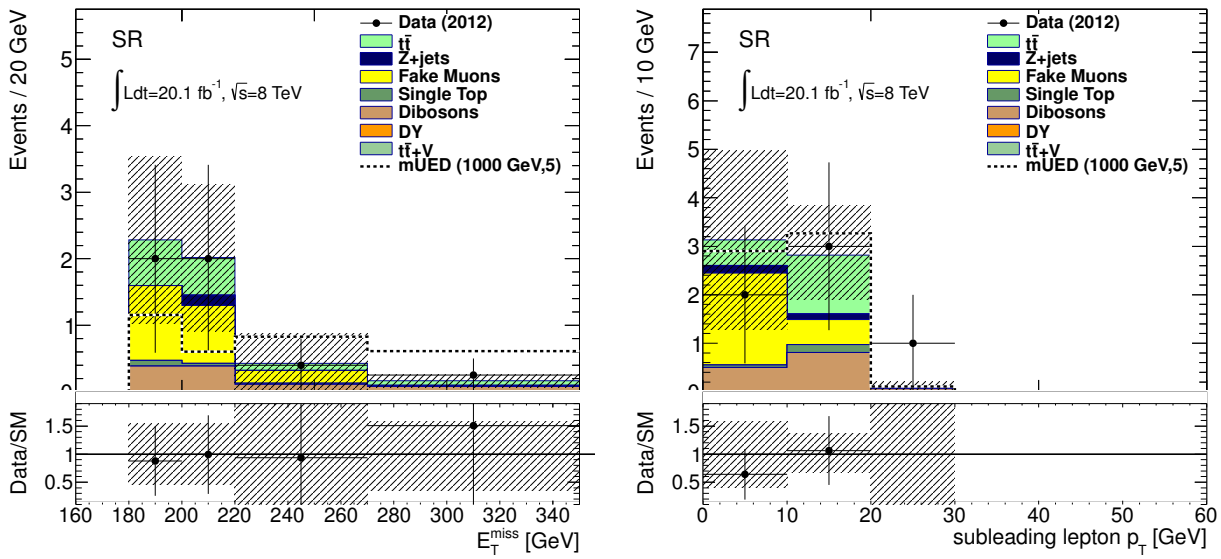

Figure 8.5: E_T^{miss} and $p_T^{2^{\text{nd}}\mu}$ distributions in the signal region. The $t\bar{t}$ MC is normalised in the fit to the data, and the data-driven estimation is performed for the fake muon background. The uncertainty band includes MC statistical, b-tagging, JES, JVF, JER, lepton energy scale/resolution, E_{T}^{miss} scale/resolution and fake muon background related uncertainties.

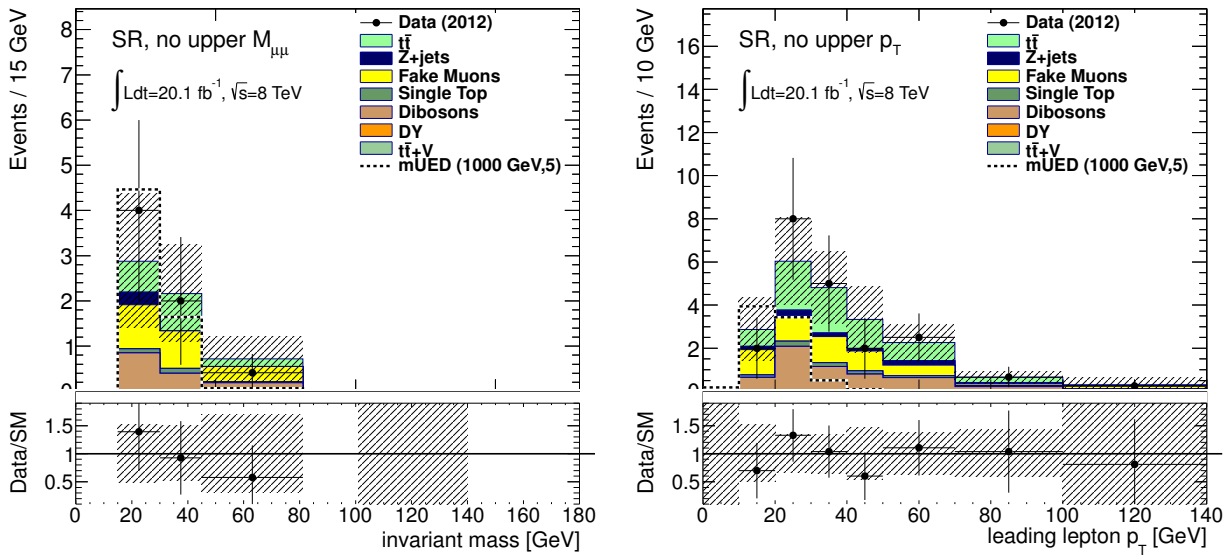

Figure 8.6: $M_{\mu\mu}$ and $p_T^{1^{\text{st}}\mu}$ distributions. All the signal region selection requirements are applied, except the requirement on the variable shown: $M_{\mu\mu} < 60$ GeV is not applied on the left, while $p_T^{1\text{st}\ \mu} < 25$ GeV is omitted on the right. the signal region. The $t\bar{t}$ MC is normalised in the fit to the data, and the data-driven estimation is performed for the fake muon background. The uncertainty band includes MC statistical, b-tagging, JES, JVF, JER, lepton energy scale/resolution, E_{T}^{miss} scale/resolution and fake muon background related uncertainties.

8.2 Limits

Given the absence of an excess above the Standard Model background expectation, the model-independent upper limits at 95% CL are set on the number of non-SM events in the signal region, while the model-specific interpretation is provided in terms of the limits on the mUED parameters. Limits are evaluated in hypothesis tests in which a signal+background model is tested against the background-only assumption (see Chapter 7). The profile log likelihood ratio is used as a test statistic, and the $\mathrm{CL_S}$ method is employed for testing the exclusion of a new physics hypothesis and deriving the upper limits.

8.2.1 Model independent limits

Model independent limits are placed on the visible cross section of a non-SM process, defined as the product of the acceptance, reconstruction efficiency and the production cross section (see Appendix B for more details), evaluated inside the signal region. The number of events in the signal region is used as an input to the fit, and an additional parameter μ_{Sig} is introduced – it represents the non-SM signal strength (constrained to be non-negative). No model-specific assumptions are made for the signal, and no signal-related nuisance parameters are included in the fit. Potential signal contamination in the control region is ignored, which leads to conservative background estimate in the signal region. The input number of signal events in the signal region is set to one, and the signal strength parameter is scanned from $\mu_{\mathrm{Sig}} = 0$ to a value of $\mu_{\mathrm{Sig}} = 20$, in steps of 1. Each time a hypothesis test is performed in which the data is tested against the background+signal model, where the amount of signal contribution is determined by μ_{Sig}. The result of the hypothesis test, obtained by using the asymptotic formulae for the PDF of the test statistic, is delivered in terms of a $\mathrm{CL_S}$ value for each μ_{Sig} being tested. The result of the scan is shown in Fig. 8.7. The upper limit on the number of non-SM events in the signal region is identified as the μ_{Sig} for which the $\mathrm{CL_S}$ value (signified by p-value in Fig. 8.7) was found to be 0.05. The upper limit on the observed cross section $\langle \epsilon\sigma \rangle^{95}_{\mathrm{obs}}$ is obtained by dividing the limit on the number of non-SM events by the integrated luminosity of 20.1 fb^{-1}. The confidence level observed for the background-only hypothesis in this test is denoted as CL_b.

For the purpose of deriving the discovery p-value, the fit is run in the discovery mode, with the data being tested against the background-only hypothesis. The p-value gives the probability that the event yield obtained in a single hypothetical background-only experiment (with $s = 0$) is greater than that observed in this dataset. Since the observed number of data events is consistent with the background-only expectation, one-sided p-value is found to be 0.5. The difference between the p-value and the CL_b mentioned above is in the test statistic used – for the former the conditional profile likelihood is calculated with a signal strength μ_{Sig} set to 0, while the latter uses $\mu_{\mathrm{Sig}} = 1$. The model-independent limits, along with the discovery p-value, are shown in Tab. 8.6.

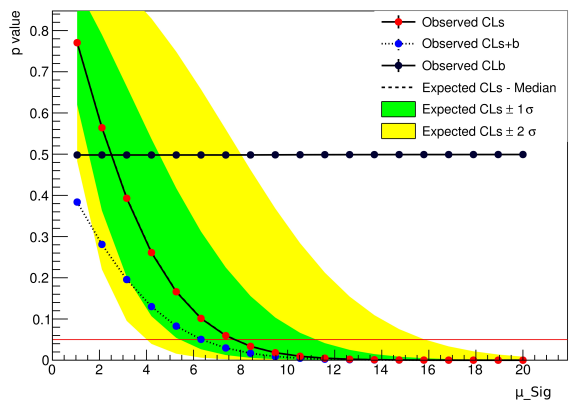

Figure 8.7: Scan of μ_{Sig} when deriving the model independent upper limit on the visible BSM cross section. The result is obtained by using the asymptotic formulae for the PDF of the test statistic. Observed CL_S, $\text{CL}_\text{s+b}$ and CL_b values are shown in red, blue and black dots, respectively. The median expected CL_S is denoted as a black dashed line, residing directly below the observed one, with the green (yellow) bands indicating the $\pm 1\sigma$ ($\pm 2\sigma$) uncertainty on the expected CL_S.

	$\langle\epsilon\sigma\rangle^{95}_{\text{obs}}$[fb]	S^{95}_{obs}	S^{95}_{exp}	CL_b	$p(s=0)$
SR	0.39	7.7	$7.8^{+3.5}_{-2.4}$	0.50	0.50

Table 8.6: Left to right: 95% CL upper limits on the visible cross section ($\langle\epsilon\sigma\rangle^{95}_{\text{obs}}$) and on the number of signal events (S^{95}_{obs}). The third column (S^{95}_{exp}) shows the 95% CL upper limit on the number of signal events, given the expected number (and $\pm 1\sigma$ excursions on the expectation) of background events. The last two columns indicate the CL_B value, i.e. the confidence level observed for the background-only hypothesis, and the discovery p-value ($p(s=0)$).

8.2.2 Exclusion fit and interpretation

As no excess above the SM expectation is observed, the model-dependent interpretation is given by placing the exclusion limits on the mUED model. For this purpose the fit is rerun in the exclusion mode, in which a signal MC sample is taken into account in both the control and signal regions. The signal sample has the same systematic uncertainties assigned to as the background samples. In addition, a nuisance parameter covering both the signal cross section and the acceptance uncertainties is added. The signal strength is a free floating parameter μ_{Sig}, the same as $\mu_{t\bar{t}}$. The number of events in the signal region is now also included as an input to the fit, and $\mu_{t\bar{t}}$ and μ_{Sig} are simultaneously extracted.

An example of a result of the exclusion fit using the ($R^{-1} = 900$ GeV, $\Lambda R = 10$) point is shown in Tab. 8.7. As the signal contamination in the control region is zero, $\mu_{t\bar{t}}$ is not affected by the presence of the signal, and is the same as in the case of the background-only fit. The MC signal expectation in the signal region is about 8 events, significantly overshooting the observed data, thus the μ_{Sig} is fitted to only 0.01. The large uncertainty on the signal contribution is a result of relatively large anti-correlations in the signal region (about 50%) between the fake muon background and μ_{Sig} (see Appendix B).

The exclusion fit is run for each point in the mUED signal grid, and each time a hypothesis test is performed using the CL_S method. The probability density functions used in the CL_S calculation are obtained using the asymptotic formulae. The signal point is considered excluded at 95% confidence level (CL) if the CL_S value is found to be smaller than 0.05. Fig. 8.8 is showing the 95% CL exclusion contour in the $R^{-1} - \Lambda R$ plane. The red curve shows the observed limit calculated by using the nominal signal cross sections. The limits calculated with the nominal cross section modified up or down by the amount the theoretical uncertainty on the signal (which includes both the cross section uncertainty and the uncertainty on the acceptance) are represented by red dotted curves. The expected exclusion limit in the background only hypothesis is shown by the blue dashed line, and the yellow band indicates the $\pm 1\sigma$ variations on the expected limit due to the experimental and background-only theory uncertainties. As the expected and observed numbers of events in the signal region are in excellent agreement, the expected and observed exclusion contours lie exactly on top of each other.

The most stringent limits are obtained for $\Lambda R = 5$ signal points, where values of R^{-1} (approximately corresponding to the LKP mass) are excluded up to 940 GeV. This region corresponds to mUED models with relatively highly compressed mass spectra, and is theoretically best motivated part of the phase space (see discussion in Sec. 1.7 of Chapter 1). The limit gets weaker for higher values of ΛR, where the mass splittings between KK states become larger, resulting in more energetic objects (jets, leptons) in the final state. The sensitivity of the analysis in this region is decreased due to the requirement of soft leptons with an upper bound of 25 GeV on their p_T, which reduces the acceptance for models producing harder leptons (as well as due to the relatively loose requirements on jet momenta). The analysis again looses the sensitivity for highly compressed points with $\Lambda R = 2$, where the signal acceptance is decreased due to extremely low p_T leptons, falling even below the threshold of 6 GeV. Values of R^{-1}

	TCR	SR
Observed events	138	6
Total fitted events	138.01 ± 12.55	6.07 ± 4.14
Fitted mUED (900 GeV, 10) events	0.00 ± 0.00	$0.08^{+5.13}_{-0.08}$
Fitted $t\bar{t}$ events	114.48 ± 15.53	1.78 ± 0.77
Fitted Z+jets events	2.69 ± 1.49	0.28 ± 0.19
Fitted single-top events	14.66 ± 4.97	0.24 ± 0.14
Fitted dibosons events	3.38 ± 1.65	1.37 ± 0.53
Fitted $t\bar{t}$+V events	1.35 ± 0.39	0.00 ± 0.00
Fitted fake muon events	$1.45^{+5.83}_{-1.45}$	2.32 ± 2.10
Total exp. events	189.96 ± 12.35	15.16 ± 4.25
MC exp. mUED (900 GeV, 10) events	0.00 ± 0.00	8.33 ± 2.77
MC exp. $t\bar{t}$ events	166.36 ± 8.32	2.60 ± 1.09
MC exp. Z+jets events	2.69 ± 1.50	0.28 ± 0.20
MC exp. single-top events	14.67 ± 4.97	0.24 ± 0.14
MC exp. dibosons events	3.38 ± 1.65	1.37 ± 0.54
MC exp. $t\bar{t}$+V events	1.35 ± 0.39	0.00 ± 0.00
data-driven exp. fake muon events	$1.50^{+5.87}_{-1.50}$	$2.34^{+2.38}_{-2.34}$
$\boldsymbol{\mu_{t\bar{t}}}$	0.69 ± 0.10	
$\boldsymbol{\mu}_{\mathrm{Sig}}$	$0.01^{+2.44}_{-0.01}$	

Table 8.7: Exclusion fit results for the control and signal regions. The lower part of the table gives the nominal MC (data-driven) expectations before the fit, for comparison. Z+jets background includes the Drell-Yan contribution.

below 780 GeV are excluded for any $\Lambda R > 2$. In comparison to previous ATLAS searches in 0- and 2-lepton channels (see Fig. 1.11), the limit on R^{-1} has been extended by ~ 100 GeV (~ 50 GeV) for $\Lambda R = 5$ ($\Lambda R = 20$), thus successfully covering the region targeted by the analysis.

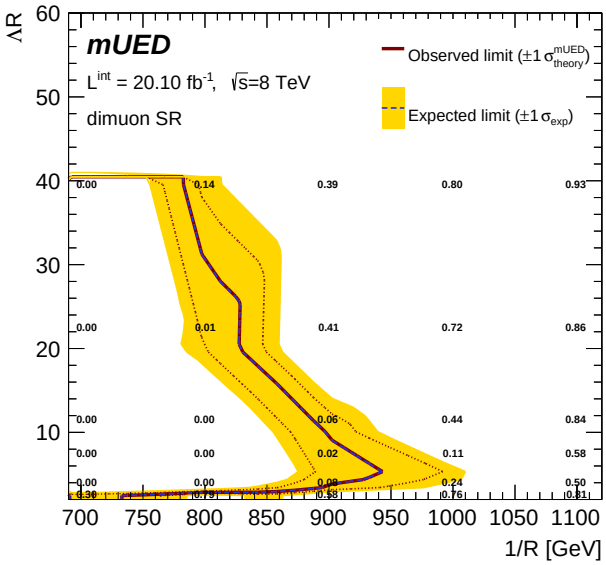

Figure 8.8: 95% CL exclusion limits in the mUED model. The blue dashed line shows the expected limits, with the yellow band indicating the $\pm 1\sigma$ variation in the median expected limit due to the experimental and background-only theory uncertainties. The observed nominal limit is indicated by the solid dark red line with the dark red dotted lines being obtained by taking into account the theoretical uncertainties on the signal cross section. The numbers inside the plot show the observed $\mathrm{CL_S}$ values.

8.2.3 Combination with hard dilepton analysis

The soft dimuon analysis presented in this thesis was specifically designed to cover low ΛR values of mUED model. A hard dilepton analysis targetting SUSY models with lepton rich signatures was conducted in ATLAS at the same time [117]. Since both mUED and SUSY signatures, within a certain set of models, are characterised by cascade decay chains ending with the lightest particle of the model producing a relatively large E_T^{miss}, the hard dilepton analysis naturally yielded some sensitivity within the mUED model. For the final publication the two analysis are thus combined. Both analyses use the same 8 TeV dataset, object definitions and Monte Carlo samples, and employ the same fitting strategy to estimate the contribution of dominant backgrounds. Since the control and signal regions are not completely orthogonal between the analyses, full statistical combination of the results is not possible. Instead, the combination was done by taking the best expected exclusion limit at each signal point in the mUED grid. The result is shown in Fig. 8.9. The hard dilepton analysis requires two leptons with $p_T > 10$, 14

GeV and is therefore sensitive to mUED models with larger mass splittings, i.e. $\Lambda R \geq 13$. The soft dimuon analysis remains dominant for signals with smaller mass splittings. The two analyses are nicely complimentary in covering the mUED space, resulting in the combined limit being relatively uniform for all ΛR and excluding values of R^{-1} up to 950 GeV.

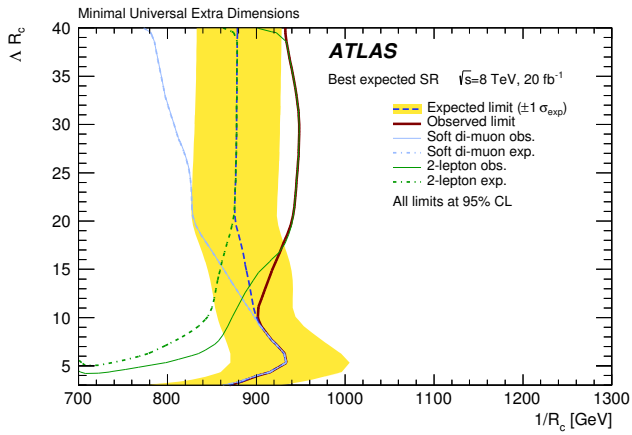

Figure 8.9: 95% CL exclusion limits from the combination of the soft dimuon and hard dilepton analyses in the mUED model [117]. The blue dashed line shows the expected limits, with the yellow band indicating the $\pm 1\sigma$ variation in the median expected limit due to the experimental and background-only theory uncertainties. The observed nominal limit is indicated by the solid dark red line with the dark red dotted lines being obtained by taking into account the theoretical uncertainties on the signal cross section. The blue and green full (dashed) lines show the observed (expected) exclusion obtained by the soft dimuon and hard dilepton analyses, respectively.

Chapter 9

Summary and conclusion

The search for the Minimal Universal Extra Dimensions (mUED) in the final state involving two low momentum muons, jets and missing transverse energy (E_T^{miss}) with the ATLAS detector was presented in this thesis. The analysis used the full 2012 dataset of pp collisions at the centre-of-mass energy of 8 TeV, amounting to the integrated luminosity of 20.1 fb^{-1}.

The mUED model is a very interesting extension of the Standard Model of particle physics, in particular due to a viable dark matter candidate it offers in the form of the lightest Kaluza-Klein particle (LKP) - the Kaluza-Klein (KK) photon. The KK photon is, along with the supersymmetric neutralino, one of the most plausible candidates for a weakly-interacting massive particle (WIMP) form of dark matter. Since mUED states contribute to the electroweak precision observables only at the loop level, the KK photon is allowed to be as light as few hundred GeV and is accesible at the LHC. The mUED mass spectrum for the theoretically most motivated part of the parameter space is relatively compressed, resulting in low momentum (soft) objects (jets, leptons) in the final state. Thus the characteristic signature of mUED at the LHC consists or relatively soft leptons and jets, in addition to the E_T^{miss} caused by the LKP escaping detection. The LHC limits on the LKP mass prior to this analysis have been relatively weak owing in large part to the mUED signature characterised by soft objects – the final state which is challenging in the high-luminosity and high-energy collisions at the LHC. The work for this thesis was conducted within a larger ATLAS analysis effort focusing on the final states involving at least one lepton, in addition to jets and missing transverse energy, and having the interpretation within the supersymmetric models.

In terms of the Standard Model backgrounds, one of the main challenges for the soft-lepton final states consisted in reducing and controlling the processes involving fake (non-prompt) leptons. Thus a large part of the research in this thesis was dedicated to optimising the selection for real (prompt) leptons having low momentum (low momentum is defined as $6(7) < p_T < 25$ GeV for muons (electrons)). The most important handle for distinguishing real from fake leptons proved to be the isolation – the amount of energy flow around a lepton candidate measured by the calorimeter and the tracking systems. After the dedicated study, the rate of fake muons with $p_T < 25$ GeV being identified as prompt was reduced by 50%, resulting

in $20\% - 25\%$ increase in the signal-to-background ratio. Similar increase of the signal-to-background ratio was achieved for electrons as well. The optimised isolation was adopted for soft leptons in all analyses in the joint publication [117]. The improvement proved to be of special importance for the soft dimuon final state, as the fake muon background is one of the dominant processes in the signal region.

As the processes involving fake muons are not expected to be reliably simulated in the Monte Carlo, the contribution of this background to the signal region was estimated in a fully data-driven way. The isolation efficiencies of fake and real muons were measured in the data, and used as an input to the matrix method. Other dominant background is the top-quark pair production ($t\bar{t}$). It was estimated in a semi-data-driven way, relying on a good description of the process by the Monte Carlo simulation, but adjusting the overal normalisation of the sample to the data. The normalisation factor was extracted in a profile log-likelihood fit in a dedicated control region, and the result was extrapolated to the signal region. For other minor backgrounds (dibosons, single-top, $t\bar{t}$+V and Z+jets) a purely Monte Carlo-based estimation was used. The total Standard Model background in the signal region was estimated to be 6.02 ± 2.61 events.

No excess above the Standard Model expectation was found in the signal region, with the observed data events being 6. Model-independent upper limit on the visible cross section of 0.39 fb was derived using the $\mathrm{CL_S}$ method. The result was interpreted also in the context of the mUED model. Limits were set in the $\Lambda R - R^{-1}$ plane, where R^{-1} is the compactification radius of the extra dimension, Λ is the ultra-violet cut-off scale of the theory and the parameter ΛR characterises the mass splittings between the KK states. The most stringent limits are obtained for $\Lambda R = 5$ region, where values of R^{-1} (approximately corresponding to the LKP mass) are excluded up to 940 GeV. The $\Lambda R \leq 5$ region is also theoretically best motivated part of the phase space, as ΛR values above 5 would result in the instability of the Higgs vacuum. Compared to previous ATLAS and CMS searches, the limit on R^{-1} has been extended by ~ 100 GeV (~ 50 GeV) for $\Lambda R = 5$ ($\Lambda R = 20$) region, thus successfully covering the compressed-spectrum models targeted by the analysis, and bridging the gap between 0-lepton searches (sensitive to even more compressed mass spectra at $\Lambda R \leq 3$) and searches involving hard leptons (usually sensitive to models with $\Lambda R \geq 10$).

The analysis presented in this thesis places the most stringent limits on the LKP mass for $\Lambda R \sim 5$ region up to date. It is the first dedicated search for mUED in the final state involving two soft muons, the signature which is challenging in the high interaction-rate environment of the LHC *pp* collisions. The analysis has been designed and optimised primarily for the mUED signal, however, other BSM models, such as compressed Supersymmetry, could also result in similar final states, extending the significance of this work beyond testing the mUED model. Since the soft-lepton signatures, produced by new-physics models with compressed mass spectra, are not well covered by analyses typically relying on hard objects in the final state, it might be the reason new physics has not been observed yet. Subsequent reinterpretations of the model-independent limits on the visible cross section derived in this thesis could constrain other BSM scenarios resulting in similar signatures.

In view of the coming LHC Run II with the increased centre-of-mass energy of 13 TeV, the prospects for mUED search are becoming even more tantalising. If the LKP is the dark-matter particle, the preferred value for its mass, based on dark matter relic density, should lie in $1300-1500$ GeV range. Provided the Standard Model backgrounds are controlled sufficiently well, the increase in mUED cross sections at higher energies could increase the signal-to-background ratio enough to probe this interesting region.

Appendix A

More details for the theory

A.1 Symmetries in the Standard Model

Symmetries play a central role in particle physics [1],[8]. The property of a symmetry transformation of a physical system is that it leaves certain features of the system unchanged, i.e. invariant. An important implication of this observation is the existence of conservation laws in physics. In 1918 Emmy Noether proved her famous theorem that states that whenever there is a continuous symmetry of Lagrangian, there is a conservation law associated to it. For example, as a result of the invariance of physics laws under spatial and time translations (global continuous symmetries), momentum and energy are the corresponding conserved, i.e. time-independent, quantities. In quantum mechanics the symmetry of exchange of identical particles lead to a classification of all elementary particles as either bosons or fermions. The bosonic wave function is invariant under interchange of two identical particles, while the fermionic one changes sign when two identical particles are interchanged.

In the Standard Model the theories of the three fundamental non-gravitational forces are based on the principle of local gauge invariance. The SM gauge symmetry group is well established $\mathrm{SU}(3)_C \times \mathrm{SU}(2)_L \times \mathrm{U}(1)_Y$, where the $\mathrm{SU}(3)_C$ part corresponds to QCD (quantum chromodynamics), as the theory of the strong interactions, and the $\mathrm{SU}(2)_L \times \mathrm{U}(1)_Y$ is the gauge group of Glashow-Salam-Weinberg (GSW) theory of unified electromagnetic and weak interactions. The local gauge invariance implies the existence of massless spin 1 bosons which mediate the interaction. The $\mathrm{SU}(3)_C$ symmetry gives rise to 8 massless gluons with colour as the corresponding quantum number. The quantum numbers of $\mathrm{SU}(2)_L \times \mathrm{U}(1)_Y$ symmetry are weak isospin and hypercharge, with $W^{\pm}$ and Z vector bosons for weak interaction, and photon mediating the electromagnetic force. However, the gauge symmetry group $\mathrm{SU}(2)_L \times \mathrm{U}(1)_Y$ is spontaneously broken by the Higgs mechanism down to U(1) of electromagnetism, and, as a result, the weak bosons acquire mass.

A.1.1 Gauge symmetries

In the framework of Lagrangian field theory particle equations of motion can be obtained from the Euler-Lagrangian equation

$$\partial_\mu \left(\frac{\partial \mathcal{L}}{\partial(\partial_\mu \phi)} \right) - \frac{\partial \mathcal{L}}{\partial \phi} = 0, \tag{A.1}$$

where $\phi(x_\mu)$ is a field describing the particle, ∂_μ stands for $\frac{\partial}{\partial x_\mu}$, and $\mu = 1, ..., 4$ are the space-time indices. Any symmetry of the physical system is reflected in the Lagrangian being invariant under the corresponding unitary transformation. To illustrate the principle of the local gauge symmetry, let us take as an example a Lagrangian describing a free fermion of mass m

$$\mathcal{L} = i\bar{\psi}\gamma_\mu \partial^\mu \psi - m\bar{\psi}\psi \tag{A.2}$$

If inserted into the Eq (A.1), it yields Dirac equation

$$(i\gamma_\mu \partial^\mu - m)\psi = 0, \tag{A.3}$$

where γ_μ are the Dirac matrices. The Lagrangian (A.2) is invariant under the global unitary phase transformation of the form $\psi \rightarrow \psi' \equiv e^{i\alpha}\psi$, where "global" refers to the phase α not having any dependence on the space-time coordinate x. If, however, we require the local symmetry, the Lagrangian has to be invariant under the transformation

$$\psi(x) \rightarrow e^{i\alpha(x)}\psi(x). \tag{A.4}$$

Due to the derivative in (A.2), this implies introducing a new field A_μ transforming as

$$A_\mu(x) \rightarrow A_\mu(x) + \frac{1}{e}\partial_\mu \alpha(x). \tag{A.5}$$

and adding an additional term to the Lagrangian in the form of $e\bar{\psi}\gamma^\mu A_\mu \psi$. This term represents the interaction between matter and gauge fields with the coupling strength e. Additionally, a kinetic energy term of the gauge fields should be added and the full Lagrangian then becomes

$$\mathcal{L} = \bar{\psi}(i\gamma_\mu \partial^\mu - m)\psi + e\bar{\psi}\gamma^\mu A_\mu \psi - \frac{1}{4}F_{\mu\nu}F^{\mu\nu}, \tag{A.6}$$

where $F_{\mu\nu}$ is the field strength tensor satisfying

$$F_{\mu\nu} = \partial_\nu A_\mu - \partial_\mu A_\nu - ie[A_\mu, A_\nu]. \tag{A.7}$$

Since the addition of a mass term $\sim m^2 A_\mu A^\mu$ is prohibited by gauge invariance, the gauge particle must be massless. In the case of Abelian U(1) symmetry, the commutator vanishes, $[A_\mu, A_\nu]$=0, and the Lagrangian (A.6) describes the interacting theory of QED (quantum electrodynamics). In an analogous way, by imposing local gauge invariance of non-Abelian $SU(3)_C$ symmetry, a QCD Lagrangian can be obtained.

A.1.2 QCD Lagrangian

With the reasoning analogous to the one from section A.1.1, the locally gauge invariant QCD Lagrangian reads:

$$\mathcal{L} = \bar{q}(i\gamma_\mu \partial^\mu - m)q - g(\bar{q}\gamma^\mu T_a q)G^a_\mu - \frac{1}{4}\mathcal{G}^a_{\mu\nu}\mathcal{G}^{\mu\nu}_a, \tag{A.8}$$

where q and G^a_μ denote the quark and gluon fields, respectively, and $\mathcal{G}$ is the field strength tensor. The same Lagrangian term applies to every quark color (red, blue, green), and flavour (u,d,c,s,t,b). For $\mathrm{SU}(3)_C$ color interactions, the simple phase transformation $e^{i\alpha_a(x)}$ has to be replaced by a unitary operator acting in the 3-dimensional color-space

$$q(x) \to e^{i\alpha_a(x)T_a} q(x), \tag{A.9}$$

where T_a with $a = 1, .., 8$ are a set of linearly independent 3×3 traceless matrices, and α_a are the group parameters. The Gell-Mann matrices λ_a[1] are the conventional choice for the generators of color transformations, $T_a = \frac{\lambda_a}{2}$. The T_a matrices satisfy the commutation relations

$$[T_a, T_b] = i f_{abc} T_c, \tag{A.10}$$

where f_{abc} are the structure constants characterising the group. Imposing the local invariance requires introducing 8 massless gluon fields transforming as

$$G^a_\mu \to G^a_\mu - \frac{1}{g}\partial_\mu \alpha_a - f_{abc}\alpha_b G^c_\mu. \tag{A.11}$$

The last term appears due to the non-Abelian nature of $\mathrm{SU}(3)_C$. The field strength tensor $\mathcal{G}^a_{\mu\nu}$ is defined as

$$\mathcal{G}^a_{\mu\nu} = \partial_\mu G^a_\nu - \partial_\nu G^a_\mu - g f_{abc} G^b_\mu G^c_\nu. \tag{A.12}$$

The QCD Lagrangian (A.8) is also invariant to the global U(1) phase transformations. This symmetry leads to the barion conservation number.

A.1.3 Electroweak Lagrangian

Let us write out the complete electroweak Lagrangian in several parts. The kinetic energies and self-interactions of $W^\pm$, Z, γ are contained in

$$\mathcal{L}_K = -\frac{1}{4}\boldsymbol{W}_{\mu\nu}\mathbf{W}^{\mu\nu} - \frac{1}{4}B_{\mu\nu}B^{\mu\nu}. \tag{A.13}$$

Lepton and quark kinetic energies and their interactions with $W^\pm$, Z, γ have the form

$$\mathcal{L}_I = \bar{L}\gamma^\mu \left(i\partial_\mu - g\frac{1}{2}\boldsymbol{\tau}\cdot\boldsymbol{W_\mu} - g'\frac{Y}{2}B_\mu\right) L + \bar{R}\gamma^\mu \left(i\partial_\mu - g'\frac{Y}{2}B_\mu\right) R, \tag{A.14}$$

where L denotes a left-handed fermion doublet, and R denotes a right-handed fermion singlet. Generators of $\mathrm{SU}(2)_L$ symmetry, usually the Pauli matrices, are denoted as $\boldsymbol{\tau}$. $W^{\pm}$, Z, γ and Higgs masses and couplings are contained in

$$\mathcal{L}_H = \left| \left(i\partial_\mu - g\frac{1}{2}\boldsymbol{\tau}\cdot\mathbf{W}_\mu - g'\frac{Y}{2}B_\mu \right) \right|^2 \phi - V(\phi), \tag{A.15}$$

where $V(\phi)$ is the Higgs potential. Finally, lepton and quark masses and couplings to Higgs can be written as

$$\mathcal{L}_M = -G_\ell \left(\bar{\nu}\ ,\ \bar{\ell}\right)_L \phi\, \ell_R - G_d \left(\bar{q}_u\ ,\ \bar{q}_d\right)_L \phi\, q_R^d - G_u \left(\bar{q}_u\ ,\ \bar{q}_d\right)_L \phi_c\, q_R^u + h.c., \tag{A.16}$$

where ϕ is the Higgs field giving mass to lower members of the weak isospin doublets, and ϕ_c form of the field gives mass to the upper members of quark doublets:

$$\phi = \frac{1}{\sqrt{2}}\begin{pmatrix} 0 \\ v + h(x) \end{pmatrix}, \quad \phi_c = \frac{1}{\sqrt{2}}\begin{pmatrix} v + h(x) \\ 0 \end{pmatrix}. \tag{A.17}$$

The couplings of Higgs to fermions (G_ℓ, G_d, G_u) are free parameters, i.e. the fermion masses are not predicted by the model. The relation between Higgs vacuum-expectation value v, $\mathrm{SU}(2)_L$ coupling g and weak interaction coupling G is given by

$$\frac{1}{2v^2} = \frac{g^2}{8M_W^2} = \frac{G}{\sqrt{2}}, \tag{A.18}$$

from which, using the empirical value for G, follows that v=246 GeV. The electroweak theory successfully predicted $W^{\pm}$ and Z masses using the relations [9]

$$M_W \simeq 38.6\mathrm{GeV}\ /\ \sin\theta_W\ , \quad M_Z \simeq M_W\ /\ \cos\theta_W. \tag{A.19}$$

A.2 Large Extra Dimensions

The idea of large extra dimensions (LED) was proposed by Arkani-Hamed, Dimopulous and Dvali (ADD) [27]. The ADD approach attempts to solve the hierarchy problem by introducing extra dimensions compactified a la Kaluza-Klein in which only gravity can propagate. All the other fields are localised on the SM brane in the $(4 + N)$-dimensional space. Our 4D gravitational potential

$$V(r) = \frac{1}{M_{Pl}^2}\frac{m_1 m_2}{r}, \tag{A.20}$$

can be generalized to the $(4 + N)$-dimensional space as

$$V(r) = \frac{1}{M_D^{N+2}}\frac{m_1 m_2}{r^{N+1}}, \tag{A.21}$$

where M_D is the fundamental Planck scale in the $(4+N)$-dimensional world. At distances $r << R$, where R is the size of N extra dimensions, Eq. (A.21) describes the fundamental $(4+N)$-dimensional gravitational potential. However, at distances much greater than the ED size, $r >> R$, the gravitational flux in ED can only go as far as R, and the potential in Eq. (A.21) is modified to

$$V(r) = \frac{1}{M_D^{N+2} \cdot R^N} \frac{m_1 m_2}{r}. \tag{A.22}$$

Comparing Eq. (A.20) to Eq. (A.21) we find the relation between the 4D Planck scale M_{Pl}, the fundamental Planck scale in $(4+N)$ dimensions M_D, and the radius of the extra dimensions R as

$$M_{Pl}^2 \sim M_D^{N+2} R^N. \tag{A.23}$$

For large enough R and/or N, the $(4+N)$-dim gravity in Eq. (A.21) can be made as strong as desired. At distances large compared to the size R, the effective 4D gravitational potential assumes our familiar $1/r$ form with the effective 4D M_{Pl} of $\sim 10^{19}$ GeV. The gravity is effectively "diluted" and its projection on our SM 4-dim brane is thus so much weaker in scale than the other forces.

By setting the $(4+N)$-dim gravity scale to be of the size $M_D \sim$ TeV and adjusting the number of extra dimensions N, the size of ED can be as large as thenth of a mm[1] ($\sim$ eV^{-1}, equivalently). In the effective 4D theory, the 5D graviton field will appear as a massless graviton plus an infinite tower of 4D KK gravitons with the mass splitting of $\sim 1/R$ (which can be as small as an eV). Each of the KK excitations will have the interaction strength of $1/M_{Pl}$ with the normal matter. However, since their mass is so small, a large number of these KK gravitons is accesible at $\sim$ TeV energies. For example, in the case of $n = 7$ ED with the radius of the smallest one being ~ 1 fm, as many as 10^4 KK gravitons are accesible along each ED, translating into a total of $10^{4N} = 10^{28}$ modes which can be excited [118]. Thus the gravitational interaction is effectively magnified by a large factor, which can then have significant phenomenological consequences. For example, a gluon created in a proton-proton collision could radiate a graviton, resulting in a "monojet" signature - a jet recoiling against a graviton which produces only missing transverse momentum in the detector (Fig. A.1 left). Another effect of gravitons would be an enhancement Drell-Yan or diboson spectrum at high invariant masses due to additional diagrams involving virtual graviton exchange (Fig. A.1 right). Yet another interesting signature of ADD is a black hole production – lowering the gravity scale down to TeV level means we could observe quantum black holes at the LHC.

In ADD scenario, the fundamental question about the hierarchy is actually not completely gone - the energy hierarchy between Planck and weak scales is converted into the geometrical hierarchy of this (4+N)-dim world, the question why the radii of these ED are so much larger than the thickness of our SM brane in the extra dimensions.

[1]Recent tests of the gravitational inverse-square law constrain the size of the gravity-only ED to be below $0.01 - 0.1$ mm [23], [24].

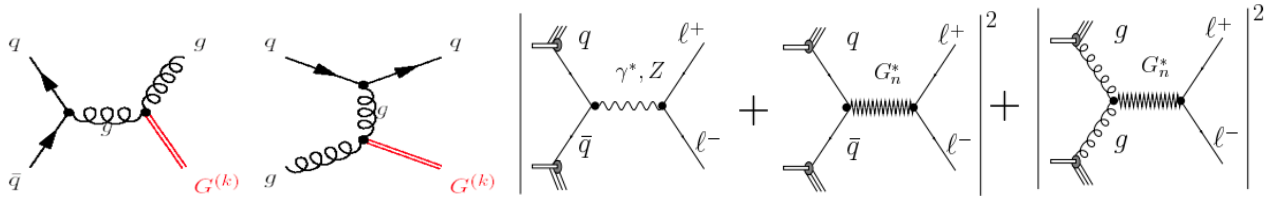

Figure A.1: Feynman diagrams including effects of ADD gravitons. Left: graviton production in association with a jet (monojet signature) produces large missing transverse energy in the detector. Right: Virtual graviton exchange modifies the Drell-Yan cross section [118].

The downside of the ADD scenario is that having the Planck scale at a few TeV makes it impossible for the coupling constants to meet at one point, i.e. there is no GUT (unless the log running of the constants is modified to a power-like running). Another issue arises with the proton stability - at the scales at which gravity is strong, the barion and lepton number (global charges) conservation can be violated, thus enabling proton to decay. For example, a black hole can swallow the proton, or a wormhole[2] can suck the global charge from our universe and dump it to another one. Such effects can, however, be avoided by e.g localising quark and lepton fields at the opposite z sides of our D-brane (z is the ED direction) [119]. This scenario also has a good point for flavorodynamics - if we assume the brane is 4-layered (1 layer corresponding to Higgs, and other 3 layers to 3 generations of fermions), then 3rd generation being the closest to the Higgs makes them naturally heavier (Fig. A.2).

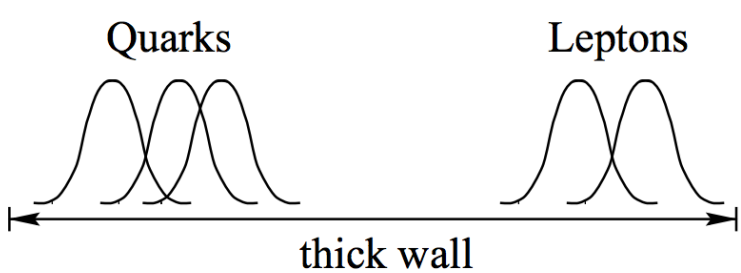

Figure A.2: Profile of Standard Model fermion wave functions (vertical axis) in the extra dimensions (horizontal axis). The fermions freely propagate in SM 3+1 dimensions (not shown) and are stuck at different locations along the extra-dimensional z coordinate of the SM brane. The gauge and Higgs fields' wave functions occupy the whole width of the thick wall. The overlap between fermion and Higgs wave functions gives the strength of Yukawa coupling. If quarks and leptons live on opposite ends of the wall protons are stable [119].

[2] A wormhole is a hypothetical passage through space-time that could create shortcuts between two otherwise distant points of the space-time (also known as Einstein-Rosen bridge).

A.3 Warped Extra Dimensions

Another ED scenario addressing the hierarchy problem is the warped extra dimensional approach proposed by Randal and Sundrum [28]. Here the ED is not flat, but is "warped", i.e. the four-dimensional metric is multiplied by a warp factor of $e^{-2kr_c\phi}$, where k is the curvature (of the Planck-scale order), $0 \leq \phi \leq \pi$ is the coordinate for an extra dimension, and r_c is the size of the ED. The gravity originates on the positive tension Planck-scale brane at $\phi = 0$. The SM brane with negative tension bounds the ED at $\phi = \pi$. The M_{Pl}-size operators will suffer the exponential suppression along the 5th dimension – on the $\phi = \pi$ brane it will be $\Lambda \sim M_{Pl}e^{-2kr_c\pi}$. If we require Λ to be about 1 TeV, then everything on the SM brane will naturally be of the weak scale – masses, forces, etc. (Fig. A.3 left). This is already achieved for $kr_c \approx 10$, meaning the hierarchy problem can be naturally solved by taking the only fundamental scale in the problem for the size of the ED – $r \sim 1/M_{Pl}$. The source of the hierarchy between the Planck and the weak scale is an exponential function of the compactification radius, and not the largeness of the radius itself (making the gravity diluted), as is the case for e.g. flat ED in ADD case.

The finite Randal-Sundrum (RS) extra dimension gives the tower of KK gravitons. They all interact with the fields on the SM brane with a $\sim$ TeV-scale coupling, by construction. The 0th mode is massless and its wave function has exponentially small overlap with the weak brane, yielding our well-known 4D gravity. Higher KK modes, which can be produced if there is enough energy available, decay to pairs of SM particles and can be observed at the LHC as spin-2 resonances (e.g. in diphoton or dilepton channels). In RS model it is also possible that other SM fields propagate in the ED [120]. Since the branes are so close, the wave function would not leak a lot, and we could observe e.g. the KK resonances of other bosons. In fact, due to the hierarchy problem, the only field really confined to the weak brane is the Higgs. The overlap of the wave function of other particles propagating in the bulk with the weak brane would determine the mass of the particle (Fig. A.3 right).

The RS scenario is also possible with the infinite 5th dimension [121]. The hierarchy problem is solved as long as the Higgs field is confined to the weak brane, and the 0th graviton mode is exponentially suppressed there. In this case, higher KK graviton modes (in fact a continuum) do not produce resonances. Instead, they decay to sub-TeV gravitons producing the missing energy signature, similar to ADD scenario.

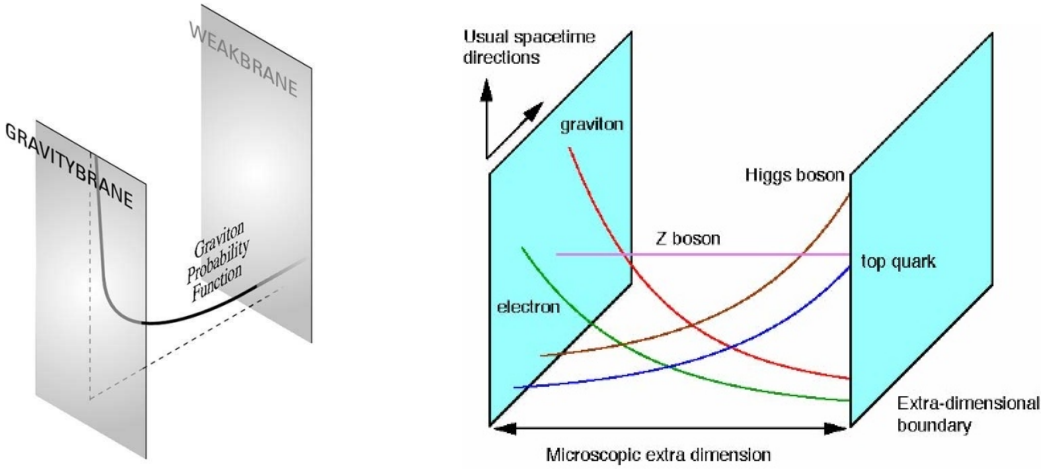

Figure A.3: Randal-Sundrum model of warped extra dimension. Left: Gravity is exponentially suppressed on the weak brane. Right: Overlaps of particle wave functions with the Higgs brane determine their mass.

Appendix B

More details on the results

B.1 Acceptance, efficiencies and cross sections of the mUED signal

Visible cross section of a process is defined as

$$\sigma_{vis} = \sigma_{theo} \times \mathcal{A} \times \epsilon, \tag{B.1}$$

where $\mathcal{A}$ is the acceptance and ϵ is the experimental efficiency. In practice, the acceptance is computed by dividing the number of MC events at the truth level (before the detector reconstruction simulation) in the signal region by the total number of events generated. The acceptance times the efficiency is calculated by dividing the number of MC events in the signal region after the reconstruction by the product of the production cross section and the integrated luminosity. Finally, the reconstruction efficiency can be evaluated by simply dividing those two numbers. $\mathcal{A}$, ϵ and $\mathcal{A} \times \epsilon$, along with the production sections for all the generated mUED points, are shown in Figs. B.1 and B.2.

B.2 Systematic uncertainties in the validation regions

Tables B.1-B.3 are showing five dominant sources of systematic uncertainties for the background-only fit in each validation region.

B.3 Additional exclusion-fit tables

The breakdown of the uncertainty on the total background estimate in the signal region for the exclusion fit performed for the (R^{-1} = 900 GeV, $\Lambda R = 10$) point is shown in Tab. B.4. The uncertainties on the signal normalisation and on the fake muon background estimation are dominant. The after-fit values of individual nuisance parameters are shown in Fig. B.3.

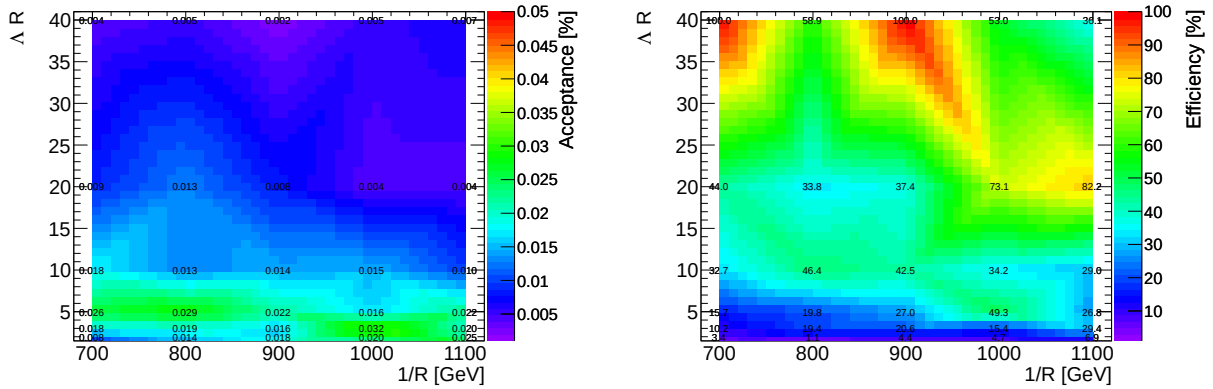

Figure B.1: Signal acceptance and experimental efficiecies for all the generated mUED points.

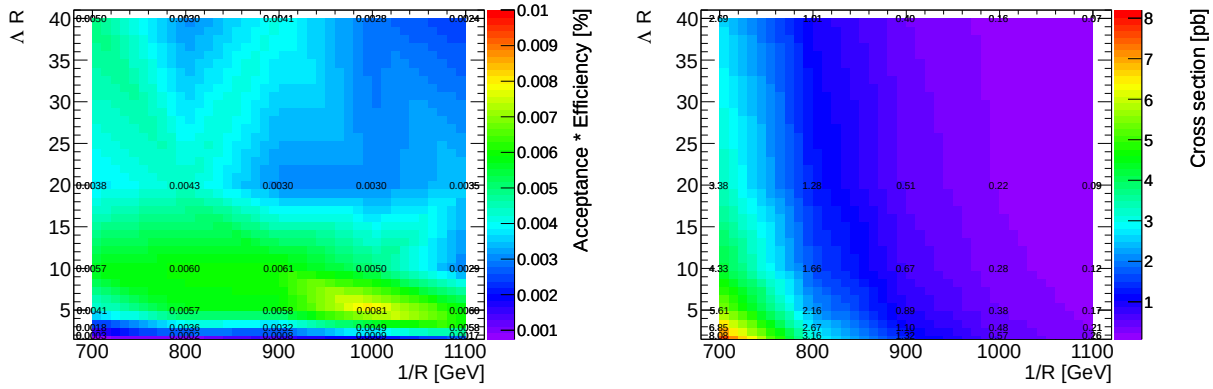

Figure B.2: Acceptance times the experimental efficiecies and cross sections for all the generated mUED points.

Systematic uncertinties (background-only fit)	VR1
Total background expectation	116.67
Total statistical ($\sqrt{N_{\text{exp}}}$)	$\pm$10.80
Total background systematic	$\pm$21.78 [18.67%]
Fake muons prediction	$\pm$17.25 [14.8%]
$\mu_{t\bar{t}}$	$\pm$11.40 [9.8%]
$t\bar{t}$: Powheg vs. Alpgen	$\pm$5.59 [4.8%]
Trigger efficiency	$\pm$5.17 [4.4%]
Lepton efficiencies	$\pm$4.21 [3.6%]

Table B.1: Breakdown of the dominant systematic uncertainties on the background estimate in VR1. The individual uncertainties can be correlated, and do not necessarily add up quadratically to the total background uncertainty. The percentages show the size of the uncertainty relative to the total expected background. Only five dominant sources of the uncertainty are shown.

Systematic uncertinties (background-only fit)	VR2
Total background expectation	47.08
Total statistical ($\sqrt{N_{\text{exp}}}$)	$\pm$6.86
Total background systematic	$\pm$9.51 [20.21%]
Dibosons: theory envelope	$\pm$4.16 [8.8%]
$t\bar{t}$: theory envelope	$\pm$3.50 [7.4%]
B-tagging: b-tag efficiency	$\pm$2.98 [6.3%]
$t\bar{t}$: Powheg vs. Alpgen	$\pm$2.96 [6.3%]
B-tagging: light-jet mistag efficiency	$\pm$2.92 [6.2%]

Table B.2: Breakdown of the dominant systematic uncertainties on the background estimate in VR2. The individual uncertainties can be correlated, and do not necessarily add up quadratically to the total background uncertainty. The percentages show the size of the uncertainty relative to the total expected background. Only five dominant sources of the uncertainty are shown.

Systematic uncertinties (background-only fit)	VR3
Total background expectation	21.55
Total statistical ($\sqrt{N_{\text{exp}}}$)	± 4.64
Total background systematic	± 7.46 [34.62%]
Fake muons prediction	± 6.74 [31.3%]
$\mu_{t\bar{t}}$	± 2.24 [10.4%]
$t\bar{t}$: Powheg vs. Alpgen	± 2.04 [9.5%]
Lepton efficiencies	± 1.14 [5.3%]
Trigger efficiency	± 0.87 [4.0%]

Table B.3: Breakdown of the dominant systematic uncertainties on the background estimate in VR3. The individual uncertainties can be correlated, and do not necessarily add up quadratically to the total background uncertainty. The percentages show the size of the uncertainty relative to the total expected background. Only five dominant sources of the uncertainty are shown.

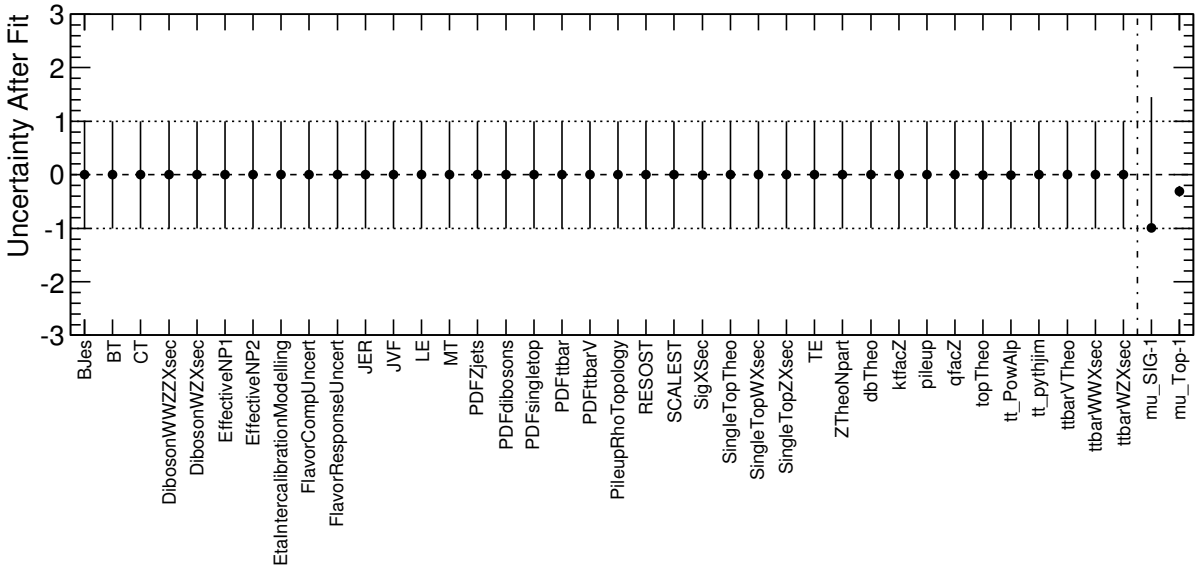

Figure B.3: Nuisance parameters values and their errors in the signal region after the exclusion fit performed for the ($R^{-1} = 900$ GeV, $\Lambda R = 10$) mUED point.

Systematic uncertainties (exclusion fit, $R^{-1} = 900$ GeV, $\Lambda R = 10$)	SR
Total background expectation	6.07
Total statistical ($\sqrt{N_{\text{exp}}}$)	± 2.46
Total background systematic	± 4.14 [68.23%]
μ_{Sig}	± 5.13 [84.4%]
Fake lepton prediction	± 2.10 [34.5%]
$t\bar{t}$: Powheg vs. Alpgen	± 0.51 [8.4%]
MC statistics	± 0.41 [6.8%]
JES: flavor composition	± 0.32 [5.2%]
$t\bar{t}$: theory envelope	± 0.31 [5.2%]
Dibosons: theory envelope	± 0.30 [4.9%]
$t\bar{t}$: Pythia vs. Herwig/Jimmy	± 0.27 [4.4%]
$\mu_{t\bar{t}}$	± 0.27 [4.4%]
JES: EffectiveNP2	± 0.23 [3.8%]
B-tagging: light-jet mistag efficiency	± 0.22 [3.7%]
B-tagging: b-tag efficiency	± 0.22 [3.6%]
JES: flavor response	± 0.21 [3.5%]
JES: b-jets	± 0.21 [3.5%]
Trigger efficiency	± 0.19 [3.1%]
JES: EtaIntercalibrationModelling	± 0.14 [2.3%]
Single-top: theory envelope	± 0.13 [2.1%]
Lepton efficiency	± 0.11 [1.9%]
Z+jets: renormalisation scale	± 0.09 [1.5%]
Jets: resolution	± 0.09 [1.5%]
JES: EffectiveNP1	± 0.08 [1.3%]
E_T^{miss}: scale	± 0.08 [1.3%]
JES: PileupRhoTopology	± 0.07 [1.2%]
Z+jets: ME partons	± 0.07 [1.2%]
Dibosons: PDF	± 0.06 [0.93%]
WW/ZZ: cross section	± 0.06 [0.93%]
Lumi	± 0.05 [0.78%]
Z+jets: factorisation scale	± 0.04 [0.63%]
B-tagging: c-jet mistag efficiency	± 0.04 [0.61%]
Single-top: PDF	± 0.03 [0.53%]
Signal uncertainties	± 0.02 [0.35%]
Z+jets: PDF	± 0.02 [0.32%]
Pileup	± 0.02 [0.31%]

Table B.4: Breakdown of the dominant systematic uncertainties on the background estimate in the signal region, after the exclusion fit. The individual uncertainties can be correlated, and do not necessarily add up quadratically to the total background uncertainty. The percentages show the size of the uncertainty relative to the total expected background. The uncertainties amounting to less than 0.3% are not shown.

B.4 Correlation matrices for the background-only and the exclusion fit

The matrices showing correlations between different nuisance parameters in the background-only and exclusion fits are shown in Figs. B.4 and B.5. For the background-only fit, the anti-correlation between the trigger efficiency uncertainty and the normalisation parameter $\mu_{t\bar{t}}$ is the largest, followed by the anti-correlations between the uncertainty on the fake muon prediction and $\mu_{t\bar{t}}$, and between theoretical uncertainty on the single-top prediction and $\mu_{t\bar{t}}$. These correlations reflect the fact that different shifts of nuisance parameter values may lead to the same result. Whether, e.g., the trigger efficiency parameter value is increased, or $\mu_{t\bar{t}}$ is decreased, the resulting data vs. SM expectation agreement in the control region will be the same and the fit can not distinguish between these two configurations. For the exclusion fit, in addition to the same anti-correlations observed for $\mu_{t\bar{t}}$, μ_{Sig} is found to be anti-correlated with the uncertainty on the fake muon background estimation, as this is the largest systematic in the signal region.

B.5 Observed upper limits on the signal cross section

The upper limit on the signal cross section is derived for each $(R^{-1}, \Lambda R)$ point. The number of signal events in the signal region is taken from the MC expectation for the $(R^{-1}, \Lambda R)$ point in question. The signal strength parameter is scanned from $\mu_{\mathrm{Sig}} = 0$ up to a reasonably high value, depending on the model. Each time a hypothesis test is performed in which the data is tested against the background+signal model, where the amount of signal contribution is determined by μ_{Sig}. The result of the scan for the ($R^{-1} = 900$ GeV, $\Lambda R = 10$) point is shown in Fig. B.6. The value of μ_{Sig} for which the $\mathrm{CL_S}$ value (signified p-value in Fig. B.6) results in 0.05 was found to be close to 1, meaning the cross section of the ($R^{-1} = 900$ GeV, $\Lambda R = 10$) point is just about excluded, and lies on top of the exclusion contour in Fig. B.7. The upper limits on the signal cross sections are shown as black numbers in the Fig. B.7. The upper limits on the signal points inside the excluded region are smaller than the theoretical cross sections, while the limits on the points which are not excluded are higher than their respective theoretical cross sections.

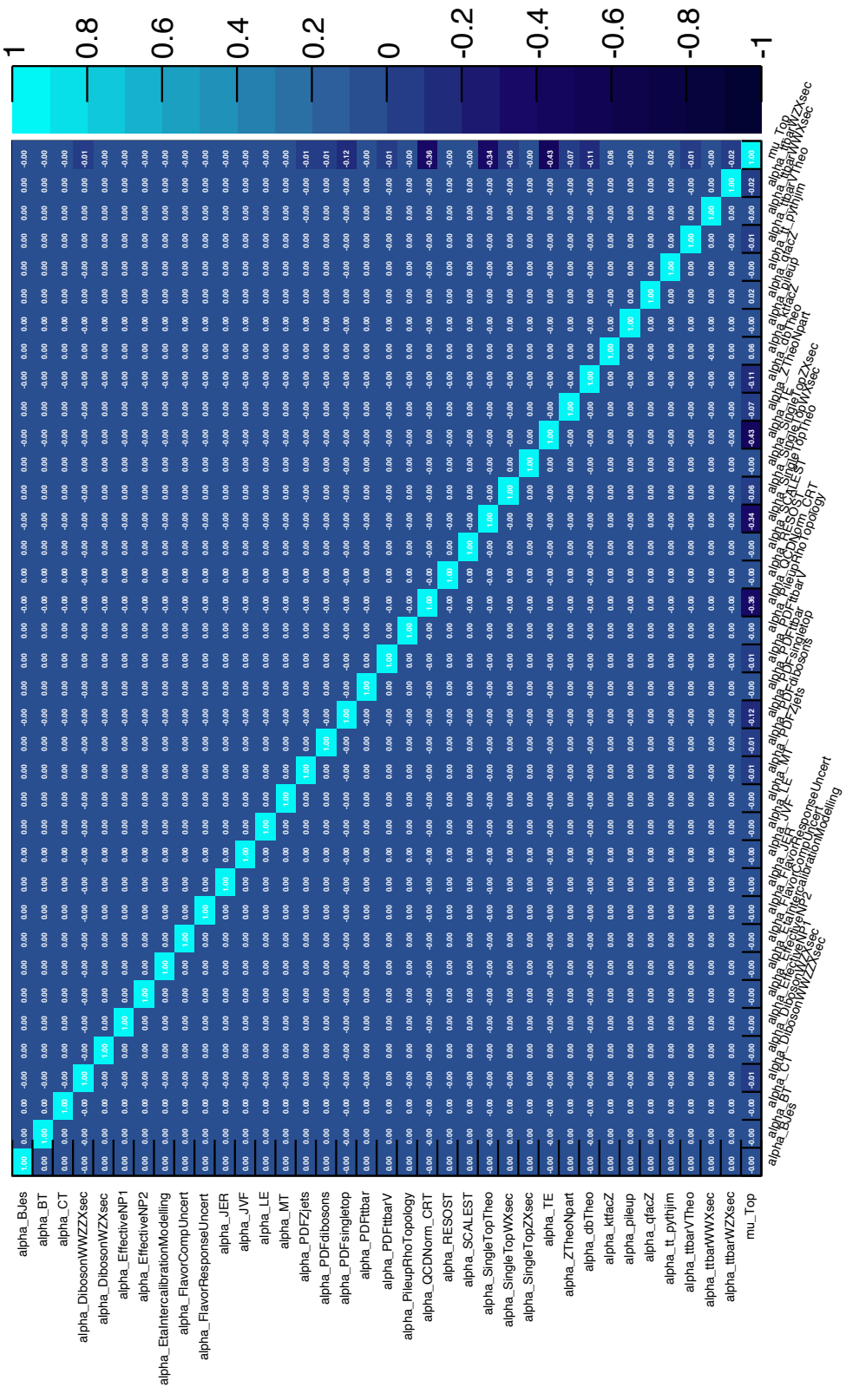

Figure B.4: Correlation matrix of the nuisance paramaters in the background-only fit.

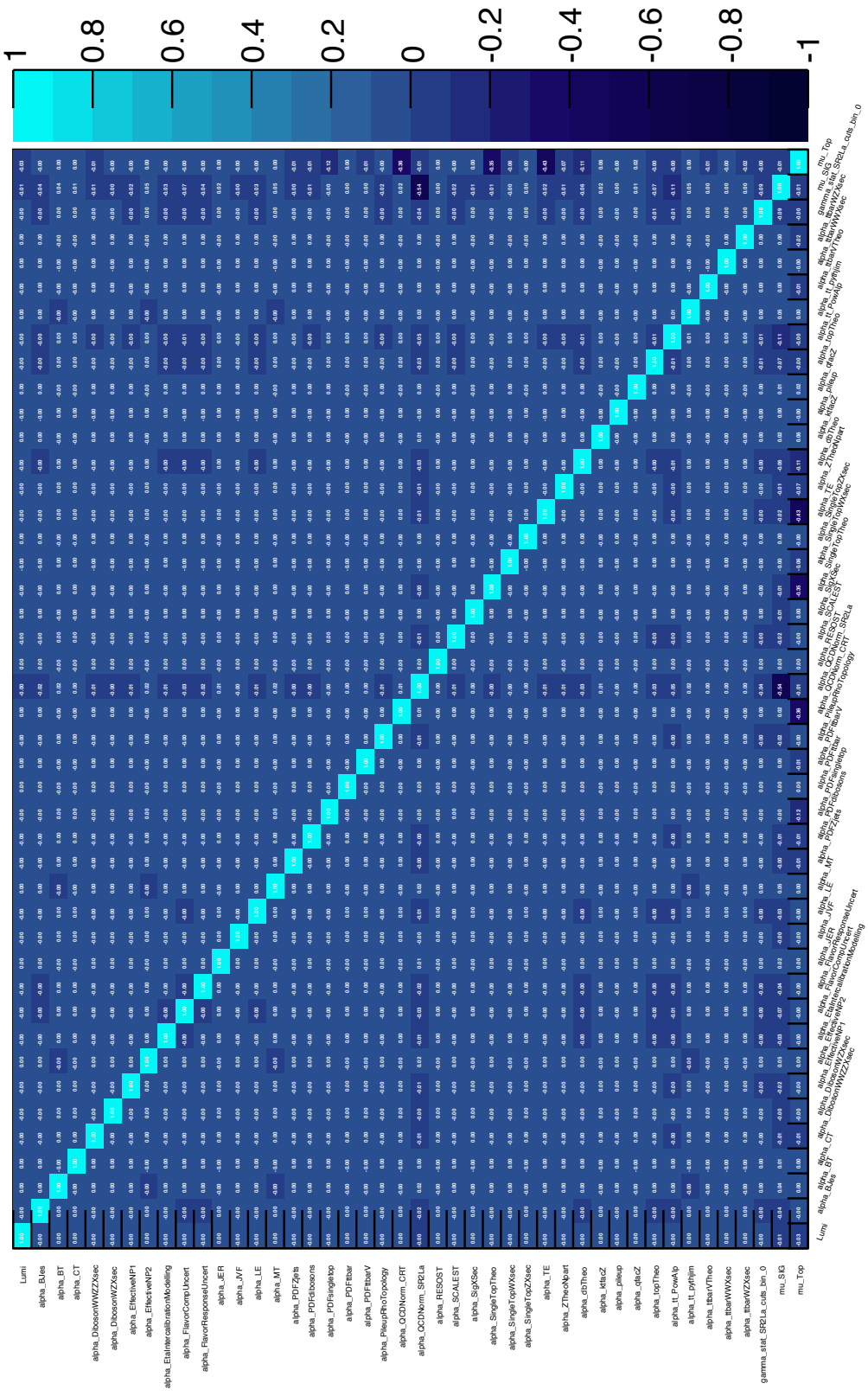

Figure B.5: Correlation matrix of the nuisance parameters in the exclusion fit. mUED signal with $R^{-1} = 900$ GeV and $\Lambda R = 10$ is used.

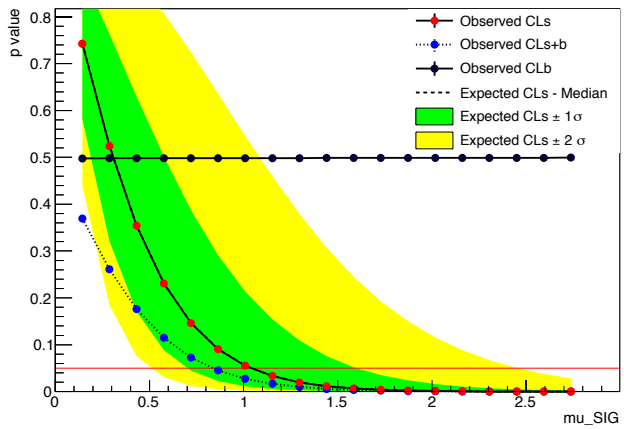

Figure B.6: Scan of μ_{Sig} when deriving the upper limit on the visible cross section of the ($R^{-1} = 900$ GeV, $\Lambda R = 10$) signal model. The result is obtained by using the asymptotic formulae. Observed $\mathrm{CL_S}$, $\mathrm{CL_{s+b}}$ and $\mathrm{CL_b}$ values are shown in red, blue and black dots, respectively. The median expected $\mathrm{CL_S}$ is denoted as a black dashed line, residing directly below the observed one, with the green (yellow) bands indicating the $\pm 1\sigma$ ($\pm 2\sigma$) uncertainty on the expected $\mathrm{CL_S}$.

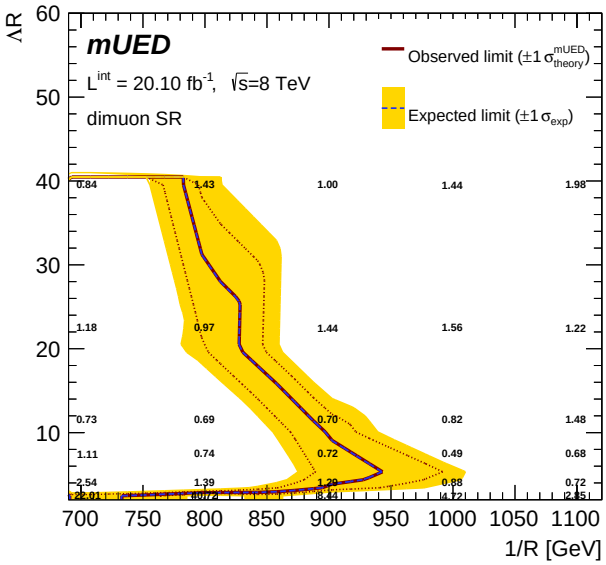

Figure B.7: 95% CL exclusion limits in the mUED model. The blue dashed line shows the expected limits, with the yellow band indicating the $\pm 1\sigma$ variation in the median expected limit due to the experimental and background-only theory uncertainties. The observed nominal limit is indicated by the solid dark red line with the dark red dotted lines being obtained by taking into account the theoretical uncertainties on the signal cross section. The numbers inside the plot show the 95% CL upper limits on the visible cross sections, in fb.

Bibliography

[1] A. D. Martin and F. Halzen, *Quarks and Leptons: An Introductory Course in Modern Particle Physics*, Wiley, New York, 1984.

[2] F. Englert and R. Brout, *Broken Symmetry and the Mass of Gauge Vector Mesons*, Phys. Rev. Lett **13**, 321 (1964), `http://journals.aps.org/prl/pdf/10.1103/PhysRevLett.13.321`.

[3] Peter W. Higgs, *Broken Symmetries and the Masses of Gauge Bosons*, Phys. Rev. Lett **13**, 508 (1964), `http://journals.aps.org/prl/pdf/10.1103/PhysRevLett.13.508`.

[4] ATLAS Collaboration, *Observation of a new particle in the search for the Standard Model Higgs boson with the ATLAS detector at the LHC*, Phys. Lett. B **716** (2012) 1, `arXiv:1207.7214 [hep-ex]`.

[5] CMS Collaboration, *Observation of a new boson at a mass of 125 GeV with the CMS experiment at the LHC*, Phys. Lett. B **716** (2012) 30, `arXiv:1207.7235 [hep-ex]`.

[6] "The Nobel Prize in Physics 2013", *Nobelprize.org*, `http://www.nobelprize.org/nobel_prizes/physics/laureates/2013/`.

[7] Wikipedia, *Standard Model*, `http://en.wikipedia.org/wiki/Standard_Model`.

[8] David J. Gross, *The role of symmetry in fundamental physics*, Proc. Natl. Acad. Sci. USA, Vol. 93, 1996, `http://www.pnas.org/content/93/25/14256.full`.

[9] Jonathan L. Rosner, *The Standard Model in 2001*, `arXiv:hep-ph/0108195v6`.

[10] C.D. Froggatt, H.B. Nielsen, *Trying to understand the Standard Model parameters*, Surveys High Energ.Phys. **18** (2003), `arXiv:hep-ph/0308144`.

[11] Annika H. G. Peter, *Dark Matter: A Brief Review*, `arXiv:1201.3942 [astro-ph.CO]`.

[12] Hsin-Chia Cheng, Jonathan L. Feng, Konstantin T. Matchev, *Kaluza-Klein Dark Matter*, Phys. Rev. Lett. **89**, 211301 (2002), `arXiv:hep-ph/0207125`.

[13] G. Servant and T. M. P. Tait, *Is the lightest Kaluza-Klein particle a viable dark matter candidate?*, Nucl. Phys. B. **650** 391 (2003), `arXiv:hep-ph/0206071`.

[14] K.Griest, *Cross sections, relic abundance, and detection rates for neutralino dark matter*, Phys.Rev. D **38**, 2357 (1988), .

[15] Jaan Einasto, *Dark Matter*, Astronomy and Astrophysics 2010, `arXiv:0901.0632 [astro-ph.CO]`.

[16] *Does Dark Matter affect the motion of the Solar System?*, `http://scienceblogs.com/startswithabang/2013/07/03/does-dark-matter-affect-the-motion-`

[17] H. Kurki-Suonio, *Physics of the Cosmic Microwave Background and the Planck Mission*, `http://arxiv.org/abs/1012.5204v1`.

[18] Planck Collaboration, *Planck 2013 results. XVI. Cosmological parameters*, `arXiv:1303.5076`.

[19] WMAP web page, `http://lambda.gsfc.nasa.gov/product/map/current/`.

[20] G.Steigman and M.S.Turner, *Cosmological constraints on the properties of weakly interacting massive particles*, Nucl. Phys. B. **253**, 375 (1985).

[21] D. Hooper and S. Profumo, *Dark matter and collider phenomenology of universal extra dimensions* , Phys. Rept. **453** (2007) 29-115, `arXiv:hep-ph/0701197`.

[22] G. Steigman, B. Dasgupta, J. F. Beacom, *Precise Relic WIMP Abundance and its Impact on Searches for Dark Matter Annihilation*, Phys.Rev. D**86** (2012) 023506, `http://arxiv.org/abs/1204.3622`.

[23] D.J. Kapner et all., *Tests of the Gravitational Inverse-Square Law below the Dark-Energy Length Scale*, Phys.Rev.Lett. **98**, 021101 (2007), `http://arxiv.org/abs/hep-ph/0611184`.

[24] S.-Q. Yang et all., *Test of the Gravitational Inverse Square Law at Millimeter Ranges*, Phys.Rev.Lett. **108**, 081101 (2012).

[25] M. Shifman, *LARGE EXTRA DIMENSIONS: Becoming acquainted with an alternative paradigm*, Int.J.Mod.Phys. **A25**, 199 (2010), `arXiv:0907.3074v2`

[26] T. Appelquist, H.-C. Cheng, and B. A. Dobrescu, *Bounds on universal extra dimensions*, Phys. Rev. **D64** (2001) 035002, `arXiv:hep-ph/0012100`.

[27] N. Arkani-Hamed, S. Dimopoulos and G. Dvali, *The Hierarchy Problem and New Dimensions at a Millimeter*, Phys. Lett. **B429**, 263 (1998), `arXiv:hep-ph/9803315v1`.

[28] L. Randall and R. Sundrum, *A Large Mass Hierarchy from a Small Extra Dimension*, Phys. Rev. Lett **83**, 3370 (1999), `arXiv:hep-ph/9905221`.

[29] H.-C. Cheng, K. Matchev, and M. Schmaltz, *Bosonic Supersymmetry? Getting Fooled at the LHC*, Phys. Rev. **D66** (2002) 56006., `arXiv:hep-ph/0205314v1`

[30] Cosmin Macesanu, *The Phenomenology of Universal Extra Dimensions at Hadron Colliders*, Int.J.Mod.Phys. **A21** (2006) 2259-2296, `arXiv:hep-ph/0510418`.

[31] Super-Kamiokande Collaboration, *Search for proton decay via $p \to \nu K^+$ using 260 kiloton·year data of Super-Kamiokande*, Phys.Rev. D **90** (2014) 072005.

[32] Thomas Appelquist, Bogdan A. Dobrescu, Eduardo Ponton, Ho-Ung Yee, *Proton Stability in Six Dimensions*, Phys.Rev.Lett. **87** (2001) 181802, `arXiv:hep-ph/0107056`.

[33] Bogdan A. Dobrescu, Erich Poppitz, *Number of Fermion Generations Derived from Anomaly Cancellation*, Phys.Rev.Lett. **87** (2001) 031801, `arXiv:hep-ph/0102010`.

[34] G. Burdman and A. G. Dias, *The Little Hierarchy in Universal Extra Dimensions* , JHEP **0701** (2007) 041, `http://arxiv.org/abs/hep-ph/0609181`.

[35] Hsin-Chia Cheng, Konstantin T. Matchev, Martin Schmaltz, *Radiative Corrections to Kaluza-Klein Masses*, Phys.Rev. **D66:**036005,2002, `arXiv:hep-ph/0204342`.

[36] A. Belyaev, M. Brown, J. Moreno, C. Papineau, *Discovering Minimal Universal Extra Dimensions (MUED) at the LHC*, JHEP **1306**, (2013) 080, `arXiv:1212.4858v4`.

[37] E. Komatsu et. al., *Seven-Year Wilkinson Microwave Anisotropy Probe (WMAP) Observations: Cosmological Interpretation*, Astrophys. J. Suppl. 192:18 2011, `arXiv:1001.4538`.

[38] Takuya Kakuda, Kenji Nishiwaki, Kin-ya Oda, Ryoutaro Watanabe, *Universal extra dimensions after Higgs discovery*, Phys.Rev. **D88**, 035007 (2013), `arXiv:1305.1686 [hep-ph]`.

[39] M. E. Peskin and T. Takeuchi, *A New constraint on a strongly interacting Higgs sector*, Phys.Rev.Lett. **65** (1990), 964967.

[40] M. E. Peskin and T. Takeuchi, *Estimation of oblique electroweak corrections*, Phys.Rev. **D46**(1992), 381409.

[41] G. Belanger, M. Kakizaki, A. Pukhov, *Dark matter in UED : the role of the second KK level*, JCAP **1102** (2011), 009, `arXiv:1012.2577 [hep-ph]`.

[42] D0 Collaboration, *Search for universal extra dimensions in $p\bar{p}$ collisions*, Phys. Rev. Lett. **108**, 131802 (2012), `arXiv:1112.4092 [hep-ex]`.

[43] ATLAS Collaboration, *Search for strongly produced supersymmetric particles in decays with two leptons at $\sqrt{s}$= 8 TeV*, ATLAS-CONF-2013-089, `http://cds.cern.ch/record/1595272`.

[44] ATLAS Collaboration, *Search for squarks and gluinos with the ATLAS detector in final states with jets and missing transverse momentum and 20.3 fb^{-1} of $\sqrt{s}$ = 8 TeV proton-proton collision data*, ATLAS-CONF-2013-047, `http://cds.cern.ch/record/1547563`.

[45] ATLAS Collaboration, *Search for squarks and gluinos in events with isolated leptons, jets and missing transverse momentum at $\sqrt{s}$=8 TeV with the ATLAS detector*, ATLAS-CONF-2013-062, `http://cds.cern.ch/record/1557779`.

[46] Lisa Edelhuser, Thomas Flacke, Michael Krmer, *Constraints on models with universal extra dimensions from dilepton searches at the LHC*, JHEP **1308** (2013) 091, `arXiv:1302.6076 [hep-ph]`.

[47] CMS Collaboration, *Search for Resonances in the Dilepton Mass Distribution in pp Collisions at $\sqrt{s}$ = 8 TeV*, CMS-PAS-EXO-12-061, (2012).

[48] Jonathan M. Cornell, Stefano Profumo, William Shepherd, *Dark Matter in Minimal Universal Extra Dimensions with a Stable Vacuum and the "Right" Higgs*, Phys. Rev. **D89**, 056005 (2014), `arXiv:1401.7050 [hep-ph]`.

[49] S. Bethke, *The 2009 World Average of α_S*, Eur. Phys. J. **C64** (2009) 689, `http://arxiv.org/abs/0908.1135`.

[50] P. Nadolsky, J. Gao, M. Guzzi, J. Huston, H.-L. Lai, Z. Li, J. Pumplin, D. Stump, C.-P. Yuan, *Progress in CTEQ-TEA PDF analysis*, `http://arxiv.org/abs/arXiv:1206.3321`.

[51] G. P. Salam, *Elements of QCD for hadron colliders*, `arXiv:1011.5131v2 [hep-ph]`.

[52] ATLAS Public Results Web Page, http://twiki.cern.ch/twiki/bin/view/AtlasPublic/.

[53] ATLAS Collaboration, *The ATLAS Experiment at the CERN Large Hadron Collider*, JINST **3** (2008) S08003.

[54] ATLAS Collaboration, *Improved luminosity determination in pp collisions at $\sqrt{s}$ = 7 TeV using the ATLAS detector at the LHC*, Eur. Phys. J. **C73** (2013) 2518, `http://arxiv.org/abs/1302.4393`.

[55] S. van der Meer, *Calibration of the effective beam height in the ISR*, Tech. Rep. CERN-ISR-PO-68-31, 1968.

[56] GEANT4 Collaboration, S. Agostinelli et al., *GEANT4: A Simulation toolkit*, Nucl. Instrum. Meth. **A506** (2003) 250-303.

[57] S. Catani, F. Krauss, R. Kuhn, B.R. Webber, *QCD Matrix Elements + Parton Showers*, JHEP **0111** 063 (2001), `http://arxiv.org/abs/hep-ph/0109231v1`.

[58] T. Sjostrand, S. Mrenna, and P. Skands, *PYTHIA 6.4 physics and manual*, JHEP **05** (2006) 026, `arXiv:hep-ph/0603175`.

[59] Corcella, G. and others, *HERWIG 6: An Event generator for hadron emission reactions with interfering gluons (including supersymmetric processes)*, JHEP **0101** (2001) 010, `arXiv:hep-ph/0011363 [hep-ph]`.

[60] Butterworth, J.M. and Forshaw, Jeffrey R. and Seymour, M.H., *Multiparton interactions in photoproduction at HERA*, Z. Phys. **C72** (1996) 637646, `arXiv:hep-ph/9601371 [hep-ph]`.

[61] T. Gleisberg et al., *Event generation with Sherpa 1.1*, JHEP **02** (2009) 007, `0811.4622 [hep-ph]`.

[62] M. L. Mangano, M. Moretti, F. Piccinini, R. Pittau, and A. D. Polosa, *ALPGEN, a generator for hard multiparton processes in hadronic collisions*, JHEP **0307** (2003) 001, `arXiv:hep-ph/0206293 [hep-ph]`.

[63] J. Alwall, M. Herquet, F. Maltoni, O. Mattelaer, and T. Stelzer, *MadGraph 5 : Going Beyond*, JHEP **1106** (2011) 128, `arXiv:1106.0522 [hep-ph]`.

[64] B. P. Kersevan and E. Richter-Was, *The Monte Carlo event generator AcerMC version 2.0 with interfaces to PYTHIA 6.2 and HERWIG 6.5*,`arXiv:hep-ph/0405247 [hep-ph]`.

[65] S. Frixione and B. R. Webber, *Matching NLO QCD computations and parton shower simulations*, JHEP **0206** (2002) 029, `arXiv:hep-ph/0204244 [hep-ph]`.

[66] S. Frixione, P. Nason, G. Ridolfi, *A Positive-Weight Next-to-Leading-Order Monte Carlo for Heavy Flavour Hadroproduction*, JHEP **0709** (2007) 126, `arXiv:hep-ph/0707.3088`.

[67] P. Nason, *A New Method for Combining NLO QCD with Shower Monte Carlo Algorithms*, JHEP **11** (2004) 040, `arXiv:hep-ph/0409146`.

[68] S. Frixione, P. Nason and C. Oleari, *Matching NLO QCD computations with Parton Shower simulations: the POWHEG method*, JHEP **11** (2007) 070, `arXiv:hep-ph/0709.2029`.

[69] S. Alioli, P. Nason, C. Oleari, E. Re, *A general framework for implementing NLO calculations in shower Monte Carlo programs: the POWHEG BOX*, JHEP **06** (2010) 043, `arXiv:hep-ph/1002.2581`.

[70] Roberto Pittau, *Status of MadLoop/aMC@NLO*, http://arxiv.org/abs/1202.5781.

[71] K. Melnikov and F. Petriello, *Electroweak gauge boson production at hadron colliders through O(alpha(s)**2)*, Phys. Rev. **D74** (2006) 114017, arXiv:hep-ph/0609070 [hep-ph].

[72] M. Aliev et al., *HATHOR: HAdronic Top and Heavy quarks crOss section calculatoR*, Comput. Phys. Commun. **182** (2011) 10341046, arXiv:1007.1327 [hep-ph].

[73] N. Kidonakis, *Next-to-next-to-leading-order collinear and soft gluon corrections for t-channel single top quark production*, Phys. Rev. **D83** (2011) 091503, arXiv:1103.2792 [hep-ph].

[74] N. Kidonakis, *NNLL resummation for s-channel single top quark production*, Phys. Rev. **D81** (2010) 054028, arXiv:1001.5034 [hep-ph].

[75] N. Kidonakis, *Two-loop soft anomalous dimensions for single top quark associated production with a W- or H-*, Phys. Rev **D82** (2010) 054018, arXiv:1005.4451 [hep-ph].

[76] J. M. Campbell, R. Ellis, and D. L. Rainwater, *Next-to-leading order QCD predictions for W + 2 jet and Z + 2 jet production at the CERN LHC*, Phys. Rev. **D68** (2003) 094021, arXiv:hep-ph/0308195 [hep-ph].

[77] J. M. Campbell and R. K. Ellis, *$t\bar{t}$ W production and decay at NLO*, JHEP **1207** (2012) 052, arXiv:hep-ph/1204.5678 [hep-ph].

[78] A. Lazopoulos, T. McElmurry, K. Melnikov, and F. Petriello, *Next-to-leading order QCD corrections to t t Z production at the LHC*, Phys.Lett. **B666** (2008) 62, arXiv:hep-ph/0804.2220 [hep-ph].

[79] J. Pumplin et al, *New generation of parton distributions with uncertainties from global QCD analysis*, JHEP **0207** (2002) 012, arXiv:hep-ph/0201195 [hep-ph].

[80] H.-L. Lai et al., *New parton distributions for collider physics*, Phys. Rev. **D82** (2010) 074024, arXiv:1007.2241 [hep-ph].

[81] S. Catani, L. Cieri, G. Ferrera, D. de Florian, M. Grazzini, Phys. Rev. Lett. **103** 082001 (2009), arXiv:0903.2120 [hep-ph]; S. Catani, M. Grazzini, Phys. Rev. Lett. **98** 222002 (2007), hep-ph/0703012.

[82] Martin, A.D. and Stirling, W.J. and Thorne, R.S. and Watt, G., *Update of parton distributions at NNLO*, Phys. Lett. **B652** (2007) 292299, arXiv:0706.0459 [hep-ph].

[83] M. Bahr et al., *Herwig++ Physics and Manual*, Eur.Phys. J. **C58** (2008) 639-707, http://xxx.lanl.gov/abs/0803.0883.

[84] ATLAS Collaboration, *Performance of the ATLAS Inner Detector Track and Vertex Reconstruction in the High Pile-Up LHC Environment*, ATLAS-CONF-2012-042, `https://cds.cern.ch/record/1435196`.

[85] ATLAS Collaboration, *Performance of primary vertex reconstruction in proton-proton collisions at* $\sqrt{s} = 7$ *TeV*, ATLAS-CONF-2010-069, `https://cds.cern.ch/record/1281344`.

[86] R. Fruhwirth, W. Waltenberger, P. Vanlaer, *Adaptive vertex fitting*, J. Phys. **G34** (2007).

[87] ATLAS Collaboration, *Measurement of the muon reconstruction performance of the ATLAS detector using 2011 and 2012 LHC proton-proton collision data*, submitted to EPJC, `http://arxiv.org/abs/1407.3935`.

[88] ATLAS Collaboration, *A measurement of the ATLAS muon reconstruction and trigger efficiency using* J/Ψ *decays*, ATLAS-CONF-2011-021, `https://cds.cern.ch/record/1336750`.

[89] ATLAS Collaboration, *Preliminary results on the muon reconstruction efficiency, momentum resolution, and momentum scale in ATLAS 2012 pp collision data*, ATLAS-CONF-2013-088 (2013), `https://cds.cern.ch/record/1580207/`.

[90] ATLAS collaboration, *Electron reconstruction and identification efficiency measurements with the ATLAS detector using the 2011 LHC proton-proton collision data*, Eur. Phys. **J. C74** (2014) 2941, `http://arxiv.org/abs/1404.2240`.

[91] ATLAS collaboration, *Electron efficiency measurements with the ATLAS detector using the 2012 LHC proton-proton collision data*, ATLAS-CONF-2014-032, `https://cds.cern.ch/record/1706245`.

[92] ATLAS Collaboration, *Electron and photon energy calibration with the ATLAS detector using LHC Run 1 data*, submitted to EPJC, `http://arxiv.org/abs/1407.5063`.

[93] M. Aharrouche et al. [ATLAS Electromagnetic Barrel Calorimeter Collaboration], *Energy Linearity and Resolution of the ATLAS Electromagnetic Barrel Calorimeter in an Electron Test-Beam*, Nucl. Instrum. Meth. **A 568** (2006) 601, `http://arxiv.org/abs/physics/0608012v1`.

[94] M. Cacciari, G. P. Salam, and G. Soyez, *The anti-kt jet clustering algorithm*, J. High Energy Phys. **04** (2008), `arXiv:0802.1189 [hep-ph]`.

[95] ATLAS Collaboration, *Jet energy measurement with the ATLAS detector in proton-proton collisions at* $\sqrt{s} = 7$ *TeV*, Eur. Phys. J. **C73** (2013) 2304, `arXiv:1112.6426 [hep-ex]`.

[96] ATLAS Collaboration, *Jet energy scale and its systematic uncertainty in proton-proton collisions at $\sqrt{s}$ = 7 TeV with ATLAS 2011 data*, ATLAS-CONF-2013-004 (2013), `http://cds.cern.ch/record/1509552`.

[97] ATLAS Collaboration, *Pile-up subtraction and suppression for jets in ATLAS*, ATLAS-CONF-2013-083, `https://cds.cern.ch/record/1570994`.

[98] ATLAS Collaboration, *Jet energy resolution in proton-proton collisions at $\sqrt{s} = 7$ TeV recorded in 2010 with the ATLAS detector*, Eur. Phys. J. **C73** 3 (2013) 2306, `http://arxiv.org/abs/1210.6210`.

[99] ATLAS Collaboration, *Commissioning of the ATLAS high-performance b-tagging algorithms in the 7 TeV collision data*, ATLAS-CONF-2011-102, `http://cds.cern.ch/record/1369219`.

[100] ATLAS Collaboration, *Measurement of the b-tag Efficiency in a Sample of Jets Containing Muons with 5 fb^1 of Data from the ATLAS Detector*, ATLAS-CONF-2012-043, `http://cds.cern.ch/record/1435197`.

[101] ATLAS Collaboration, *b-Jet Tagging Efficiency Calibration using the System8 Method*, ATLAS-CONF-2011-143, `http://cds.cern.ch/record/1386703`.

[102] ATLAS Collaboration, *Measuring the b-tag efficiency in a top-pair sample with 4.7 fb^1 of data from the ATLAS detector*, ATLAS-CONF-2012-097, `http://cds.cern.ch/record/1460443`.

[103] ATLAS Collaboration, *b-jet tagging calibration on c-jets containing D^+ mesons*, ATLAS-CONF-2012-039, `http://cds.cern.ch/record/1435193`.

[104] ATLAS Collaboration, *Measurement of the Mistag Rate with 5 fb^1 of Data Collected by the ATLAS Detector*, ATLAS-CONF-2012-040, `http://cds.cern.ch/record/1435194`.

[105] ATLAS Collaboration, *Performance of Missing Transverse Momentum Reconstruction in ATLAS studied in Proton-Proton Collisions recorded in 2012 at $\sqrt{s}$= 8 TeV*, ATLAS-CONF-2013-082 (2013), `http://cds.cern.ch/record/1570993/`.

[106] ATLAS Collaboration, *Performance of missing transverse momentum reconstruction in proton-proton collisions at 7 TeV with ATLAS*, Eur. Phys. J. **C72** (2012) 1844, `http://xxx.lanl.gov/abs/1108.5602`.

[107] Robert D. Cousins, James T. Linnemann, Jordan Tucker, *Evaluation of three methods for calculating statistical significance when incorporating a systematic uncertainty into a test of the background-only hypothesis for a Poisson process*, Nuclear Instruments and Methods in Physics Research **A 595** (2008) 480–501, `http://arxiv.org/abs/physics/0702156`.

[108] M. Baak, G.J. Besjes, D. Cote, A. Koutsman, J. Lorenz, D. Short, *HistFitter software framework for statistical data analysis*, `http://arxiv.org/abs/1410.1280`.

[109] K. Cranmer, *HistFactory User Guide*, `https://twiki.cern.ch/twiki/pub/RooStats/WebHome/HistFactoryLikelihood.pdf`

[110] *Internal:* ATLAS Collaboration, *Setting exclusion limits in ATLAS supersymmetry searches with a likelihood ratio based method*, Tech.Rep. ATL-COM-PHYS-2011-004, CERN, 2011.

[111] G. Cowan, *Statistics for Searches at the LHC*, `http://arxiv.org/abs/1307.2487`.

[112] S. Wilks, *The Large-Sample Distribution of the Likelihood Ratio for Testing Composite Hypotheses*, Ann. Math. Statist. **9** (1938) 6062.

[113] A. Wald, *Tests of Statistical Hypotheses Concerning Several Parameters When the Number of Observations is Large*, Transactions of the American Mathematical Society, Vol. **54**, No. 3, (1943) 426482.

[114] G. Cowan, K. Cranmer, E. Gross, and O. Vitells, *Asymptotic formulae for likelihood-based tests of new physics*, Eur. Phys. J. **C71** (2011) 1554, `arXiv:1007.1727 [physics.data-an]`.

[115] A. Read, *Presentation of search results: the CLs technique*, Journal of Physics G: Nucl. Part. Phys. **28** (2002) 2693–2704.

[116] S. Frixione, E. Laenen, P. Motylinski, B. Webber, C. D. White, *Single-top hadroproduction in association with a W boson*, JHEP **0807** (2008) 029, `http://arxiv.org/abs/0805.3067v1`.

[117] ATLAS Collaboration, *Search for squarks and gluinos in events with isolated leptons, jets and missing transverse momentum at* $\sqrt{s} = 8$ *TeV with the ATLAS detector*, submitted to JHEP, `arXiv:1501.03555`.

[118] Greg Landsberg, *Collider Searches for Extra Dimensions*, ECONF **C040802:** MOT006, 2004, `arXiv:hep-ex/0412028`.

[119] N. Arkani-Hamed and M. Schmaltz, *Hierarchies without Symmetries from Extra Dimensions*, Phys. Rev. D **61**, 033005 (2000), `arXiv:hep-ph/9903417v1`.

[120] Tony Gherghetta, *TASI Lectures on a Holographic View of Beyond the Standard Model Physics*, `arXiv:1008.2570 [hep-ph]`.

[121] L. Randall and R. Sundrum, *An Alternative to Compactification*, Phys. Rev. Lett **83**, 4690 (1999), `arXiv:hep-th/9906064`.

Acknowledgements

I would like to thank my thesis advisor Makoto Tomoto, first of all, for encouraging me to apply for the PhD program of Nagoya University and for supporting me during the application procedure. I appreciate very much being given this opportunity. I am also deeply thankful for his mentoring and all the physics discussions during the course of my studies. I would also like to express my gratitude to Naoko Kanaya for introducing me into the SUSY group and following my analysis from the its beginning, till the end. Without her help, it would have been almost impossible to push my research all the way from the initial studies and into the final ATLAS publication.

I am very happy to have been part of the SUSY strong production ≥ 1 lepton team. Good communication and genuine collaboration between the members provided me with a highly motivating and warm research environment. It is great pleasure to have been working with all the people involved in the group. I would also like to express gratitude to all the Nagoya ATLAS members, especially my senpai from whom I have received a lot of tutoring during my early research.

Finally, I thank all my friends and more than friends for all the emotional support during hard times, as well as all the nice times spent together both at CERN and in Nagoya. Lastly, I thank my family for always encouraging me to go for what I want and always providing a safe place to rest from the world.

Thank you all!